

THESIS

**Measurement of Cosmic Microwave  
Background Polarization Power Spectra  
at 43 GHz with Q/U Imaging Experiment**

(QUIET実験による43GHzでの宇宙マイクロ波背景放射偏光パワースペクトラムの測定)

A dissertation submitted to  
Astronomical Institute, Graduate School of Science,  
Tohoku University  
for the degree of Doctor of Philosophy

Yuji CHINONE

茅根 裕司

2010 (平成22年)



# Abstract

We can access the cosmological inflationary era and test the inflation theory by measuring polarization of the Cosmic Microwave Background radiation (CMB) precisely. The CMB polarization  $B$ -mode, which is defined as a curl component of the CMB polarization map on the sky, is related to primordial gravitational waves which were produced during inflation. According to the cosmological inflation theory, the potential energy of the scalar field is responsible for the exponential expansion of the universe at the very early time. Hence we can DIRECTLY probe inflation by observing the  $B$ -mode, and access the energy scale of the inflationary era, which is considered to be at the GUT (Grand Unified Theory) scale ( $\approx 10^{16}$  GeV).

The Q/U Imaging Experiment (QUIET) aims to detect the  $B$ -mode. Since amplitude of the  $B$ -mode is expected to be smaller than 100 nK, we need very sensitive polarimeters. We choose a polarimeter based on coherent technology and HEMT (High Electron Mobility Transistor) amplifiers because of their advantages for systematic errors. We developed two of the most sensitive polarimeter arrays today, one of which is composed of 19 modules at the Q-band (43 GHz) and the other is with 90 modules at the W-band (95 GHz). QUIET is located on the Chajnantor plateau in the Atacama desert of northern Chile at an altitude of 5,080m. The site is one of the best places for CMB observations because of high altitude, dry, and good weather throughout the year. We observed between 2008 October and 2010 December and collected over 10,000 hours of data.

It is important to not only develop a sensitive polarimeter array, but also perform both observations and data processes in the way that systematic errors can be reduced. We performed effective observations and analyses in which we adopted the following techniques; modulation, demodulation, and double-demodulation; calibrations with various sources; Mizuguchi-Dragone optics; boresight rotations; constant elevation scans; taking cross-correlations in power spectrum estimation; and many sets of validation tests called “null suites”.

From the Q-band data, we obtain the  $E$ -mode,  $B$ -mode, and  $EB$  power spectra at multipole range of  $25 \leq \ell \leq 475$ . The  $E$ -mode signals are detected with more than  $6\sigma$

significance in the range of the first peak ( $25 \leq \ell < 175$ ), which is consistent with the fiducial  $\Lambda$ CDM model. We also detect polarized foreground signal at lowest multipole of the  $E$ -mode with  $3\text{-}\sigma$  significance for one of our observation fields, which is consistent with Galactic synchrotron emission. We do not detect the  $B$ -mode and place an upper limit on the tensor-to-scalar ratio of  $r < 2.2$  at 95% confidence level. All the systematic errors are much lower than the statistical errors. In particular, the contaminations to the primordial  $B$ -mode spectrum at  $\ell < 100$  are lower than the level of  $r = 0.1$ . This result demonstrates that our technology and methodology worked very well, and promises that we can improve results in a future experiment with hundreds or thousands of polarimeter modules.

# Acknowledgments

I would like to thank Makoto Hattori (服部 誠) for his great support for my undergraduate and graduate studies at Tohoku University. He told me pleasure of studying physics, astrophysics, cosmology, and making experiments by my own hand. Additionally he led me into the field of CMB, which is one of the most interesting targets in science today. I still remember his special seminars and our discussions, which sometimes (always?) continued until midnight, and they made me who I am today.

Masashi Hazumi (羽澄 昌史) is my supervisor at High Energy Accelerator Research Organization (KEK). I would like to thank him for giving me the opportunity to write my Ph.D dissertation on the QUIET experiment, which is a unique and advanced CMB polarization experiment in the world. There had been no CMB polarization experiment in Japan until he started his new laboratory at KEK about three years ago. At that time, he invited me in QUIET and encouraged me to jump into a real experiment.

I would like to thank Bruce Winstein, who was the PI of QUIET, for involving me into the QUIET collaboration. He was one of the greatest persons in experimental particle physics and also the CMB experiments today. He was very unique, brilliant and warm-hearted person. I could enjoy my stay at the University of Chicago about eight months in total with his kind support. The sad thing is that he passed away on February 28th, 2011. I am very sad that we will never enjoy QUIET with him forever and I deeply regret that I was not able to show my dissertation to him.

Osamu Tajima (田島 治) is my teacher of an experiment in physics at KEK and Chicago. I would like to thank him for telling me what is a real experiment and data analysis. Before I joined in QUIET, I analyzed only very clean data such as simulated data or ideal data. He told me that the most important things in data analysis is to manage real data, which are very dirty for the most part. I also have great regard for his ability that he handles everything in the laboratory and data analysis very quickly with incredible quality. With his great supports, I was able to finish my dissertation.

I am grateful to Masaya Hasegawa (長谷川 雅也) for his assistance to my life at KEK. When I started my academic life at KEK about three years ago, I was not familiar with high energy physics because my original field was astronomy. He told me a lot of things

on high energy physics. Additionally, he helped not only my first oversea trip to Chicago but also first stay in Chile. His great supports made it easier to spend my academia life at KEK, Chicago, and Chile.

I am grateful to Akito Kusaka (日下 暁) for his kindness and exact supports for my study. When I could not tell my analysis well in the QUIET telecon because of my “bad” English, he would translate it into “good” English for everyone. He is one of the most clever persons I have ever seen. I leaned a lot of things from him—e.g. how to analyze the data efficiently; how to make complicated problems simpler; how to manage the telecon smoothly which usually became complicated, and so on.

I would like to thank Makoto Nagai (永井 誠) and Koji Ishidoshiro (石徹白 晃治), who were new postdocs after I started my KEK life. Since Makoto’s specialty was radio astronomy and Koji’s specialty was direct detection of gravitational waves by interferometers, discussions with them about not only CMB but also a lot of things—e.g. radio and terahertz astronomy, the galactic foreground, gravitational waves, detection of gravitational waves, laser interferometers and so on—were very interesting, exciting and helpful to write my dissertation.

I thank the Chicago QUIET group (Bruce, Akito, Colin, Ali, and Immanuel). I could enjoy staying on the University of Chicago for about eight months (2 months  $\times$  4) with their support and kindness. I believe that my experience in Chicago is precious and irreplaceable in my life forever.

I would also like to thank all the people in Astronomical Institute, Tohoku University and the KEK CMB group for their warm-hearted supports. I could spend great time on Sendai for six years and on Tsukuba for three years. Both Sendai and Tsukuba are the most suitable places for academic research.

At the end, I would like to send my best thanks to my parents and brother for their supports during my student life.

# Contents

<b>1</b>	<b>Introduction</b>	<b>13</b>
1.1	The Big Bang Theory . . . . .	13
1.1.1	The Success in Cosmology . . . . .	13
1.1.2	The Big Bang Problems . . . . .	17
1.2	The Inflationary Universe . . . . .	18
1.2.1	A Solution to the Big Bang Problems . . . . .	18
1.2.2	How to Inflate the Universe? . . . . .	19
1.2.3	The Primordial Perturbations . . . . .	21
1.3	Probing Inflation . . . . .	25
1.3.1	CMB Polarization as a Probe of Inflation . . . . .	25
1.3.2	Status of CMB Measurements . . . . .	29
1.4	QUIET . . . . .	31
<b>2</b>	<b>Instrument</b>	<b>37</b>
2.1	Overview . . . . .	37
2.2	Polarimeter Module . . . . .	40
2.2.1	Polarimeter On a Chip . . . . .	40
2.2.2	Principle of Polarization Measurement . . . . .	43
2.2.3	Requirement of ADC Sampling and Phase Switching Rate . . . . .	44
2.2.4	Impact of the Demodulation and Double-Demodulation for “Science Band” . . . . .	44
2.3	Far-Sidelobes . . . . .	47
2.4	Instrument Characterization . . . . .	47

<b>3</b>	<b>Observation</b>	<b>51</b>
3.1	Observation Site . . . . .	51
3.2	Observation Patch . . . . .	53
3.3	Observation Time . . . . .	55
3.4	Observation Strategy . . . . .	55
<b>4</b>	<b>Calibration</b>	<b>57</b>
4.1	Overview . . . . .	57
4.1.1	Goals of Calibration . . . . .	57
4.1.2	Calibration Sources . . . . .	58
4.2	Tau A . . . . .	59
4.2.1	Accuracy of Tau A Measurements . . . . .	59
4.2.2	Observation Strategy . . . . .	63
4.2.3	Analysis . . . . .	65
4.2.4	Results on the Center Module . . . . .	72
4.2.5	Results on the Off-center Modules . . . . .	72
4.2.6	Result of the Beamwidth . . . . .	75
4.2.7	Conclusions . . . . .	77
4.3	Detector Responsivity . . . . .	77
4.3.1	Responsivity Ratio . . . . .	77
4.3.2	PWV and Elevation Dependence . . . . .	78
4.3.3	Time Variation . . . . .	80
4.3.4	Summary of Our Detector Responsivity Uncertainties . . . . .	82
4.4	Detector Angle . . . . .	82
4.5	$I \rightarrow Q/U$ Leakage . . . . .	83
4.6	Pointing . . . . .	86
4.7	Beam Profile and Window Function . . . . .	86
<b>5</b>	<b>Analysis Procedure</b>	<b>91</b>
5.1	TOD Data Processing . . . . .	92
5.1.1	Pre-Processing . . . . .	92
5.1.2	Noise Modeling . . . . .	94



5.1.3	Filtering . . . . .	95
5.2	Map-making . . . . .	99
5.3	Power Spectrum Estimation . . . . .	102
5.3.1	MASTER and Pseudo- $C_\ell$ Estimator . . . . .	102
5.3.2	Cross-Correlation . . . . .	103
5.3.3	$E$ - $B$ Mixing . . . . .	104
5.3.4	Error Estimation . . . . .	104
<b>6</b>	<b>Data Selection</b>	<b>105</b>
6.1	Baseline Selection and Baseline Data Set . . . . .	106
6.2	Sun Contamination . . . . .	106
6.2.1	The Sun-centered Map . . . . .	108
6.2.2	Estimation of the Sun Contamination Effect on the Maps and Power Spectra . . . . .	109
6.2.3	Removing the Sun Contamination . . . . .	112
6.3	Bad Weather Selection . . . . .	112
6.4	Noise Model Validation . . . . .	113
6.5	Azimuth Slope Selection . . . . .	113
6.6	Type-B Selection . . . . .	113
6.7	Summary of the Data Selection . . . . .	114
<b>7</b>	<b>Analysis Validation</b>	<b>117</b>
7.1	Overview . . . . .	117
7.2	Null Tests—Estimating Hidden Biases with Null Power Spectra . . . . .	118
7.3	Consistency Among Different Configurations . . . . .	123
<b>8</b>	<b>Results</b>	<b>127</b>
8.1	Power Spectra ( $C_\ell^{EE}$ , $C_\ell^{BB}$ , and $C_\ell^{EB}$ ) . . . . .	127
8.2	Foreground . . . . .	130
8.2.1	Compact Radio Sources . . . . .	131
8.2.2	Galactic Diffuse Synchrotron . . . . .	131
8.3	Primordial Gravitational Waves . . . . .	134

<b>9</b>	<b>Systematic Errors</b>	<b>139</b>
9.1	Overview and Summary . . . . .	139
9.2	Multiplicative Responsivity Error . . . . .	142
9.3	Responsivity . . . . .	143
9.4	Polarization Angle . . . . .	143
9.5	Pointing . . . . .	144
9.6	Beam Window Function . . . . .	144
9.7	Far-Sidelobe Contamination due to the Sun . . . . .	145
9.8	Instrumental Polarization . . . . .	145
9.9	Ground-pickup Signals . . . . .	145
9.10	Type-B Glitch . . . . .	146
9.11	Data Selection Bias . . . . .	146
<b>10</b>	<b>Conclusions</b>	<b>147</b>
<b>A</b>	<b>Basic Formula of CMB Angular Power Spectrum</b>	<b>151</b>
A.1	Basic Formula . . . . .	151
A.2	Knox Formula . . . . .	152
<b>B</b>	<b>Formula How QUIET Polarimeters Measure Polarization Signal with Suppressing the <math>1/f</math> Noise</b>	<b>155</b>
B.1	Basic Definition . . . . .	155
B.2	Demodulation and Total Power . . . . .	158
B.3	Double-Demodulation . . . . .	160
<b>C</b>	<b>Impact of Possible Responsivity Fluctuation</b>	<b>163</b>
C.1	Overview . . . . .	163
C.2	Derivation of Formula . . . . .	163
C.3	Requirement for QUIET Q-band . . . . .	166
<b>D</b>	<b>Calibration Sources</b>	<b>169</b>
D.1	Sky dips . . . . .	169
D.1.1	Overview . . . . .	169

D.1.2	TOD Analysis . . . . .	170
D.1.3	Sky Temperature Correction . . . . .	170
D.1.4	Results . . . . .	171
D.2	The Moon . . . . .	172
D.2.1	Overview . . . . .	172
D.2.2	Measurements, Analysis, and Results . . . . .	172
D.3	Sparse Wire Grid . . . . .	173
<b>E</b>	<b>Antenna-to-Thermodynamic Correction</b>	<b>177</b>
<b>F</b>	<b>Power Spectrum Estimation in the Null Tests</b>	<b>179</b>
<b>G</b>	<b>Experiment Summary Table</b>	<b>181</b>



# Chapter 1

## Introduction

### 1.1 The Big Bang Theory

#### 1.1.1 The Success in Cosmology

Remarkable advances in observational cosmology over the two decades gave us a collective understanding of components in the universe and evolution of space. General relativity enabled us to make a testable theory of the universe. Based on general relativity, the expansion of the universe is associated with the energy density in it. Hence the evolution of the flat universe is determined by the Friedmann equation

$$H^2(t) = \frac{8\pi G}{3}\rho(t), \quad (1.1)$$

where  $H(t)$  is the “Hubble” expansion rate as a function of time and  $\rho(t)$  is the energy density in the universe as a function of time too. The Hubble expansion rate is defined as

$$H(t) \equiv \frac{da(t)/dt}{a(t)}, \quad (1.2)$$

where  $a(t)$  is the scale factor of the Friedmann-Robertson-Walker (FRW) metric given by

$$g_{\mu\nu} = \begin{pmatrix} -1 & 0 & 0 & 0 \\ 0 & a^2(t) & 0 & 0 \\ 0 & 0 & a^2(t) & 0 \\ 0 & 0 & 0 & a^2(t) \end{pmatrix}, \quad \text{with metric signature } (-, +, +, +). \quad (1.3)$$

Based on Equation (1.1), the universe was a very hot and dense state at the early time, and cooled by expansion. This “Big Bang” scenario has a great predictive power for the evolution of the universe. One of the greatest predictions is the abundance of light elements —  $^4\text{He}$ , deuterium,  $^3\text{He}$ , and lithium — created at the early universe. This “Big Bang Nucleosynthesis” is well probed by a lot of observations [1].

Another prediction is the Cosmic Microwave Background radiation (CMB). The CMB is a relic of a hot and dense state of the universe. At the early time, the universe was very hot and dense. It means that the universe was dominated by the radiation. At this “radiation-dominated era”, the photons were in thermodynamic equilibrium and the universe was a perfect cavity of a blackbody. Hence the spectrum of the photons should be described as Planck’s law

$$I_\nu(T) = \left( \frac{2h\nu^3}{c^2} \right) \frac{1}{\exp\left( \frac{h\nu}{k_B T} - 1 \right)}. \quad (1.4)$$

As the universe expanded, the temperature of the universe went down. When the temperature went down to about 3,000 Kelvin, the photons did not have enough energy to ionize the atoms, then the universe was suddenly neutralized. This moment is called “recombination” or “last scattering”<sup>a</sup>. After the recombination, the photons traveled freely through the universe without interacting with matter. Since the universe was expanding while the photons were traveling freely, the temperature of the photons went down. This effect is called “redshift”. In spite of redshift, the blackbody spectrum given as Equation (1.4) was kept because CMB photons never interact with matter. For this reason, we observe it as a perfect blackbody. The Far Infrared Absolute Spectrometer (FIRAS) on the Cosmic Microwave Background Explorer (COBE) satellite, which was launched on November 18, 1989, successfully measured the blackbody spectrum at a temperature of 2.725 Kelvin [2, 3, 4] (Figure 1.1) with an excellent precision.

The CMB anisotropy also has played a great role in understanding the early universe and the evolution of the structures of the universe. The CMB anisotropy was discovered by the Differential Microwave Radiometer (DMR) on the COBE satellite. The early universe was not completely smooth because there were small perturbations in the cosmic

---

<sup>a</sup>The surface at that moment is called the “Last Scattering Surface (LSS)”.

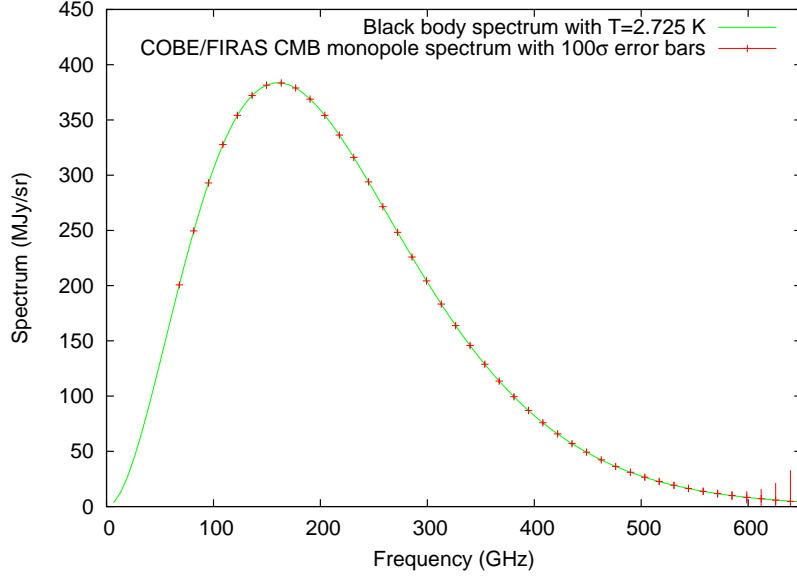


**Figure 1.1:** CMB monopole spectrum with  $100\sigma$  error bars (red markers) measured by FIRAS on the COBE satellite. The data are available from [5]. The green solid line represents the ideal blackbody spectrum with a temperature of 2.725 Kelvin.

plasma, which were reflected in the physics called “acoustic oscillation”. At the early universe, the photons were affected by gravity and Compton scattering with free electrons. The electrons were tightly coupled to the protons. Both of them were also affected by the gravity. Moreover, neutrinos and dark matter, which are only affected by gravity and predicted from many observations [6, 7], were also affected by the gravitational force. All the components were connected via the metric which determines the gravitational force and the state of each component is described as the Boltzmann equation. Therefore, we can construct a series of the equations that govern the evolution of perturbations in the universe. These equations are known as “Boltzmann-Einstein equations”<sup>b</sup>. As long as the perturbations are small, we can predict its evolution completely. This is an advantage of the perturbation theory. Based on this theory, the calculation of the CMB anisotropy was carried out by the middle of 1990’s [11]; therefore, we were ready to compare the prediction with observations.

Figure 1.2 shows the CMB anisotropy measured by the Wilkinson Microwave Anisotropy Probe (*WMAP*) satellite from 2001 to 2008<sup>c</sup>. A lot of cold and hot spots with an angu-

<sup>b</sup>There are a lot of good textbooks [8, 9, 10] which describe the equations from first principals.

<sup>c</sup> The *WMAP* satellite ended science observations on August 20, 2010. The final data products will

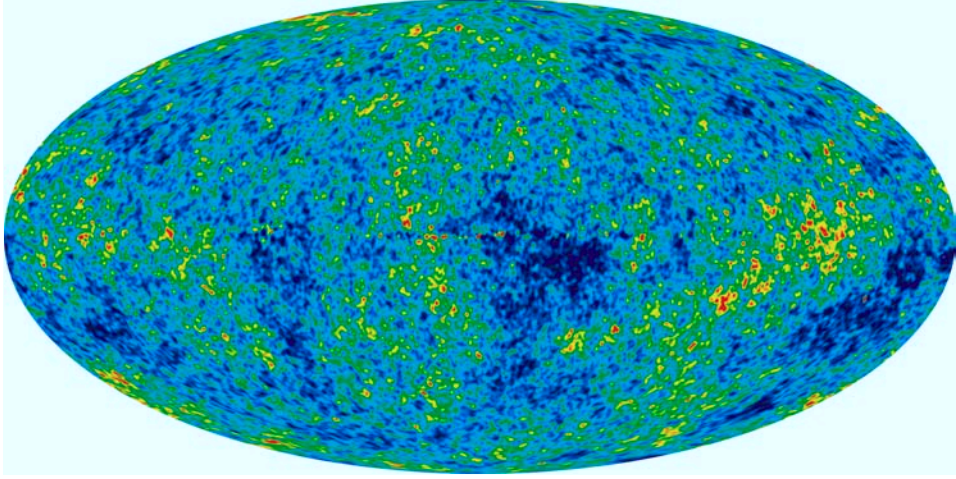


**Figure 1.2:** The CMB temperature anisotropy map measured by the *WMAP* satellite in the Galactic coordinate system with the center of the Galaxy at the center of Mollweide projection [12]. The map is shown linearly scaled to  $\pm 200 \mu\text{K}$ .

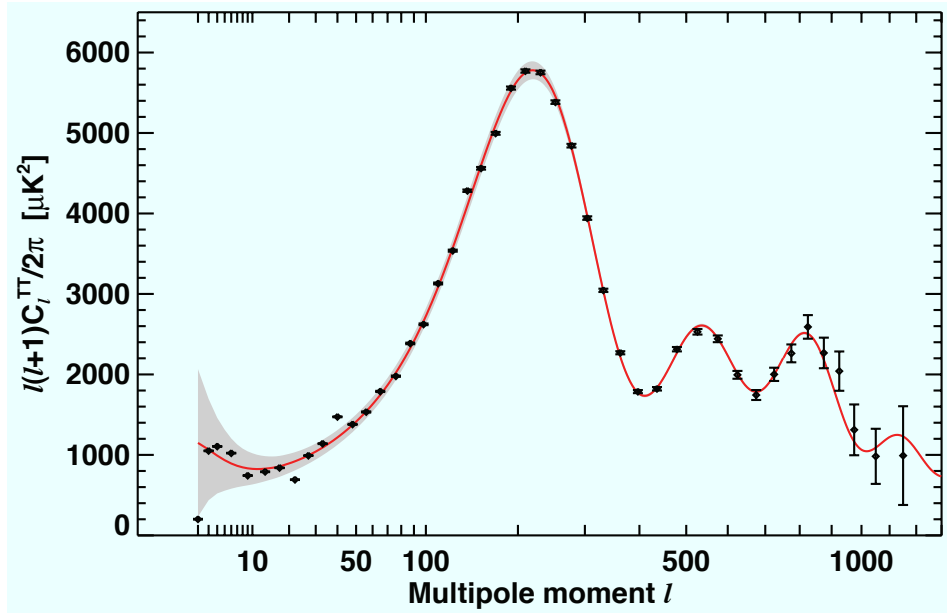


**Figure 1.3:** The CMB temperature anisotropy power spectrum from the *WMAP* satellite [13]. The horizontal axis represents spherical multipole moments defined by  $\ell = 180^\circ/\theta$ , where  $\theta$  is an angular scale of the anisotropy. The vertical axis represents the RMS of the CMB temperature anisotropy in  $\mu\text{K}^2$  units. The black dots are the measurements, and the red solid line represents the best fit of the theoretical prediction to the data. The gray band represents cosmic variance.



lar scale of a few degrees are found in the map. These typical features come from the “acoustic oscillation” due to the oscillation of the cosmic plasma at the recombination.

Performing a spherical harmonic transform on that map, we obtain CMB temperature anisotropy power spectrum shown in Figure 1.3. Comparing the power spectrum with the theory, we can get a lot of cosmological information including the following:

- The age of the universe is 13.73 billion years old within 1 % precision.
- The curvature of the universe is within 1 % of the flat Euclidean space.
- Baryons are only 4.6 % (within 0.1 % precision) of the energy density of the universe.
- The dark matter is 23.3 % (within 1.3 % precision) of the energy density of the universe.
- The dark energy, which causes the late expansion and acceleration of the universe, is 72.1 % (within 1.5 % precision) of the energy density of the universe.

The model which provides the above cosmological information is called the concordance  $\Lambda$ CDM, or simply  $\Lambda$ CDM. This is the standard cosmological model today because it can account for many cosmological observations such as galaxy surveys and supernova surveys, as well as the CMB observations.

The excellent success on the CMB temperature anisotropy measurement (also the other cosmological observations) puts the Big Bang theory on a firm basis and elevates cosmology from speculation to precision science. However, the Big Bang theory is not perfect.

### 1.1.2 The Big Bang Problems

The Big Bang theory successfully explains a lot of observed phenomena; however, it is incomplete because there remain certain puzzles incapable of explaining:

1. *Horizon Problem:* Observations of the CMB temperature anisotropy imply the causality across distances on the sky which correspond to “super-horizon” scales on

---

be released by 2012.

the LSS. At super-horizon scales, two points are causally disconnected. On the LSS, the region which was able to be causally connected corresponds to only about a few degrees on the scale today. The CMB is observed with nearly the same temperature in all directions on the sky<sup>d</sup>. There is no way to establish thermal equilibrium if these regions were never in causal contact before the last scattering.

2. *Flatness Problem:* All the observations today including CMB measurements show that the universe is spatially very flat. A flat universe is not a reasonable solution in the Big Bang theory because that is just one point in the parameter space. To explain the present geometrical flatness of space requires an extreme fine-tuning in the Big Bang theory.
3. *Origin of the Structures:* The universe today has rich structures on various scales. The structures have been evolved with gravitational instability, for that the seed was needed. If there is no seed, any instability never grew up. From CMB observations, we know that the universe has almost scale-invariant structures. It is possible to construct a theory which predicts just scale-invariant structures like the Harrison-Zeldovich-Peebles (HZP) spectrum [14, 15, 16]. However the Big Bang theory itself can not predict it naturally.

These three big problems and relics problem associated with such as magnetic monopoles and so on are the remaining puzzles of the Big Bang theory. An extraordinary exponential expansion at the early universe can solve these problems naturally. This is called cosmological “Inflation”.

## 1.2 The Inflationary Universe

### 1.2.1 A Solution to the Big Bang Problems

By the inflation theory, each of these problems is resolved by an assumption that the early universe went through a very short period of an extremely accelerated expansion

---

<sup>d</sup>The CMB temperature anisotropy has already been observed. But its amplitude is as  $10^5$  times small as the average temperature.

[17, 18, 19, 20, 21, 22, 23]. At that moment, the universe inflated by a factor of at least  $10^{26}$  within less than  $10^{-34}$  seconds. In this picture, each problem mentioned above can be solved simultaneously:

1. *Horizon Problem:* The physical wavelength of fluctuations was stretched by the expansion of the universe. The whole observable universe at the present time ( $10^{26}$  m) originated from a smooth and causally connected patch of space smaller than  $10^{-26}$  m in diameter before this rapid expansion epoch.
2. *Flatness Problem:* Even if the early universe was positively or negatively curved, the early exponential expansion of the universe naturally stretched it to flat.
3. *Origin of the Structures:* Scale-invariant perturbations were naturally expected by quantum fluctuations of a scalar field at the early universe, which drove the accelerating expansion. The fact leads to the perspective that not only the large scale structures in the universe but also small scale structures—for example, the solar system, the earth, and even human beings, originated from quantum scalar perturbations at the very early universe.

Moreover, any monopoles existing at the early universe were diluted to a negligible density level in the observable universe today. Therefore the inflation theory is a good solution for the Big Bang problems.

### 1.2.2 How to Inflate the Universe?

What kind of energy can drive the universe to the exponential expansion? Based on general relativity, the expansion of the universe is associated with the energy in it. Energy which has negative pressure only can inflate the universe. Ordinary matter (relativistic and non-relativistic) and radiation, which always have positive or no pressure, can not. A generic scalar field is one of the solutions though we do not know what it is yet. Here I will discuss inflation in terms of this scalar field.

The energy-momentum tensor for the field ( $\phi$ ) is given by

$$T^{\alpha}_{\beta} = g^{\alpha\nu} \frac{\partial\phi}{\partial x^{\nu}} \frac{\partial\phi}{\partial x^{\beta}} - g^{\alpha}_{\beta} \left[ \frac{1}{2} g^{\mu\nu} \frac{\partial\phi}{\partial x^{\mu}} \frac{\partial\phi}{\partial x^{\nu}} + V(\phi) \right]. \quad (1.5)$$

Here  $g^{\mu\nu}$  is the metric of the early universe and  $V(\phi)$  is the potential of the field. Assumed that  $\phi$  is mostly homogeneous, the field is described as

$$\phi(\vec{x}, t) = \phi^{(0)}(t) + \delta\phi(\vec{x}, t), \quad (1.6)$$

where  $\phi^{(0)}(t)$  is a zeroth-order homogeneous part and  $\delta\phi(\vec{x}, t)$  is the first order perturbation, which comes from quantum fluctuations. At first, we consider the zeroth-order homogeneous part, and its energy density and pressure, then its time evolution.

The time-time component of  $T^\alpha_\beta$  is equal to the energy density of the scalar field:

$$\rho = \frac{1}{2} \left( \frac{d\phi^{(0)}}{dt} \right)^2 + V(\phi^{(0)}). \quad (1.7)$$

The pressure for the homogeneous field is given by the space-space component as

$$p = \frac{1}{2} \left( \frac{d\phi^{(0)}}{dt} \right)^2 - V(\phi^{(0)}). \quad (1.8)$$

In Equations (1.7) and (1.8), the first term of the right-hand side is the kinetic energy density of the field, and the second term is its potential energy density. From Equation (1.7), we can consider an analogy to a single particle motion  $x(t) = \phi^{(0)}(t)$  in a potential  $V(\phi^{(0)}(t))$  for the dynamics of the homogeneous scalar field shown in Figure 1.4.

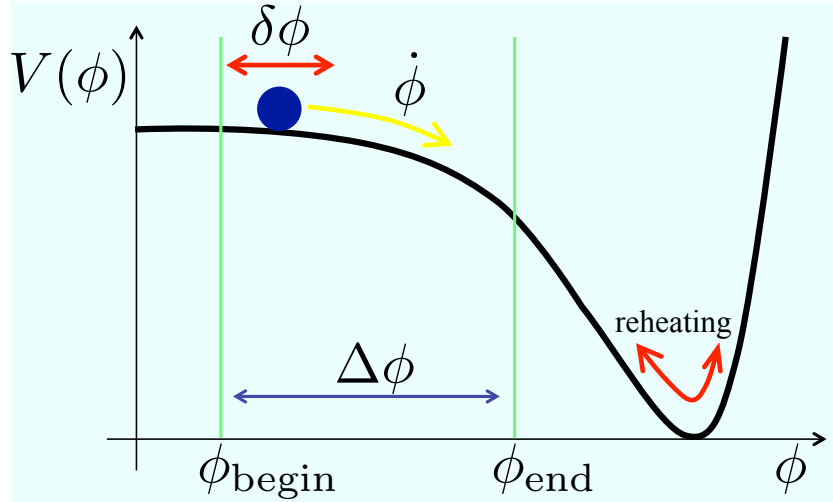


**Figure 1.4:** One of examples of the potential of a scalar field. The expansion happens when the field potential  $V(\phi^{(0)})$  dominates over its kinetic energy  $(1/2)(\dot{\phi}^{(0)})^2$ . The primordial perturbation  $\delta\phi$  is created by quantum fluctuations. After the end of inflation, reheating occurs, which makes the universe hot.

From Equations (1.7) and (1.8), negative pressure which is needed to inflate the universe is realized when the potential energy is much larger than the kinetic energy. Most models of “slow-roll” inflation, in which the homogeneous field varies slowly, can realize it naturally. In this case, the energy is almost constant during the inflation; therefore the field energy can inflate the universe successfully. After the end of inflation, the energy of the scalar field is converted into radiation [24]. This “reheating” process realizes the expected “hot” Big Bang universe.

### 1.2.3 The Primordial Perturbations

During inflation, the universe consisted of the uniform scalar field and the uniform background metric. The field fluctuated quantum mechanically as described in Equation (1.6). This mechanism created both scalar perturbations and tensor perturbations [25, 26, 27]<sup>e</sup>.

These perturbations were created on sub-horizon scales, on which physics can causally act during the inflation era. The perturbations were stretched out to super-horizon scales, on which physics can not act at all, by the expansion of the universe. Since the perturbations were frozen out on super-horizon scales, their RMS amplitudes remained constant. Since horizon grew after inflation, the perturbations re-entered the horizon.

#### 1.2.3.1 The Scalar Perturbations

The primordial scalar perturbation is given by the power spectrum of the curvature perturbation on the uniform-density hypersurfaces ( $\zeta$ ) [28],

$$\langle \zeta_{\vec{k}} \zeta_{\vec{k}'} \rangle \equiv (2\pi)^3 \delta^3(\vec{k} - \vec{k}') P_s(k), \quad n_s - 1 \equiv \frac{d \ln(k^3 P_s)}{d \ln k}. \quad (1.9)$$

Here the curvature perturbation in the case of slow-roll inflation is defined as

$$-\zeta \equiv \Psi + \frac{\delta\rho}{\dot{\rho}} H \approx \Psi + \frac{\delta\phi}{\dot{\phi}^{(0)}} H, \quad (1.10)$$

where  $\Psi$  is the Newtonian potential, and  $\vec{k}$  is a wave number vector. In the spatially-flat gauge, perturbations in  $\zeta$  are associated with perturbations in the inflation field with

---

<sup>e</sup>This mechanism also created vector perturbations. However the vector perturbations on large scales decayed by the exponential expansion unless they were driven by anisotropic stress. Thereby it is natural that only scalar perturbations and tensor perturbations are focused on here.

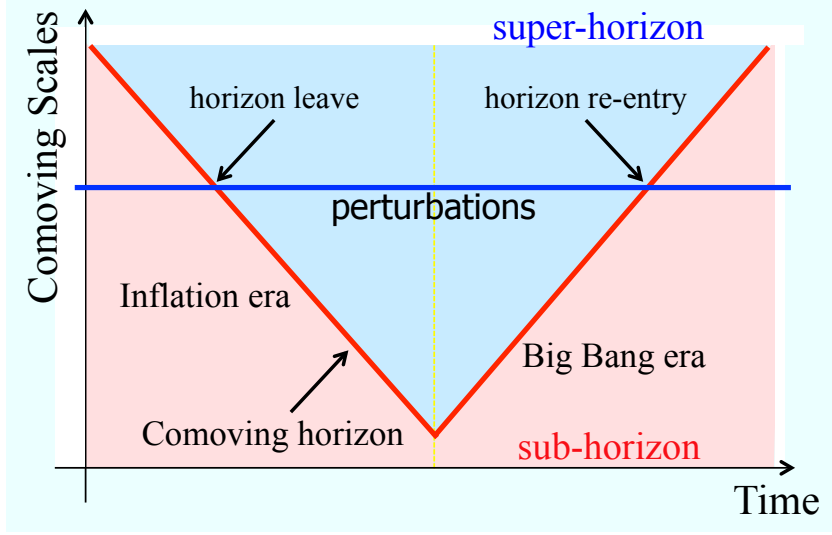


**Figure 1.5:** Evolution of the perturbations in the inflationary universe. On sub-horizon scales (light red area), the perturbations which were created during the inflation era left the horizon at first. The perturbations on super-horizon scales (light blue area) were frozen out. After the inflation era, the perturbations entered the horizon again and re-started to interact physically.

$\Psi = 0$ . Therefore the power spectrum of  $\zeta$  and that of  $\delta\phi$  are related as follows

$$\langle \zeta_{\vec{k}} \zeta_{\vec{k}'} \rangle = \left( \frac{H}{\dot{\phi}(0)} \right)^2 \langle \delta\phi_{\vec{k}} \delta\phi_{\vec{k}'} \rangle. \quad (1.11)$$

In the case of slow-roll inflation, quantum fluctuations of a light scalar field around a smooth background scale with the Hubble expansion rate are given by follows [29],

$$\langle \delta\phi_{\vec{k}} \delta\phi_{\vec{k}'} \rangle = (2\pi)^3 \delta(\vec{k} - \vec{k}') \left( \frac{H^2}{2k^3} \right). \quad (1.12)$$

The power spectrum of perturbations is to be evaluated at the time of leaving the horizon of a given perturbation ( $k = aH$ ). Therefore fluctuations of the scalar field create the power spectrum:

$$P_s(k) = \left( \frac{H}{\dot{\phi}(0)} \right)^2 \left( \frac{H^2}{2k^3} \right) \Big|_{k=aH} \quad (1.13)$$

### 1.2.3.2 The Tensor Perturbations

During inflation, quantum fluctuations also generate tensor metric perturbations ( $h_{ij}$ ) [17]. The tensor perturbations in the gravitational metric are called “gravitational waves”<sup>f</sup>. With an analogy to the harmonic oscillator, their power spectrum is given by that of the massless field:

$$P_t(k) = 64\pi G \left( \frac{H^2}{2k^3} \right) \bigg|_{k=aH}, \quad n_t \equiv \frac{d \ln(k^3 P_t)}{d \ln k}. \quad (1.14)$$

### 1.2.3.3 The Slow-Roll Predictions

In case of slow-roll inflation, we can relate the predictions between  $P_s(k)$  and  $P_t(k)$  with the energy density of the scalar field:

$$P_s(k) = \frac{16\pi^2}{3k^3} \frac{V}{\epsilon m_{\text{pl}}^4} \bigg|_{k=aH}, \quad P_t(k) = \frac{256\pi^2}{3k^3} \frac{V}{m_{\text{pl}}^4} \bigg|_{k=aH}. \quad (1.15)$$

Here  $m_{\text{pl}}$  is the planck mass defined as  $m_{\text{pl}} \equiv G^{-1/2} = 1.2209 \times 10^{19} \text{ GeV}$ , and  $\epsilon$  is defined as a time derivative of the inverse Hubble expansion rate given by

$$\epsilon \equiv -\frac{\dot{H}}{H^2} = 4\pi G \left( \frac{\dot{\phi}^{(0)}}{H} \right)^2 \approx \frac{1}{16\pi G} \left( \frac{V'}{V} \right)^2, \quad (1.16)$$

where  $\epsilon$  is also related to a first-order derivative of the energy density of the scalar field. In addition, we also define the second-derivative of the energy density of the scalar field

$$\eta \equiv \frac{1}{8\pi G} \frac{V''}{V}. \quad (1.17)$$

From Equations (1.15) and (1.16), measuring the amplitude of  $P_t$  is equal to measuring  $V$ , and measuring the amplitude of  $P_s$  is equal to measuring  $V, V'$  at the same time. From Equation (1.15), the tensor-to-scalar ratio,  $r$ , is defined as

$$r \equiv \frac{P_t(k)}{P_s(k)} = 16\epsilon. \quad (1.18)$$

Moreover after some calculations, we obtain

$$n_s - 1 = 2\eta - 6\epsilon = 2\eta - \frac{r}{8}; \quad n_t = -2\epsilon; \quad r = -8n_t. \quad (1.19)$$

---

<sup>f</sup>Not “gravity waves” but “gravitational waves”. Gravity waves are generated in a fluid medium which has the restoring force of gravity. These two are essentially different from each other.

These are called “slow-roll consistency relations”. Equation (1.18) and current results of the temperature anisotropy<sup>g</sup> imply the following relations between the energy scale of inflation  $V^{1/4}$  and the tensor-to-scalar ratio  $r$ :

$$V^{1/4} = 1.06 \times 10^{16} \left( \frac{r}{0.01} \right)^{1/4} \text{ GeV}. \quad (1.20)$$

For this reason, if we can detect the tensor-to-scalar ratio at the level of  $r = 0.01$ , we can access extremely high energy scale, which is comparable to that of the GUT (Grand Unified Theory) scale ( $\approx 10^{16}$  GeV). This has a big impact on high-energy physics because even the most ambitious design for future accelerators will never reach this energy scale<sup>h</sup>.

Today there are lots of inflation models. Each of them predicts a different tensor-to-scalar ratio. Here I summarize three frequently discussed models in the literature and give predicted values:

- *Single-field power-law inflation* is characterized by a scalar field potential of  $V(\phi) \propto e^{\phi/\mu}$ , where  $\mu$  is a mass scale. In this model, there is a relation  $r = 8(1 - n_s) \sim 0.3$ <sup>i</sup>.
- *Chaotic inflation* has a scalar field potential of  $V(\phi) \propto (\phi/\mu)^p$ . Here  $p$  is empirically less than 10. In this model, there is a relation  $r = 8[p/(p+2)](1 - n_s) \sim 0.06$  at  $p = 0.1$ .
- *Spontaneous symmetry-breaking (SSB) inflation* features a scalar field potential of  $V(\phi) \propto [1 - (\phi/\nu)^2]^2$ . This model is parameterized by  $\nu$ . The relation between  $n_s$  and  $r$  can not be written in a simple way. [31] predicts  $r \sim 0.05$ .

To summarize this section, if we measure the tensor-to-scalar ratio via the CMB polarization  $B$ -mode signal induced by primordial gravitational waves to the level of  $r = 0.01$ , we can test many inflation models and shed light on high energy physics. In the next section, I describe how we can measure  $r$  from CMB observations.

---

<sup>g</sup>The temperature anisotropy from the *WMAP* [30] gives the power of the scalar fluctuations of  $A_s = (2.441^{+0.088}_{-0.092}) \times 10^{-9}$  at  $k_{\text{pivot}} = 0.002 \text{ Mpc}^{-1}$ .

<sup>h</sup>The highest energy achieved today is about 10 TeV ( $10^{13}$  eV), which is as  $10^{12}$  times small as the GUT scale.

<sup>i</sup>The spectral index of the scalar perturbations is  $n_s = 0.963 \pm 0.012$  from the *WMAP* [30].



## 1.3 Probing Inflation

### 1.3.1 CMB Polarization as a Probe of Inflation

Today the CMB polarization is one of the most important tools to probe inflation because we can access primordial gravitational waves created during the inflation era by measuring the CMB polarization [32, 33]. Perturbations which were just re-entering at the recombination and reionization era imprint the primordial gravitational waves into the CMB.

The scalar perturbations make density fluctuations via gravitational potential, which induce acoustic oscillations in the cosmic plasma. Acoustic oscillations then create the CMB temperature anisotropy on typical angular scales as already shown in Figure 1.3. The scalar perturbations also induce positive-parity scalar “ $E$ -mode” in the CMB polarization via Thomson scattering of the local quadrupole of the temperature anisotropy (Figure 1.6). Primordial gravitational waves (tensor perturbations) induce negative-parity tensor “ $B$ -mode” (Figures 1.7 and 1.8) in the same way of the scalar. Because of that, we can determine the amplitude of primordial gravitational waves by measuring the  $B$ -mode signal as well as the tensor-to-scalar ratio.

The  $B$ -mode signal is usually described as an angular power spectrum ( $C_\ell^{BB}$ ). The definition and formalism are found in Appendix A. Figure 1.9 shows predicted CMB power spectra for the temperature anisotropy and polarization of the  $E$ -mode and  $B$ -mode. Adopting the cosmological parameters except the tensor-to-scalar ratio from the concordance  $\Lambda$ CDM model with an assumption of the tensor index  $n_t = 0^j$ , the  $B$ -mode power spectrum is proportional to the concordance template by the tensor-to-scalar as shown in Figure 1.9. Many experiments, which have an enough sensitivity to detect the  $B$ -mode to  $r = \mathcal{O}(10^{-2})$  level, are planned, and certain ones are ongoing.

In contrast to CMB polarization experiments, a direct detection of primordial gravitational waves by very large interferometers is another way to test inflation [31, 38]. The interferometers have a potential to detect primordial gravitational waves of higher frequencies than the CMB polarization<sup>k</sup>, which re-entered horizon during the radiation-

---

<sup>j</sup>This breaks the slow-roll consistency relation, but it is still a good approximation often used.

<sup>k</sup>Primordial gravitational waves have very huge frequency range from  $10^{-18}$  Hz to  $10^9$  Hz to the

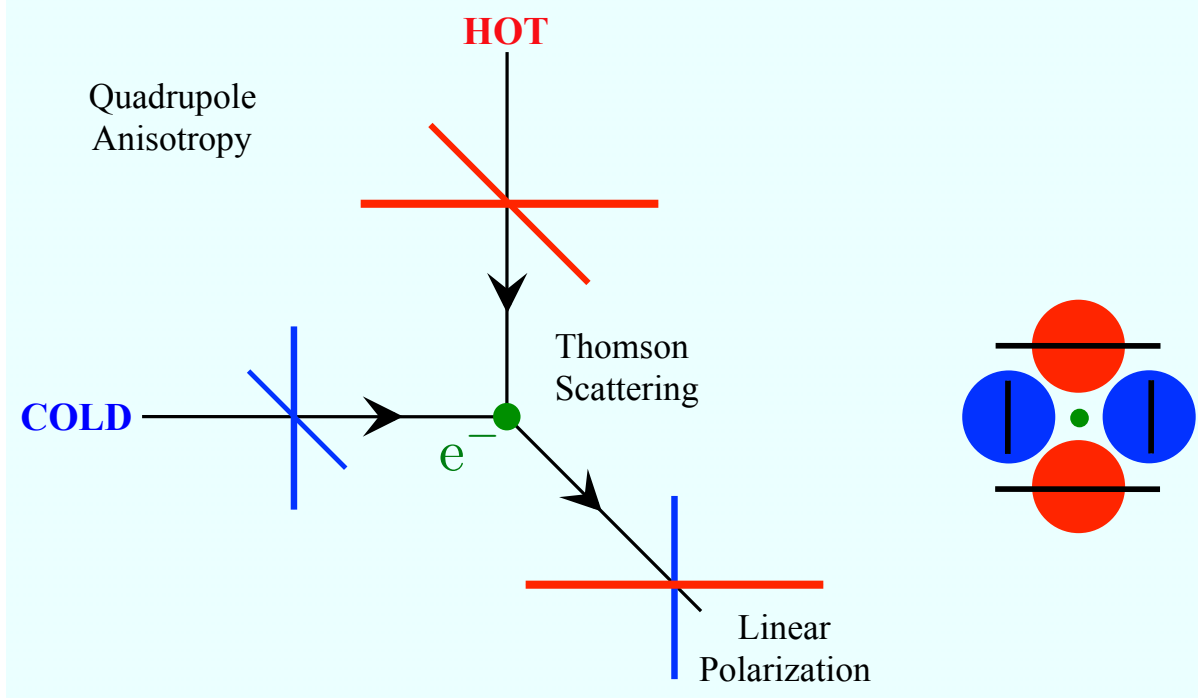


**Figure 1.6:** Left: Thomson scattering with a quadrupole anisotropy of the CMB temperature creates linear polarization. Red (blue) lines represent hot (cold) photons respectively [34] (not representing redshift or blueshift, but hot or cold). The photons with quadrupole anisotropy scatters into linear polarization while isotropic radiation does not. The reasons are as follows: Probability of the Thomson scattering into a direction  $\vec{n}$  is proportional to  $d\sigma/d\Omega(\vec{n}) = (3/8\pi) \sigma_T (\vec{\epsilon}_{\text{in}} \cdot \vec{\epsilon}_{\text{out}})^2$  where  $\vec{\epsilon}_{\text{in}}$  is a polarization vector of the incident photon,  $\vec{\epsilon}_{\text{out}}$  is that of the outgoing photon, and  $\sigma_T$  is the Thomson cross section. Because of that, in case of a  $90^\circ$  scattering with a polarization vector perpendicular to the plane of the scattering, the probability is  $d\sigma/d\Omega(\vec{n}) = (3/8\pi) \sigma_T$ ; by contrast, in case of  $90^\circ$  scattering with a polarization vector parallel to the plane of the scattering, the probability is zero. For this reason, probability of a photon being scattered to outside of the plane containing the quadrupole anisotropy depends on  $(\vec{\epsilon}_{\text{in}} \cdot \vec{\epsilon}_{\text{out}})^2$ . Coupled with the existence of the quadrupole anisotropy, the fact leads to linear polarization. Right: Direction of the linear polarization induced by a quadrupole anisotropy aligns with the cold lobe.

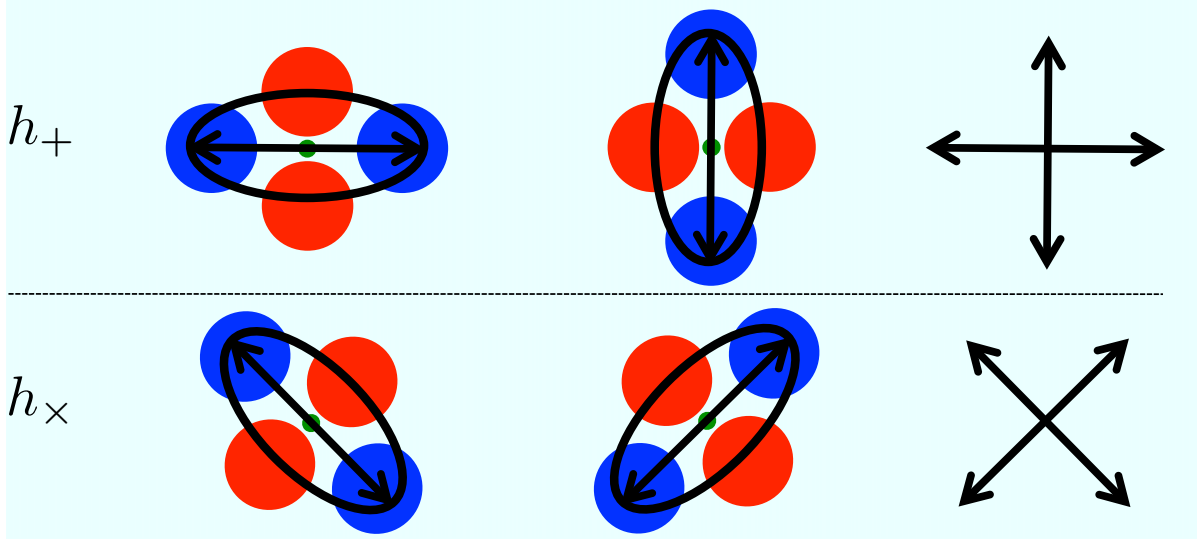


**Figure 1.7:** Linear polarization induced by gravitational waves. The metric on the LSS oscillates in a cruciform manner, then they make photons hot (cold) toward the electron by gravitational blueshift (redshift). Thereby, they create the local quadrupole temperature anisotropy on the LSS. Top: The effect of a plus-polarized ( $h_+$ ) gravitational waves on photons and their making polarization direction. Bottom: That of a cross-polarized ( $h_\times$ ) ones.

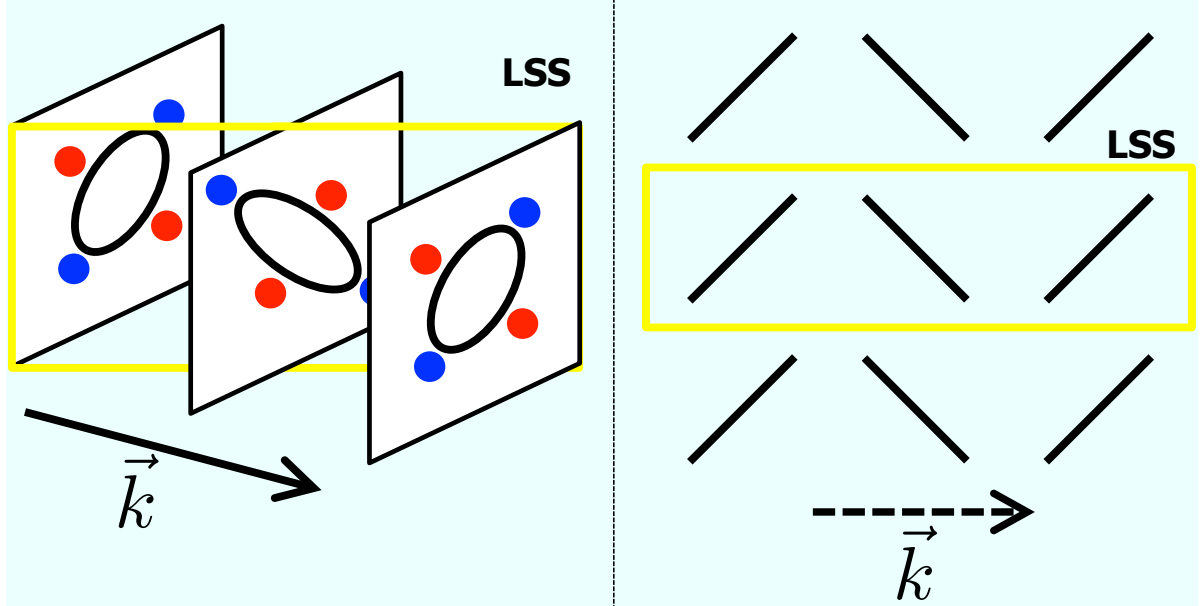


**Figure 1.8:** Negative-parity tensor  $B$ -modes induced by gravitational waves. Left: Gravitational waves pass through the LSS along  $\vec{k}$  direction, and create linear polarizations. Right: Polarization patterns on the LSS. The direction is not aligned with orientation of the wave vector, but aligned by  $\pm 45^\circ$ . This alignment is the hallmark of the  $B$ -mode.



**Figure 1.9:**  $\Lambda$ CDM power spectra for the  $TT$  ( $C_\ell^{TT}$ , red line),  $EE$  ( $C_\ell^{EE}$ , green line), and  $BB$  correlations (blue lines from top to bottom correspond to  $C_\ell^{BB}$  with  $r = 1.00, 0.10$  and  $0.01$ ; dashed line corresponds to the gravitational lensing [35]). Due to the reionization bump, the rough relation of  $C_\ell^{BB}/C_\ell^{EE} \approx r$  holds at large angular scales ( $\ell \leq 10$ ) because  $C_\ell^{EE}$  is almost proportional to the amplitude of the scalar perturbations, while  $C_\ell^{BB}$  is almost proportional to that of the tensor perturbations. Among the  $BB$  power, roughly speaking, the relation of  $C_\ell^{BB}(r_i) = (r_i/r_j)C_\ell^{BB}(r_j)$  is valid with an assumption of  $n_t = 0$ . For the  $B$ -mode, the primordial  $B$ -mode is dominated at large angular scales ( $\ell \leq 100$ ); however, the  $B$ -mode power due to the gravitational lensing exceeds at small angular scales ( $\ell \geq 200$ ). Acoustic oscillations resulting from the fact that the cosmic plasma is tightly coupled with the photons are found in the  $TT$  and  $EE$  power spectra. The  $BB$  power has no acoustic oscillations and dump, on the contrary, because of the tight coupling. More details on the CMB phenomena are found in [32, 36]. All the theoretical (predicted) power spectra are calculated by CAMB [37].

dominated era. The sensitivity of the interferometers today is about seven orders of magnitude worse than that of the CMB experiments (Figure 1.10) [39]. Some (mostly spaceborne) interferometer projects, which have a enough sensitivity to detect primordial gravitational waves as much as the CMB polarization experiments, are planned; however, those instruments involve massive technological challenges. It takes optimistically many decades to be developed and launched.

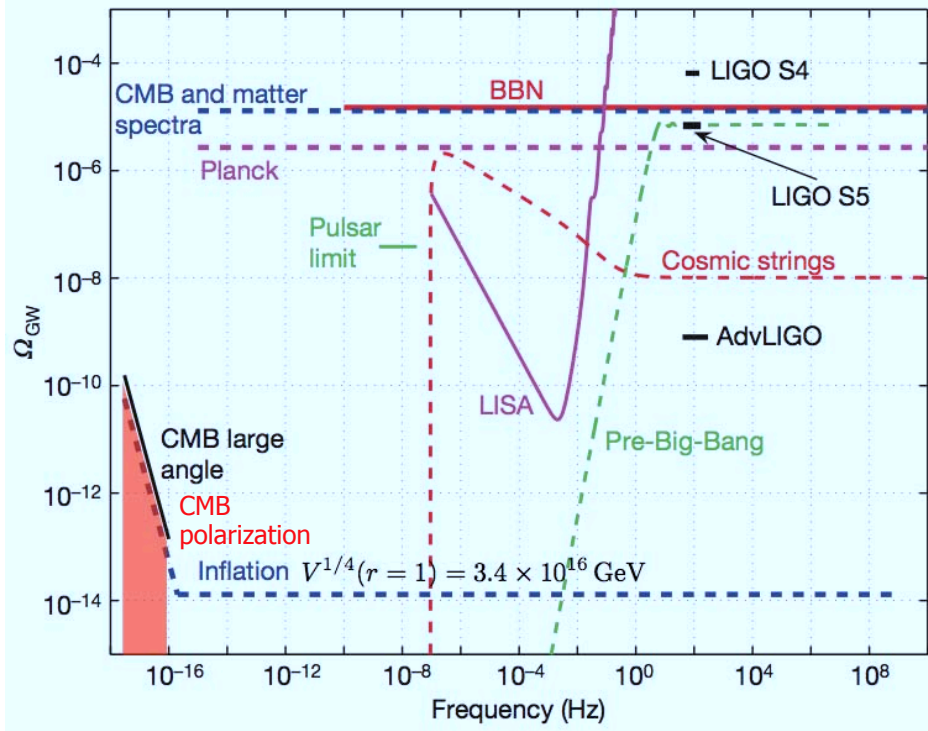


**Figure 1.10:** Energy density of primordial gravitational waves ( $\Omega_{\text{GW}}$ ) as a function of frequency to today's horizon scale. Sensitivity curves of interferometer experiments (LIGO, AdvLIGO, and LISA), CMB experiments, and today's limits are also shown on the plot. The plot comes from [39] with a small modification. The  $\Omega_{\text{GW}}$  sensitivity of CMB polarization experiments (red region) is evaluated by [40].

### 1.3.2 Status of CMB Measurements

Today the primordial gravitational waves are not discovered yet. We have just upper limits on the tensor-to-scalar ratio. Various experiments reported the upper limits at 95% confidence level from the  $B$ -mode measurements:

---

today's horizon scale.

- $r < 0.72$  from the  $B$ -mode measurement by BICEP [41],
- $r < 2.1$  from the  $B$ -mode measurement in the seven-year *WMAP* result [30],
- $r < 1.6$  from the  $B$  and  $E$ -mode measurement in the seven-year *WMAP* result,
- $r < 0.93$  from the  $B$ -mode,  $E$ -mode, and  $TE$  power spectra in the *WMAP* result,

and from the CMB measurements with both temperature and polarization information:

- $r < 0.36$  from the temperature and polarization power spectra in the *WMAP* result,
- $r < 0.33$  by the *WMAP* result with other CMB data of ACBAR [42] and QUaD [43],
- $r < 0.25$  from the *WMAP* result with ACT data [44],

and with combination of low-redshift observations

- $r < 0.24$  from the *WMAP* result with the Baryon Acoustic Oscillation (BAO) data [45] and the Hubble constant ( $H_0$ ) measurements [46],
- $r < 0.20$  from the *WMAP* result with BAO, and the supernova data (SN) called “Constitution” samples [47],
- $r < 0.19$  from the *WMAP* result with ACT, BAO, and  $H_0$  data.

The limit from the  $B$ -mode measurements is still  $r = \mathcal{O}(1)$  level (Figure 1.11). The lowest upper limit is obtained from the CMB temperature measurement with BAO and  $H_0$  data. This value is mostly determined by the temperature anisotropy from gravitational waves at large angular scales ( $\ell < 10$ ) and lower-redshift observations (BAO,  $H_0$ , and SN), which break so-called “ $n_s$ – $r$ ” degeneracy (Equation (1.19)). Since the temperature measurement at large angular scales already reached the limit by cosmic variance (see Appendix A.2), the limit on  $r$  will not be improved very much by measuring the temperature anisotropy more precisely at small scales in the future. In addition, the  $E$ -mode measurements do not help to improve the limit much from the above results too.

The  $B$ -mode measurement is the only way to improve the upper limits and be able to detect primordial gravitational waves in the future. Although the limits from the  $B$ -mode measurements were not good because polarization measurements were hard in the past,

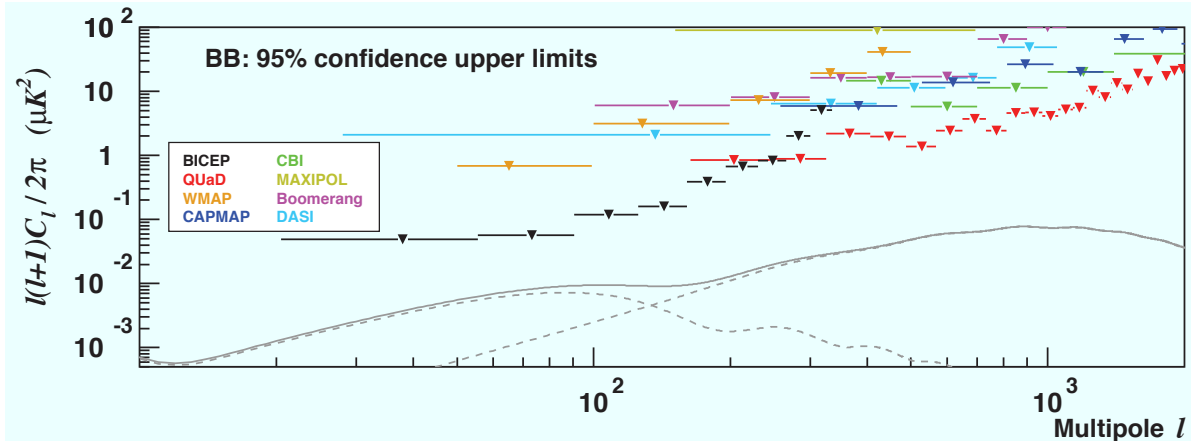


**Figure 1.11:** Today’s 95% C.L. upper limits on the  $B$ -mode power spectrum from various CMB polarization experiments [48, 49, 50, 51, 52, 53, 54, 43]. The plot is from [41]. The gray solid line represents the theoretical  $B$ -mode power given by the  $\Lambda$ CDM model with  $r = 0.1$  including both the primordial gravitational  $B$ -mode and the gravitational lensing effect.

recent rapid evolution of polarization detector technology makes it possible to certainly improve the sensitivity dramatically.

## 1.4 QUIET

The Q/U Imaging Experiment (QUIET) is one of the experiments to measure the  $B$ -mode very precisely. The QUIET observatory is located on the Chajnantor plateau in the Atacama desert of northern Chile at an altitude of 5,080 m. We developed very sensitive polarimeter arrays containing 19 modules at Q-band (43 GHz) and 90 modules at W-band (95 GHz). Using these arrays, we have observed between 2008 October and 2010 December, and collected over 10,000 hours of data.

Although our goal is to detect the  $B$ -mode, a demonstration of our unique technology and methodology is indispensable for future experiments. For this reason, the design of QUIET is scalable so that we can easily increase the number of our polarimeters, not only from 10 to 100, which has already been accomplished from the Q-band to W-band, but also from 100 to 500 and a few 1,000. Moreover QUIET is designed to suppress systematic errors, which will dominate the sensitivity on the  $B$ -mode in the near future.

Figure 1.12 shows the comparison with QUIET’s sensitivity and predicted  $B$ -mode power with certain inflation models<sup>l</sup>. That implies that we can discover the tensor-to-scalar ratio at  $r = \mathcal{O}(1)$  level from the Q-band data at  $r = \mathcal{O}(0.1)$  level from the W-band data. Furthermore, we are developing improved polarimeter arrays for the future QUIET plan (so-called “QUIET phase 2”), which has sensitivity to reach the tensor-to-scalar ratio at  $r = \mathcal{O}(0.01)$  level. That will reveal the principle of the inflationary universe.

The Galactic foreground will be major nuisance emission for CMB polarization measurement in the near future. Since QUIET is one of two experiments<sup>m</sup> after the *WMAP* satellite to measure the CMB polarization at low frequencies ( $\nu < 100$  GHz, see Figure 1.13), a study for contamination from the Galactic synchrotron emission is also a major target against the other experiments which observe at high frequencies ( $\nu > 100$  GHz), in which dust emission dominates the  $B$ -mode.

The purpose of this dissertation is to describe the measurement of CMB polarization power spectra at 43 GHz with QUIET. I summarize theory of the inflationary universe and the CMB polarization in Chapter 1. In Chapters 2 and 3, I describe instruments and observations of QUIET. After that I explain calibration procedure in Chapter 4. I describe data analysis and data selection in Chapters 5 and 6, then validate them in Chapter 7. I show results in Chapter 8 and discuss systematic errors in Chapter 9. Conclusions are found in Chapter 10.

---

<sup>l</sup>Table 1.2 show sensitivities to detect “lensing”  $B$ -mode induced by the weak gravitational lensing by the intervening large-scale structure of the universe [55]. Detecting the lensing  $B$ -mode is one of the targets of CMB polarization experiments. The most interesting information obtained from this is absolute mass of neutrino. More details are found in [56]. Table 1.3 provides sensitivities to detect “reionization bump” of  $B$ -mode at large angular scales induced on reionization era. Detecting reionization bump is also one of the targets; however it is hard to observe from the ground because it appears at large angular scales such as  $\ell < 10$ .

<sup>m</sup>The other is *PLANCK* satellite [57].



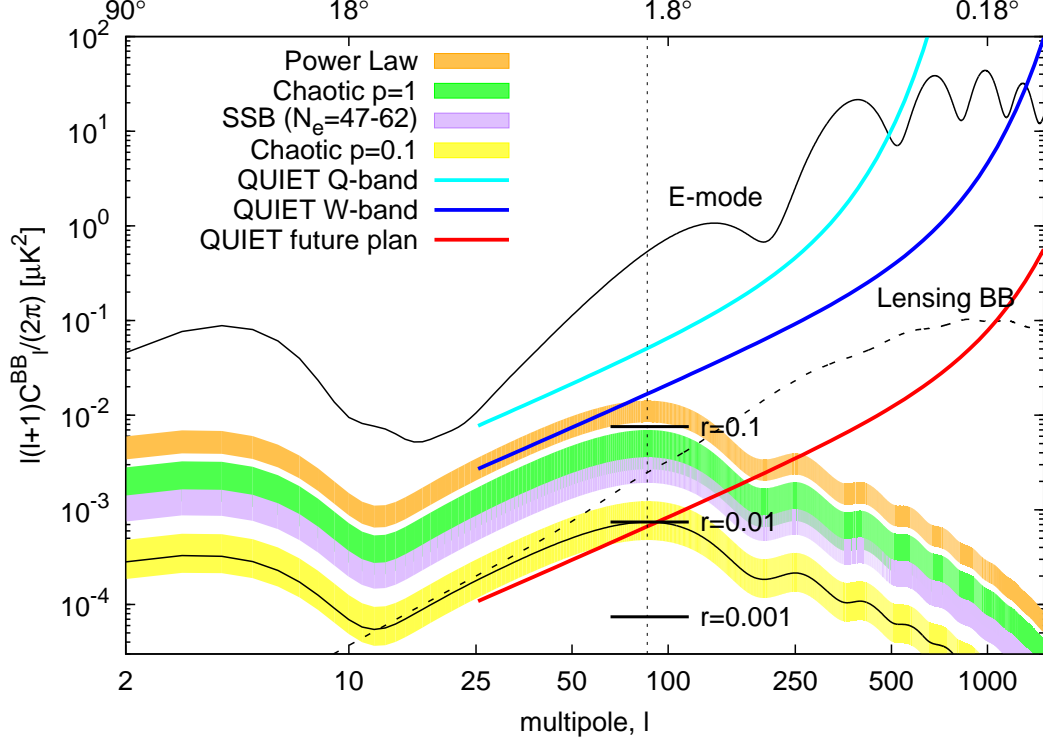


**Figure 1.12:**  $B$ -mode power spectrum comparison with QUIET’s  $1\text{-}\sigma$  error (band-combined with  $\Delta\ell = 50$ , including cosmic variance) and predictions from certain inflation models as described in § 1.2.3.3. The sensitivity of “QUIET Q-band” (cyan line) is given by so-called “Knox formula” ([58], Appendix A.2) with the design spec as follows:  $f_{\text{sky}} = 2.424\%$  ( $\approx 1,000 \text{ deg}^2$ ); array sensitivity of  $60 \mu\text{K}\sqrt{\text{s}}$ ; beam width of  $27'$  (FWHM); observing time of 3,500 hours. The sensitivity of “QUIET W-band” (blue line) is also given with the same specifications except that the beamwidth is improved to  $11'$  and observing time is 10,000 hours. The “QUIET future plan” (red line) will improve sensitivity by a factor of about 25 (500 polarimeters with about a half of the noise temperature of phase 1), which results in detectability of  $\Delta r = \mathcal{O}(0.01)$  level. Details on required sensitivities to detect  $B$ -mode are found in Table 1.1.

$\mathcal{C}_{\ell_{\text{LSS}}}^{BB} \mu\text{K}^2$		$\mu\text{K}'$	$\mu\text{K}\sqrt{s}_{(f_{\text{sky}}=1)}$	$\mu\text{K}\sqrt{s}_{(f_{\text{sky}}=0.03)}$
Primordial GW	$r = 1 \quad 8 \times 10^{-2}$	42	19	110
	$r = 10^{-1} \quad 8 \times 10^{-3}$	13	6	35
	$r = 10^{-2} \quad 8 \times 10^{-4}$	4	2	11
	$r = 10^{-3} \quad 8 \times 10^{-5}$	1	1	4

**Table 1.1:** Required sensitivities to detect  $B$ -mode polarization signal at the first peak.  $\mathcal{C}_{\ell_{\text{LSS}}}^{BB} \equiv \ell_{\text{LSS}}(\ell_{\text{LSS}} + 1)C_{\ell_{\text{LSS}}}^{BB}/(2\pi)$  corresponds to  $B$ -mode power at the first peak around  $\ell_{\text{LSS}} \sim 90$ . The third column shows required sensitivities to make  $3\text{-}\sigma$  detection of the  $B$ -mode power. These are given by  $\omega^{-1/2} = \left\{2\pi\mathcal{C}_{\ell_{\text{LSS}}}^{BB}(\Delta\ell)^{1/2}/(3\ell_{\text{LSS}}[\ell_{\text{LSS}} + 1])\right\}^{1/2} (10800/\pi) \mu\text{K}'$  from so-called ‘‘Knox formula’’ ([58], Appendix A.2). The fourth and fifth columns also show those in  $\mu\text{K}\sqrt{s}$  units in cases of the full sky observation and a partial sky one ( $f_{\text{sky}} = 0.03$ ) respectively for 1-year observation. This is also given by  $\text{NEQU} = 0.46 \times \omega^{-1/2} \mu\text{K}' f_{\text{sky}}^{-1/2} t_{\text{yr}}^{1/2} \mu\text{K}\sqrt{s}$  with an assumption of no loss of observation time and data due to analysis. All the sensitivities are band-combined with  $\Delta\ell = 50$ .

$\mathcal{C}_{\ell_{\text{lens}}}^{BB} \mu\text{K}^2$		$\mu\text{K}'$	$\mu\text{K}\sqrt{s}_{(f_{\text{sky}}=1)}$	$\mu\text{K}\sqrt{s}_{(f_{\text{sky}}=0.03)}$
Lensing $B$ -mode	$1 \times 10^{-1}$	5	2	13

**Table 1.2:** Required sensitivities to detect  $B$ -mode polarization signal at the peak of the lensing power around  $\ell_{\text{lens}} \approx 900$ . Definition of each column are the same as the above.

$\mathcal{C}_{\ell_{\text{re}}}^{BB} \mu\text{K}^2$		$\mu\text{K}'$	$\mu\text{K}\sqrt{s}_{(f_{\text{sky}}=1)}$
Reionization bump	$r = 1 \quad 3 \times 10^{-2}$	302	138
	$r = 10^{-1} \quad 3 \times 10^{-3}$	96	44
	$r = 10^{-2} \quad 3 \times 10^{-4}$	30	14
	$r = 10^{-3} \quad 3 \times 10^{-5}$	10	4

**Table 1.3:** Required sensitivities to detect  $B$ -mode polarization signal at the reionization bump at  $\ell_{\text{re}} = 2\text{--}6$ . Definitions of each column are the same as the above except band-combined with  $\Delta\ell = 5$ . Observation of whole the sky must be needed because the reionization bump appears on large angular scales.

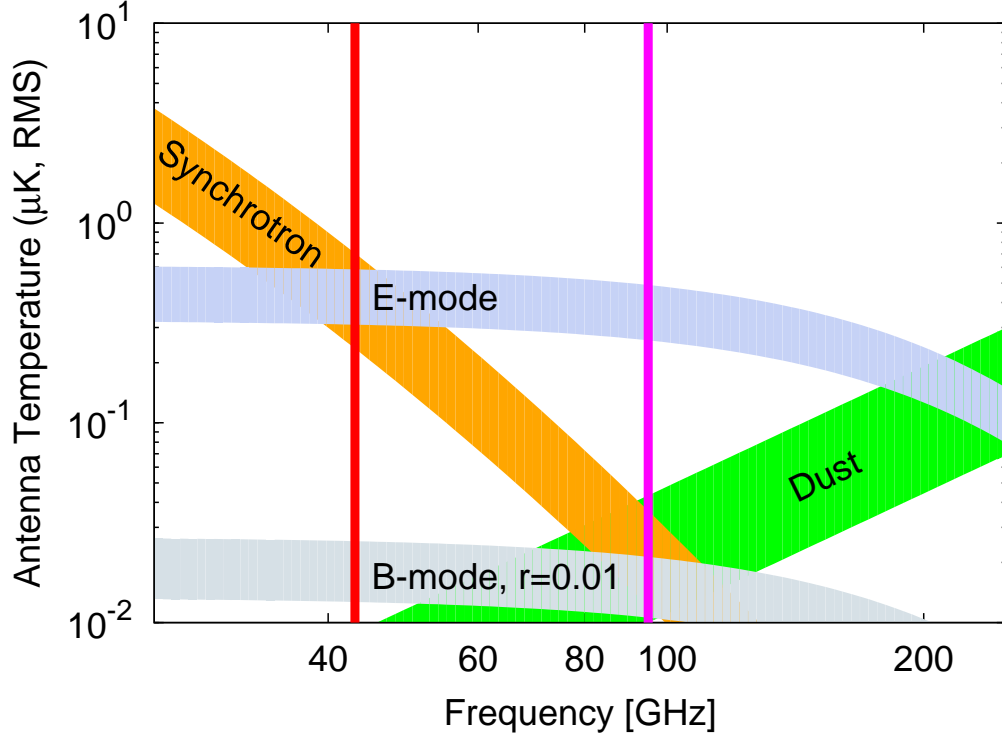


**Figure 1.13:** Frequency spectra of the Galaxy emission at large angular scales ( $\ell \approx 50$ ) are shown by orange band for synchrotron emission and green band for dust emission with the frequency range of QUIET Q-band (43 GHz, red vertical line) and W-band (95 GHz, magenta one). Compared with the  $E$ -mode signal (dark gray band), synchrotron emission dominates at the frequency lower than 90 GHz; on the other hand, dust emission dominates at the frequency higher than 90 GHz. One important thing is that dust emission has more variation than synchrotron emission generally. Amplitude of foreground emission is much bigger than that of the  $B$ -mode signal of  $r = 0.01$  in the all frequency range.



# Chapter 2

## Instrument

The QUIET Q-band instrument is discussed in this chapter. We have an array consisting of 17 low-noise correlation polarimeter modules. Each of them has four detector diodes, which can measure linear polarization and total power of radiation simultaneously. Our unique modulation techniques (“demodulation” and “double-demodulation”) provide the  $1/f$ -noise-suppressed polarization measurements, where the  $1/f$  comes from the amplifiers, detector diodes, and low frequency atmospheric fluctuations. The absence of the  $1/f$  noise makes it possible to measure CMB polarization at large angular scales. I only focus on the instrument for polarization though there are also two modules for calibration purpose and measuring the temperature anisotropy.

### 2.1 Overview

The QUIET optics is composed of a 1.4 m of the crossed Mizuguchi-Dragone (MD) dual reflective telescope [59, 60]. The crossed MD technique is very compact with low cross polarization effect and a large diffraction-limited field of view. QUIET is a first experiment to introduce it to CMB observations [61]. Figure 2.1 shows a diagram of the optics and a path of the incident light. The incident light on the primary mirror is reflected toward the secondary mirror, then reflected again and focused into an array of circular corrugated feedhorns. Since we need a large number of detectors to measure the CMB polarization, we made an array of feedhorns called “platelet array” [62] which is to assemble a whole array of feedhorns by making hole patterns on thin plates, then stacking

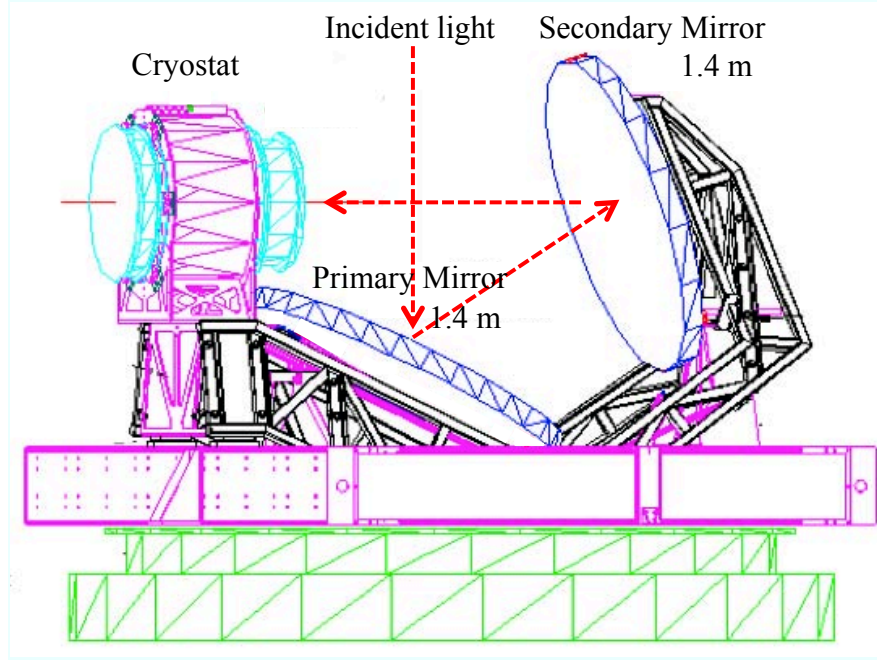


**Figure 2.1:** Diagram of the QUIET optics mounted the platform. The telescope is based on the crossed MD dual reflective optics. The primary mirror is a parabolic mirror of 1.4 m in diameter, and the secondary one is a concave hyperbolic mirror of 1.4 m in diameter. Dotted red lines correspond to a path of incident light. After reflected on the primary and secondary mirror, the incident light is focused into the feedhorns in the cryostat.



**Figure 2.2:** Top-view picture of the Q-band platelet array, which is composed of 19 feedhorns. All the polarimeter modules are attached at the other side with septum polarizers.

the plates (Figure 2.2). The whole optics provide a full width at half maximum (FWHM) beamsize of  $27'.3$ , and a field of view (for the main lobe or main beam) of  $7^\circ$  for the Q-band.

The incident light goes into each feedhorn, then it enters a septum polarizer [63]. The septum polarizer separates the incident light into left-circularly polarized radiation and right-one. After that, the separated lights go into two waveguide ports of a correlation polarimeter module separately. In the module, each light is amplified, the phase is shifted, the power is split, and resulting signals are coupled with each other. After passing band-pass filters, the coupled signals are rectified and received with detector diodes; thereby, the module outputs the Stokes  $\pm Q$ ,  $\pm U$ , and  $I$  parameters simultaneously. The septum polarizer and bandpass filters are designed to allow the maximum range of frequencies. More details on the polarimeter module and how it effectively measures polarization are described in § 2.2.

The module array and feedhorns are housed in a cryostat and cooled to 20 K in order to reduce instrumental noises<sup>a</sup>. The biases for the polarimeter are controlled with the electronics boards in a enclosure which is housed next to the cryostat. The temperature inside the enclosure was regulated to be  $25^\circ\text{C}$ . The polarimeter responses are read out with an ADC system in the enclosure too. We record the time-ordered data (TOD) from the polarimeters, telescope encoders, and other peripheral systems that provide housekeeping information.

The cryostat and mirrors are enclosed by an absorbing, comoving ground screen. The ground screen was designed to have two parts—an upper part and lower part; however, the upper part was not installed until the middle of W-band observation, which started after the Q-band observation. The absence of the upper part resulted in two kinds of far-sidelobes, which pick up not only ground emissions but also the Sun signal. Since these unfortunate pickups degrade the data quality, we have to treat the far-sidelobes carefully. We describe more details on the far sidelobes in § 2.3.

The mirrors, ground screen, cryostat, and electronics are mounted on the former Cosmic Background Imager (CBI) mount [64]. The CBI mount can control the three

---

<sup>a</sup>We used two CTI-Cryogenics Cryodtne 1020 two-stage refrigerators connected to CTI model 9600 compressors. Those operate as Gifford-McMahon (GM) cryocoolers.

axes: not only azimuth and elevation axes, but also a “deck” axis, which provides rotation about the axis of optical boresight. The deck rotation is useful to reduce the level of systematic contamination in both our calibration (Chapter 4) and power spectrum estimation (Chapter 5). In addition, the mount can rapidly move in the azimuth direction ( $\approx 5^\circ$  per second), which is very suitable to observe CMB polarization at large angular scales (Chapter 3).

Specific array-wide quantities are found in § 2.4. The instrumental details including modules for the temperature anisotropy are also described in [65, 66, 67].

## 2.2 Polarimeter Module

### 2.2.1 Polarimeter On a Chip

We developed unprecedentedly very small polarimeter modules, which are one of the greatest achievements of QUIET [68]. Reducing the size of a polarimeter is indispensable for CMB polarization experiments today because we need to increase the number of polarimeters on a focal plane. We have 17 correlation polarizer modules. The size of each module is only  $5.1 \times 5.1 \text{ cm}^2$ . A 30-cm-long polarimeter, by contrast, was used in the CAPMAP (the Cosmic Anisotropy Polarization Mapper) experiment [53], which is the precursor of QUIET. Our very small polarimeter module comes from a new technology called “polarimeter on a chip” [69] developed by JPL (Jet Propulsion Laboratory). It is based on the monolithic millimeter wave integrated circuit (MMIC) technology, which makes it possible to dramatically reduce the size of polarimeter components. Figure 2.3 shows the inside of a QUIET Q-band polarimeter module, which mainly consists of two waveguide inputs; six low noise amplifiers (LNAs, three for each chain) based on InP High Electron Mobility Transistors (HEMTs) manufactured using the MMIC technology; two phase switches; four bandpass filters; four detector diodes. Each LNA provides a gain of  $\sim 25 \text{ dB}$  over a bandwidth of  $\sim 20\%$ . These components operate at microwave frequencies and are connected with micro-striplines, which carry signals from the output of one device to input of the next.



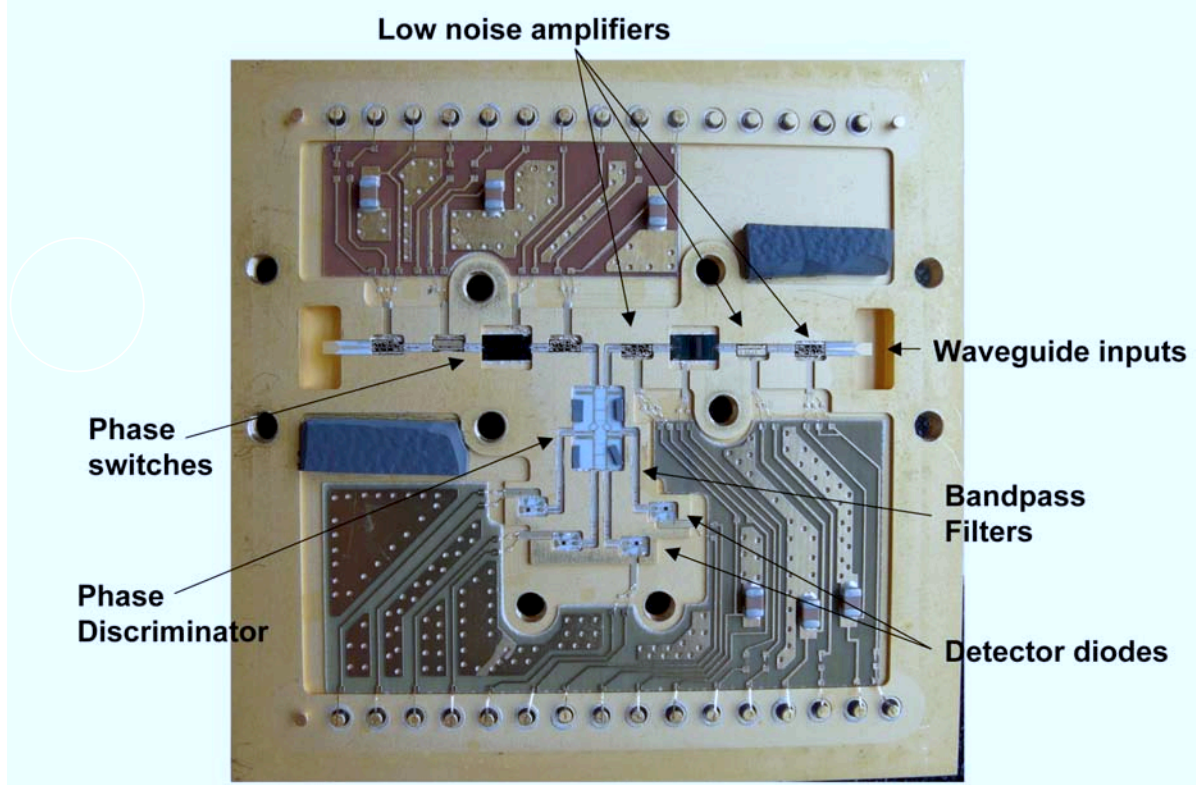


**Figure 2.3:** A photograph of the inside of a QUIET Q-band polarimeter module. Main components of the module are labeled in the photograph, and are packaged on the single chip whose size is only  $5.1 \times 5.1 \text{ cm}^2$ . The signal path runs from the waveguides to the diodes via micro-striplines. On the path, the signal is amplified by the low noise amplifiers, the phase of the signal is shifted by the phase switch, and the resulting signals are coupled on the phase discriminator with extra phase shifts. Through the bandpass filters, the detector diodes rectify the coupled signals at the end.

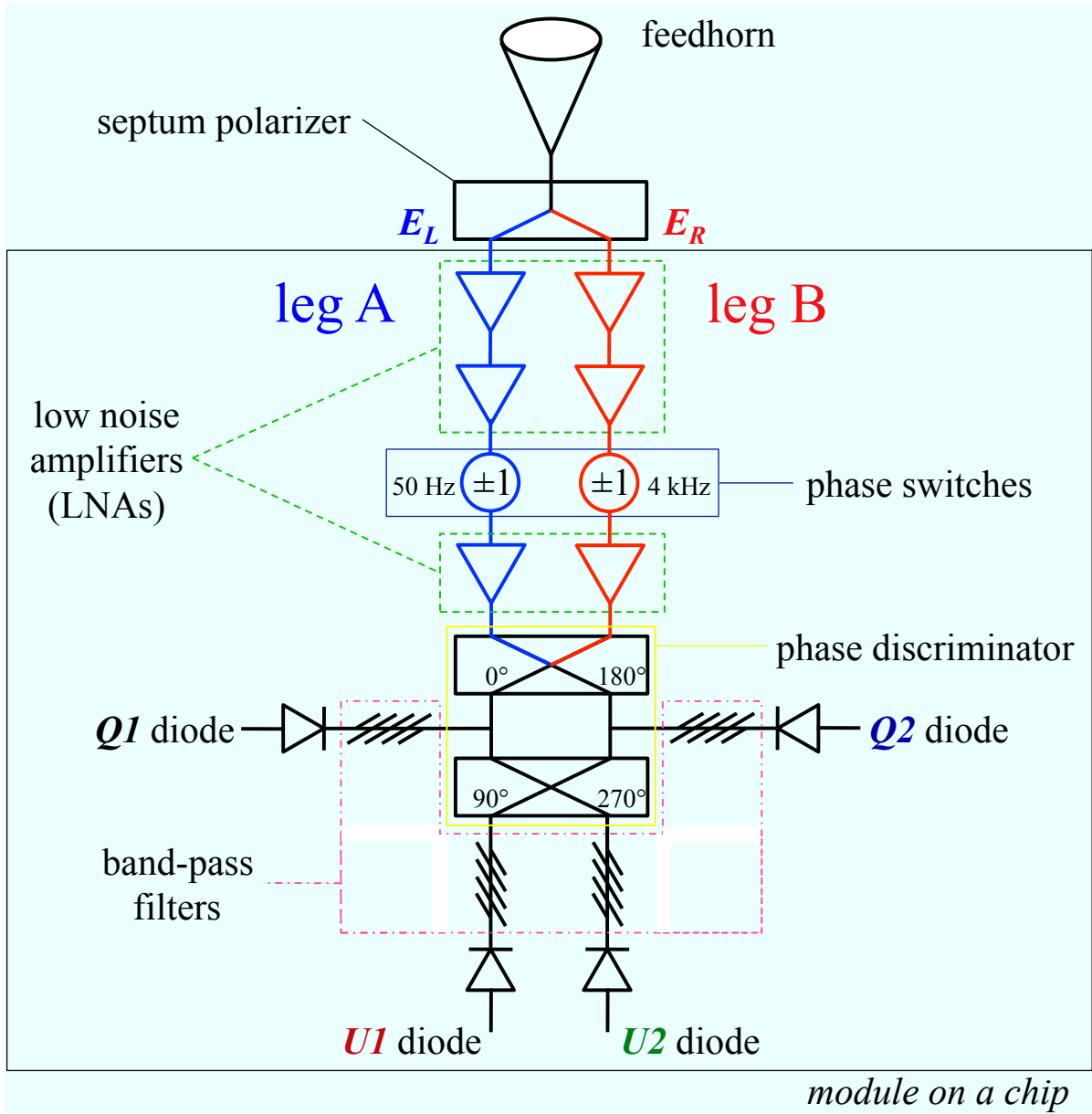


**Figure 2.4:** Schematic diagram of a QUIET Q-band polarimeter module with a feedhorn and septum polarizer. All the components except a feedhorn and septum polarizer are integrated in a module package on a chip. The incident signal runs from the top to bottom.

### 2.2.2 Principle of Polarization Measurement

The whole module schematic is shown in Figure 2.4. The polarimeter has two chains of amplifiers. We call them “legs”: leg A and leg B. Each leg has three LNAs and one phase switch. The left-circularly polarized radiation and right-one which are separated by the septum polarizer go into the leg A and leg B, respectively. On each leg, the signal from the waveguide is amplified by two LNAs, its phase is shifted by  $0^\circ$  or  $180^\circ$  (“phase switching”) synchronized with 4 kHz on the leg B or 50 Hz on the leg A. Then the signal is amplified again by the last LNA. This 4 kHz high-frequency phase switching (“demodulation”) can suppress the  $1/f$  noise due to the fluctuations of the HEMT amplifiers, detector diodes, electronics; and also low-frequency atmospheric fluctuations. Moreover, that 50 Hz low-frequency phase switching (“double-demodulation”) also suppresses the remaining  $1/f$  noise due to unequal transmission coefficients in the phase switch.

The signals from two legs are coupled on the phase discriminator (also known as the hybrid coupler), which consists of  $90^\circ$  and  $180^\circ$  couplers arranged in series. On the first stage of the phase discriminator, the signals are coupled with  $0^\circ$  or  $180^\circ$  phase shift. After that, each signal is divided by a power splitter, which diverts half the radiation power to the  $Q1 (+Q)$  or  $Q2 (-Q)$  detector diode. The remaining signals are also shifted by  $90^\circ$  or  $270^\circ$ , then coupled again. Each resulting signal goes into the  $U1 (-U)$  or  $U2 (+U)$  detector diode. The outputs of each detector diode are digitized with the ADC system with a sampling rate of 800 kHz and 18 bits precision. The digitized signals are down sampled to 100 Hz demodulated and averaged on the ADC system. Finally the resulting signals are recorded as the TOD. Full formula about polarimeter operations such as averaging, phase switching, differencing and so on, are found in Appendix B.

Meanwhile, to average the signal rather than to demodulate the signal provides the output of Stokes  $I$  parameter, which corresponds to the total power of the incident light. The total power output is useful to monitor the weather condition (Chapter 5) and the stability of the detector responsivities (Chapter 4) but suffers too much from contamination of the  $1/f$  noise to measure the CMB temperature anisotropy itself.

Bandpass filters, which are located between the phase discriminator and the diodes, limit the range of frequencies in order to minimize the spurious polarization.

### 2.2.3 Requirement of ADC Sampling and Phase Switching Rate

The LNAs (HEMT amplifiers) have the  $1/f$  noise at frequencies below about 2 kHz; unequal transmission coefficients in the phase switch have the  $1/f$  noise at lower frequencies<sup>b</sup>; therefore, 4 kHz and 50 Hz phase switching are required to reduce these contaminations. In order to reduce the effect of the ringing noise of the 4 kHz phase switching, we have to mask it, which takes about  $25\mu$  seconds. Thereby we require a precision of about  $2.5\mu$  seconds (one tenth of the ringing noise time). For this reason, we need preamplifiers operated with 400 kHz, then 800 kHz ADCs are required (twice the amplifier frequency).

Meanwhile QUIET targets to measure the  $B$ -mode polarization at an angular scale up to  $\ell_{\text{beam}} \approx 500$ , which is limited by the beamwidth, then an angular precision of about  $0.1^\circ$  (about a half of the beamwidth) is needed. Since the telescope usually scans a CMB patch by about  $2^\circ$  per second on the sky, the 50 Hz timestreams of the double-demodulation have enough angular resolution.

### 2.2.4 Impact of the Demodulation and Double-Demodulation for “Science Band”

Figure 2.5 shows TODs of the total power, demodulation, and double-demodulation. TOD of the total power are fluctuated, but those of the double-demodulation are very stable. Figure 2.6 shows their noise power spectra, which shows that the  $1/f$  noise is suppressed by phase switching by a factor of  $10^5$ . Figure 2.7 shows comparison between angular power spectra of CMB polarization and that of noise power spectrum. That implies that the  $1/f$  noise frequency is much less than our scan frequency ( $f_{\text{scan}} = 45\text{--}100$  mHz). In consequence, a “science band” of the QUIET Q-band is free from the  $1/f$  noise contamination, and is limited by our scan frequency and beamwidth.

---

<sup>b</sup>The typical frequency of the remaining  $1/f$  noise is about 100 mHz for a W-band module. The double-demodulation frequency of 50 Hz is sufficient for that. By contrast, the typical frequency for a Q-band module is much smaller than that for a W-band one.

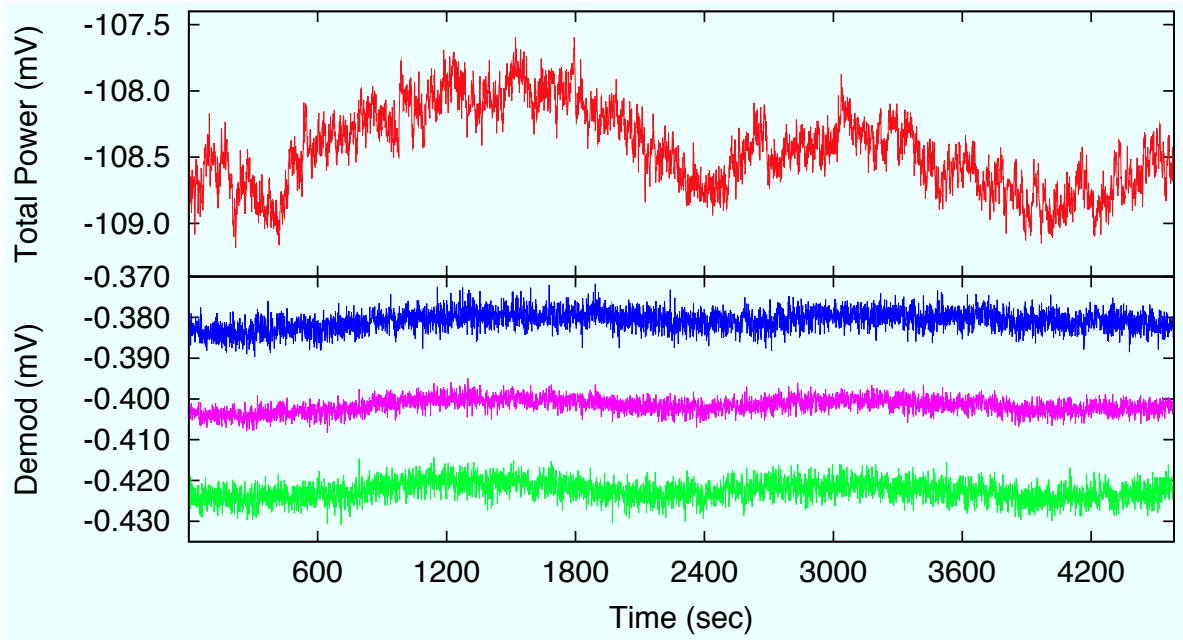


**Figure 2.5:** TODs of the total power (red line), demodulation (the green line corresponds to “+” state of the 50 Hz phase switch, and blue one corresponds to the “−” state multiplied by  $-1$  in order to obtain the same sign), and double-demodulation (magenta line) from the  $Q1$  diode during the CMB observation. The data are averaged over 1 Hz.

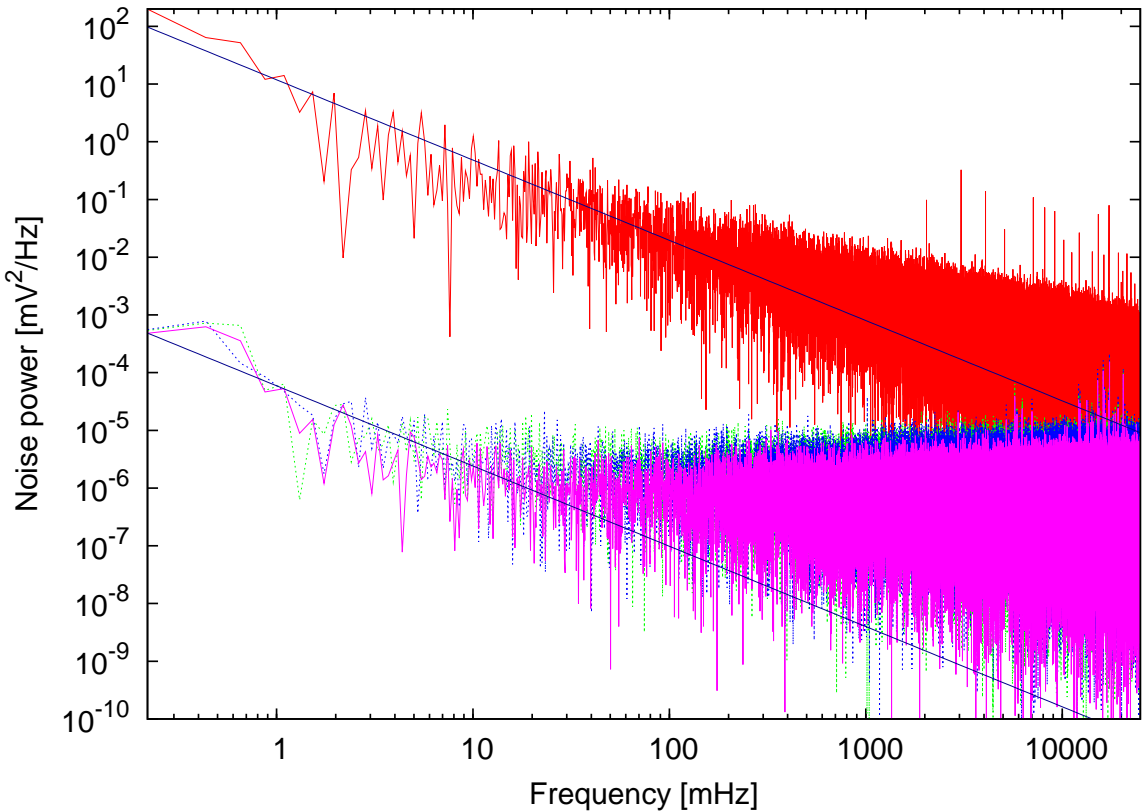


**Figure 2.6:** Comparison of noise power spectra for the total power, demodulation, and double-demodulation. Dark blue lines corresponds to the  $1/f$  component for the total power and demodulated signals, which show that phase switching suppresses the  $1/f$  noise by a factor of  $\approx 10^5$ . Definition of red, green, blue, and magenta lines are the same as those in Figure 2.5.

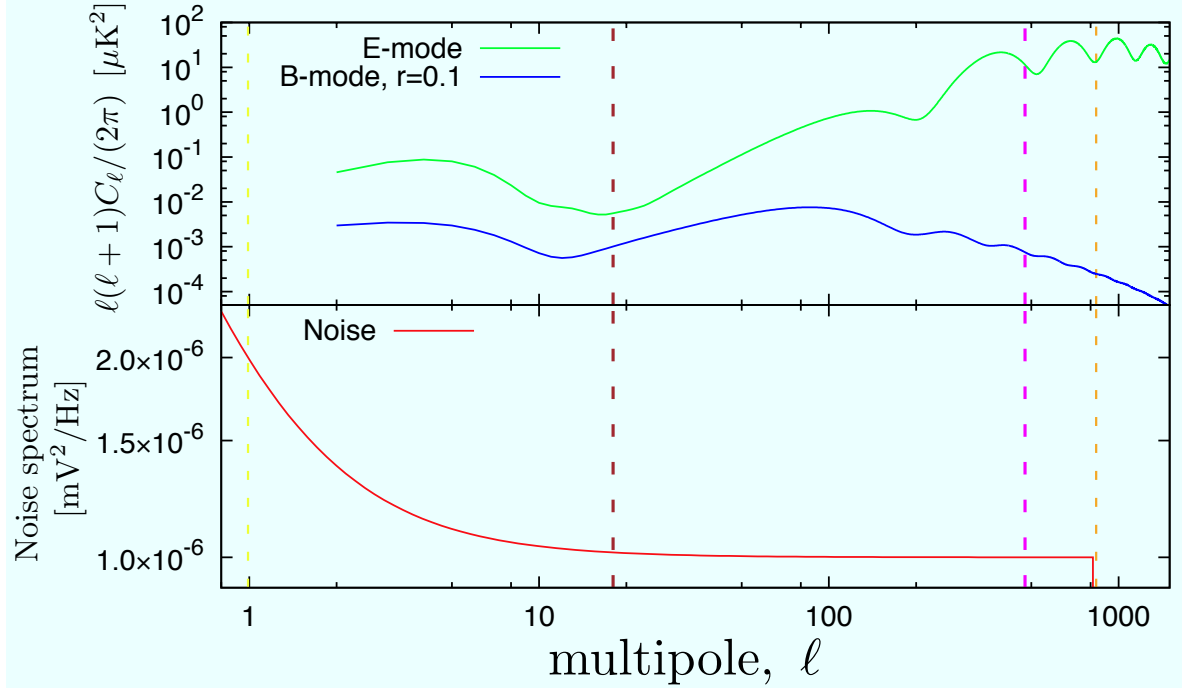


**Figure 2.7:** Comparison between angular power spectra of  $E$ -mode (green line) and  $B$ -mode (blue line,  $r = 0.1$ ) and a typical noise power spectrum obtained from the QUIET Q-band observation. For our scanning speed (typically  $5^\circ$  per second in the azimuth) and observing elevation ( $\sim 60^\circ$  as the median), the conversion from TOD frequency ( $f$ ) to angular multipole on the sky ( $\ell$ ) is given by  $\ell \approx 180f$ . The vertical dashed lines correspond to typical frequencies of our instrument:  $1/f$  noise knee frequency (yellow,  $f_{\text{knee}} \approx 5.5 \text{ mHz} \rightarrow \ell_{\text{knee}} \approx 1$ , typically), scan frequency (brown,  $f_{\text{scan}} \approx 100 \text{ mHz} \rightarrow \ell_{\text{scan}} \approx 18$ ) and beamwidth (violet,  $\ell_{\text{beam}} \approx 500$ , Chapter 3), low-pass filter (orange,  $f_{\text{low-pass}} = 4.65 \text{ Hz} \rightarrow \ell_{\text{low-pass}} \approx 800$ ) to drop the high frequency noise above 6 Hz (Chapter 5). These give our “science band” of  $f_{\text{scan}} < f < f_{\text{beam}} \rightarrow 18 < \ell < 500$ .

## 2.3 Far-Sidelobes

The main beam of the QUIET optics is well controlled; however, far-sidelobes were not managed well in the Q-band observation season. The QUIET ground screen is designed to block rays that miss the primary and secondary mirrors, then go into the modules directly (Figure 2.8). However an upper part of the ground screen had not been installed until the middle of W-band observation. That resulted in two far-sidelobes.

Figure 2.9 shows a schematic showing the location and origin of the sidelobes. We call the first far-sidelobe “triple reflection sidelobe”. Some rays reflected on the top edge of the secondary mirror go into very low part of the primary mirror; they are reflected again toward the secondary mirror; they are also reflected on the secondary mirror again and directed into the feedhorns. The geometry of this sidelobe is well understood with rays passing through the lower ground screen aperture at an angle of  $50^\circ$  from the main beam as shown in the schematic figure. The second far-sidelobe results from rays passing through the lower ground screen aperture in the opposite direction of the triple reflection sidelobe at an angle of  $60^\circ$  from the main beam and directly going into the feedhorns. We call it “spillover sidelobe”.

These two far-sidelobes were predicted by physical ray tracing simulation with GRASP<sup>c</sup>. The upper ground screen was designed to block them; however, we had no upper ground screen in the Q-band observation. We characterized the far-sidelobes by the Sun using all the CMB observation data, and found it is less than  $\approx -60$  dB level (Chapter 6). The far-sidelobes may pick up the ground emission and bright sources on the sky at that level. These effects are eliminated by the filtering, cross-correlation (Chapter 5), data selection (Chapter 6) in the analysis. Moreover, the systematic biases induced by them are evaluated to be small enough in Chapter 9.

## 2.4 Instrument Characterization

We summarize the QUIET Q-band instrument quantitatively. We discuss specific quantities again in Chapters 4, 5 and 7.

---

<sup>c</sup>A software package of physical optics simulation developed and commercially sold by TICRA.

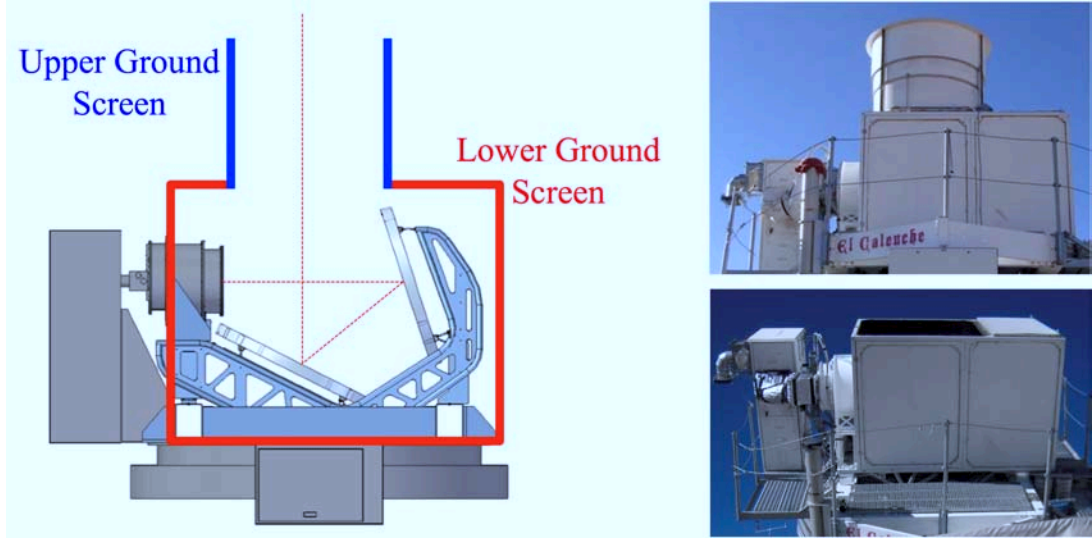


**Figure 2.8:** Diagram of the designed ground screen (left) and its picture of that (right top). The telescope has two parts, an upper and lower ground screen to block unfavorable rays; however, the upper one was not installed in Q-band observation season (right bottom).

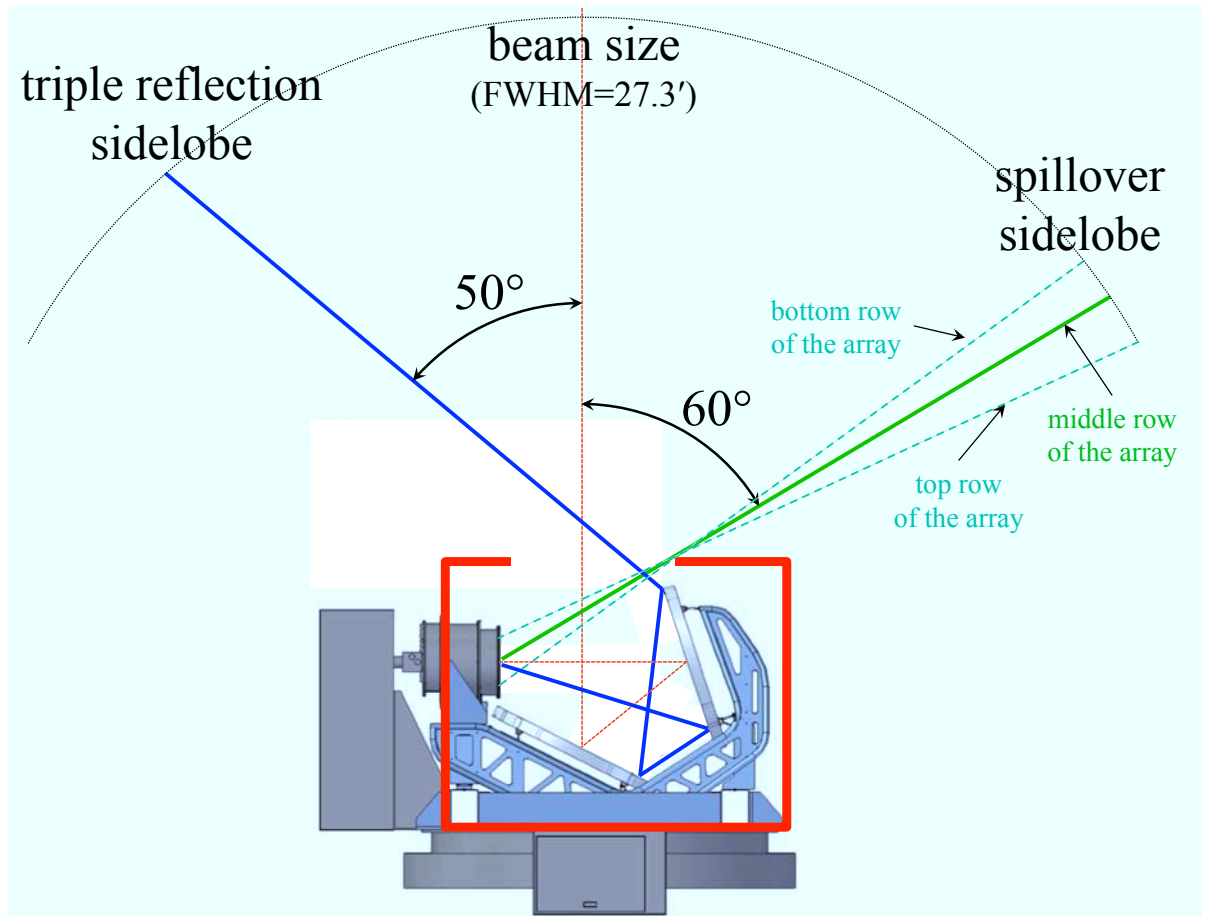


**Figure 2.9:** Location and origin of the far-sidelobes.



The solid angle of our telescope is  $76.0 \mu\text{sr}$  measured with Tau A and Jupiter observations, which is consistent with the designed value. The band-center frequency is  $43.1 \pm 0.4$  GHz determined with bandpass measurements in the lab and at the site. The bandpass measurements also provided the average bandwidth of  $7.6 \pm 0.5$  GHz (18% of the band-center frequency). The detector responsivity and preamplifier gains are well calibrated and very stable during the observation although the gain mismatch never cause instrumental polarization in our case. Meanwhile, another kind of instrumental polarization peculiar to our polarimeter module ( $I \rightarrow Q/U$  leakage) is measured fine. The typical values are 1.0% (0.2%) for the  $Q$  ( $U$ ) diodes.

Typical noise level of the polarimeter module, which has four polarization sensitive diodes, is  $280 \mu\text{K}\sqrt{\text{s}}$  in thermodynamic units relative to the CMB polarization. Since 62 polarization sensitive channels from  $17 \times 4 = 68$  channels ( $62/68 \approx 91\%$ ) were available during the observation, the array sensitivity is  $69 \mu\text{K}\sqrt{\text{s}}$ . The  $1/f$  noise knee frequency after the double-demodulation is 5.5 mHz, which is much smaller than the telescope scan frequency (45–100 mHz).

The performance of the QUIET Q-band instrument is summarized in Table 2.1.

Name	Value	Description
Array sensitivity	$69 \mu\text{K}\sqrt{\text{s}}$	
Sensitivity per module	$280 \mu\text{K}\sqrt{\text{s}}$	$Q$ and $U$ diodes combined
$1/f$ noise knee frequency	5.5 mHz	median ( $\ll f_{\text{scan}} = 45\text{--}100$ mHz)
Leakage	1.0% / 0.2%	$Q$ / $U$ diodes
Phase switch frequency	4 kHz / 50 Hz	primary (leg A) / secondary (leg B)
ADC sampling rate	800 kHz	
Number of elements	62 / 68	functional / total
Central frequency	$43.1 \pm 0.4$ GHz	average
Bandwidth	$7.6 \pm 0.5$ GHz	average
Cryostat temperature	20 K	average
Primary mirror diameter	1.4 m	
Field of view	$7^\circ$	diameter on the sky
Beamwidth	$27.3'$	FWHM ( $= \sigma\sqrt{8 \ln 2}$ )
Solid angle	$76.0 \mu\text{sr}$	
Far-Sidelobes power	$< -60$ dB	

**Table 2.1:** Summary of the QUIET Q-band instrument.

# Chapter 3

## Observation

### 3.1 Observation Site



**Figure 3.1:** Overview of the QUIET site on the Chajnantor plateau in the Atacama desert.

QUIET is located on the Chajnantor plateau in the Atacama desert of northern Chile ( $67^{\circ}45'42''\text{W}$   $23^{\circ}01'42''\text{S}$ ) at an altitude of 5,080 m (Figure 3.1). Difficulties for ground-based CMB experiments are atmospheric effects. Absorption lines from oxygen (around 60 and 120 GHz) and water vapor (20 and 180 GHz) limit access to the microwave sky as shown in Figure 3.2. Clouds and high water vapor can harm ground-based measurements. For this aspect, the Chajnantor plateau is one of the best places for CMB observation because

- Atmospheric pressure at the site is a half of that on the ground. Then high altitude suppresses contamination from oxygen.

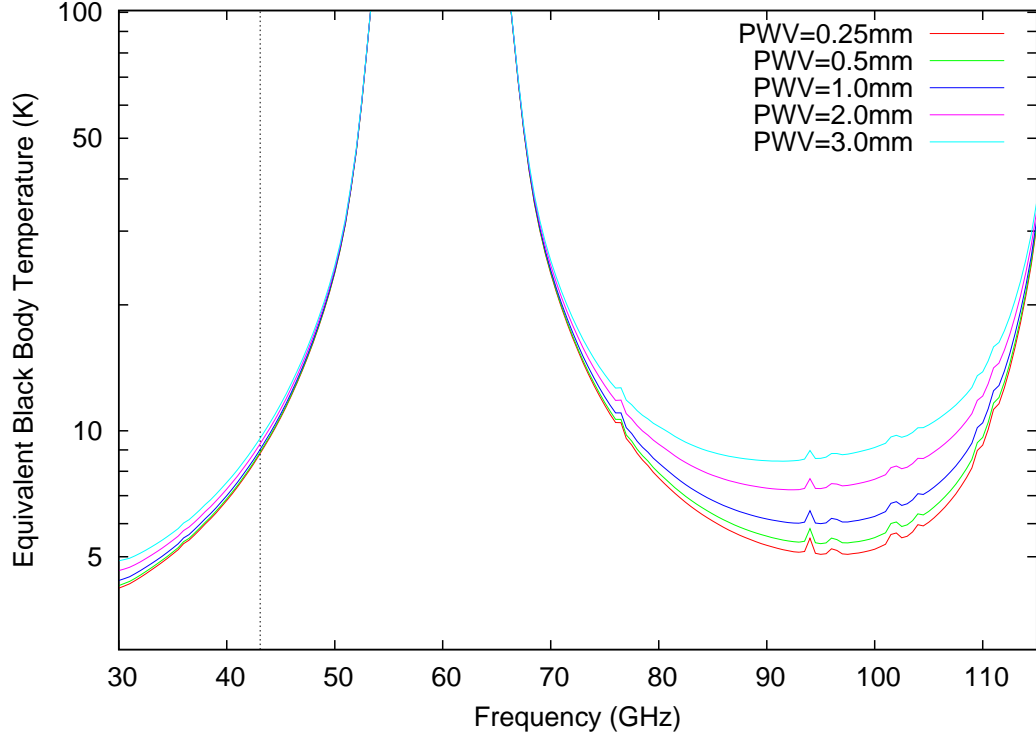


**Figure 3.2:** Equivalent blackbody (EBB) temperature of the zenith sky at the Atacama Large Millimeter Array (ALMA) site, which is very next to the QUIET site, as a function of frequency given by the Atmospheric Transmission at Microwaves (ATM) model [70]. Each line corresponds to different precipitable water vapor (PWV) values. Peaks around 60 GHz and 120 GHz are caused by absorption lines from oxygen. Though there is no line from water vapor, temperature around 90 GHz significantly increases as the PWV increases. A vertical dotted line corresponds to the Q-band frequency of 43.1 GHz.

- Dry atmosphere or low precipitable water vapor (PWV), decreases contamination from water vapor, especially for the W-band observation. Median of the PWV measured at the APEX site [71], which is located at a distance of 2.5 km from the QUIET site, was about 1.2 mm during the Q-band observation. From the Atmospheric Transmission at Microwaves (ATM) model [70], equivalent blackbody (EBB) temperature of the zenith sky was 9 K at 43.1 GHz.
- The weather is good throughout the year. We can observe with low contamination from water vapor throughout the year.

In addition to atmospheric advantages, the Chajnantor plateau has another advantage. We can access the site every day from San Pedro, where observers and engineers stay during the measurements throughout the year. It is very important for us to perform stable and reliable long-sustained observation because thousands of hours of data are needed to detect the CMB polarization.

## 3.2 Observation Patch

We observed four CMB patches and two Galactic patches on the sky. Each of them approximately covers an area of  $250 \text{ deg}^2$ . The CMB patches were chosen to avoid contamination from Galactic foregrounds, especially diffuse synchrotron emission, based on the Q-band all-sky *WMAP* temperature map (Figure 3.3). Since the sky rotates once a day in the direction of right ascension, it is natural to distribute the four patches in right ascension every  $90^\circ$ . Our first priority is to observe the four CMB patches, however, none of them is available for a few hours in a day because our Galaxy must go across the sky once a day. In that case, we observed the Galactic patches. Data of the Galactic patches is used to study foreground contaminations and the Galactic center. List of the patch locations is found in Table 3.1. Note that the patch CMB-1 is closest to the Galactic plane in the four CMB patches.

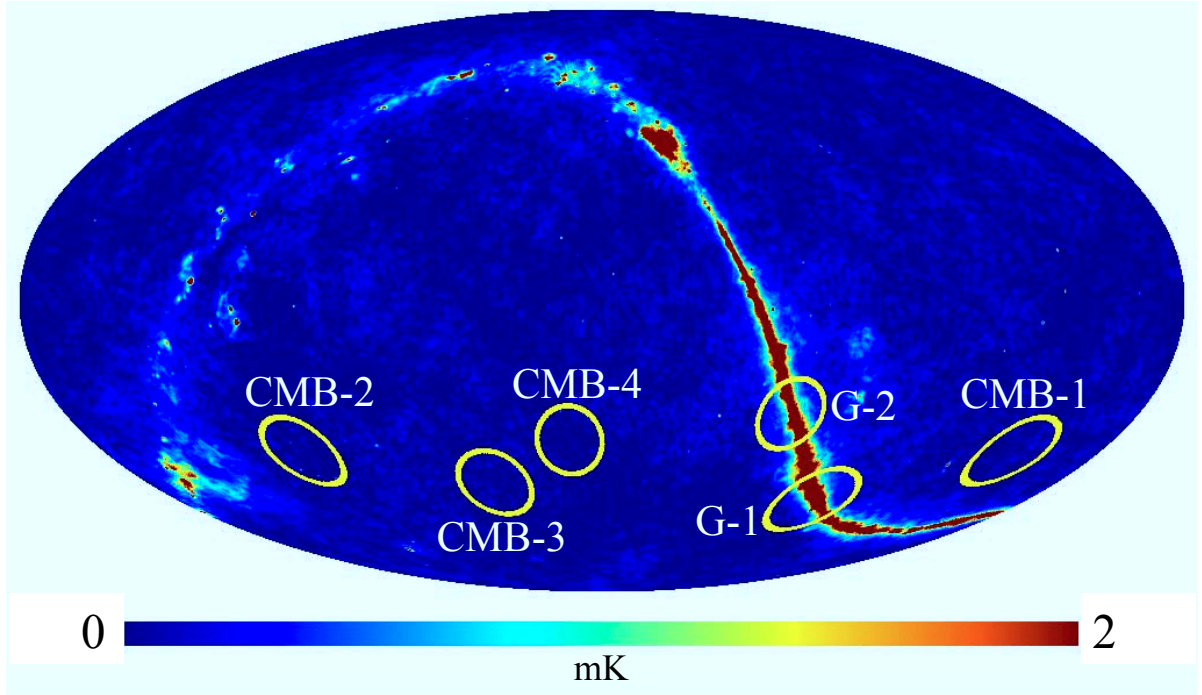


**Figure 3.3:** Four CMB patches (CMB-1,2,3,4) and two Galactic patches (G-1,2) of the QUIET observation are shown in the Q-band all-sky *WMAP* 7-year temperature map [72] in equatorial coordinates. Horizontal direction corresponds to right ascension; therefore, we observe CMB-4, 3, 2, 1, and G-2, 1 in turn everyday. Red saturated band corresponds to our galaxy, and G-2 corresponds to the Galactic center.

Patch	RA	Dec	$l$	$b$	Integration hours
CMB-1	12 <sup>h</sup> 04 <sup>m</sup>	−39° 00′	293.54°	22.77°	905 (33.9%)
CMB-2	5 <sup>h</sup> 12 <sup>m</sup>	−39° 00′	243.17°	−34.96°	703 (26.3%)
CMB-3	0 <sup>h</sup> 48 <sup>m</sup>	−48° 00′	303.48°	−69.40°	837 (31.4%)
CMB-4	22 <sup>h</sup> 44 <sup>m</sup>	−36° 00′	7.13°	−62.20°	223 (8.4%)
CMB Total					2,668
G-1	16 <sup>h</sup> 00 <sup>m</sup>	−53° 00′	329.45°	−0.47°	311 (77.2%)
G-1	17 <sup>h</sup> 45 <sup>m</sup>	−28° 56′	0.28°	−0.49°	92 (22.8%)
Galactic Total					403

**Table 3.1:** List of the patch location—RA and Dec ( $l$  and  $b$ ) with epoch J2000—and integration hours of the QUIET observation.

### 3.3 Observation Time

We began the Q-band observation on October 24, 2008 and ended it on June 13, 2009 (233 days). We took 3,458 hours of data; 77% of the data (2,668 hours) were for the CMB patches, and 12% (403 hours) were for the galactic patches (Table 3.1). The other 7% (256 hours) were for calibration sources, and the remaining 4% were rejected due to obvious instrumental and site problems. The overall operation efficiency is 63%.

### 3.4 Observation Strategy

In this section, I describe observation strategy for the CMB. The strategy for calibrations is shown in Chapter 4.

Scanning the sky, we encode signals from CMB polarization into time-ordered data (TOD). Our main target is measuring the  $B$ -mode power spectrum at large angular scales from  $1^\circ$  to  $10^\circ$ . An amplitude of scans should be wide enough to cover these angular scales. By contrast, the scan period needs to be short enough to suppress the instrumental and atmospheric  $1/f$  noise (typically  $f_{\text{knee}} = 5.5$  mHz). Accordingly, we performed a scan with a full width of  $15^\circ$  (amplitude of  $7.5^\circ$ ) on the sky in period between 10 and 20 seconds ( $1.5^\circ$ – $3^\circ$  per second on the sky<sup>a</sup>). This corresponds to a typical frequency between 45 mHz and 100 mHz, which is much shorter than the period of the  $1/f$  noise as shown in Figure 2.7.

We performed a “Constant-Elevation Scan” (CES), which consists of a series of periodic azimuth motion with a fixed elevation and boresight axes. All the modules see almost constant atmospheric signals during a CES. A typical CES has duration of from 45 minutes to 90 minutes. In this way, we avoid a possible contamination from the atmosphere because the  $I \rightarrow Q/U$  leakage is easy to harm the CMB signal although the atmosphere itself is little polarized [73, 74].

In order to cover an area of  $15^\circ \times 15^\circ$  for each patch, a CES has a full width of  $15^\circ$  on the sky and the telescope is re-pointed when the sky has drifted by  $15^\circ$  in about an hour. Since the array has about a  $7^\circ$  field of view, about  $8^\circ \times 8^\circ$  of a central area of each

---

<sup>a</sup>This corresponds to the telescope azimuth speed of  $3^\circ$ – $6^\circ$  per second if the elevation is  $60^\circ$ .

patch is observed by all the modules. Thus we can measure CMB power spectra at large angular scales.

In addition, we used diurnal sky rotation and weekly boresight rotation in order to achieve sufficient parallactic angle coverage and suppress the  $I \rightarrow Q/U$  leakages. This is another type of demodulation to reduce systematic errors.



# Chapter 4

## Calibration

### 4.1 Overview

#### 4.1.1 Goals of Calibration

The CMB polarization is fully described by the linear polarization<sup>a</sup>, which is parameterized with the Stokes  $Q$  and  $U$  parameters. To measure the linear polarization on the sky, calibration is needed. The goal of calibration is to obtain the following four quantities that are applied at the beginning of the data analysis:

- *Detector Responsivity*: Since the CMB signal is measured by a polarimeter module in units of *Voltage*, we need to convert them with thermodynamic temperature units of *Kelvin*. This conversion coefficient is called “Detector Responsivity”.
- *Detector Angle*: Since the polarization axis of each module-diode is not aligned with that on the sky coordinates system, we need to know orientation of the polarization axis, and correct it.
- *Pointing*: Mispointing leads to distortion on a polarization map, which could dilute  $E$ -mode signals and might create fake  $B$ -mode signals. We need to know which direction each detector is looking in.
- *Beam Profile*: Observed CMB signal is convolved with finite resolution of the telescope optics. We need to deconvolve the signal with the optics information.

---

<sup>a</sup>The Thomson scattering cannot create the circular polarization.

Additionally, the “ $I \rightarrow Q/U$  leakage” is also an important parameter to understand systematic bias induced by spurious polarization signals:

- $I \rightarrow Q/U$  Leakage: Instrumental imperfection leads to fake polarization signals proportional to the CMB temperature anisotropy. Since the temperature anisotropy is much bigger than the polarization, we need to understand the effect well.

### 4.1.2 Calibration Sources

There are various ways to calibrate the four quantities and the  $I \rightarrow Q/U$  leakage. We measured five sources for the calibration purpose: Tau A, the sky dips, the Moon, a rotating sparse wire grid, and Jupiter<sup>b</sup>. Table 4.1 lists each calibration quantity with sources which are used to calibrate. Table 4.2 lists the schedule and duration for each source. Among these sources, Tau A is the most important because it is the only source that is useful to simultaneously determine the absolute polarization responsivity, detector angle, beam profile, and  $I \rightarrow Q/U$  leakage with small systematic errors.

	Tau A	Moon	Wire grid	Sky dips	Jupiter
Polarization Responsivity	✓	(✓)	(✓)		
(Total Power Responsivity)		(✓)		✓	✓
Detector Angle	✓	✓	✓		
$I \rightarrow Q/U$ Leakage	✓	✓		✓	
Pointing		✓			✓
Beam Profile	✓				✓

**Table 4.1:** Calibration quantities and calibration sources. A source with a check mark can determine the corresponding quantity well. Check marks in parentheses can also be used, but with larger systematic uncertainties.

<sup>b</sup>Additionally, Venus and RCW 38 are mostly used for the calibration for the differential-temperature modules.

Source	Schedule	Duration (min.)
Tau A	every 1–2 days	20
Moon	weekly	60
Wire grid	end of the season	(†)
Sky dips	every 1.5 hours	3
Jupiter	weekly	20

**Table 4.2:** Calibration observations for the QUIET Q-band. Note (†): the wire grid measurement was only taken at the end of the season.

## 4.2 Tau A

Tau A (Taurus A, Crab nebula, M1 or NGC1952, at coordinates  $\alpha_0 = 5^{\text{h}} 34^{\text{m}} 31.97^{\text{s}}$ ,  $\delta_0 = 22^\circ 00' 52.10''$ ) is a supernova remnant that emits a highly polarized radiation due to the synchrotron radiation of the central pulsar and its interaction with the surrounding gas [75]. Tau A is the most intense polarized source in the microwave sky for the QUIET beamwidth. Therefore, Tau A is the best calibration source for polarization; we can calibrate the polarization detector responsivity, detector angle, and  $I \rightarrow Q/U$  leakage.

### 4.2.1 Accuracy of Tau A Measurements

#### 4.2.1.1 Measurements of Tau A by *WMAP* and IRAM

Tau A is well measured by the *WMAP* satellite (the seven-year paper [76] and the three-year paper [77]). We used their seven-year results for our calibration. The Tau A flux is decreasing with time at a rate of  $0.167 \pm 0.015\%$   $\text{yr}^{-1}$  at 8 GHz [78]. However, we can ignore this decrease because our Q-band season is short enough to neglect it even though the decrease stands up at the Q-band. Table 4.3 shows the intensity and polarization of Tau A for each frequency. Note that the IRAM 30 m telescope also measured Tau A at 89.19 GHz [79], however, this measurement is not compatible within  $3\text{-}\sigma$  with the intensity given by *WMAP* at 92.95 GHz. Here we do not consider this difference because we only focus on the polarized intensity at the Q-band.

	$\nu$ [GHz]	$I$ [Jy]	$P$ [Jy]	$\Pi$ [%]	$\gamma_{\text{PA}}$ [deg]
	22.70 (K)	$383.8 \pm 9.6$	$27.17 \pm 0.68$	$7.08 \pm 0.25$	$149.1 \pm 0.1$
	32.96 (Ka)	$342.8 \pm 6.4$	$23.80 \pm 0.44$	$6.94 \pm 0.18$	$149.9 \pm 0.1$
<i>WMAP</i>	40.64 (Q)	$317.7 \pm 8.6$	$22.12 \pm 0.60$	$6.97 \pm 0.27$	$150.3 \pm 0.2$
	60.53 (V)	$276.0 \pm 5.2$	$19.31 \pm 0.36$	$7.00 \pm 0.19$	$149.9 \pm 0.4$
	92.95 (W)	$232.8 \pm 9.7$	$16.60 \pm 0.73$	$7.13 \pm 0.43$	$148.9 \pm 0.7$
<i>IRAM</i>	89.19 (W)	$195.5 \pm 11.0$	$14.5 \pm 3.2$	$7.4 \pm 0.7$	$148.8 \pm 0.2$

**Table 4.3:** Intensity ( $I$ ), polarized intensity ( $P$ ), polarization fraction ( $\Pi$ ), and polarization angle ( $\gamma_{\text{PA}}$ ) of Tau A from the *WMAP* seven-year data and the IRAM 30m telescope.

#### 4.2.1.2 Polarized Tau A Intensity for the QUIET Q-band

Assuming a power-law spectrum of the polarized intensity of Tau A,  $P \propto \nu^\alpha$ , from the *WMAP* data, we obtain  $\alpha = -0.35 \pm 0.03$  and  $P = 21.71 \pm 0.23$  Jy at 43.1 GHz (Figure 4.1). The fit uncertainty is 1.1%. The polarized intensity does not change by more than 3.0%, when we change the frequency by the bandwidth (7.6 GHz). We conservatively use their quadratic sum of 3.2% for the systematic error, which is about the same size as the uncertainty of the *WMAP* results at their Q-band (2.8%)<sup>c</sup>.

#### 4.2.1.3 Jansky-to-Kelvin conversion

Tau A is small enough to be treated as a point source for our beam size. The antenna temperature of the Tau A polarization  $T_{\text{TauA}}^{\text{pol}}$  (Kelvin) is obtained from the polarized intensity  $P$  (Jansky) as follows:

$$T_{\text{TauA}}^{\text{pol}} [\text{mK}] = \Gamma [\text{mK/Jy}] \times P [\text{Jy}]. \quad (4.1)$$

Here  $\Gamma$  is the Jansky-to-Kelvin conversion factor defined as

$$\Gamma [\text{mK/Jy}] = \frac{A_e}{2k} = \frac{\lambda^2/\Omega}{2k} = \frac{c^2}{2k\nu^2\Omega} = 0.231 \times \left( \frac{\nu}{43.1 [\text{GHz}]} \right)^{-2} \left( \frac{\Omega}{76.0 [\mu\text{sr}]} \right)^{-1}, \quad (4.2)$$

where  $k$  is the Boltzmann constant,  $c$  is the speed of light,  $A_e = \lambda^2/\Omega$  is the effective area of the telescope, and  $\Omega = 76.0 \mu\text{sr}$  is the solid angle of the telescope, which was

<sup>c</sup>The difference between the *WMAP* three-year and seven-year is 6% at 43.1 GHz, which is consistent within their statistical uncertainties.

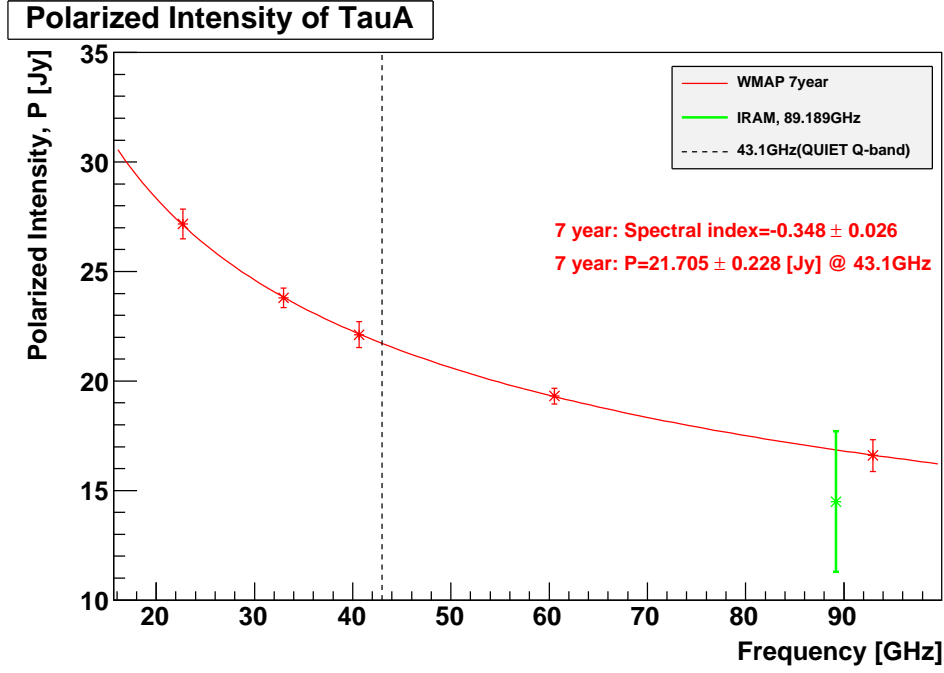


**Figure 4.1:** Variations of the polarized intensity of Tau A as a function of frequency from the *WMAP* and IRAM measurements. The red points show the data from the *WMAP* seven-year release, the red solid line corresponds to the result of a power-law fit. The green point corresponds to the IRAM measurement.

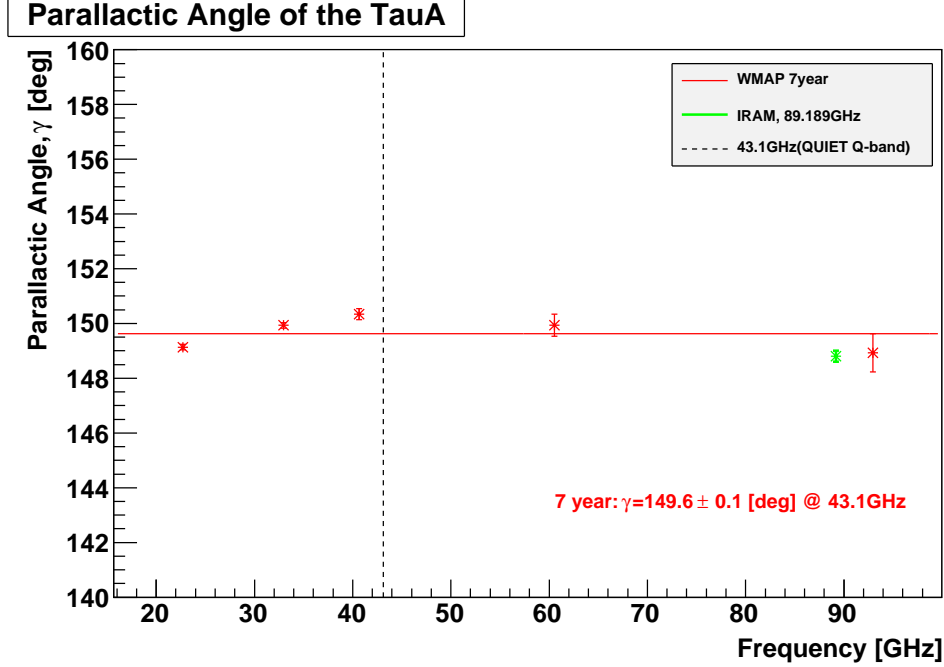


**Figure 4.2:** Variation of the parallaxic angle of Tau A as a function of frequency from the *WMAP* and IRAM measurements. Colors are used in the same way as in Figure 4.1. The red solid line corresponds to the result of a zero-polynomial fit for the *WMAP* data.

determined by Tau A and Jupiter measurements (§ 4.7) with a systematic error of 3.8%.

Hence we obtained  $T_{\text{TauA}}^{\text{pol}} = 5.02 \pm 0.25 \text{ mK}$ . The antenna-to-thermodynamic conversion is applied in the time-ordered data processing as described in Chapter 5.1.1.4.

#### 4.2.1.4 Parallactic Angle of Tau A for the QUIET Q-band

Assuming that the parallactic angle of Tau A is constant, we obtain  $\gamma_{\text{TauA}}^{\text{ref}} = 149.6^\circ \pm 0.1^\circ$  from the *WMAP* seven-year data. A linear fit to the *WMAP* data yields  $\gamma_{\text{TauA}} = 150.0^\circ \pm 0.3^\circ$ , which agrees with the linear fit within the *WMAP* systematic error of  $1.5^\circ$ <sup>d</sup>. No clear evidence for a frequency dependence between 10 to 100 GHz is found (Figure 4.2); therefore, we conclude  $\gamma_{\text{TauA}}^{\text{ref}} = 149.6^\circ \pm 1.5^\circ$  for our calibration.

#### 4.2.1.5 Polarization Fraction of Tau A for the QUIET Q-band

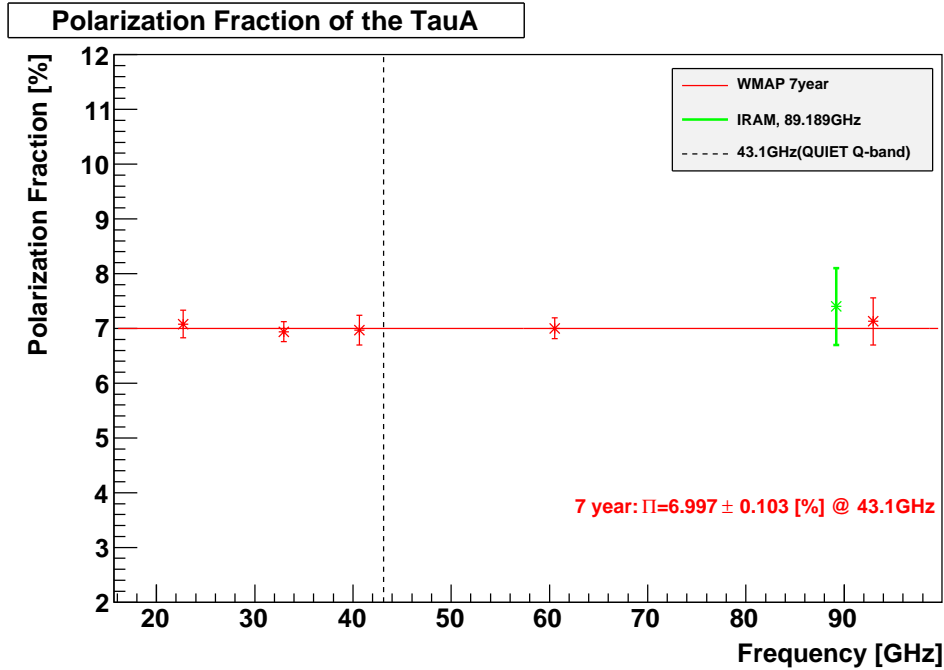


**Figure 4.3:** Variation of the polarization fraction of Tau A as a function of frequency from the *WMAP* and IRAM measurements. Colors are used in the same way as in Figure 4.1. The red solid line corresponds to the result of a zero-polynomial fit for the *WMAP* data.

We need the polarization fraction of Tau A ( $P/I \equiv \Pi_{\text{TauA}}$ ) to obtain the  $I \rightarrow Q/U$

<sup>d</sup> *WMAP* reports a  $1.5^\circ$  systematic error in the cosmological interpretation paper [30]. In the calibration sources paper [76]; however, only statistic errors shown in Table 4.3 are given.

leakage. Assuming the constant polarization fraction, we obtain  $\Pi_{\text{TauA}} = 7.00 \pm 0.10\%$  from the *WMAP* seven-year data. A linear fit yields  $\Pi_{\text{TauA}} = 7.00 \pm 0.24\%$ , which agrees with the constant case<sup>e</sup>. Since there is no evidence that the fraction depends on the frequency between 10 and 100 GHz (Figure 4.3), we adopt  $\Pi_{\text{TauA}} = 7.00 \pm 0.24\%$  for our calibration.

#### 4.2.1.6 Summary

Table 4.4 shows the summary of the calibration parameters obtained from Tau A measurements, which are to be used for the calibration analysis.

Polarization temperature	$P_{\text{TauA}}^{\text{pol}}$	5.02	$\pm$	0.25	[mK]
Parallactic angle	$\gamma_{\text{TauA}}^{\text{ref}}$	149.6°	$\pm$	1.5°	
Polarization fraction	$\Pi_{\text{TauA}}$	7.00	$\pm$	0.24	[%]

**Table 4.4:** Summary of the Tau A quantities and accuracies.

## 4.2.2 Observation Strategy

We observed Tau A from October 2008 to May 2009 with the Q-band receiver. The center module observation was taken every few days, which allows us to track time-dependent changes of the absolute detector responsivity during 8 months of our observation. We also had a few observations for each off-center module. Those measurements can allow us to check the relation among the modules. The reason why the observations of the off-center modules were not as frequent as those of the center module is that Tau A is only visible for a couple of hours per day because of the low elevation limit of our telescope ( $\sim 43^\circ$ ).

Tau A was measured in about 20 minutes almost everyday. In the measurement, we performed a series of raster scans as shown in Figure 4.4. The measurement was taken at one module for four deck angles. The reason why we could observe at only one module per day is also the elevation limit.

The height of the Tau A polarization signal varies when we change the deck angle because the deck angle rotation varies the parallactic angle compared with the Tau A

<sup>e</sup>The difference between the *WMAP* three-year and seven-year data is also negligibly small (0.05%).

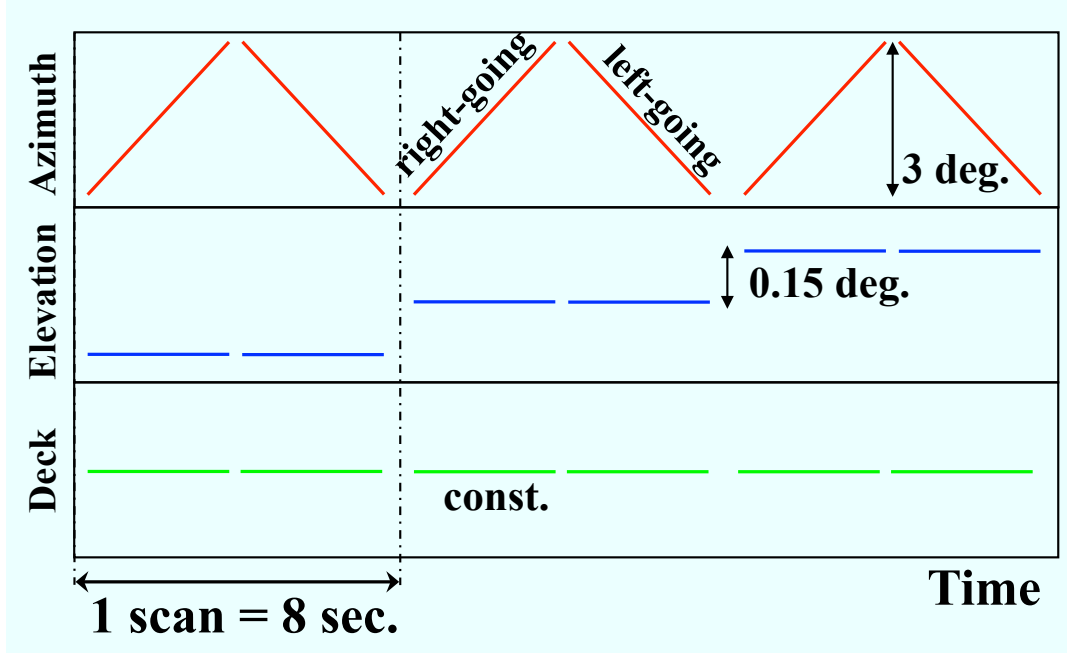


**Figure 4.4:** A part of the raster (azimuth) scans for the Tau A observation. Azimuth amplitude of the raster scan is about  $3^\circ$  and the mean scan speed is  $0.75^\circ$  per second. A half of the raster scan (right-going or left-going) takes about 8 seconds. During a pair of the raster scans, the elevation does not change. After the scans, the elevation moves about  $0.15^\circ$  upward, which is a little bit smaller than the beamwidth. A pair of the raster scans is repeated about 16 times; therefore, we can cover an area of  $2^\circ \times 2^\circ$  around Tau A. The deck angle is fixed during the raster scans. After the raster scans, the deck angle is changed by  $45^\circ$ , then we restart the measurement. A  $45^\circ$  deck angle rotation takes almost the same time as the raster scans; therefore, the Tau A measurement per one deck angle takes about 5 minutes. We usually take the data for four deck angles for 20 minutes per day.



polarization direction. Hence we can measure both the absolute polarized intensity and parallactic angle from multi-deck-angle measurements. Additionally, we can also obtain the  $I \rightarrow Q/U$  leakage from the offset level of the polarization response as a function of the parallactic angle.

### 4.2.3 Analysis

#### 4.2.3.1 Data Set

The Tau A data set we use for the calibration was taken from November 11, 2008 to May 15, 2009. After removing data with poor quality<sup>f</sup>, we have 49 observations for the center module, and 25 observations for the off-center modules in total. Table 4.5 shows the summary of the number of observations for each module.

Module	Num.	Module	Num.	Module	Num.
<i>RQ00</i>	1	<i>RQ06</i>	1	<i>RQ12</i>	2
<i>RQ01</i>	2	<i>RQ07</i>	3	<i>RQ13</i>	3
<i>RQ02</i>	1	<i>RQ08</i>	1 <sup>†</sup>	<i>RQ14</i>	2
<i>RQ03</i>	1	<i>RQ09</i>	<b>49</b>	<i>RQ15</i>	2
<i>RQ04</i>	1 <sup>†</sup>	<i>RQ10</i>	3	<i>RQ16</i>	0 <sup>†</sup>
<i>RQ05</i>	1	<i>RQ11</i>	1	<b>Total</b>	<b>74</b>

**Table 4.5:** The number of the Tau A observations for each module. The module name such as *RQXX* represents location of the module in the array. *RQ09* is the center module. Note (†): All the diodes on *RQ16*, the *Q1* diode on *RQ04*, and the *U2* diode on *RQ08* did not work in our whole observation season. We do not use these module-diodes in the CMB analysis as mentioned in Chapter 5.

---

<sup>f</sup>We do not use the data during the following periods: on December 9, 2008 because the door of the ground screen was opened during the observation; from June 12 to 14, 2009 because we observed with the old floppy AIB cables; on June 29, 2009 because the humidity was too high.

#### 4.2.3.2 TOD Fit to Extract the Polarization Response for Each Deck Angle

The common pre-processing that will be described in Chapter 5 (the Type-B correction, time-offset correction and double-demodulation) is performed at first. No pointing model is used in the pre-processing because the pointing correction does not affect the Tau A analysis.

The polarization response is extracted by fitting the TOD. The procedure is the followings. The beam profile for the Tau A signal is modeled with the two-dimensional Gaussian function. The baseline drifts induced by the atmospheric fluctuation and the  $1/f$  noise due to the HEMT amplifiers, detector diode, and electronics are modeled with a first-order polynomial for each right- or left-going raster scan. All the first-order polynomials are independent of each other, whereas the two-dimensional Gaussian function is common among all the raster scans. The duration of each raster scan ( $\sim 4$  sec.) is shorter than that of the  $1/f$  noise, whose knee frequency is about 5.5 mHz. Therefore our method is more robust against the baseline drifts than the usual subtraction in a map space after the accumulation of all the raster scans. The only disadvantage of our method is high computational cost, which is, however, acceptable in our case.

**Definition of Likelihood Function** A four-dimensional (time:  $t$ , azimuth:  $az$ , elevation:  $el$ , deck angle:  $dk$ ) maximum likelihood fit is performed. There are eight floating parameters for the Tau A signal; amplitude for each diode ( $A^i$ ), Tau A position ( $X_0, Y_0$ ), and beamwidth ( $\sigma_X, \sigma_Y$ ), where the subscript  $i$  corresponds to the index of diodes and  $X$  ( $Y$ ) corresponds to the azimuth (elevation) axis.

The amplitude of the raster scan is about  $3^\circ$ . It is small enough to use the flat cartesian coordinates system. We have two parameters for the baselines ( $a_{jk}^i$ ) and time-drifts ( $b_{jk}^i$ ) for each right-going and left-going raster scan for each diode as discussed in the previous section, where the subscript  $j$  is the index of the raster scan (a pair of the right- and left-going scans), and the subscript  $k$  is the index of the right- or left-going scan in the  $j$ th raster scan. Since the raster scan is usually repeated about 16 times for each single deck angle (the subscript  $j$  runs from 1 to 16), we usually have 264 parameters<sup>g</sup>.

---

<sup>g</sup> $4^{X_0, Y_0, \sigma_X, \sigma_Y} + 4^{\text{diodes}} \times \left( 1^{A_i} + 2^{a_{jk}^i, b_{jk}^i} \times 2^{\text{left- and right-}} \times 16^{\text{raster scans}} \right).$

The likelihood function is defined as

$$\mathcal{L} = \prod_i \prod_{jkl} f_{jkl}^i(v_{jkl}^i, t_{jkl}, az_{jkl}, el_{jkl}, dk_{jkl}, \alpha_0, \delta_0; A^i, X_0, Y_0, \sigma_X, \sigma_Y, a_{jk}^i, b_{jk}^i), \quad (4.3)$$

where  $f_{jkl}^i$  is its Probability Density Function (PDF) is given by

$$f_{jkl}^i = \exp \left[ -\frac{\{v_{jkl}^i - V_{jkl}^i(t_{jkl}, az_{jkl}, el_{jkl}, dk_{jkl}, \alpha_0, \delta_0; A^i, X_0, Y_0, \sigma_X, \sigma_Y, a_{jk}^i, b_{jk}^i)\}^2}{2\sigma_{jk}^{i\ 2}} \right], \quad (4.4)$$

where the subscript  $l$  is the index of the 50 Hz double-demodulated TOD samples, which runs from 1 to  $\sim 200$  in each right- or left-going scan in the  $j$ th raster scan,  $v_{jkl}^i$  is the diode signal, and  $\sigma_{jk}^i$  is the white noise value given by

$$\sigma_{jk}^{i\ 2} = \frac{1}{N_{jk} - 1} \sum_l (v_{jkl}^i - \bar{v}_{jk}^i)^2, \quad \text{where } \bar{v}_{jk}^i = \frac{1}{N_{jk}} \sum_l v_{jkl}^i, \quad (4.5)$$

where  $N_{jk}$  is the number of the samples. Here  $V_{jkl}^i$  consists of the Tau A signal ( $g_{jkl}^i$ ) and the baseline-drift term ( $h_{jkl}^i$ ),

$$V_{jkl}^i = g_{jkl}^i(t_{jkl}, az_{jkl}, el_{jkl}, dk_{jkl}, \alpha_0, \delta_0; A^i, X_0, Y_0, \sigma_X, \sigma_Y) + h_{jkl}^i(t_{jkl}; a_{jk}^i, b_{jk}^i), \quad (4.6)$$

where  $g_{jkl}^i$  is the two-dimensional Gaussian function as follows:

$$g_{jkl}^i = A^i \exp \left[ -\frac{\{x(t_{jkl}, az_{jkl}, el_{jkl}, dk_{jkl}) - X(t_{jkl}, \alpha_0, \delta_0) - X_0\}^2}{2\sigma_X^2} - \frac{\{y(t_{jkl}, az_{jkl}, el_{jkl}, dk_{jkl}) - Y(t_{jkl}, \alpha_0, \delta_0) - Y_0\}^2}{2\sigma_Y^2} \right]. \quad (4.7)$$

Here  $x$  ( $y$ ) is the boresight of the module in the flat coordinates system in the azimuth (elevation) direction,  $X$  ( $Y$ ) is the location of Tau A, and  $\alpha_0$  ( $\delta_0$ ) is right ascension (declination) of Tau A. The baseline-drift term ( $h_{jkl}^i$ ) is given by

$$h_{jkl}^i = a_{jk}^i + b_{jk}^i(t_{jkl} - t_{jk1}). \quad (4.8)$$

**Optimization of Likelihood Function** Best-fit parameters are found by maximizing the PDF by MINUIT function optimization library [80]. In the maximization, we should carefully choose the initial values of the parameters because we need to optimize lots of parameters. The initial values of the Tau A positions were evaluated by the moment

of a map, which is created by a simple accumulation. We also found the amplitude of Tau A from these initial positions. The offsets were calculated by an average of each right- or left-going scan, and the slopes of the baseline drift were also obtained by inclinations between the beginning and the ending of each scan. Additionally, we need to consider the procedure of the maximization of each set of the parameters. At first, the maximization on the offsets and the time-drifts was performed with the other parameters being fixed. Next, the maximization on the Tau A positions was performed. After that, the maximization on the beamwidth was done. The maximization on all the parameters were processed at the end. The whole optimization was successfully converged all the time using the above procedures. Figure 4.5 shows a typical TOD for a pair of raster scans with the results of the optimization. Figure 4.6 and 4.7 show resulting Tau A maps for each diode after the optimization.

#### 4.2.3.3 Estimating Detector Responsivity, Detector Angle, and $I \rightarrow Q/U$ Leakage from the Tau A Measurement

The series of the signal heights from four different deck angles are plotted as a function of the parallactic angle in Figure 4.8, where the parallactic angle ( $\gamma$ ) is calculated from the deck angle and boresight pointing of the module. We obtained clear sinusoidal response for each diode, which provides us three important calibration quantities: the absolute detector response, detector angle, and  $I \rightarrow Q/U$  leakage. The sinusoidal response curve for each diode is described with the following formula,

$$A^i(\gamma) = c_0^i \cos [2 (\gamma - c_1^i)] + c_2^i, \quad (4.9)$$

where  $A^i(\gamma)$  is the polarization signal height for each diode;  $c_0^i$ ,  $c_1^i$  and  $c_2^i$  are fitting parameters of the amplitude, angle, and offset, respectively, for each diode. These three parameters provide the detector responsivity ( $g_{\text{TauA}}^i$ ), detector angle ( $\gamma_{\text{TauA}}^i$ ), and  $I \rightarrow Q/U$  leakage ( $l_{\text{TauA}}^i$ ) as follows:

$$g_{\text{TauA}}^i [\text{mV/K}] = \frac{c_0^i [\text{mV}]}{T_{\text{TauA}}^{\text{pol}} [\text{mK}]} \times 10^3, \quad (4.10)$$

$$\gamma_{\text{TauA}}^i [\text{deg.}] = \gamma_{\text{TauA}}^{\text{ref}} - c_1^i, \quad (4.11)$$

$$l_{\text{TauA}}^i [\%] = \frac{c_2^i}{g_{\text{TauA}}^i T_{\text{TauA}}^{\text{unpol}}} = \frac{c_2^i}{g_{\text{TauA}}^i T_{\text{TauA}}^{\text{pol}} / \Pi_{\text{TauA}}} = \frac{c_2^i}{c_0^i} \Pi_{\text{TauA}}, \quad (4.12)$$

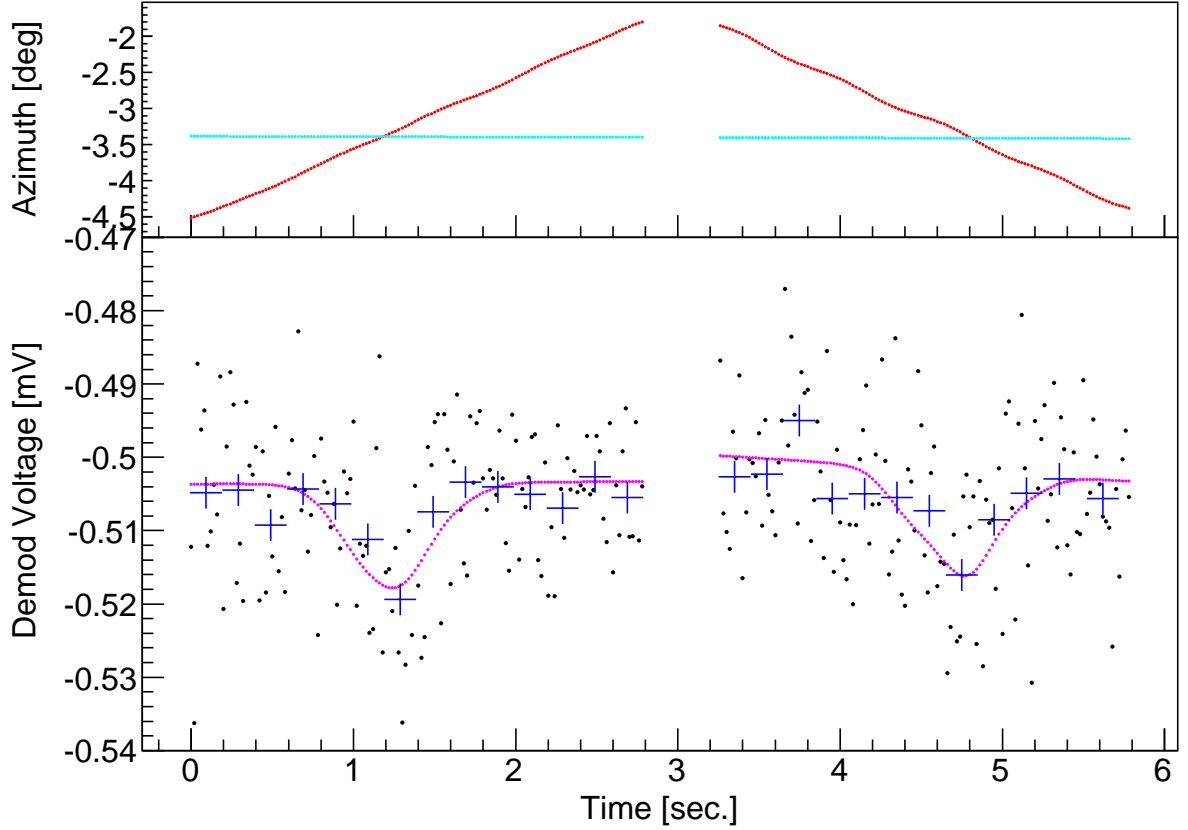


**Figure 4.5:** TOD of the telescope pointing and the diode output in a pair of raster scans. In the top figure, the azimuth angle (red lines) corresponds to  $X - X_0$  in Equation (4.7). The Tau A position in the azimuth coordinates system is shown as the cyan lines. During the scan, the elevation is constant and the difference between the telescope and Tau A, which corresponds to  $y - Y - Y_0$  in Equation (4.7), is less than  $0.1'$ . The deck angle fluctuation is also less than  $0.1'$ . The bottom figure shows time trend of the demodulated voltage of the  $Q1$  diode on the center module (black dots) and the fitted results (magenta lines), which correspond to  $v_{jkl}^{Q1}$  and  $V_{jkl}^{Q1}$  in Equation (4.6), respectively. The average of every 10 demodulated voltage samples (blue crosses) are also shown, which demonstrate that the fitting worked well. Significant Tau A signals are found when the telescope was crossing the Tau A ( $t \sim 1.2$  and  $\sim 4.8$  sec.). The RMS of the demodulated voltage is about 0.01 mV and the Tau A amplitude is about 0.013 mV. The pair scan is usually repeated 16 times with changing the elevation. Note that **the optimization is not performed for each pair of the raster scans individually but for all the raster scans at a time.**

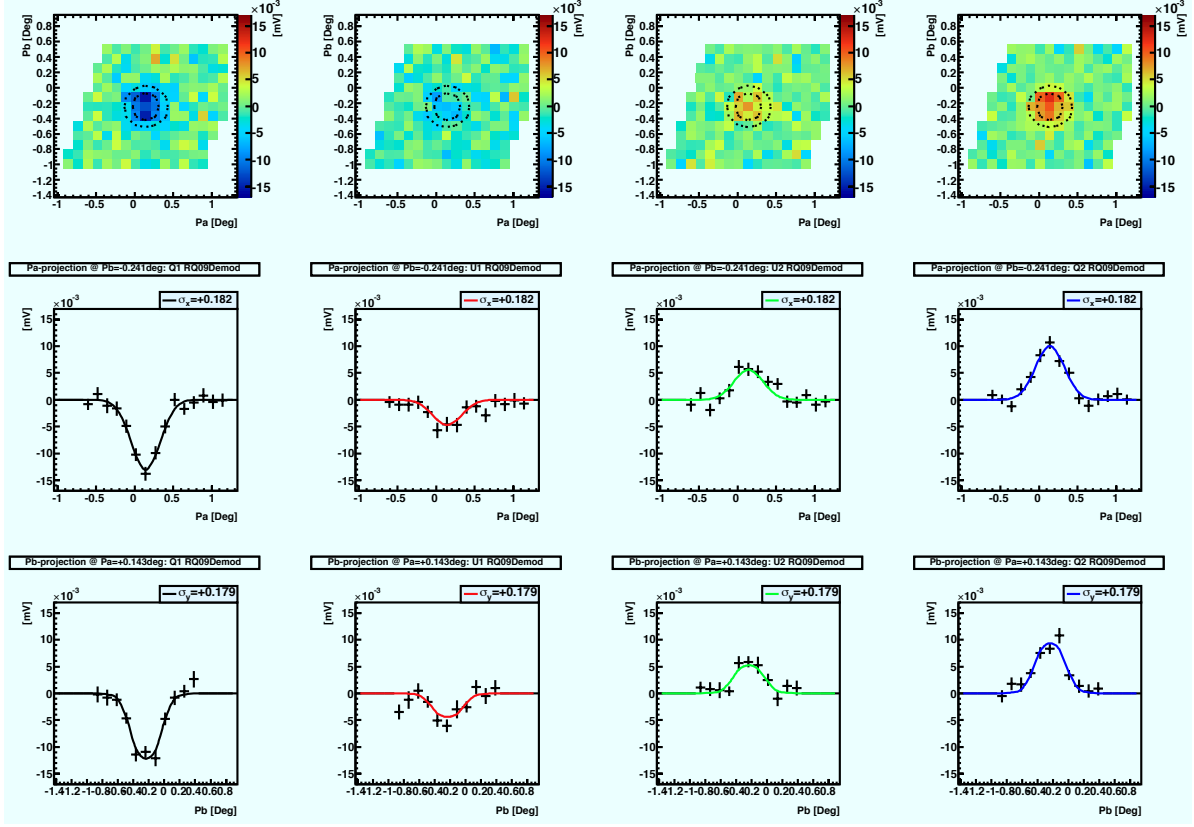


**Figure 4.6:** Tau A maps on the center module for each diode at a parallactic angle of  $3^\circ$  after the optimization. The column from the left to right corresponds to  $Q1$ ,  $U1$ ,  $U2$  and  $Q2$  diode, respectively. The first row shows the Tau A maps, in which the offsets and time-drifts are subtracted by the optimization. The contour of the first (second) dotted line from the center corresponds to  $1\text{-}\sigma$  ( $2\text{-}\sigma$ ) of the beamwidth. The second (third) row shows the projection of the Tau A maps into the azimuth (elevation) direction. The solid line and marker correspond to the fitted result and the data, respectively.

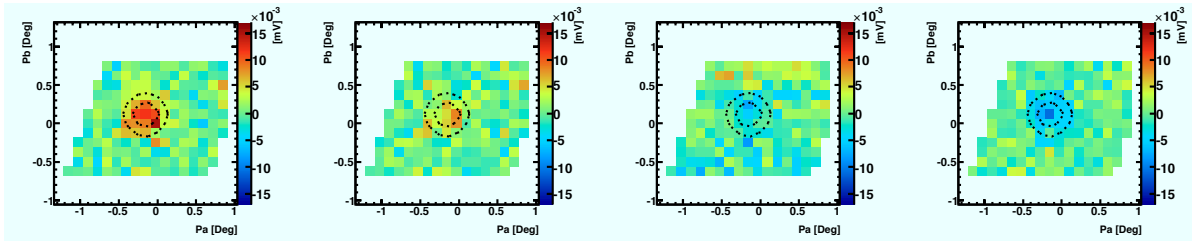


**Figure 4.7:** Tau A maps with a parallactic angle of  $97^\circ$ . The angle is shifted by about  $90^\circ$  from Figure 4.6. Amplitudes of Tau A for each diode are flipped because the polarization phases are changed by about  $180^\circ$ .

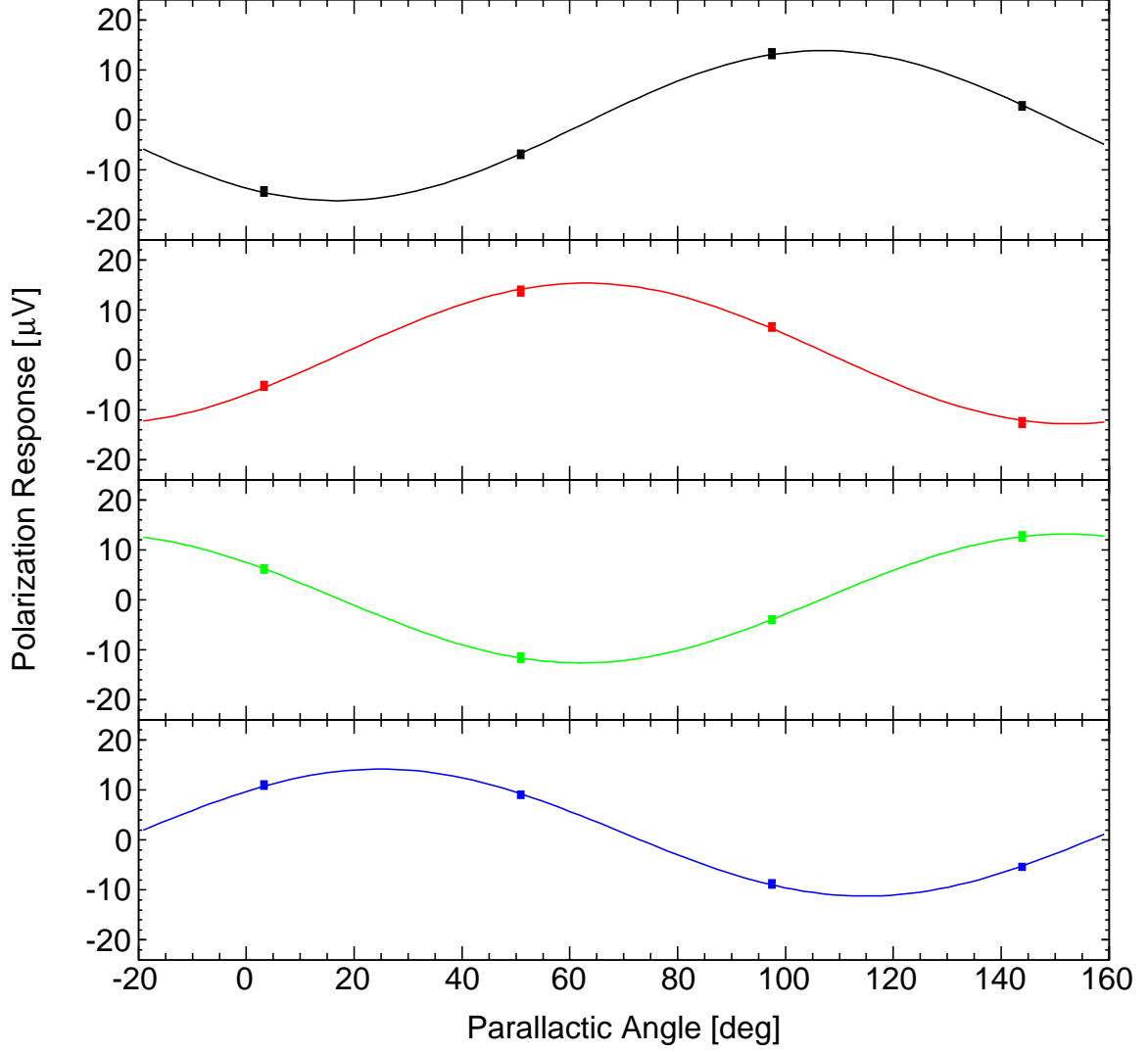


**Figure 4.8:** Detector responses from the center module to the polarization of Tau A from the observations on four parallax angles. Each measurement takes 20 minutes. The errors are as small as the points (6% of the amplitude). From top to bottom, each figure corresponds to the response of the  $Q1$ ,  $U1$ ,  $U2$  and  $Q2$  diode, which measures the Stokes  $Q$ ,  $-U$ ,  $U$  and  $-Q$  parameter. The sinusoidal curve in each figure is a fit to data.

where  $T_{\text{TauA}}^{\text{pol}}$ ,  $\gamma_{\text{TauA}}^{\text{ref}}$  and  $\Pi_{\text{TauA}}$  are defined in the previous section (Table 4.4).

## 4.2.4 Results on the Center Module

We confirmed the absolute detector responsivity, detector angle, and  $I \rightarrow Q/U$  leakage were stable and almost time-independent during our Q-band observation on the center module. Figures 4.9, 4.10 and 4.11 show these time trend and histograms, respectively. Note that the variance of the absolute detector responsivity (6%) satisfies the requirement described in Appendix C. We will discuss how the absolute responsivity is affected by the variation of PWV and elevation in § 4.3.

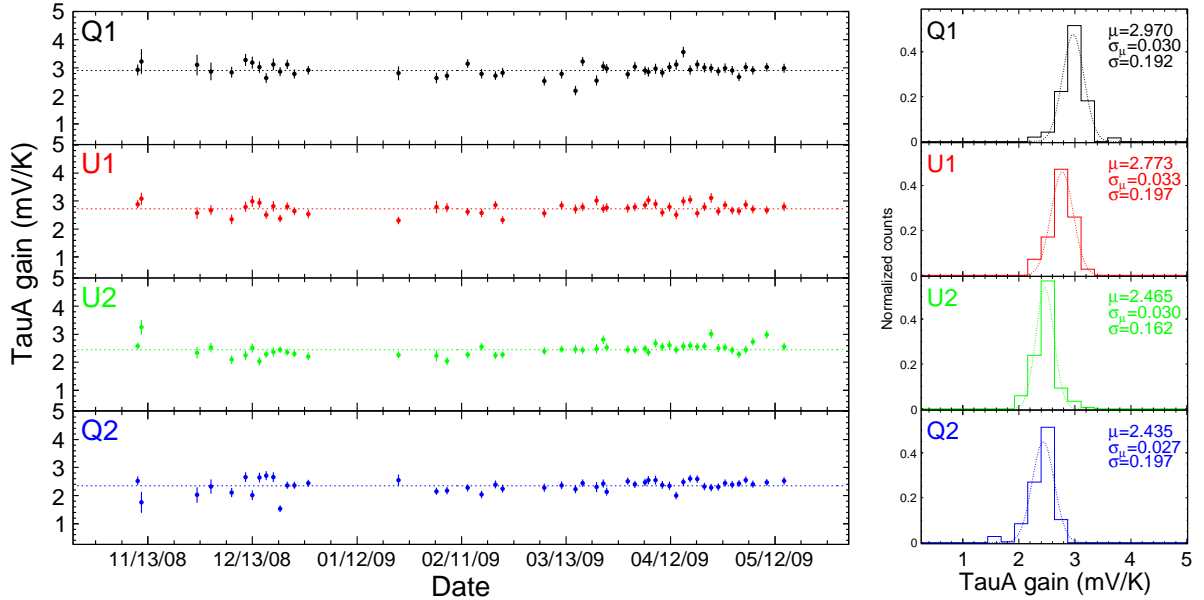


**Figure 4.9:** Left: Time trend of the detector responsivities on the center module. Right: Histograms of the left plots.

## 4.2.5 Results on the Off-center Modules

### 4.2.5.1 Absolute Detector Responsivity

We successfully obtained the responsivities on all the off-center modules. Figure 4.12 shows the variation of the absolute detector responsivities among the module-diodes. We found that a typical responsivity is 2.3 mV/K with 6% uncertainty from a single set of



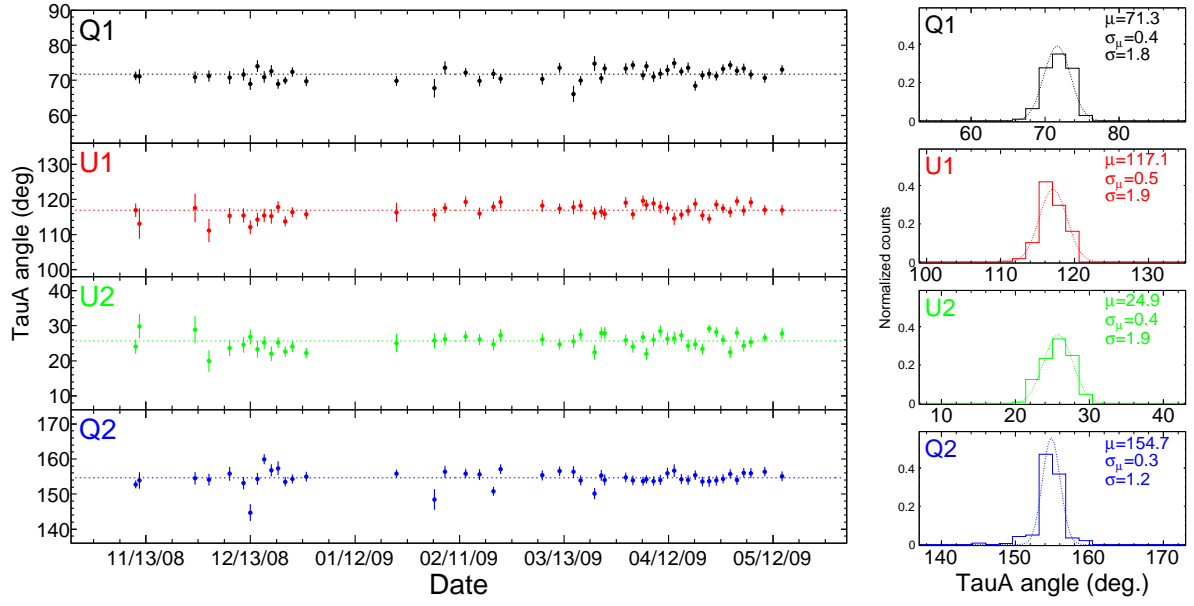


**Figure 4.10:** Left: Time trend of the detector angles on the center module. Right: Histograms of the left plots.

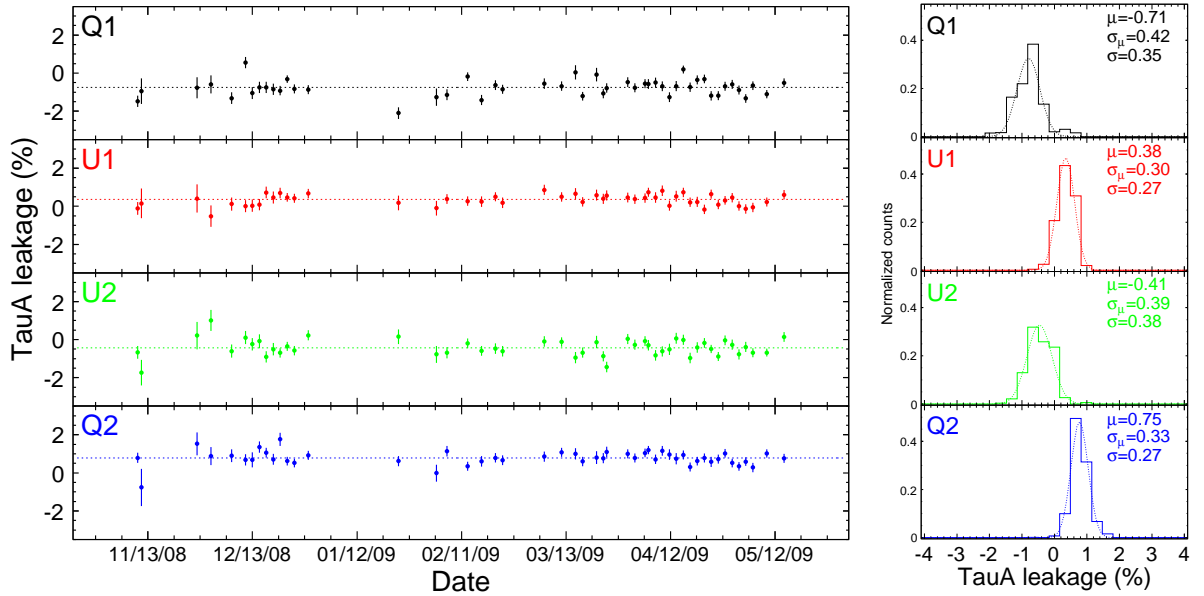


**Figure 4.11:** Left: Time trend of the  $I \rightarrow Q/U$  leakages on the center module. Right: Histograms of the left plots.

the observations, which is dominated by the statistical error. The comparison with the absolute and total power responsivity from the sky dip measurement is given in § 4.3.

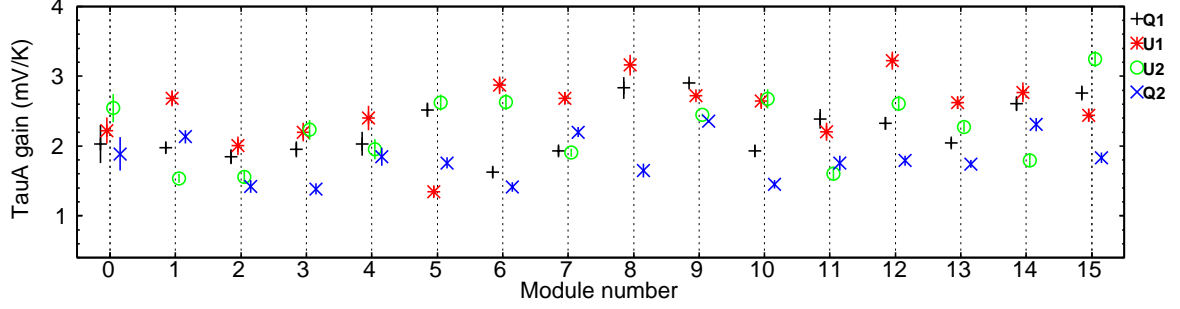


**Figure 4.12:** The detector responsivities for each module and each diode. The horizontal axis corresponds to the module number ( $RQXX$ ), and the vertical axis corresponds to the detector responsivities.

#### 4.2.5.2 Detector Angle

Figure 4.13 shows the variation of the detector angles among the different module-diodes. We found a typical error of  $2^\circ$ , which is comparable to the *WMAP* seven-year systematic error. A possible absolute and relative angle difference among the module-diodes and among various calibration sources is discussed in § 4.4.

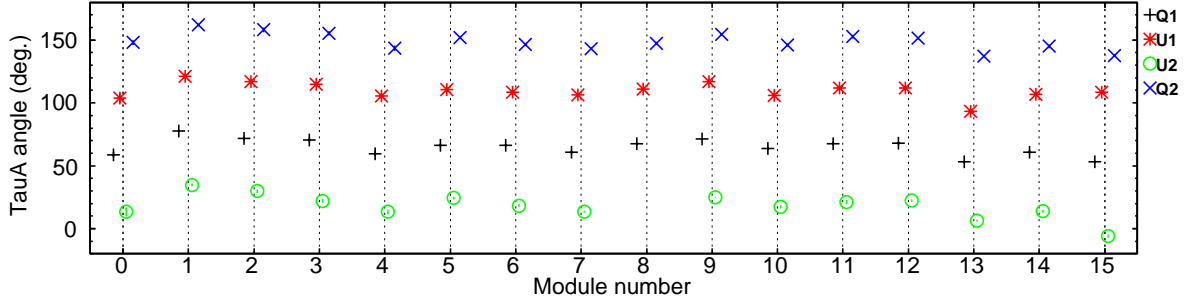


**Figure 4.13:** The detector angles for each module and each diode. The horizontal axis corresponds to the module number ( $RQXX$ ), and the vertical axis corresponds to the detector angles.

#### 4.2.5.3 $I \rightarrow Q/U$ Leakage

We obtained the leakage on all the off-center modules. Figure 4.14 shows the variation of the leakages among the module-diodes. We found a typical leakage of 0.8% (0.2%)

for  $Q$  ( $U$ ) diodes on average. A possible systematic bias among the module-diodes and calibration sources are discussed in § 4.5.

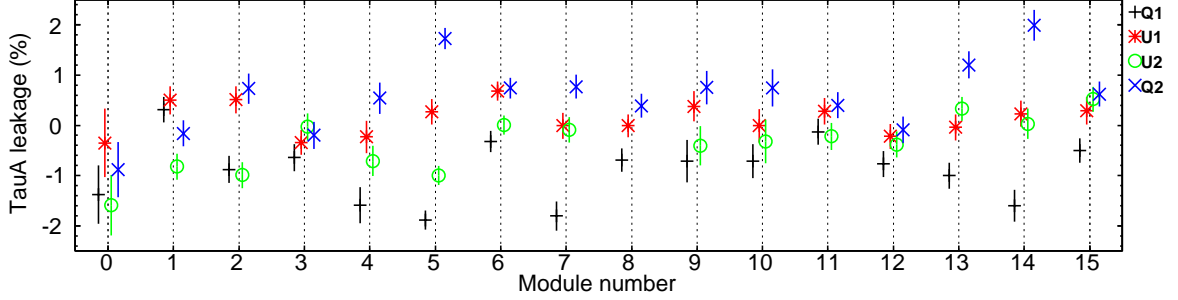


**Figure 4.14:** The  $I \rightarrow Q/U$  leakages for each module and each diode. The horizontal axis corresponds to the module number ( $RQXX$ ), and the vertical axis corresponds to the  $I \rightarrow Q/U$  leakages.

#### 4.2.6 Result of the Beamwidth

The Tau A observations also provide the beamwidth. In the analysis, we defined two-dimensional beamwidth with two independent parameters ( $\sigma_X$  and  $\sigma_Y$ ), which correspond to the azimuth direction and the elevation direction. The reason why we use two independent beamwidth is that we should check that the raster scan does not cause a significant bias on the beamwidth. The left plot in Figure 4.15 is the time trend of  $\sigma_X$  and  $\sigma_Y$  on the center module, which shows no time variations within their errors. Histograms in the right plot are projections onto their each axis of the beam. There is no systematic differences between  $\sigma_X$  and  $\sigma_Y$  within their variances. Thereby the measured beam is consistent with the circular Gaussian. The fact leads to the weighted mean of the beamwidth  $\sigma = 0.189^\circ \pm 0.001^{\text{oh}}$  (Figure 4.16). This result is consistent with the deep scan result as well as the design value within the assigned errors (§ 4.7). Assuming that the beams of the off-center modules are also the circular Gaussian, we confirmed that the off-center modules have the same beamwidth as the center module within their errors (Figure 4.17).

---

<sup>h</sup>FWHM =  $\sigma\sqrt{8\log 2} = 26.70' \pm 0.14'$ .

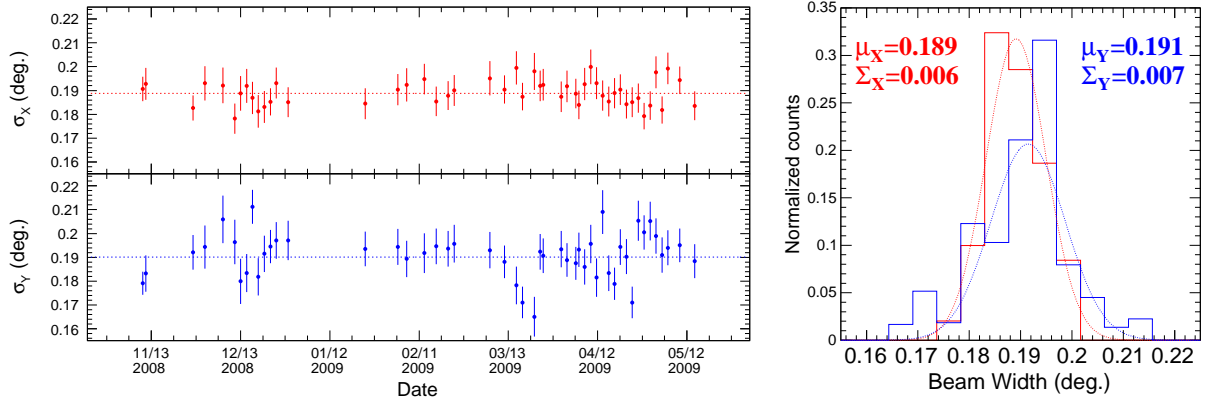


**Figure 4.15:** Left: Time trend of the beam width of the scan direction (top,  $\sigma_X$ ), and that of the elevation direction (bottom,  $\sigma_Y$ ). Right: Histograms from the left plots.

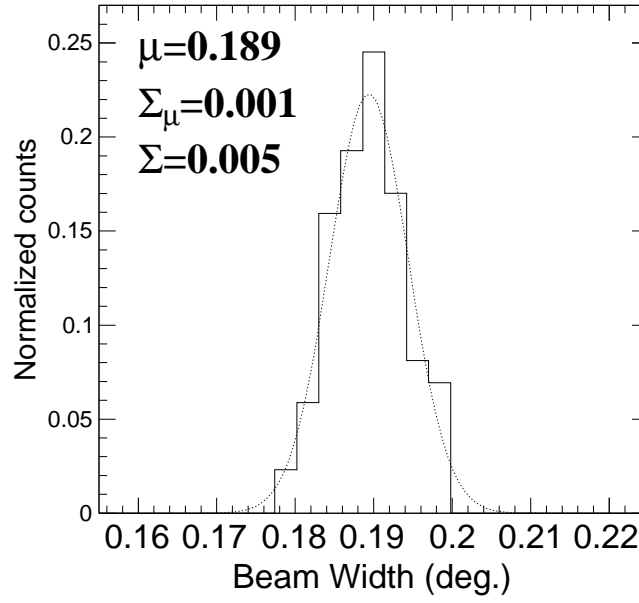


**Figure 4.16:** Histogram of the width of the circular Gaussian beam.

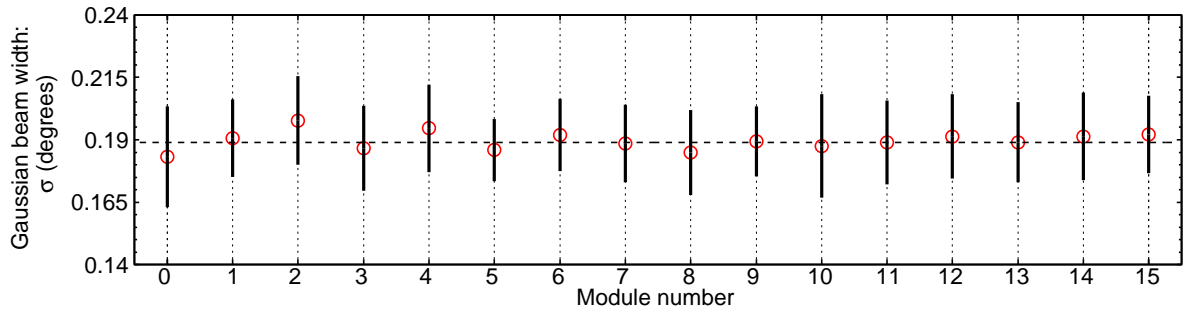


**Figure 4.17:** The circular Gaussian beamwidth for each module. The horizontal axis corresponds to the module number ( $RQXX$ ), and the vertical axis corresponds to the beamwidth.

### 4.2.7 Conclusions

The Tau A measurements provide the detector responsivity, detector angle, and  $I \rightarrow Q/U$  leakage. Since the results on the center module were very stable, we can track the time trend very well. We also have the results on the off-center modules to compare with other calibration sources. The comparison with the center and off-center modules and among the calibration sources are needed to make a calibration model. We will discuss it in the following sections.

## 4.3 Detector Responsivity

### 4.3.1 Responsivity Ratio

A detector responsivity model with the combination of the Tau A and the sky dips is used in our CMB analysis as described in Chapter 5. Whereas the Tau A is a unique calibration source to provide the polarization responsivity, it is difficult to trace the responsivities for all the module-diodes. For example, the responsivities may vary by  $\leq 10\%$  during a day due to change of thermal condition for the bias electronics. Therefore, we construct the responsivity model with the combination of the Tau A and sky dips.

The sky dips are the most frequent calibration measurements (Table 4.2), which allow us to trace time variation of the relative responsivities as described in Appendix D.1. We can also obtain the responsivity relation among the module-diodes because the sky dip is measured for the full array. The bandpass for the total power response does not match with that for the polarization response unless the transmission bandpasses for two legs on the polarimeter modules are perfectly matched<sup>i</sup>. Therefore, we need a model that determines the “absolute polarization” responsivity from the “total power” responsivity. In the actual model, we calculate a responsivity ratio between the absolute responsivities by Tau A measurements and total power responsivities by sky dips to eliminate the effect of the time variation. We determined the total power to polarization ratio,  $R_{\text{abs}}^{\text{ref}}$ , from

---

<sup>i</sup> The polarization responsivity is defined as  $2g_A(\nu)g_B(\nu)$  although the total power one is defined as  $g_A^2(\nu) + g_B^2(\nu)$  as described in Appendix B.

the center module *Q1* diode given by

$$R_{\text{abs}}^{\text{ref}} = \frac{1}{N} \sum_k^N \frac{g_{\text{TauA}}^{RQ09Q1}(t_k)}{g_{\text{skydip}}^{RQ09Q1}(t'_k)}, \quad (4.13)$$

where  $t_k$  indicates the time of each Tau A observation,  $N = 49$  is the number of the Tau A observations for the center module,  $t'_k$  is the most closest time of the sky dips measurement to the time of the Tau A measurement ( $|t_k - t'_k| < 30$  min.). We can obtain the absolute detector responsivity for each module-diode by multiplying  $R_{\text{abs}}^{\text{ref}}$  to the sky dips responsivity:

$$g^i(t) = R_{\text{abs}}^{\text{ref}} \times g_{\text{skydip}}^i(t). \quad (4.14)$$

Figure 4.18 shows the time-trend of the ratios and their histograms. Each ratio is stable and time independent. Thereby we obtained  $R_{\text{abs}}^{\text{ref}} = 0.999$  on an average. Table 4.6 shows variation of  $R_{\text{abs}}$ , if we change the reference diode(s) from the *Q1* diode on *RQ09* to the others.

$R_{\text{abs}}$ (diff. from $R_{\text{abs}}^{\text{ref}}$ )	Reference diode(s)
1.007 (0.8%)	by using an average of the four diodes at the center module.
1.004 (0.5%)	by using <i>Q2</i> as the reference.
1.006 (0.7%)	by using <i>U1</i> as the reference.
1.017 (1.8%)	by using <i>U2</i> as the reference.
0.969 (3.3%)	by using an average of the non-center modules <sup>j</sup> .

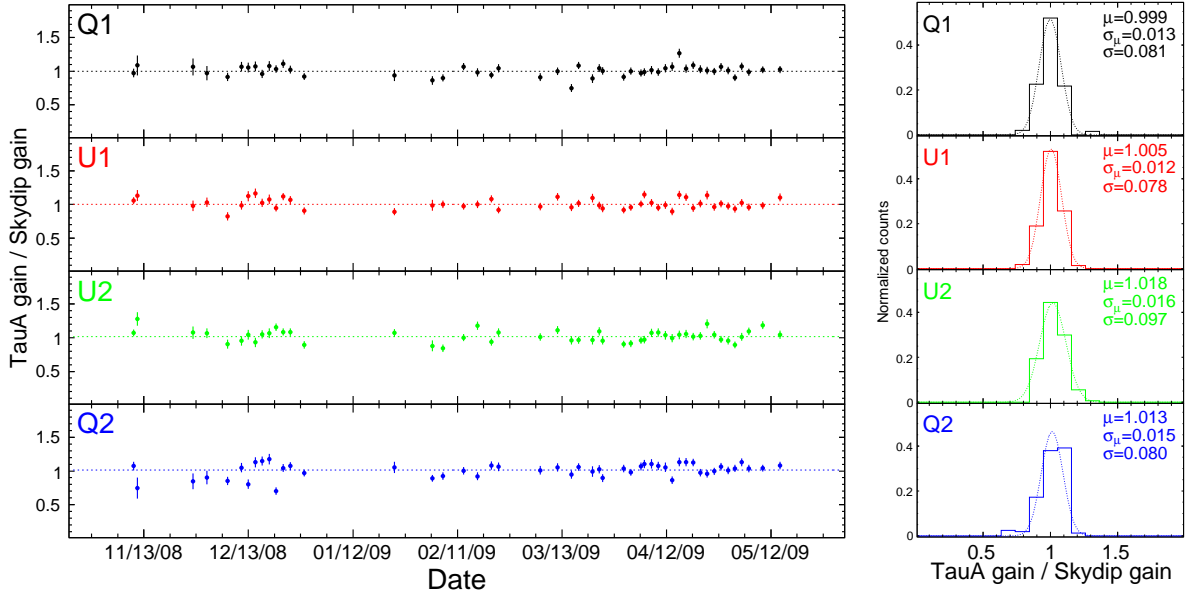
**Table 4.6:** Variation of  $R_{\text{abs}}$  if we change the reference diode(s) from the *Q1* diode on *RQ09* to the others.

We assign the biggest difference of 3.3% from #5 as a systematic error for  $R_{\text{abs}}$ . The Moon observation also provides an independent cross-check of responsivity, which is consistent with the Tau A and sky dips results within their errors.

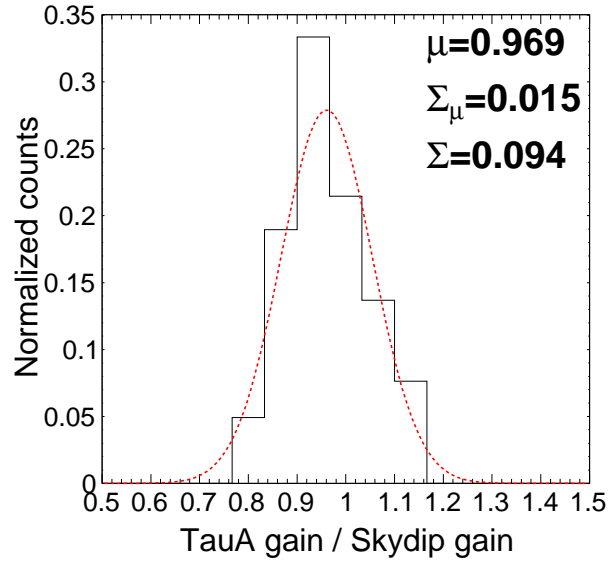
### 4.3.2 PWV and Elevation Dependence

Figure 4.21 shows the variation of Tau A responsivity as a function of the PWV. This

<sup>j</sup>Figures 4.19 and 4.20 show its ratio histogram and variation for each module and each diode.



**Figure 4.18:** Left: Time-trend of the total power to polarization ratio for the center module. Right: Histograms of the left plots.



**Figure 4.19:** Histogram of the total power to polarization ratio for the off-center modules (Figure 4.20). The mean value is shifted away from  $R_{\text{abs}} = 0.999$  by 3%.

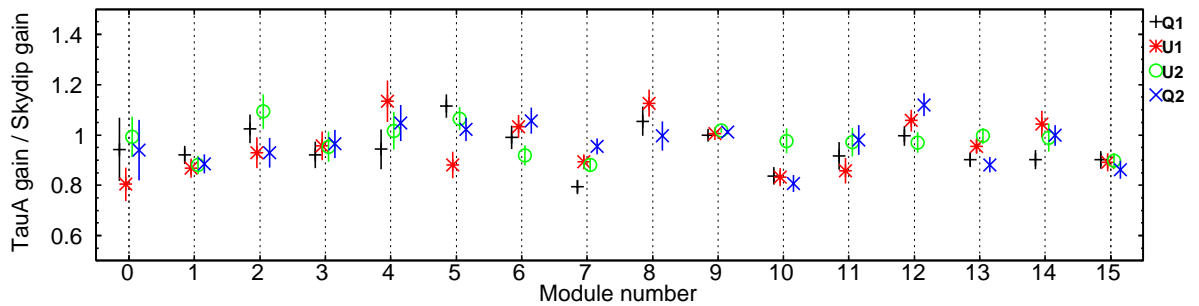


**Figure 4.20:** Variation of the total power to polarization ratio for each module and each diode. The horizontal axis corresponds to the module number ( $RQXX$ ), and the vertical axis corresponds to the ratios. These variations are dependent on the modules.

result shows that the difference in the PWV condition does not make any bias for the calibration of the absolute detector responsivity. We also confirm that the responsivity ratio is independent of the elevation as shown in Figure 4.22.

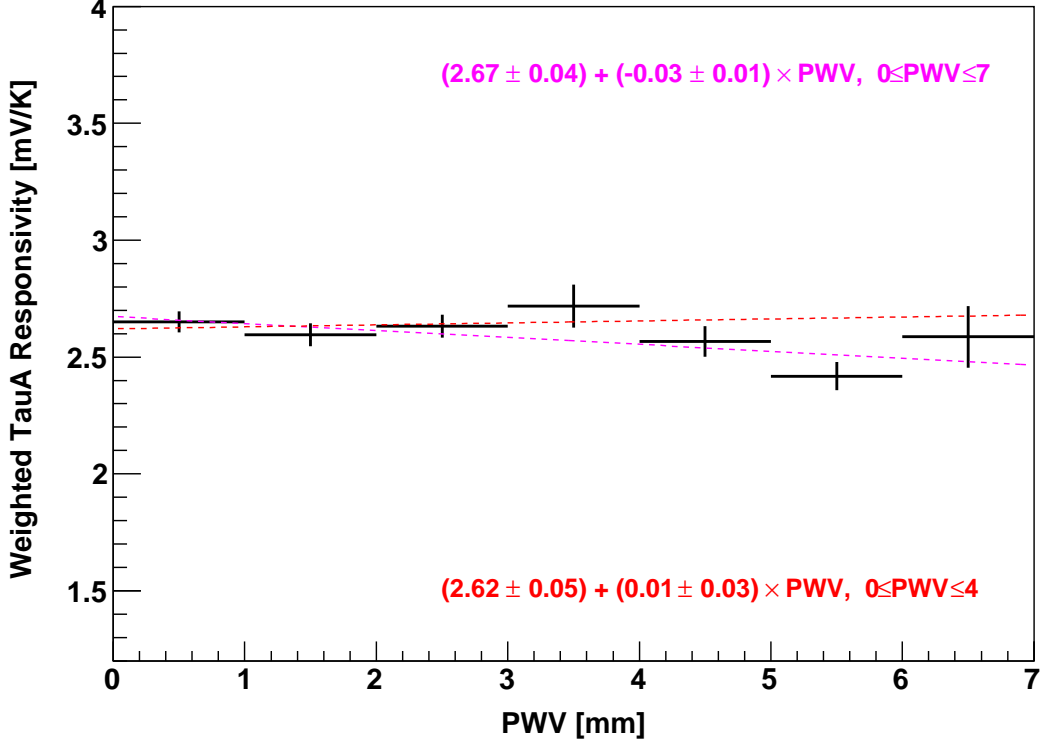


**Figure 4.21:** Variation of the detector responsivity as a function of the PWV, which was measured at the APEX site as described in Chapter 3. The vertical axis corresponds to weighted responsivity of all the diodes on the center module. Performing a first-order polynomial fit, we found that the responsivity is independent of the PWV within the statistical errors in case of the PWV less than 4 mm (red-dashed line). Note that almost all the data (about 93%) were measured at the PWV less than 4 mm. Even including the worst case of the PWV up to 7 mm (magenta line), the effect on the CMB polarization power spectrum is less than 1%. Note that the data taken with bad weather would also be rejected by the data selection as described in Chapter 6.

### 4.3.3 Time Variation

We also checked a possible time variation of the ratio. We divided data set into three time ranges; between October and December 2008; between January and March 2009;



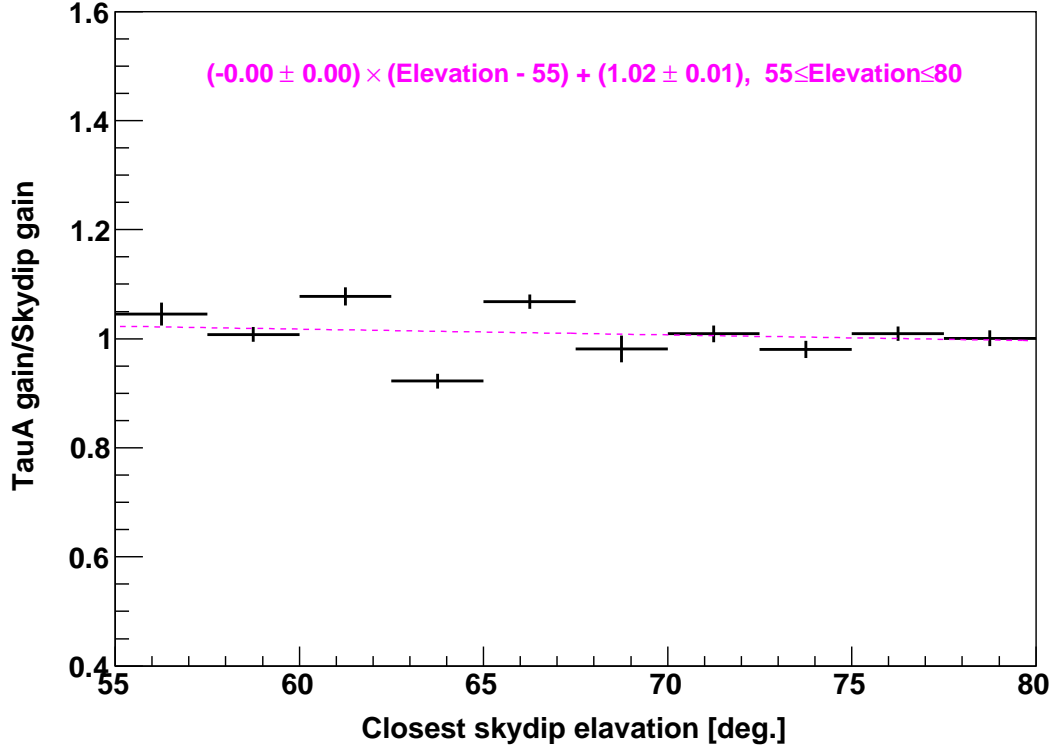


**Figure 4.22:** Variation of the total power to polarization ratio,  $R_{\text{abs}}$ , as a function of the elevation of the sky dips measurements. Performing a first-order polynomial fit, we found that the ratio is independent of the elevation within the statistical errors. The sky dip responsivity is corrected with the PWV and elevation dependence as described in Appendix D.1.

between April and June 2009. The difference among them is 1.9%. We conservatively assign it as a possible time difference of the ratio ( $R_{\text{abs}}$ ).

#### 4.3.4 Summary of Our Detector Responsivity Uncertainties

We concluded that the uncertainties of our detector responsivity are 3.2% from the uncertainty of the Tau A polarization intensity; 3.3% from the possible difference between the demod and total power responsivity; and 1.9% from the possible time-dependence of the responsivities. Furthermore, we obtain a 3.8% uncertainty from the solid angle in § 4.7. Then we determined the uncertainty is 6.3% in total. The systematic bias due to this uncertainty is evaluated in § 9.2.

### 4.4 Detector Angle

Our primary model of the detector angle comes from the observation of the radial polarization of the Moon as described in Appendix D.2. The reasons why we use the Moon results while Tau A can also provide the angle are the following:

- The Moon is bright. The angle calibration with the Moon has an advantage over Tau A for the statistical error.
- We can measure the Moon with the full array within one hour. Therefore, it allows us to obtain the detector angles of all the module-diodes simultaneously and more efficiently than Tau A.

From the Moon results, the detector angles are stable, changing less than  $0.2^\circ$  throughout the whole observation seasons, except during the period with the deck-angle-encoder problem (§ 4.6). We checked possible differences among results from Tau A, the Moon, and wire grid (Figure 4.23). Table 4.7 shows that the average differences among them.

Since it is very hard to confirm an absolute angle from the wire grid measurement, the absolute angle was defined with respect to the average Tau A angle. The large RMS differences of about  $3^\circ$  between the Moon and the others come from the Moon modeling and its error estimation. We conservatively assign the largest difference of  $1.8^\circ$  between the Moon and the wire grid as a systematic error of the angle.

Comparison	Mean (absolute)	RMS (relative)
Moon $\leftrightarrow$ TauA	1.7°	2.9°
Moon $\leftrightarrow$ Wire grid	1.8°	2.8°
TauA $\leftrightarrow$ Wire grid	(can not be defined)	1.2°

**Table 4.7:** Average angle differences among results from Tau A, the Moon, and wire grid.

There is a systematic error of 1.5° for the Tau A angle which comes from *WMAP* measurements. The mean difference between Tau A and the Moon is consistent within the systematic error plus the statistical error for both calibrations though we have not fully understood the systematic error of the Moon. These results are used to evaluate systematic effects in § 9.4.

## 4.5 $I \rightarrow Q/U$ Leakage

The  $I \rightarrow Q/U$  leakages were measured in various ways: the sky dips, variation of weather<sup>k</sup>, Tau A, and the Moon. We found inconsistency among the calibrations; the leakage from the sky dips is significantly larger than that from the others, and we also found that the Tau A result is the smallest<sup>l</sup>. Such difference can be explained by the combination of the variation of frequency dependence of each calibration source<sup>m</sup>.

The main reason of the  $I \rightarrow Q/U$  leakage is bandpass mismatch between the septum polarizer and input port of the polarimeter module. When the calibration sources have different frequency dependencies, they provide us different leakage values. Numerical simulation by using the vector noise analyzer (VNA) measurements of the septum polarizer, polarimeter bandpasses, and spectra of each source, agrees within measurement uncertainties with the tendency we found. For our CMB analysis and estimation of the systematic error induced by the CMB temperature anisotropy, the blackbody source is

<sup>k</sup>We can evaluate the leakage from data of various weather conditions because the leakage effect is highly enhanced when the weather is bad.

<sup>l</sup>The TauA provides a leakage of 0.8% (0.2%) for the  $Q$  ( $U$ ) diode respectively.

<sup>m</sup>The sky temperature and water vapor highly depend on frequency; the Moon is a blackbody, while the Tau A flux is given by a power-law with a spectral index of  $\beta = -2.35$ .

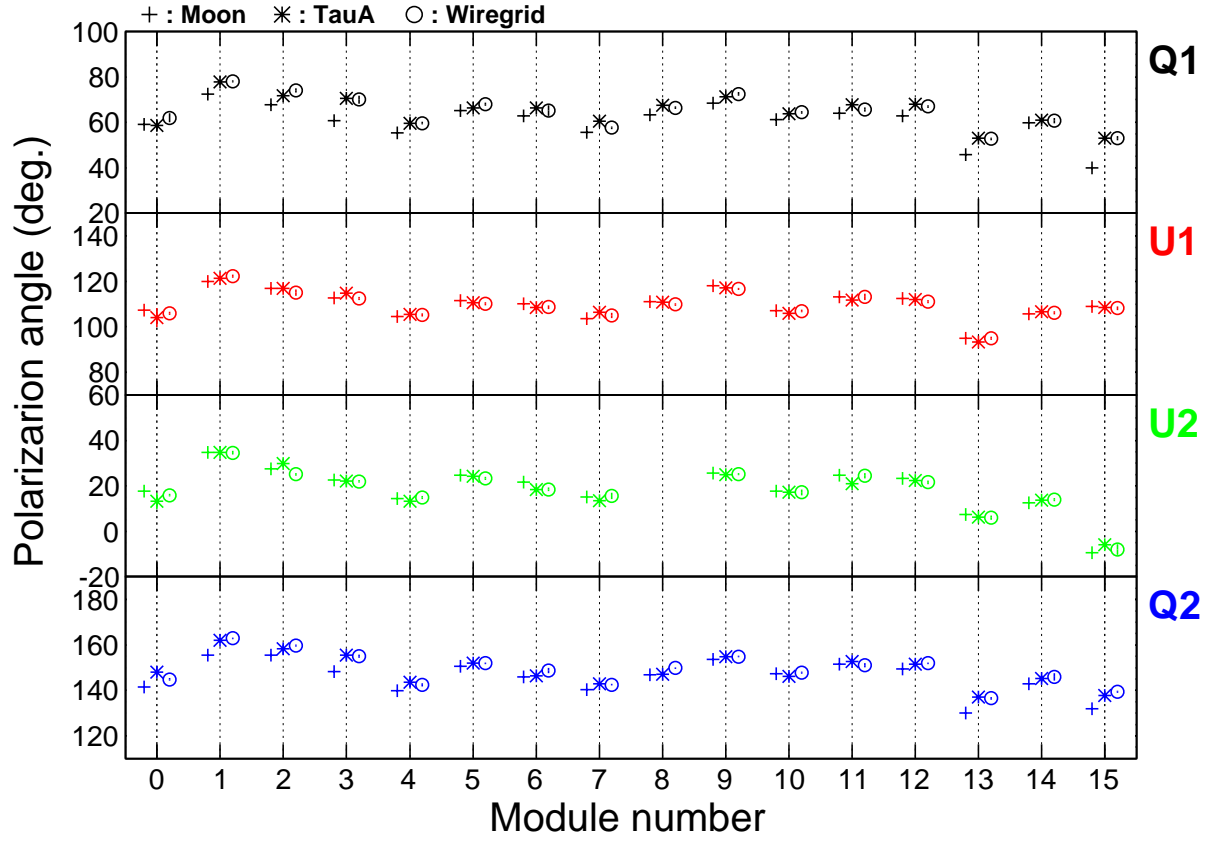


**Figure 4.23:** Comparison of the polarization angles with the measurements of the Moon(+), TauA(\*) and wire grid(o) for each module and each diode. The angles of the  $Q$  diodes from the Moon tend to be systematically different of the others. We do not fully understand the reason, although a possible systematic bias is not significant as discussed in § 9.4.

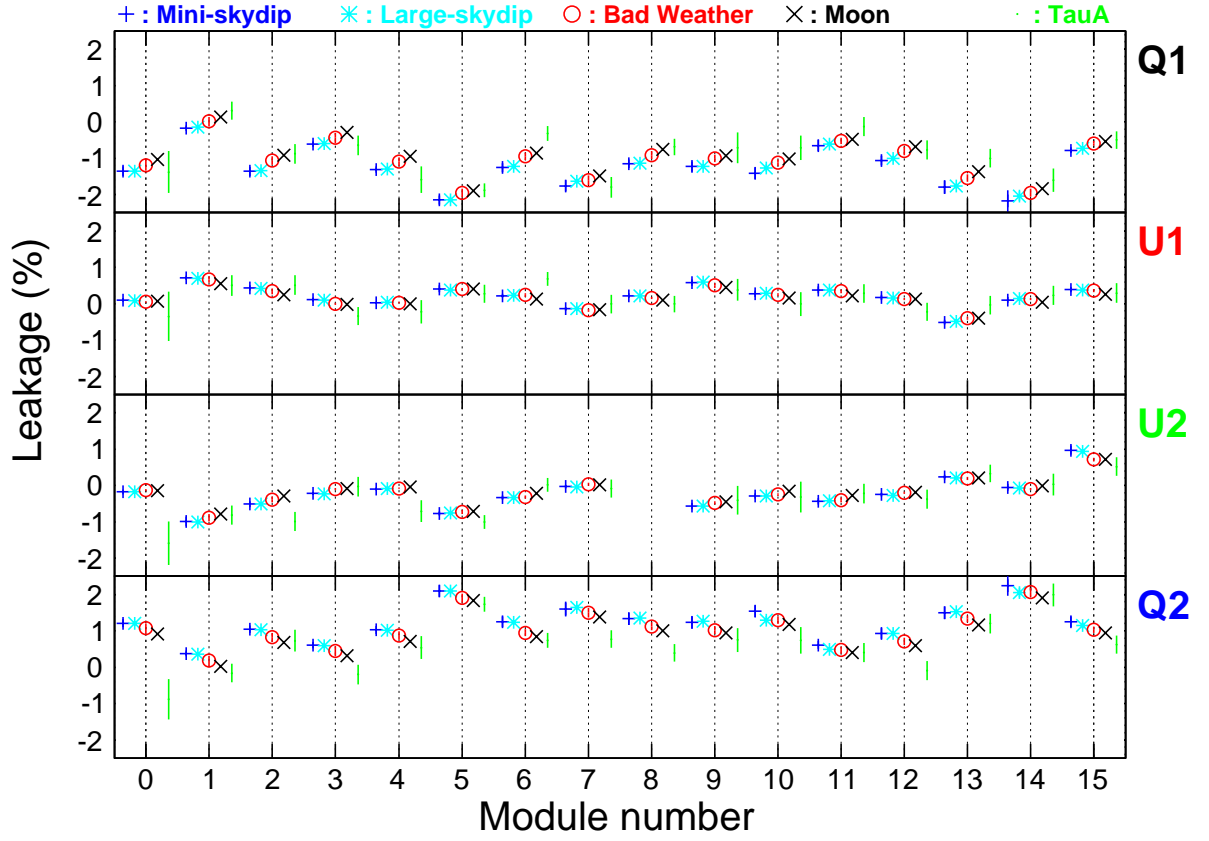


**Figure 4.24:** Comparison of  $I \rightarrow Q/U$  leakage with measurements of the mini-skydip(+), large-skydip(\*), bad weather(o), the Moon(x) and TauA(·) for each module and each diode.

the best calibration source. Therefore, we use the results from the Moon. The average magnitude of the leakage is 1.0% (0.2%) for the  $Q$  ( $U$ ) diodes respectively.

In the systematic error analysis described in § 9.8, we simulate spurious polarization signals in a map due to the leakage to estimate a possible systematic uncertainty. Note that diurnal sky rotation and weekly boresight rotation can suppress that leakage effect by an order of magnitude.

## 4.6 Pointing

A pointing model of the 3-axis mount (azimuth, elevation, and deck) and telescope motion is determined by observations of the Moon with the center module. Jupiter and Venus observations with two elements measuring the temperature anisotropy are also used. Regular optical pointing observations performed with a co-aligned telescope are taken for monitoring the time-trend of the pointing model.

We had a mechanical problem with the encoder of the deck angle during the first two months of our observation season, which lead to pointing shifts. The problem was solved later. We validated that the encoder shifts are less than  $2^\circ$  using the Moon pointing observation compared with the Jupiter and Venus observations. Systematic uncertainties induced by this problem will be discussed in § 9.5.

After fixing the deck angle problem, no clear time-dependent variation of the pointing model is found. With our pointing model, the difference between the beginning and ending of our whole observation season is smaller than  $1'$ . The pointing difference between the center module and the others is determined with Moon and Jupiter observations. The standard deviation of pointing errors on the map is  $3.5'$ .

## 4.7 Beam Profile and Window Function

In addition to regular Tau A observations for the polarization modules, we also performed special deep Tau A observations for the differential-temperature modules to map the beam profile of our telescope. The average FWHM is  $27.3'$  across the array. The uncertainty on the center module and the differential-temperature modules at the edge of the array

is  $\pm 0.1'$ . On non-center polarization modules, the uncertainty is larger ( $1.8'$ ) because of fewer observations. We found that the beam elongation is very small at 1% level, whose effect is suppressed by diurnal sky rotation and weekly boresight rotation.

A one-dimensional symmetrized beam profile was modeled as a sum of six even Gauss-Hermite terms [81, 82]. The symmetrized beam is given by

$$b^S(\theta) = \exp\left(-\frac{\theta^2}{2\sigma_h^2}\right) \sum_{i=0}^{m_h} a_{2i} H_{2i}\left(\frac{\theta}{\sigma_h}\right), \quad (4.15)$$

where  $\theta$  is the angular distance from the beam center,  $\sigma_h$  is the Gaussian beamwidth,  $H_{2i}(\theta/\sigma_h)$  is the Hermite polynomial of order  $2i$  (on chapter 22 in [83]). We determined these expansions by  $m_h = 2$  ( $i = 0, 1, 2$ ), comparing with the data. From the fitting results, the  $m_h$  coefficients  $a_{2i}$  and the  $m_h \times m_h$  covariance matrix  $C^{aa'}$  were computed. Figure 4.25 shows the QUIET Q-band beam profile from the Tau A measurements.

The basis functions for the 6 Gauss-Hermit terms are defined as

$$\Phi_{2i2j}(\vec{x}) \propto H_{2i}(x'_1) H_{2j}(x'_2) \exp(-\vec{x}' \cdot \vec{x}'/2), \quad (4.16)$$

where the primed coordinates  $\vec{x}'$  rotates into a system which is aligned with axes of the Gaussian and scaled by  $\sigma_h$  [84]. We evaluated the leakage beam profiles from those terms on that coordinate system. We use them for the systematic error analysis (§ 9.8).

The beam window function was computed separately for each Hermit polynomial:

$$B_{\ell i} = 2\pi \int d(\cos \theta) \exp\left(-\frac{\theta^2}{2\sigma_h^2}\right) H_{2i}\left(\frac{\theta}{\sigma_h}\right) P_\ell(\cos \theta), \quad (4.17)$$

where  $P_\ell(\theta)$  is the Legendre polynomial. The full window function is given by

$$B_\ell = \sum_{i=0}^{m_h} a_{2i} B_{\ell i}. \quad (4.18)$$

From Equation (4.18), we can determine the covariance matrix between  $B_\ell$  and  $B_{\ell'}$  as

$$\Sigma_{\ell\ell'}^B = \sum_{i,j=0}^{m_h} \frac{\partial B_\ell}{\partial a_{2i}} C_{ij}^{aa'} \frac{\partial B_{\ell'}}{\partial a_{2j}} = \sum_{i,j=0}^{m_h} B_{\ell i} C_{ij}^{aa'} B_{\ell' j}, \quad (4.19)$$

which allows us to evaluate the covariance matrix of the window function. Figure 4.26 shows the beam window function and its uncertainty. We use this window function and its uncertainty for the CMB analysis as described in Chapter 5 and the systematic error analysis as described in § 9.6.

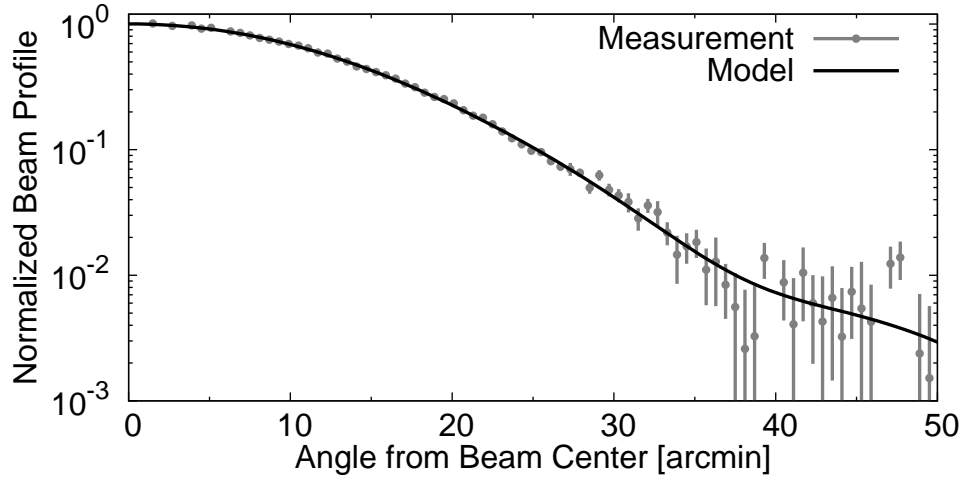


**Figure 4.25:** Symmetrized polarization beam profile from the Tau A measurements on the center module evaluated with Equation (4.15).

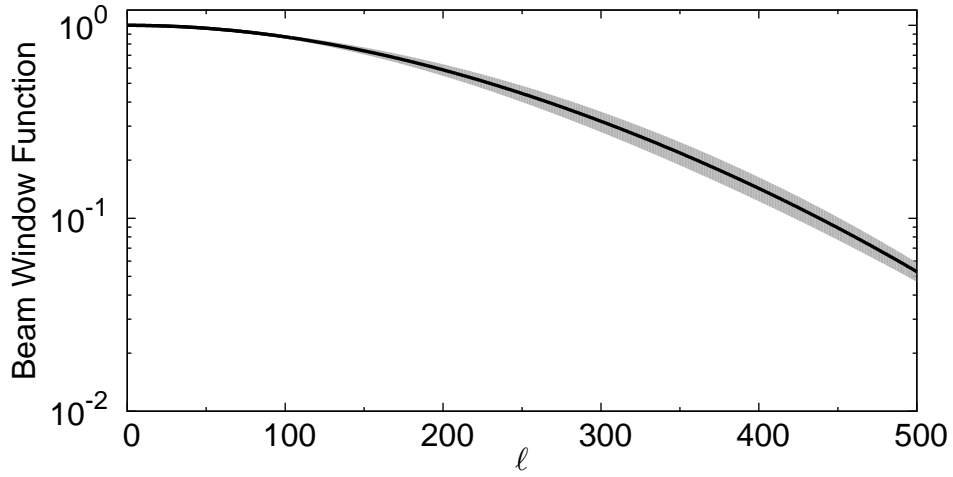


**Figure 4.26:** Window function evaluated from the beam profile with the statistical error (gray band) given by Equations (4.17), (4.18) and (4.19).



We computed the beam solid angle by integrating that model out to  $54'$  (roughly  $-28$  dB level). The beam solid angle on the center module, the differential-temperature module, and the average of all the modules are  $74.3 \pm 0.7 \mu\text{sr}$ ,  $78.3 \pm 0.4 \mu\text{sr}$ , and  $76 \mu\text{sr}$ , respectively. The difference between the polarization and differential-temperature beam profile is 3.8%. This uncertainty also propagates to the uncertainty of the responsivity as mentioned in § 4.2.1.3.



# Chapter 5

## Analysis Procedure

Our analysis consists of the following steps:

1. TOD Data Processing

- (a) *Pre-processing*: application of the calibration and pointing model which are determined in Chapter 4 to the TOD; correction of the known TOD problems and so on.
- (b) *Noise Modeling*: check and characterization of the TOD noise properties.
- (c) *Filtering*: suppression of the  $1/f$  noise and whitening for the TOD.

2. Map-making: making polarization maps from the resulting TOD.

3. Power Spectrum Estimation: evaluating polarization angular power spectra  $C_\ell^{XX}$ , where  $XX$  represents a flavor of  $\{EE, BB, EB\}$  from the resulting polarization maps.

4. Cosmological Analysis: estimating the tensor-to-scalar ratio.

In addition, management of the data quality is also required to control systematic biases in CMB analysis, which is discussed in Chapter 6.

Note that the TOD of a single (module) diode for a single CES are fundamental and minimum data units of our analysis. We call it “CES-diode” hereafter. The length of a normal CES-diode is  $\lesssim 1.5$  hours.

## 5.1 TOD Data Processing

The TOD taken in our CMB measurements are electric signals. In order to extract CMB signals from those “raw” TOD, we have to convert them into the calibrated and cleaned TOD for each CES-diode. We checked the properties of the module noise—white noise level, knee frequency of the  $1/f$  noise, and slope of that. After that, we applied certain filters to subtract undesirable contaminations such as low-frequency noise due to the  $1/f$  noise from the instruments and atmospheric fluctuation, ground emission through the far-sidelobes, and also high-frequency noise.

### 5.1.1 Pre-Processing

#### 5.1.1.1 Correcting “Type-B” Glitch

Since our analog-to-digital converter (ADC) has a small differential non-linearity, which creates certain glitches in the TOD (labeled “Type-B” glitch, shown as a left plot on Figure 5.1), we have to correct it at first. The non-linearity happens every 1,024 bits, and roughly 14% of the data are contaminated by the glitches. Since our modules have the  $I \rightarrow Q/U$  leakage, we can discover a non-linear relation between the total power and (double-)demodulation data (right in Figure 5.1). We corrected the glitches by this relation. The systematic bias due to imperfection of the Type-B correction is discussed in § 9.10.

#### 5.1.1.2 Correcting Timing-Offset and Applying Pointing Model

We designed that the module outputs are synchronized with the telescope encoder outputs. However, we found a disagreement between them from the Moon observations. When the telescope was scanning the Moon in the right-going direction, the signal from the Moon was shifted toward the right; when the telescope was scanning the Moon in the left-going direction, the signal was shifted toward the left. The fact leads that the module data always has time lag behind the telescope encoder data. We found the lag is 2.5 samples (= 25 msec). The time lag is very stable and constant throughout the whole observation season; therefore, we corrected it in the analysis. After that, the pointing

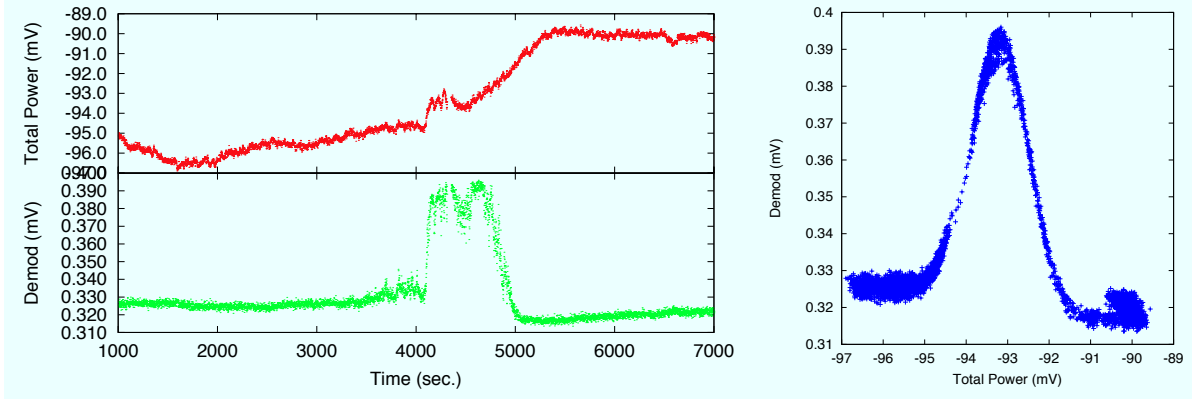


**Figure 5.1:** Left panels shows the time-trend of the module outputs (averaged with 1 Hz). Red dots in top panel correspond to the total power outputs, green dots in bottom panel correspond to the double-demodulated outputs before the Type-B correction. The Type-B glitches happened on time between 4,000 seconds. and 5,000 seconds. Right panel shows the correlation between the total power and demod outputs. Peak around  $-93$  mV in the total power indicates the location of the ADC non-linearity.

model determined by the calibration (Chapter 4) was applied.

#### 5.1.1.3 Double-Demodulation and Applying Detector Responsivities

After that, we double-demodulated the demodulated TOD as described in Chapter 2.2. We also applied the calibration model determined in Chapter 4 to the resulting TOD.

#### 5.1.1.4 Applying Antenna-to-Thermodynamic Units Correction

We applied the antenna-to-thermodynamic temperature correction. It is straight and useful to define quantities in antenna temperature units for calibration purpose. On one hand, antenna temperature is the natural unit for all the calibration purposes; on the other hand, thermodynamic temperature is convenient for CMB purpose. For this reason, it is best to stick to antenna temperature units in the calibration. We switch from antenna temperature units to thermodynamic temperature units here.

The antenna-to-thermodynamic conversion for both the CMB temperature anisotropy and polarization is given by

$$f(\nu, T_{\text{CMB}}) = \frac{(e^x - 1)^2}{x^2 e^x}; \quad \text{where } x = \frac{h\nu}{kT_{\text{CMB}}}. \quad (5.1)$$

Hence the conversion factor for our Q-band is  $f(\nu = 43.1 \text{ GHz}, T_{\text{CMB}} = 2.725 \text{ K}) = 1.049$  for temperature units, and  $f^2 = 1.100$  for the square of temperature units, which are used in power spectrum, where we use the CMB monopole temperature of  $T_{\text{CMB}} = 2.725 \text{ K}$  [3]. The figure of Equation (5.1) for the frequency between 10 GHz and 150 GHz is found in Appendix E.

### 5.1.2 Noise Modeling

After the pre-processing, we performed a Fourier transform on the TOD for each CES-diode to model the noise power spectrum. In the calculation, the noise power spectrum is binned as follows:

- First 20 Fourier modes are left un-binned.
- Fourier modes from 21 to 1,000 are averaged into bins, which are increasing their width proportional to mode numbers.
- Higher Fourier modes ( $> 1,000$ ) are averaged into bins, which are increasing their width proportional to the square root of mode numbers.

A model of the noise power spectrum used here is a simple  $1/f$  noise plus white noise defined as

$$\hat{\Sigma}(f; \sigma_0, f_{\text{knee}}, \alpha) = \sigma_0^2 \left[ 1 + \left( \frac{f_{\text{knee}}}{f} \right)^\alpha \right], \quad (5.2)$$

where  $\sigma_0$  represents the white noise level (typically  $625 \mu\text{K}\sqrt{\text{s}}$ ),  $f_{\text{knee}}$  is the knee frequency (typically 5.5 mHz), at which the power spectrum equals to twice the white noise level, and  $\alpha$  corresponds to the slop of the  $1/f$  noise component. The TOD also contain of the CMB signals; however, the noise is dominated for each CES-diode.

We obtained the best fit noise model by minimizing the log-likelihood function

$$\log \mathcal{L}(\sigma_0, f_{\text{knee}}, \alpha) = \sum_k \left[ N_k \left( \log \hat{\Sigma}_k + \frac{\Sigma_k}{\hat{\Sigma}_k} \right) \right], \quad (5.3)$$

where  $\Sigma_k$  and  $\hat{\Sigma}_k$  are the noise power spectrum of data and that of the model, respectively;  $N_k$  is the number of the frequency modes. Figure 5.2 shows an example of a binned noise power spectrum and its model fitting.

In the fitting, small disagreements between the model and data due to the scan-synchronous signal, weather conditions, and undesirable features at high frequencies are usually found. When the sidelobes are picking up emission from the ground, a narrow spike is created at the scan frequency (typically from 45 mHz to 100 mHz as shown in Figure 5.3). The atmospheric condition slowly changing during a single CES creates a broadband bump around scan frequencies too. Some narrow spikes at high frequencies of above 4 Hz happens (Figure 5.4), which we can not completely understand that reason. All the disagreements may lead to mis-estimate the noise model. For this reason, the noise fitting is performed excluding scan frequency ranges and frequencies above 4.6 Hz, which is the same as the cutoff frequency of the low-pass filter described in the next section.

We evaluated the white noise correlations between two  $Q$  and  $U$  diodes in the same module because the white noise in a diode pair on the same module has positive correlation. This correlation (typically the correlation coefficient is 0.22 averaging over a  $Q$  and  $U$  diode pair) makes the sensitivity of a  $Q$  or  $U$  diode pair better than we expect if we ignore the correlation.

We also evaluated certain quantities characterizing the features of the TOD such as glitch/jump statistics, weather statistics given by the TOD of total power, goodness of filtering explained in the next section as well as the noise model. These quantities are used for the study of the data selection as discussed in Chapter 6.

### 5.1.3 Filtering

Our map-making is optimized for the TOD with the white noise model; therefore, filtering for whitening the TOD is needed before map-making. Our filterings (itself and their threshold) are determined by a lot of trials and errors of the null suites described in Chapter 7.

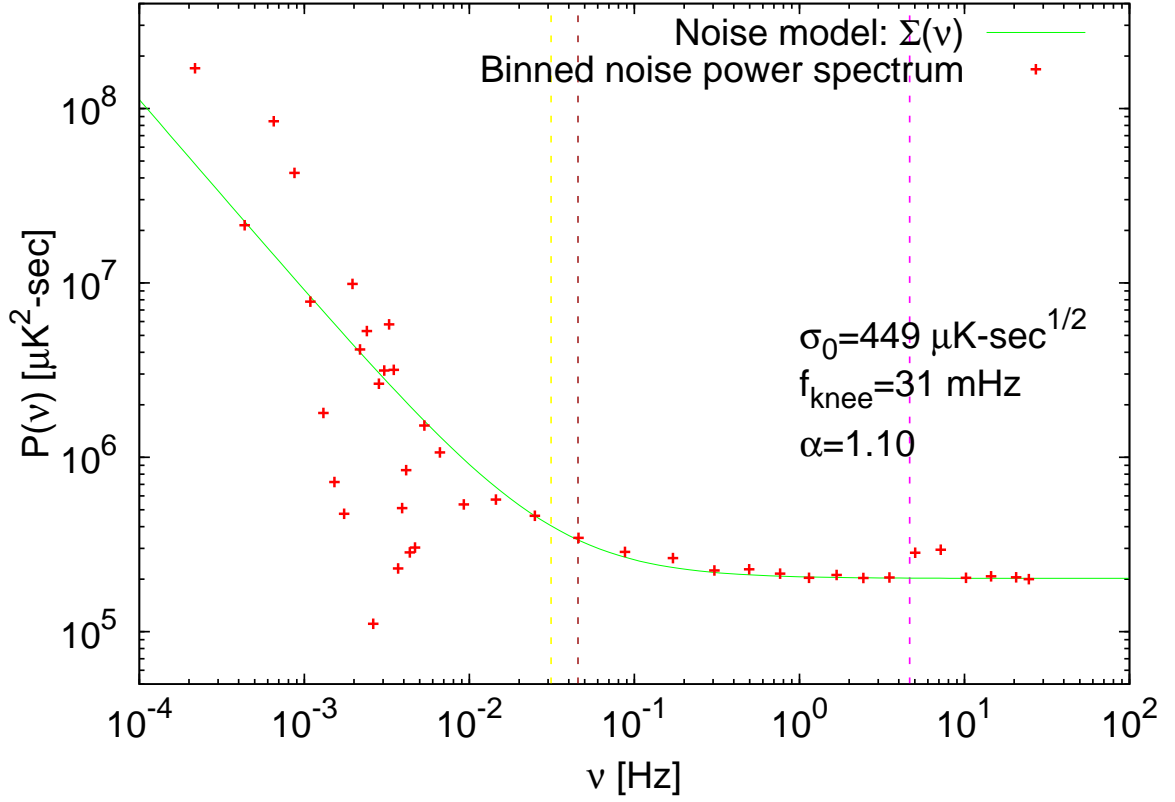


**Figure 5.2:** Binned noise power spectrum (red dots) and model (green line) from a certain CES-diode. By fitting the model with binned power spectrum, we found  $\sigma_0 = 449 \mu\text{K}\sqrt{\text{s}}$ ,  $f_{\text{knee}} = 31 \text{ mHz}$ , and  $\alpha = 1.10$  for this CES-diode. The vertical yellow, brown, and magenta lines correspond to the knee frequency, scan frequency, and high-frequency cut-off, respectively.

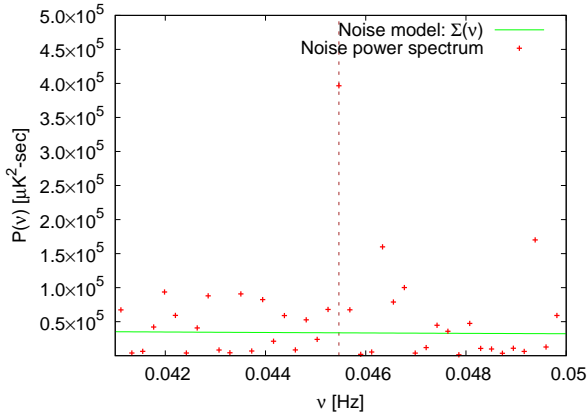


**Figure 5.3:** Zoom in around the scan frequency of the above plot. The scan-synchronous signal is found at 45.4 mHz.

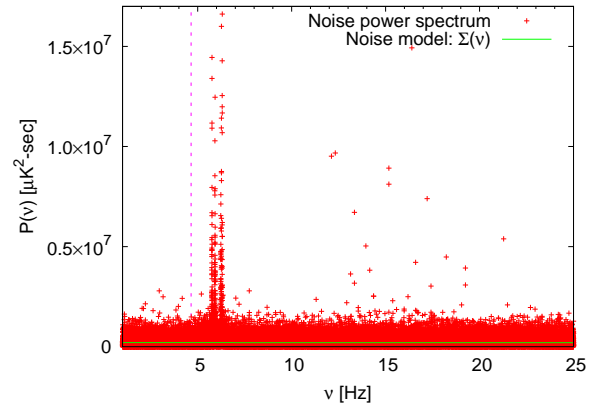


**Figure 5.4:** Zoom in around 4 Hz of the above plot. The high-frequency noise is found at frequencies above 4.6 Hz.



### 5.1.3.1 Low-pass Filter

In order to drop the high frequency noise above 6 Hz, we multiplied the noise power spectrum by a low-pass filter which is given by

$$H(f; f_0 = 4.6 \text{ Hz}, f_1 = 4.7 \text{ Hz}) = \begin{cases} 1, & f \leq f_0 \\ \frac{1}{2} \left[ 1 + \cos \left\{ \pi \left( \frac{f - f_0}{f_1 - f_0} \right) \right\} \right], & f_0 < f \leq f_1 \\ 0, & f > f_1 \end{cases} \quad (5.4)$$

which sharply falls off from one to zero between  $f_0 = 4.6 \text{ Hz}$  and  $f_1 = 4.7 \text{ Hz}$ .

### 5.1.3.2 High-pass Filters (Azimuth Cleaning)

After the low-pass filter, we subtracted a first-order polynomial from each half-scan (left- or right-going azimuth scan) to suppress the  $1/f$  noise from the module as well as ground pickup and atmospheric contamination. This subtraction plays a high-pass filter with twice the scan frequencies. Since the variation of those azimuth slopes during a single CES is sensitive to bad weather, this variation is used to eliminate the bad weather period of the data in the next chapter (Chapter 6).

The last filter removes the ground emission due to azimuth structures. We created a one-dimensional azimuth map for each CES-diode by accumulating and projecting all the scans into azimuth direction, which provides structure of the ground emission although emission from the atmosphere is almost constant in a single CES. We subtracted that structure from the TOD for each CES-diode.

Figure 5.5 shows the same noise power spectrum of Figure 5.2 but cleaned by the low- and high-pass filters. This spectrum shows that our filters work well and the filtered TOD are almost white in so-called “science band” of QUIET described in Chapter 2.2.4.

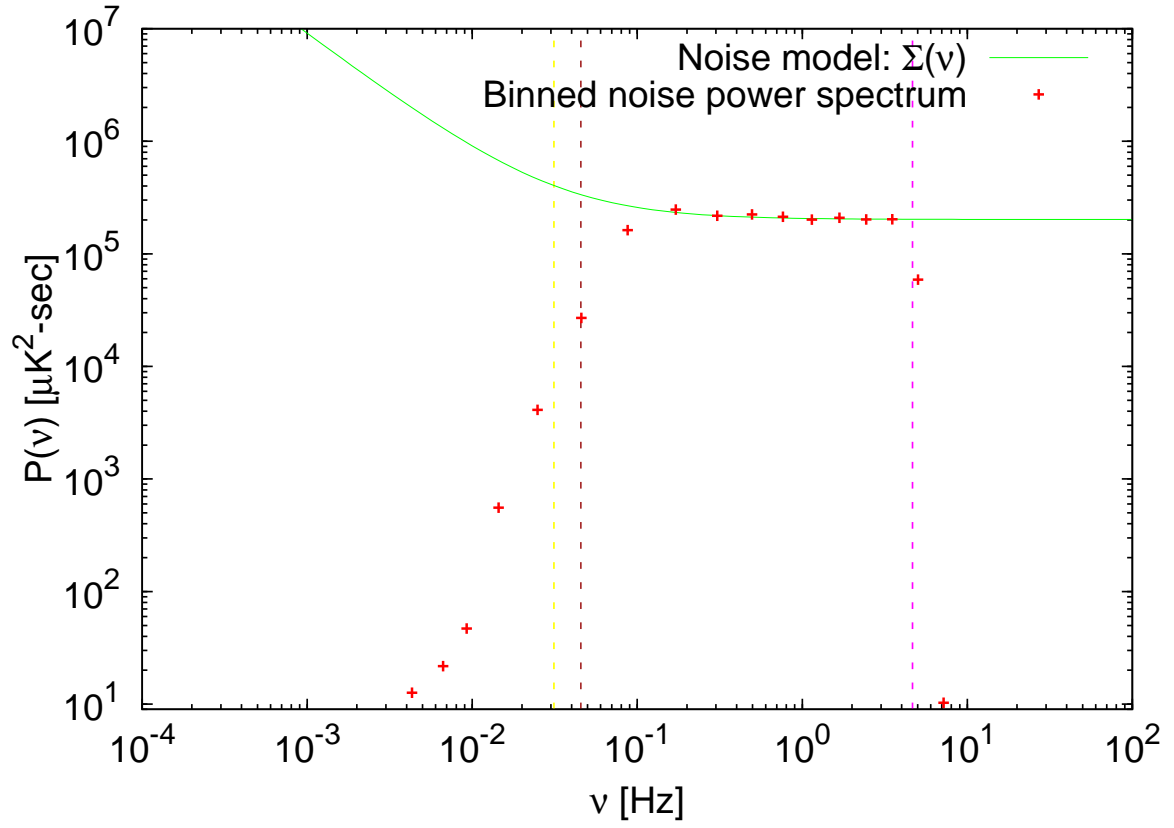


**Figure 5.5:** Cleaned noise power spectrum of Figure 5.2 by the low- and high-pass filters. The noise power above 4.6 Hz and below twice the scan frequency is suppressed.

## 5.2 Map-making

After all the TOD processing, we made polarization maps. For simplification, we consider the maps ( $\vec{m}$ ) for a single pixel and sample defined as

$$\vec{m} = \begin{pmatrix} \hat{Q} \\ \hat{U} \end{pmatrix} = (\mathbf{P}^t \mathbf{N}^{-1} \mathbf{P})^{-1} \mathbf{P}^t \mathbf{N}^{-1} \vec{d}, \quad (5.5)$$

where  $\mathbf{P}$  is a pointing matrix described as

$$\mathbf{P} \equiv \begin{pmatrix} \cos 2\psi_{Q1} & \sin 2\psi_{Q1} \\ \cos 2\psi_{U1} & \sin 2\psi_{U1} \\ \cos 2\psi_{U2} & \sin 2\psi_{U2} \\ \cos 2\psi_{Q2} & \sin 2\psi_{Q2} \end{pmatrix} \quad (5.6)$$

from a pointing model and parallactic angle ( $\psi_i$ ) calculated from the detector angle, which are determined by the calibration discussed in Chapter 4;  $\mathbf{N}^{-1}$  is a inverse noise matrix given as

$$\mathbf{N}^{-1} \equiv \begin{pmatrix} \sigma_{Q1}^2 & 0 & 0 & 0 \\ 0 & \sigma_{U1}^2 & 0 & 0 \\ 0 & 0 & \sigma_{U1}^2 & 0 \\ 0 & 0 & 0 & \sigma_{Q2}^2 \end{pmatrix}^{-1} \quad (5.7)$$

where  $\sigma_i$  is the white noise level defined in the previous section;  $\vec{d} = (d_{Q1}, d_{U1}, d_{U2}, d_{Q2})^t$  corresponds to a single sample of the TOD. Accumulating set of the CES-diodes which has passed the data selection described in Chapter 6, we made not  $\vec{m}$  maps themselves but  $\tilde{\mathbf{N}} = \mathbf{P}^t \mathbf{N}^{-1} \mathbf{P}$  matrix and  $\vec{m} = \mathbf{P}^t \mathbf{N}^{-1} \vec{d}$  maps separately. In that case, the noise matrix multiplied by pointing matrices from the both side of  $\mathbf{N}^{-1}$  is described as

$$\tilde{\mathbf{N}} = \mathbf{P}^t \mathbf{N}^{-1} \mathbf{P} = \begin{pmatrix} A_{ss} & A_{cs} \\ A_{cs} & A_{cc} \end{pmatrix} \quad (5.8)$$

with

$$A_{cc} \equiv \sum_i \frac{\cos^2 2\psi_i}{\sigma_i^2}, \quad A_{cs} \equiv \sum_i \frac{\cos 2\psi_i \sin 2\psi_i}{\sigma_i^2}, \quad A_{ss} \equiv \sum_i \frac{\sin^2 2\psi_i}{\sigma_i^2}, \quad (5.9)$$

where  $i$  runs over four diodes ( $Q1, U1, U2$  and  $Q2$ ). The  $\vec{m}$  map is also defined as

$$\vec{m} = \mathbf{P}^t \mathbf{N}^{-1} \vec{d} = \sum_i \begin{pmatrix} \frac{\cos 2\psi_i}{\sigma_i^2} d_i \\ \frac{\sin 2\psi_i}{\sigma_i^2} d_i \end{pmatrix}. \quad (5.10)$$

In case of multiple samples of time, we can simply extend Equation (5.5) to

$$\vec{m} = \begin{pmatrix} \hat{Q} \\ \hat{U} \end{pmatrix} = \left[ \sum_t \tilde{N}(t) \right]^{-1} \sum_t \vec{m}(t). \quad (5.11)$$

Equation (5.11) shows that we can accumulate  $\tilde{N}$  matrices and  $\vec{m}$  maps separately. This equation is valid not only multiple samples of time but also those of module-diode<sup>a</sup>. For this reason, we usually accumulate the matrices and maps by CES-diode units. Equation (5.11) also shows that we only have to invert  $\tilde{N}$  once in the whole map-making process. The above equations and relations for single pixel map is also valid for multi-pixel case because all the pixel are independent in our case. Figure 5.6 shows the Stokes  $Q$  and  $U$  maps from our observation of the patch CMB-1<sup>b</sup>.

By contrast, the above equations are not completely true because of noise correlations among diodes and filtering effects as introduced in the previous section. These effects are corrected in power spectrum estimation as discussed in the next section by comparing them with Monte Carlo (MC) simulations.

We use the Hierarchical Equal Area isoLatitude Pixelization of a sphere (HEALPix) [85] to make a map with equal area pixels. A general advantage of the HEALPix for the CMB analysis is that the HEALPix is optimized to calculate the spherical harmonic transform<sup>c</sup>. The pixel resolution of the HEALPix is characterized by a parameter of  $N_{\text{side}}$ . We use  $N_{\text{side}} = 256$ , which corresponds to the pixel resolution of  $\theta_{\text{pix}} = \Omega_{\text{pix}}^{1/2} = \sqrt{\pi/(3N_{\text{side}}^2)} \approx 13.7'$ . This is sufficient for our requirement of multipole range by  $\ell_{\text{max}} \approx 500$ , which is limited by our beamwidth.

---

<sup>a</sup>The summation running through four diodes in Equations (5.9) and (5.10) has already been performed. But the summation is not necessary at that time in general.

<sup>b</sup>data selection described in Chapter 6 has been applied.

<sup>c</sup>However we do not make full use of this advantage because we observe very small area on the sky and use the Fast Fourier Transform (FFT) technique with the flat sky approximation.

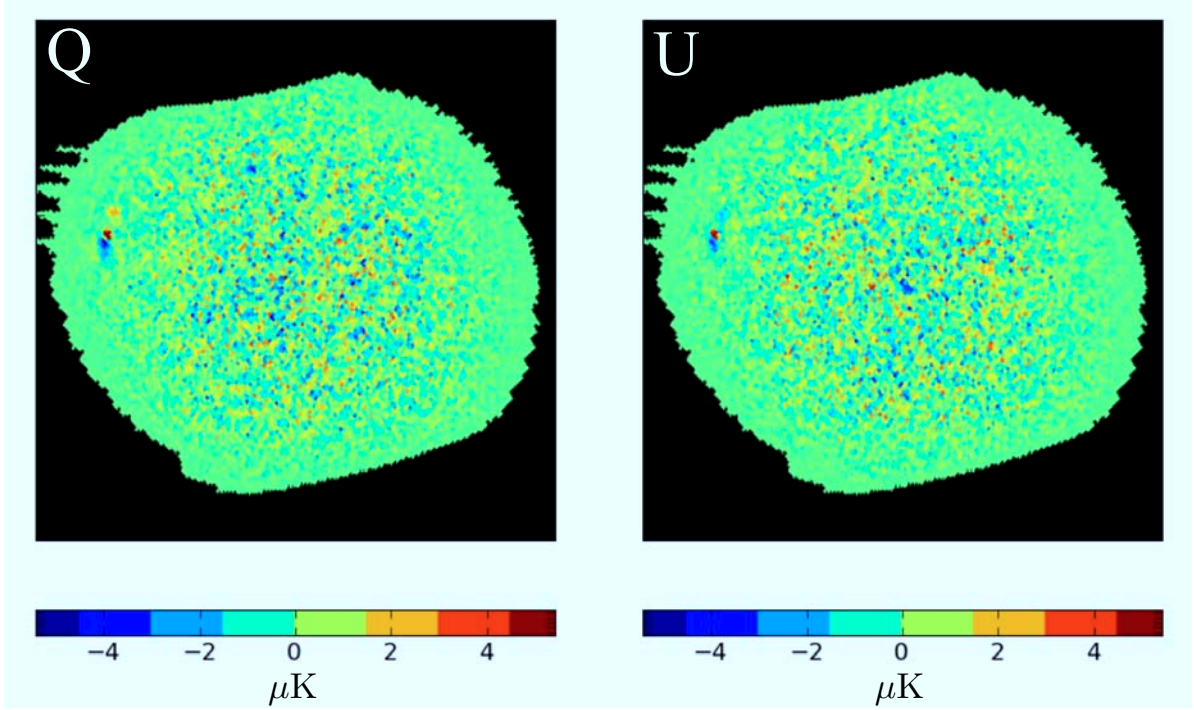


**Figure 5.6:** Polarization maps of the Stokes  $Q$  (left) and  $U$  (right) from the Q-band data for the patch CMB-1 after the data selection (Chapter 6). A point like source around the left center in both maps is Centaurus A (Cen A). Note that we do not use these maps to evaluate power spectra in Chapter 8 because we use cross-correlations of maps separated by the pointing division as discussed in the next section. These maps just demonstrate how our map-making works well.

## 5.3 Power Spectrum Estimation

### 5.3.1 MASTER and Pseudo- $C_\ell$ Estimator

We use the MASTER (Monte Carlo Apodized Spherical Transform Estimator) technique [86, 87, 88] to estimate power spectrum. This technique is based on a pseudo- $C_\ell$  power spectrum estimation and MC simulations. The MASTER technique is widely used in a lot of CMB experiments. This is much more computationally efficient than the Maximum Likelihood (ML) technique [89, 90], which is also common to CMB data analysis. This computational advantage make it easier to iterate lots of the null tests (Chapter 7) and evaluate various types of systematic errors (Chapter 9).

The pseudo- $C_\ell$  technique allows us to estimate the true underlying power spectrum recovered from power spectrum with non-uniform partial sky map [91]. The pseudo- $C_\ell$  power spectrum ( $\tilde{C}_\ell$ ) from the map ( $\hat{m}$ ) is defined as

$$\tilde{a}_{\ell m} = \int d\Omega(\vec{n}) W(\vec{n}) \hat{m}(\vec{n}) Y_{\ell m}^*(\vec{n}) \approx \sum_i \Omega_i W_i \hat{m}_i Y_{\ell m}^*(i) \rightarrow \tilde{C}_\ell = \frac{1}{2\ell+1} \sum_{m=-\ell}^{+\ell} |\tilde{a}_{\ell m}|^2, \quad (5.12)$$

where  $p$  is a pixel in  $\hat{m}$ ;  $\Omega_i$  is the solid angle of a pixel;  $W_i$  is a weighting function of a pixel, which is usually inversely proportional to square of the noise in a pixel; and  $Y_{\ell m}$  is spherical harmonics. The pseudo- $C_\ell$  power spectrum is related to true power spectrum ( $C_\ell$ ) as

$$\langle \tilde{C}_\ell(\hat{m}) \rangle = \sum_{\ell'} M_{\ell\ell'} F_{\ell'} B_{\ell'}^2 \langle C_{\ell'} \rangle + \langle \tilde{N}_{\ell'} \rangle, \quad (5.13)$$

where  $B_\ell$  is the beam window function determined in Chapter 4;  $M_{\ell\ell'}$  is a mode-mode coupling kernel resulting from the cut sky, which depends on the weighting function which includes the geometry of the partial sky [92] (see appendix A in [86] for more details);  $F_\ell$  is a transfer function which models the effect of the filters and determined by noiseless CMB simulations;  $\tilde{N}_\ell$  is a noise bias. Though we discussed Equation (5.13) as the temperature anisotropy, it can be generalized to the polarization anisotropy.

We binned  $C_\ell$  into nine bandpowers  $C_b$  in the Q-band analysis in order to maximize the signal-to-noise ratio considering a mode-mode coupling of each bandpower. The bandpowers are equally spaced in multipole moment with widths of  $\Delta\ell=50$  from  $\ell_{\min} = 25$  to  $\ell_{\max} = 475$ , which results in almost independent bandpowers. QUIET does not have

the sensitivity of angular scales bigger than  $\theta \approx 180^\circ/\ell_{\min} \approx 8^\circ$ , which is almost the same size of central area of each CMB patch and that of angular scales smaller than  $\theta \approx 180^\circ/\ell_{\max} \approx 23'$ , which is almost the same size of our beamwidth.

### 5.3.2 Cross-Correlation

CMB signal is common during the whole observation season; on the other hand, module noise is randomly fluctuated in each CES-diode. For this reason, the harmonic coefficients of the observed CMB signal are correlated among CES-diods for each patch. But those of the noise are NOT correlated. We took the correlations among CES-diods (so-called “cross-correlation”) and did not take the correlation within each CES-diode (so-called “auto-correlation”). Taking the cross-correlation, the noise bias in Equation (5.13) is naturally dropped as the follows<sup>d</sup>:

$$\left\langle \tilde{C}_\ell(\hat{m}_i, \hat{m}_j) \right\rangle_{i \neq j} = \sum_{\ell'} M_{\ell\ell'} F_{\ell'} B_{\ell'}^2 \langle C_{\ell'} \rangle. \quad (5.15)$$

Here  $\tilde{C}_\ell(\hat{m}_i, \hat{m}_j)$  denotes the cross pseudo power spectrum of  $\hat{m}_i$  and  $\hat{m}_j$ .

With a lot of trials and errors of the null suites (Chapter 7), we found that the cross-correlation among the pointing divisions which are defined as the telescope orientation (azimuth) and boresight rotation (deck) is the best for our data set. In this case, we made all the maps for each CES-diode; separated them in the  $10 \times 6 = 60$  pointing divisions of the azimuth-deck angle (subscripts  $i, j$  correspond to these divisions); accumulated the maps in each division; then took correlations among these divisions. These cross-correlations can eliminate not only the noise bias but also residual contamination from ground emission due to the ground structures, the far-sidelobes, and time-depending effects in the data set. A disadvantage of the cross-correlation is statistical loss due to not including auto-correlation. Taking the cross-correlation and dropping the auto-correlation increased the statistical errors by  $\approx 3\%$  on the power spectrum.

---

<sup>d</sup>We used an equivalent formula to Equation (5.15)

$$\left\langle \tilde{C}_\ell(\hat{m}_i, \hat{m}_j) \right\rangle_{i \neq j} = \left\langle \tilde{C}_\ell(\hat{m}) \right\rangle - \sum_i \left\langle \tilde{C}_\ell(\hat{m}_i) \right\rangle \quad (5.14)$$

in the analysis. Here  $\hat{m}$  is a map from all the data set.

### 5.3.3 $E$ – $B$ Mixing

We can not uniquely separate any polarization field into pure  $E$  and  $B$ -modes on the partial sky though we can do that on the full sky [93]. This is known as “ $E$ – $B$  mixing problem” in the CMB polarization analysis. Since the  $E$ -mode power is generally much bigger than the  $B$ -mode power, we have to manage the  $E \rightarrow B$  leakage due to the mixing. Certain general solutions [94, 95, 96] for the mixing have been developed and confirmed that they can archive a tensor-to-scalar ratio of  $r = \mathcal{O}(10^{-2})$  level with realistic inhomogeneous noise; complex boundaries; point source masking; and noise level comparable to what is expected for next generation experiments. However, compared with the QUIET noise level, contribution of the additional variance to the  $B$ -mode power due to the mixing does not matter to us. For this reason, we only assigned it as a part of the statistical error.

### 5.3.4 Error Estimation

We adopted frequentest two-sided 68% confidence intervals of power spectrum which are evaluated by the full-pipeline MC simulations as the statistical errors. We computed the likelihood function based on the confidence intervals which are modeled with [97], and calibrated them by using the MC simulations of more than 2,000 realizations with and without CMB signal. The likelihood function is also used for cosmological analysis as described in Chapter 8.



# Chapter 6

## Data Selection

Since the CMB polarization signal is extremely small, degradation of the data quality may cause unexpected bias for the results of power spectra. Unless we can perfectly estimate those biases, we have to eliminate or minimize them. Data selection is the way to control such hidden systematic biases. Major reasons of data quality degradation are:

- (A) malfunction of the instruments,
- (B) instrumental trouble or its imperfection,
- (C) rapid variation of atmospheric condition,
- (D) picking up ground emissions.

In the following section, we define four criterion categories of the data selection:

- *Baseline Selection* drops the (A). We define the baseline CES-diode set (so-called “official QUIET dataset”) after this selection.
- We have two major selections for (B):
  - *Sun Sidelobes Selection* removes contamination from the Sun induced by the far-sidelobes as described in § 2.3.
  - *Type-B Selection* eliminates the failure of the Type-B glitch correction as described in § 5.1.1.1.

- Selections for *bad weather*, *noise model*, and *azimuth slopes* are sensitive to the (C) and (D).

We determined our 33 data selection criteria in these four categories through the null tests described in the next chapter.

## 6.1 Baseline Selection and Baseline Data Set

We rejected the data of six diodes at first—all the diodes on *RQ16*, *Q1* diode on *RQ04*, and *U2* diode on *RQ08*, which did not function during the whole Q-band observation. We rejected entire diodes for bad run CESes—for example, malfunction of the telescope control, unexpected power-off of the bias electronics, and so on. We simply dropped very short CESes whose duration is less than 1,000 seconds because they are too short to perform the noise fitting well. Table 6.7 shows the baseline CES-diodes set (and summary of the data selection). The ratio of the baseline CES-diodes for each CMB patch to the total CES-diodes is almost consistent with observation time as described in Chapter 3<sup>a</sup>.

## 6.2 Sun Contamination

The QUIET telescope has two undesirable far-sidelobes (triple reflection sidelobe and spillover sidelobe) as described in § 2.3. The far-sidelobes sometimes pick up not only the ground emission but also the unignorable signal from the Sun. Whereas the azimuth filtering (§ 5.1.3) removes the ground structure every half-scans, and azimuth structures during a single CES; we sometimes find that the contamination still remains on the map as shown in Figure 6.1. That is the evidence of the contamination from the Sun. The physical relationship between the telescope boresight and the Sun location can be understood as shown in Figure 6.2.

We have to suppress the degradation due to the far-sidelobes to control systematic biases like the *WMAP* [98] and QUaD [99] performed.

---

<sup>a</sup>The difference in those two ratios results from un-uniform baseline selection.

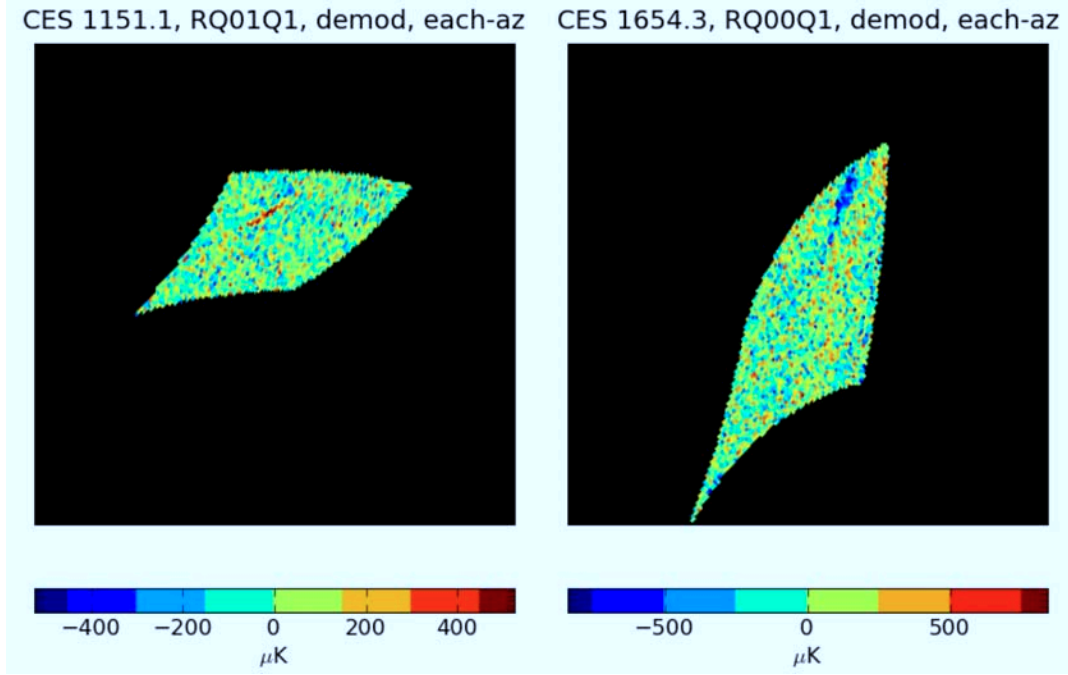


**Figure 6.1:** Example maps in the Galactic coordinate system for the triple reflection sidelobe (left), and spillover sidelobe (right) from a single CES-diode after all the filtering. The triple reflection sidelobe has spot-like feature on the center, and spillover sidelobe has blob-like feature on the top right.

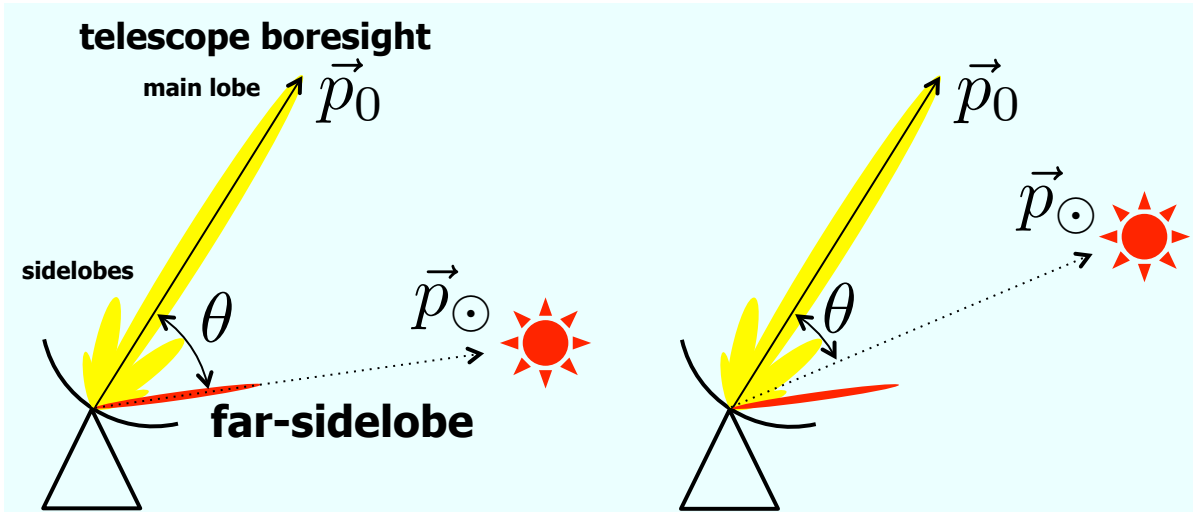


**Figure 6.2:** Left: we observe the Sun signal when the far-sidelobe sees the Sun even though the mainlobe does not see the Sun. Right: we do not observe the Sun signal because both the mainlobe and far-sidelobe do not see the Sun. The far-sidelobe direction ( $\theta$ ) is characterized by the angle between the telescope boresight ( $\vec{p}_0$ ) and Sun direction ( $\vec{p}_\odot$ ).

### 6.2.1 The Sun-centered Map

We characterized the far-sidelobes by using the Sun, which is the brightest source on the sky. For each feedhorn, we made the “Sun-centered map” by the following procedure:

1. All the TOD pre-processing except the pointing are performed.
2. The Sun-centered coordinate system  $(\theta, \phi)$  is defined as

$$\theta \equiv \arccos(\vec{p}_{\odot} \cdot \vec{p}_0), \quad \phi \equiv \arctan\left(\frac{\vec{p}_{\odot} \cdot \vec{r}_0}{\vec{p}_{\odot} \cdot \vec{s}_0}\right), \quad (6.1)$$

where  $\vec{p}_0$  is the pointing vector of the telescope boresight;  $\vec{s}_0$  is the orientation vector defined as a reference orientation in the plane perpendicular to  $\vec{p}_0$ ;  $\vec{r}_0 = \vec{p}_0 \times \vec{s}_0$ ; and  $\vec{p}_{\odot}$  is the pointing vector of the Sun. The coordinates could also be referred to these as “instrumental coordinates” since the coordinate system is fixed to the instrument. Figure 6.3 shows schematic definition of this coordinate system.

3. A new Sun-centered pointing model is applied to each CES-diode data.
4. We make maps of the baseline dataset and accumulate them for each module-diode.  
because the location of the sidelobes for each module depends on the feedhorn position on the array.

Figure 6.4 shows the Sun-centered coordinate maps for certain modules, which provide both the location and intensity of the Sun contamination. The triple reflection sidelobe has sharp shape (spike); by contrast, the spillover sidelobe has blobs at large angular scales. Their locations, especially for the spillover sidelobe, depend on the feedhorn position on the array as shown in Figure 2.9. We can determine that the power of the far-sidelobes is less than  $-60$  dB level from the maps because the polarization signal induced by the Sun through the far-sidelobes is between hundreds microkelvin and 1 millikelvin compared with the Sun signal of about 6,000 K. The ray-tracing simulation and the measurement using the high power noise source on the W-band receiver support the results. It is notable that the noise level of the Sun-centered maps is about  $20 \mu\text{K}$ , which is limited by the white noise level itself.

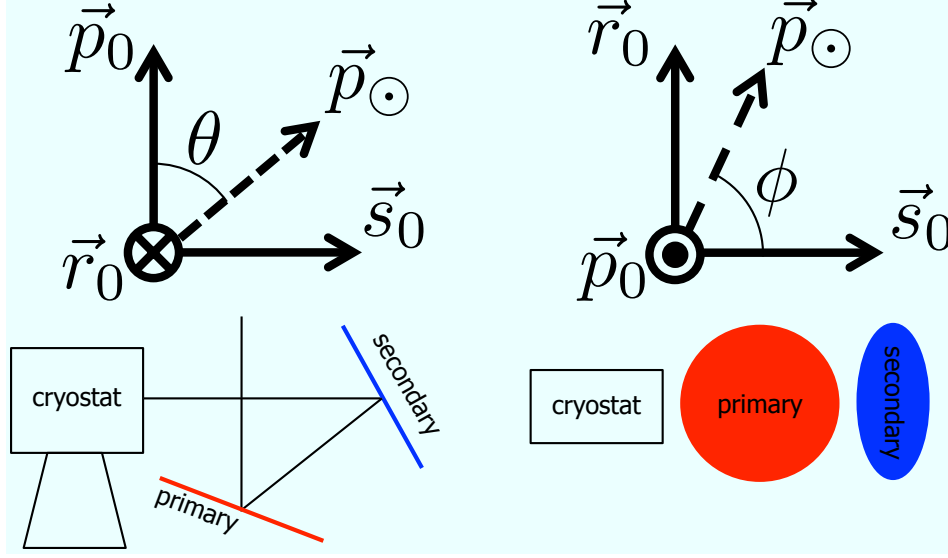


**Figure 6.3:** Schematic definition of the Sun-centered coordinate system. Left: side view of the coordinate system.  $\theta$  corresponds to angle between the Sun ( $\vec{p}_\odot$ ) and the telescope boresight ( $\vec{p}_0$ ). Right: top view of the coordinate system.  $\phi$  corresponds to orientation of the Sun ( $\vec{p}_\odot$ ) with respect to the direction of the telescope ( $\vec{s}_0$ ).

## 6.2.2 Estimation of the Sun Contamination Effect on the Maps and Power Spectra

We estimated the Sun contamination effect on power spectra. Since we have known both location and intensity of the Sun contamination from the Sun-centered maps, it is possible to pick up CES-diodes which have the contamination. Moreover, it is also possible to simulate the effect of the contamination for each CES-diode based on each Sun-centered maps and accumulate them.

Figure 6.5 shows the accumulated simulation maps with the Sun contamination for the patch CMB-2 and 3, which are most contaminated patches. Significant contaminations are found in the maps. Figure 6.6 shows power spectra based on them, which correspond to power spectra of the Sun contamination. We found significant bias as the same size as the statistical error at large angular scales. However, this bias is suppressed by a factor of a hundred because this comes from only 14% of the total CES-diodes and the

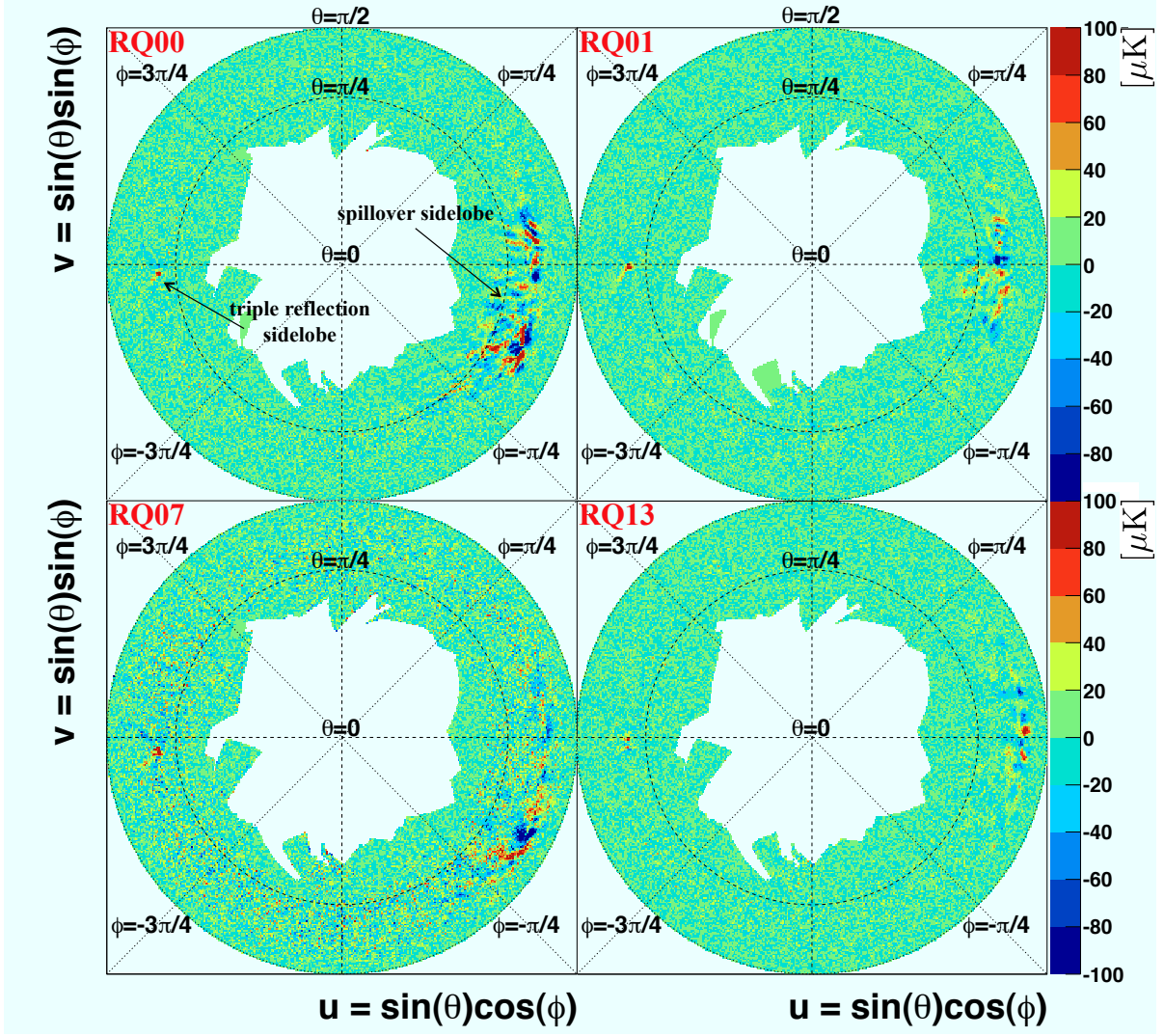


**Figure 6.4:** Polarized intensity maps of the far-sidelobes for certain modules (*RQ00*, *RQ01*, *RQ07* and *RQ13*, from the left top to bottom right). The maps are shown in the  $u$ - $v$  coordinate system defined as  $u = \sin \theta \cos \phi$  and  $v = \sin \theta \sin \phi$ . *RQ00* and *RQ01* are located at the bottom row of the array, *RQ07* is located at the middle row, and *RQ13* is located below *RQ07* (the second top row).  $\theta$  corresponds to an angle relative to the telescope boresight (see left figure on Figure 6.3), and  $\phi$  corresponds to direction angle with respect to the boresight ( $\phi = 0$  is the direction in front of the cryostat, see right figure on Figure 6.3). Here we only show  $0^\circ \leq \theta < 90^\circ$  (above the deck platform; no data in  $\theta < 30^\circ$  because of not pointing near the Sun). The spike at  $(\theta, \phi) \approx (50^\circ, 180^\circ)$  corresponds to the triple reflection sidelobe; the blobs around  $(\theta, \phi) \approx (60^\circ, 0^\circ)$  corresponds to the spillover sidelobe. These locations are consistent with those in the schematic picture of Figure 2.9. Moreover, the position of the spillover sidelobe highly depends on the feedhorn position. The  $\theta$  angle for the top feedhorns (*RQ13* in this figure) tends to be larger than that for the bottom (*RQ00* and *RQ01* in this figure), which is also consistent with Figure 2.9.

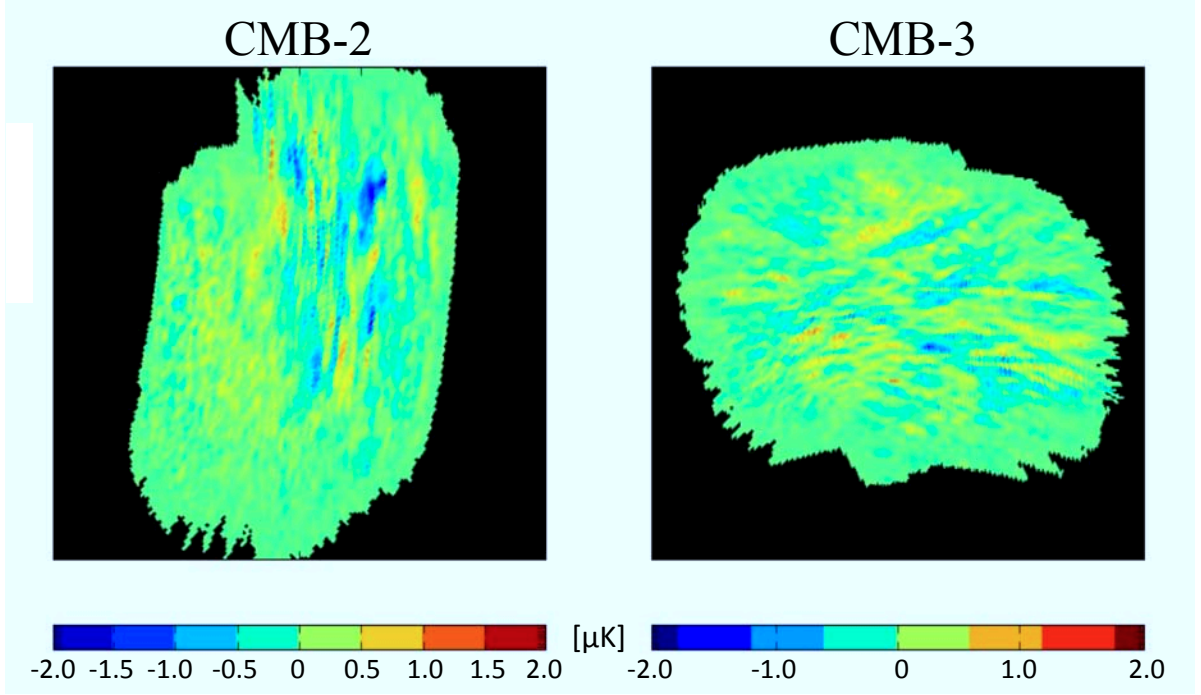


**Figure 6.5:** Simulated Sun contaminated maps (left: CMB-2, right: CMB-3) in the Galactic coordinates system. Blobs structure mainly comes from the spillover sidelobe. Spikes from the triple reflection sidelobe are averaged out although blobs from the spillover sidelobe are not because the blobs widely spread over large angular scales as shown in Figure 6.4.

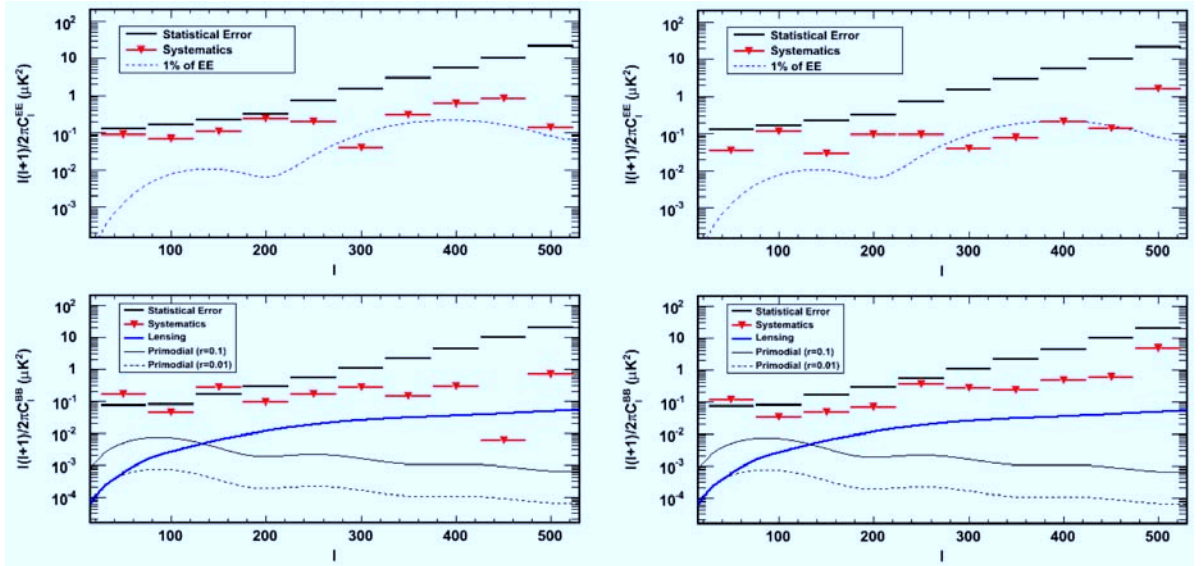


**Figure 6.6:** Power spectra of the simulated Sun contaminated maps as shown in Figure 6.5 (left: CMB-2, right: CMB-3; top:  $E$ -mode, bottom:  $B$ -mode). The amplitude at angular scale less than  $\ell = 200$  is equal with the statistical error ( $\approx 10^{-1} \mu\text{K}^2$ ) for each case. These are not negligible.

contamination will be diluted with the other CES-diodes which have no contamination<sup>b</sup>.

### 6.2.3 Removing the Sun Contamination

We confirmed that the Sun contamination effect on power spectra is small from the simulations; however, there is no guarantee that we perfectly understand the effect of the Sun contamination. Hence we conservatively dropped the CES-diodes which might have the Sun contamination. This selection results in controlling the systematic bias induced by the Sun contamination. The criteria were determined based on the Sun-centered maps for each module, by which we can determine which CES-module might see the Sun. About 3% point from the baseline dataset is rejected by this selection. Possible residuals after the removal are discussed in § 9.7.

## 6.3 Bad Weather Selection

Since we employed a series of constant elevation scans, the response of the total power detector is constant if atmospheric condition is stable. The large variation of the total power response indicate instability of atmospheric condition, and this corresponds to “bad weather”. The bad weather, i.e., fluctuation of atmosphere emission, does not create any polarization signals [73, 74] for perfect instruments. However, the bad weather causes the effects on the polarization response as follows:

- fluctuation of the spurious polarization due to the  $I \rightarrow Q/U$  leakage,
- fluctuation of the white noise level due to the sky temperature variation.

The total power data serve as an excellent weather monitor rather than the polarization ones do. We evaluated the total power RMS every 10 seconds, which is almost equal to the scan period. This RMS value is very sensitive to the structure on the sky synchronized with the scan.

---

<sup>b</sup>The suppression factor is inversely proportional to the squared number of the data because the Sun contamination effect comes from a signal.



## 6.4 Noise Model Validation

Since we assume that our detector noise is simply described as the  $1/f$  noise model (Equation (5.2)), disagreement between data and the model results in mis-estimation of maps and power spectrum. We checked three frequency ranges for the filtered data: a narrow range around the scan frequency (typically from 45 mHz to 100 mHz); a range from twice the scan frequency, which corresponds to the half-scan, to 1 Hz; a range from 1 Hz to 4.6 Hz, which is sensitive for the stability of the white noise level. The first two are sensitive for remaining scan synchronous signals due to pickup of the ground emissions as well as the white noise. We checked the  $1/f$  knee frequency and removed the individual CES-diodes which have unusual high knee frequency comparing with the mean distribution. The bad knee frequency could be related to the bad weather changing during a single CES.

We also checked outliers of the TOD in the time domain. We calculated glitch statistics every 0.02, 0.1, and 1 seconds, then the CES-diode which has outliers greater than  $6\text{-}\sigma$  is rejected.

## 6.5 Azimuth Slope Selection

Azimuth slope of the polarization response on the TOD for each scan which is given by the azimuth filter described in § 5.1.3.2 is also related to the bad weather and picking up the ground emissions due to the  $I \rightarrow Q/U$  leakage. The selection based on the azimuth slope helps to eliminate the residual contaminations which still remain after the azimuth filter and the bad weather selection. This is used as a complementary selection to bad weather compared with selection of the total power RMS.

## 6.6 Type-B Selection

We cut individual CES-diodes which have still non-linearity relation between the total power and demodulation data after the Type-B correction. This selection also rejects data which were bad thermal regulation of the electronics and cryostat as well as the Type-B failure. We show that any residual contamination is small enough to the statistical error

and much less than primordial  $B$ -mode signals of the tensor-to-scalar ratio at the level of  $r = 0.1$  in § 9.10.

## 6.7 Summary of the Data Selection

Table 6.7 shows our data selection and its efficiency among the CMB patches. Since we equally applied the data selection for each patch, their efficiencies are not uniform reflecting their own features—mostly variation of the atmospheric condition due to the time of the observation (daytime or night). The patch CMB-1 was mostly observed at the night, when the atmospheric condition tends to be stable; the patch CMB-3 was taken at the day, when the atmosphere tends to be unstable.

We have to decide how good the data selections work. The criteria of the data selections are determined by trials and errors of the null suites described in Chapter 7 before seeing the results themselves. We had repeated the null suites again and again by changing the configuration of the data selection criteria until the effect of the data selection was negligible and all the null-suites were passed.

Patch	Total			Uniquely Cut									
	Baseline	Accepted		Bad Weather	Noise Model	Azimuth Slopes	Sun Sidelobes	Type-B					
CMB-1	46,915	38,334	81.7%	1,550	3.3%	5,697	12.1%	2,266	4.8%	1,566	3.3%	1,342	2.9%
CMB-2	38,006	25,574	67.3%	4,216	11.1%	7,725	20.3%	4,644	12.2%	4,143	10.9%	1,746	4.6%
CMB-3	38,922	21,797	56.0%	8,294	21.3%	12,489	32.1%	10,425	26.8%	5,805	14.9%	3,355	8.6%
CMB-4	14,718	10,397	70.6%	1,760	12.0%	3,024	20.5%	2,806	19.1%	669	4.5%	638	4.3%
All Patches	138,561	96,102	69.4%	15,820	11.4%	28,935	20.9%	20,141	14.5%	12,183	8.8%	7,081	5.1%

**Table 6.1:** Summary of selection efficiencies in CES-diode units and percentage to the baseline. “Total” shows number of baseline CES-diodes, which only pass the overall cut, and that of accepted CES-diodes, which pass all the cuts. “Uniquely Cut” shows number of CES-diodes, which are cut by only each criterion but no others. The efficiencies among four patches are not uniform because of differences in the weather condition. The CMB-1 was mostly observed in the night, when the atmosphere tends to be stable; The CMB-3 was mostly observed in the day, when the atmosphere tends to be stable. Because of that, many CES-diodes in the CMB-3 are rejected by not only the weather-related cuts (bad weather, noise model, and azimuth slopes) but also the sun sidelobes cut.



# Chapter 7

## Analysis Validation

### 7.1 Overview

The data selection criteria and other analysis methods were finalized based on validation tests, which are described in this chapter. The purpose of data selection is controlling the hidden systematic biases related to the data quality as described in Chapter 6. We need a way to evaluate possible biases in our dataset. The null suite frameworks provide the way to us.

One of the most important things in those frameworks is that we never reveal the non-null power spectra themselves during the analysis in order to avoid the experimenter bias [100]. Another important thing is that only the pseudo- $C_\ell$  technique described in § 5.3.1 can realize the null suites completely because this technique is computationally efficient. On the other hand, the maximum likelihood (ML) technique is too computationally expensive to complete the null suites.

In the QUIET analysis, we performed two validation tests: one is null test, and the other is blind comparison. We discuss a null-test analysis in § 7.2, a blind analysis is explained in § 7.3. After that, we summarize the final results of the null suites.

## 7.2 Null Tests—Estimating Hidden Biases with Null Power Spectra

The whole data are split into two datasets by certain criterion—for example, good weather vs. bad weather, telescope pointing high elevation vs. low elevation, and so on (see below); then two maps ( $m_0$  and  $m_1$ ) are made from each dataset. We make a difference map,  $m_{\text{diff}} = (m_0 - m_1)/2$ , then calculate power spectra,  $C_\ell^{\text{null}}(m_{\text{diff}})$ , from the  $m_{\text{diff}}$  for a flavor of  $EE, BB, EB$ . The amplitude of the power spectra should be zero (“null”) within their statistic errors because the CMB signal is common and the noise is independent in the two maps<sup>a</sup>. In the case that the difference map has a systematic bias, we obtain non-null power spectra. The “null tests”, in which we check whether the power spectrum from the various datasets is null or not, are the way to estimate the hidden bias.

We have 42 null tests. The criteria to divide the data are chosen to be sensitive for various contaminations as the followings:

- A) **Ten tests** divide the data by the telescope pointing and the array orientation. These tests target undesirable effects due to different configuration of the pointing and array.
- B) **Ten tests** divide the data by environment conditions such as humidity, ambient temperature, and these seasonal trend. These tests target possible effects due to changing surrounding conditions and season variation.
- C) **Nine tests** divide the data by the combination of the modules and diodes such as module position on the array and shared electronics. These tests target artifact effect of the electronics and instrumental polarization due to the combination of these modules and diodes.
- D) **Eight tests** divide the data by properties and results of the TOD processing. These tests target possible residuals of the TOD filtering and data selection.

---

<sup>a</sup> The simple difference map,  $m_{\text{diff}}$ , does not provide “perfect” null spectrum except the ideal case because of the filtering effect for each dataset. We have to consider differences among the divided datasets: noise maps, transfer functions, and cross-linking effect. More details are found in Appendix F.

**E) Five tests** divide the data by the distance from the telescope boresight or far-sidelobes to bright sources such as the Sun, Moon, and the Galactic plane. These tests target contaminations from not only the main beam but also the two far-sidelobes.

The details of the criteria are listed in Table 7.1. Although we had more null tests at the first stage of the null suites, we dropped some tests because they were not independent of the others well. The null tests described above are almost independent with each other. The data using in different null tests are correlated with only 8.8% on average.

We obtain  $EE$ ,  $BB$ , and  $EB$  power spectra from each null test; however, we only use  $EE$  and  $BB$  because the  $EB$  power spectrum is null in the first place even though not taking difference of the maps. However, we also evaluate the  $EB$  power for consistency because the failure in the  $EE$  and  $BB$  power also leads to that in  $EB$  power. As described in Chapter 5.3.1, we have nine points from a binned bandpower spectrum per one flavor. From 42 (41) null tests and four CMB patches<sup>b</sup>, 3,006 null power spectrum points<sup>c</sup> are obtained. Figure 7.1 shows an example of the null power spectra of certain test for the patch CMB-1.

For each spectrum point ( $C_b^{\text{null}}$ ) of null-bandpower, we define the statistics of  $\chi_{\text{null}}^2 \equiv (C_b^{\text{null}}/\sigma_b)^2$ , where  $\sigma_b$  is the standard deviation of  $C_b^{\text{null}}$  from the MC simulations. This  $\chi_{\text{null}}^2$  statistic is NOT completely distributed according to the  $\chi^2$  distribution because each spectrum point is a little bit correlated and slightly non-Gaussian due to the small number of modes at low  $\ell$ . We run MC simulations of whole the null tests to take into account these effects. We also evaluate the statistics of  $\chi_{\text{null}} \equiv C_b^{\text{null}}/\sigma_b$ . This is NOT the  $\chi^2$  statistics BUT the  $\chi$  statistics. Both  $\chi_{\text{null}}^2$  and  $\chi_{\text{null}}$  statistics are sensitive to systematics bias in the null spectra. On one hand, the  $\chi_{\text{null}}^2$  statistic is more responsive to outliers; on the other hand, the  $\chi_{\text{null}}$  statistic is more sensitive to small bias.

Figure 7.2 provides the distribution of the Probability To Exceed (PTE)<sup>d</sup> calculated

---

<sup>b</sup>The patch CMB-4 has only 41 null tests. because one null test can not work because there is no enough data for this test.

<sup>c</sup>  $3^{\text{patches}} \times 9^{\text{binned } C_\ell} \times 2^{EE, BB} \times 42^{\text{null tests}} + 1 \times 9 \times 2 \times 41$

<sup>d</sup>The PTE is defined as

$$p(\chi_{\text{null}}^2) = \int_{\chi_{\text{null}}^2}^{\infty} f(z) dz \quad (7.1)$$

where  $f(z)$  is the  $\chi_{\text{null}}^2$  distribution from MC simulations.

	CES with the patch rising vs. setting.
	Three divisions of CES by deck angle.
A)	Three divisions of CES by parallactic angle.
	Data from left- vs. right-going telescope scan motion.
	Data from accelerating vs. decelerating telescope scan motion.
	Division of CES with high vs. low ambient humidity.
	Division of CES with large vs. small humidity changing.
	Division of CES with high vs. low bias electronics temperature.
	Division of CES with large vs. small bias electronics temperature changing.
B)	Division of CES with fast vs. slow electronics temperature changing.
	Division of CES with high vs. low cryostat temperature.
	Division of CES with large vs. small cryostat temperature changing.
	The first half of the season vs. the second half of the season.
	Division of CES based on whether the scan period is an integral multiple of the cryostat cold head pumping period.
	The central seven modules vs. the peripheral modules.
	Modules with high vs. low $I \rightarrow Q/U$ leakage.
	Modules with high vs. low averaged $1/f$ noise knee frequency.
C)	Modules with high vs. low bandpass center frequency.
	$Q$ vs $U$ diodes.
	Diodes whose total power sometimes shifts abruptly vs. diodes not having such shifts.
	CES-diodes with more vs. less excess noise power at high frequencies (2–15 Hz).
	Division of CES by averaged responsivity (high vs. low).
	Division of CES-diodes by responsivity of each diode compared to its average.
D)	Division by CES-diodes with high vs. low Type-B glitch of double-demodulated data.
	Two divisions by weather quality based on total power RMS statistics every 10 sec.
	CES-diodes with high vs. low white noise levels.
	Moon proximity to the main beam.
E)	Far-sidelobe elevation high vs. low.
	Two Divisions based on proximity of the two far-sidelobes to the Galaxy.

**Table 7.1:** List of 42 null tests.



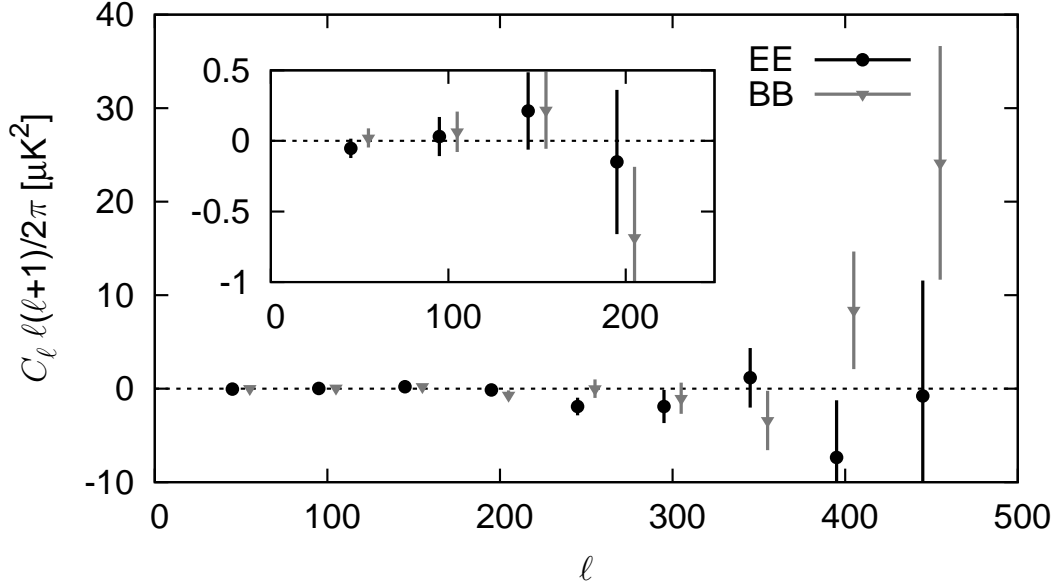


**Figure 7.1:**  $EE$  and  $BB$  null power spectra from the null test of  $Q$  vs.  $U$  diodes for the patch CMB-1.

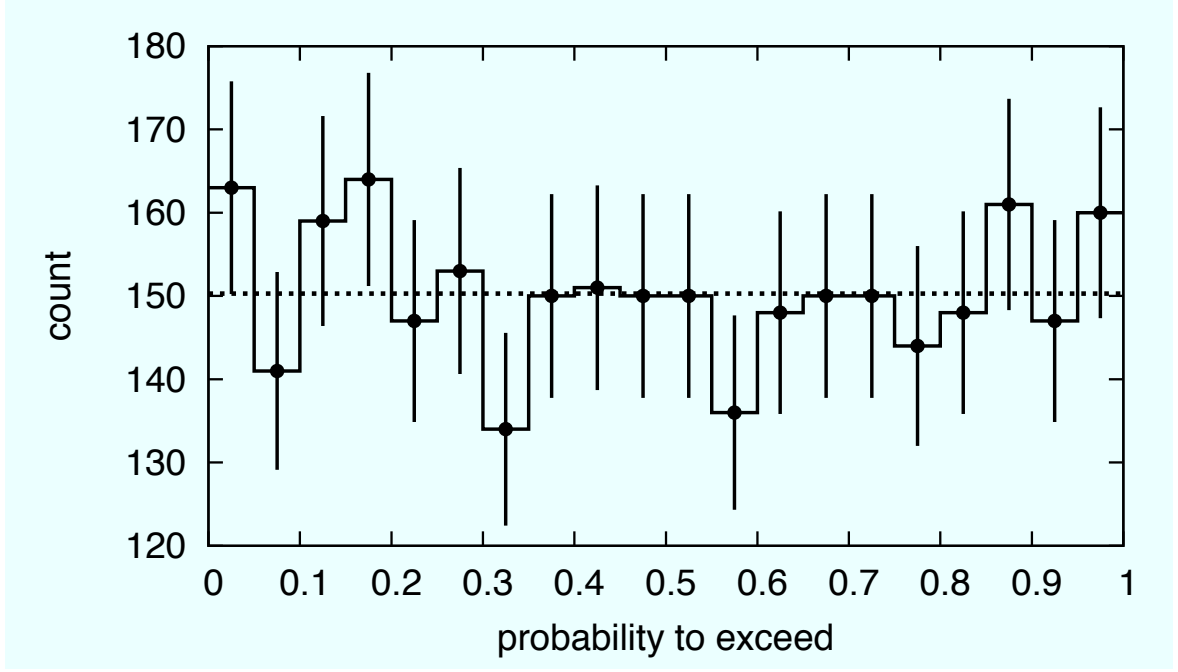
from the  $\chi^2_{\text{null}}$  statistics compared with the MC simulations of 1024 realizations. The distribution is uniform within their error bars as expected. The  $\chi^2_{\text{null}}$  statistics are summed over all the bins and all the null tests and the number of  $\chi^2_{\text{null}}$  samples is 756 (738)<sup>e</sup> for the patch CMB-1,2,3 (4), respectively. The PTEs in each patch division are 44% for CMB-1; 19% for CMB-2; 16% for CMB-3; 68% for CMB-4. These results are statistically reasonable. Moreover we checked various sample divisions summed up over all the null tests for each  $\ell$  bin (summing 42 (41) samples, and getting 9 individuals for  $EE$  and/or  $BB$ ); over all the  $\ell$  bins for each null test (summing 9 samples, and getting 41 (42) individuals for  $EE$  and/or  $BB$ ); and not sum up (getting 378 (369) individuals for  $EE$  and/or  $BB$ ). We confirmed no anomaly among them.

Figure 7.3 shows the distribution of the  $\chi_{\text{null}}$  statistics compared with the MC simulations. The  $\chi_{\text{null}}$  distribution is consistent with the simulations as expected.

On the middle stage of the null suites, we found an obvious positive bias of the  $\chi_{\text{null}}$  distribution. Although on the final stage, including auto-correlations in power spectrum estimation, we found a positive  $\chi_{\text{null}}$  shift of 21%. Dropping auto-correlations and taking

---

<sup>e</sup>ginned  $C_\ell \times 2^{EE, BB} \times 42(41)^{\text{null tests}}$ . If the  $\chi^2_{\text{null}}$  distribute according to the  $\chi^2$  statistics, these numbers in the text represent degrees of freedom.



**Figure 7.2:** The PTE distribution calculated from the  $\chi_{\text{null}}^2$  statistics compared with the MC simulations of 1024 realizations. The distribution is uniform within their error bars as expected.

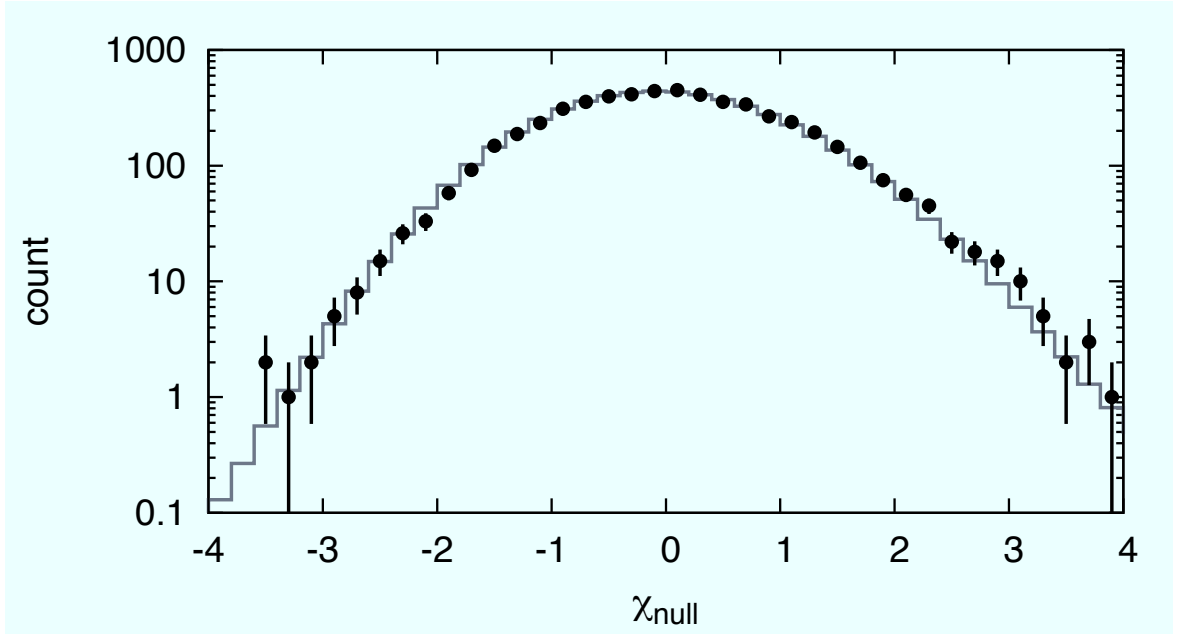


**Figure 7.3:** Histogram of the  $\chi_{\text{null}}$  statistics (black circles) and the average of 1024 MC realizations (gray histogram). Both the data and MC distributions imply similar non-Gaussianity as expected.

only cross-correlations from day-by-day datasets, the shift decreased to 10%, but there was still positive bias. After repeating trials and errors, we found that the bias became zero when we separated the data by the pointing divisions (azimuth and deck angle divisions) as described in § 5.3.2 and took only cross-correlations among them.

Our study and result imply that not only the  $\chi^2_{\text{null}}$  statistics but also the  $\chi_{\text{null}}$  statistics are useful to eliminate unknown contaminations and biases. In our analysis, if we only used the  $\chi^2_{\text{null}}$  statistics, we had not been able to find the contamination due to taking day-by-day cross-correlations. Another important thing is that the power spectrum estimator taking only cross-correlations can exclude unknown contamination. For this reason, the pseudo- $C_\ell$  estimator with taking cross-correlations is superior to the ML technique for unknown contamination and bias as well as computational cost.

One possibility of the unknown contamination is residual ground pickup due to the far-sidelobes (§ 2.3). Since the pointing of the far-sidelobes depends on not only the azimuth direction but also the deck angle, we can eliminate the contamination by taking cross-correlations among the azimuth and deck divisions.

### 7.3 Consistency Among Different Configurations

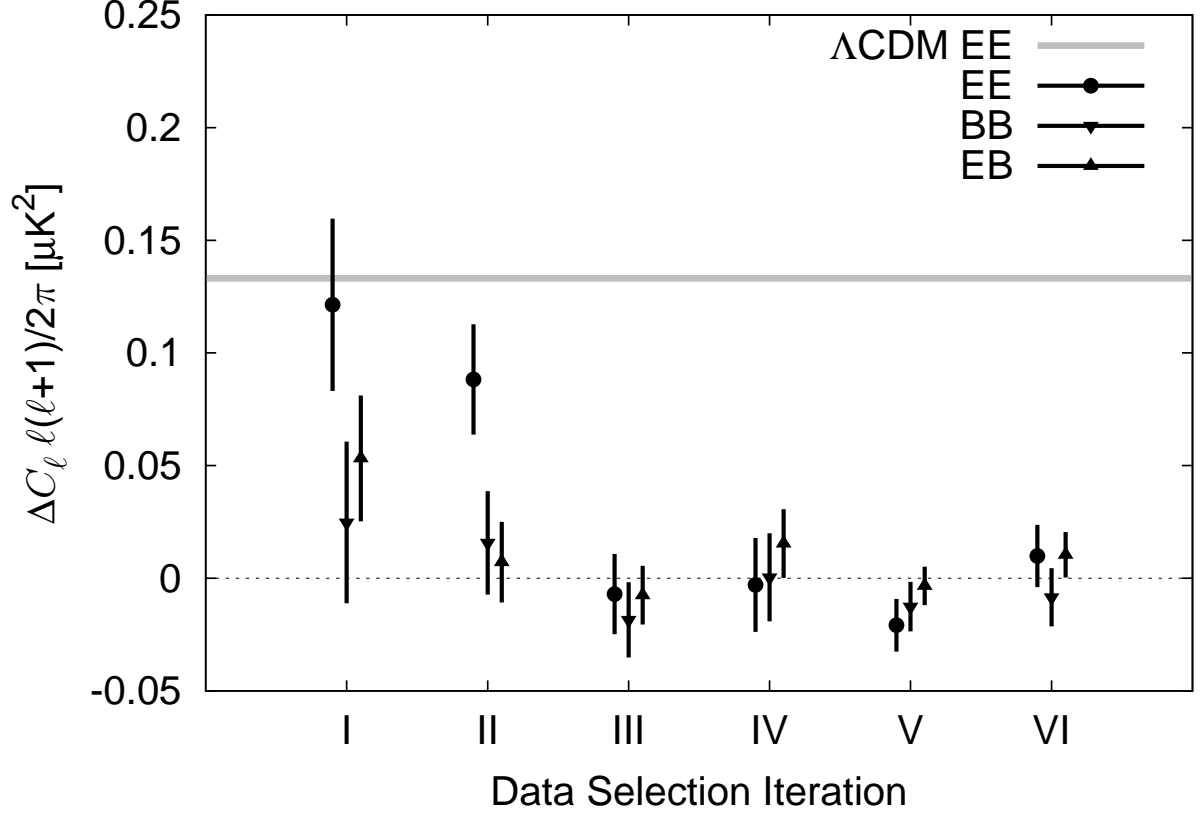
We calculated the difference of the power spectra between any two iterations of the null-suites. Significant power spectrum differences among different stage of the null suites, which have different selection configurations, imply improvement or retreat for bias managements. When taking the difference of the power spectra, we not only NEVER SEE the non-null power but also RANDOMLY FLIP the sign of the difference so that we NEVER KNOW the direction of the difference. If we know the direction of the difference, this could introduce experimenter bias easily. This blind comparison can eliminate these bias effectively. The iteration of the data selection would had ended when further iterations only resulted in statistically expected fluctuations.

Figure 7.4 shows power spectrum difference between the final dataset and the earlier dataset. The difference decreased with increment of the iterations, and the latter half of the iterations were consistent with the statistical fluctuation which is expected from the dataset difference due to changing the selection criteria. We can learn two important

things from this plot:

- (a) the iteration based on the null tests eliminated the huge bias as much as the  $\Lambda$ CDM prediction of  $EE$  power at  $25 \leq \ell \leq 75$ .
- (b) the null tests significantly detected the smaller bias than the statistical fluctuation due to changing the selection criteria.

These are evidence that the null test is a powerful framework to detect hidden bias and improve the analysis procedure before seeing the results.



**Figure 7.4:** Power spectrum difference between the final dataset and six datasets of the iterations before the final one, whose number is ordered by date. Data points come from the lowest  $\ell$  bin ( $25 \leq \ell \leq 75$ ) from the patch CMB-1. The statistical error with final dataset is about  $0.10 \mu K^2$  for the  $B$ -mode. The error bar which is expected fluctuations due to changing a dataset is much smaller than the statistical one, especially the latter iterations. As the iterations advance toward the end (I→VI), both the difference and fluctuation are smaller. Vertical solid line corresponds to the non-null  $\Lambda$ CDM prediction for the  $E$ -mode. This figure also shows the first stage of the null tests (I) is very “bad” because the  $E$ -mode power of the null map is NOT null, which is as almost the same power as that of the  $\Lambda$ CDM prediction. On the other hand, the latter stages of the null tests (III–VI) are “good”.



# Chapter 8

## Results

We finally obtain the CMB polarization angular power spectra from the QUIET Q-band measurements. We summarize our power spectra and evaluate the tensor-to-scalar ratio from the results in this chapter. We also discuss the detection of foreground emissions.

### 8.1 Power Spectra ( $C_\ell^{EE}$ , $C_\ell^{BB}$ , and $C_\ell^{EB}$ )

Figure 8.1, 8.2, and Table 8.1 show our  $EE$ ,  $BB$ , and  $EB$  power spectra, respectively, and the  $EE$  power spectrum of the fiducial  $\Lambda$ CDM cosmology, which comes from the best fit model of the seven-year *WMAP* [30]. We show only the statistical errors in this chapter; systematic errors are discussed in Chapter 9.

Using only one free parameter ( $q$ ) to the  $EE$  power spectrum, we model our results

$$C_b^{EE}(q) = qC_b^{EE,\text{fiducial}}, \quad (8.1)$$

then maximize the likelihood function defined as

$$\mathcal{L}(q) \propto \frac{-\mathbf{d}^T(q)\mathbf{C}^{-1}(q)\mathbf{d}(q)/2}{\sqrt{|\mathbf{C}(q)|}}, \quad (8.2)$$

where  $\mathbf{d}(q)$  denotes the difference between our results and the models, and  $\mathbf{C}(q)$  denotes the covariance matrix of  $\mathbf{d}(q)$  not involved with the systematic errors because they are small enough to ignore. One-dimensional brute-force likelihood maximization was performed, which is not limited by computational resource in our case. We found  $q = 0.87 \pm 0.10$  (Figure 8.3). The  $\chi^2$  value comparing with the fiducial  $\Lambda$ CDM model

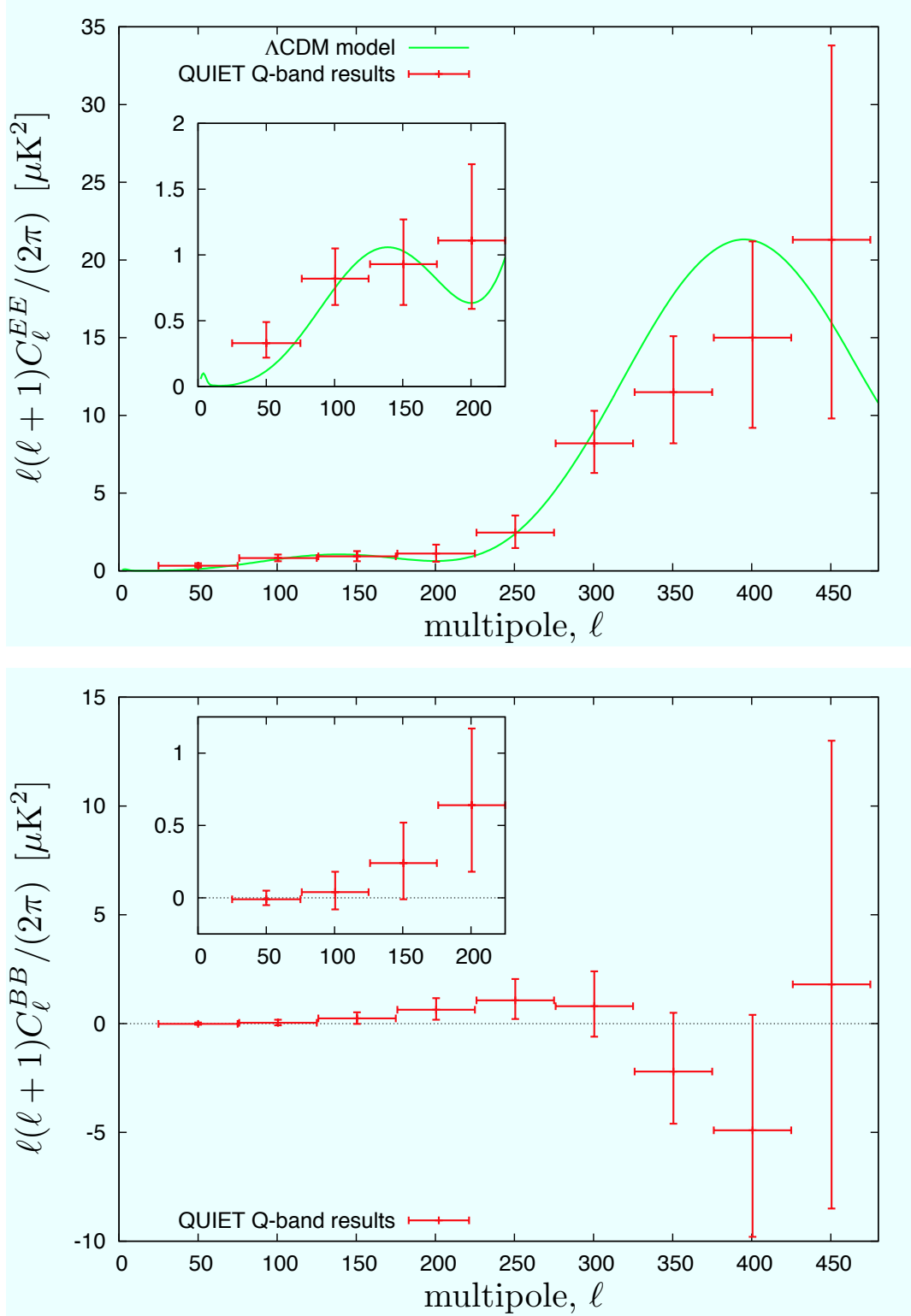


**Figure 8.1:**  $EE$ ,  $BB$  power spectra from QUIET Q-band measurements, in which all the four patches are combined with the likelihood model based on [97] as explained in Chapter 5.3.2. The error is assigned as frequentest 68% confidence intervals. The  $EE$  power at the lowest  $\ell$  bin contains the Galactic synchrotron emission from the patch CMB-1 (§ 8.2).



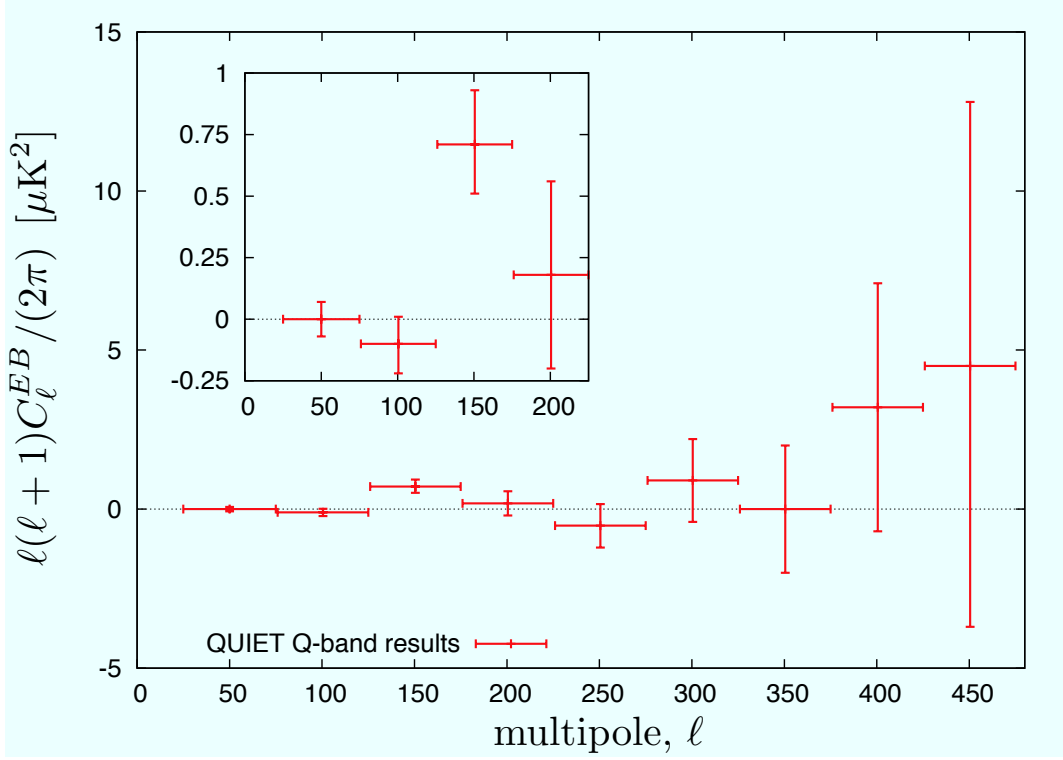


**Figure 8.2:**  $EB$  power spectrum from QUIET Q-band measurements as same as Figure 8.1.

multipole			$\mathcal{C}_b \equiv \ell(\ell+1)C_\ell^{XX}/(2\pi) \mu\text{K}^2$		
$b$	$\ell_{\min}$	$\ell_{\max}$	$EE$	$BB$	$EB$
1	25	75	$^{\dagger}0.33^{+0.16}_{-0.11}$	$-0.01^{+0.06}_{-0.04}$	$0.00^{+0.07}_{-0.07}$
2	76	125	$0.82^{+0.23}_{-0.20}$	$0.04^{+0.14}_{-0.12}$	$-0.10^{+0.11}_{-0.12}$
3	126	175	$0.93^{+0.34}_{-0.31}$	$0.24^{+0.28}_{-0.25}$	$0.71^{+0.22}_{-0.20}$
4	176	225	$1.11^{+0.58}_{-0.52}$	$0.64^{+0.53}_{-0.46}$	$0.18^{+0.38}_{-0.38}$
5	226	275	$2.46^{+1.10}_{-0.99}$	$1.07^{+0.98}_{-0.86}$	$-0.52^{+0.68}_{-0.69}$
6	276	325	$8.2^{+2.1}_{-1.9}$	$0.8^{+1.6}_{-1.4}$	$0.9^{+1.3}_{-1.3}$
7	326	375	$11.5^{+3.6}_{-3.3}$	$-2.2^{+2.7}_{-2.4}$	$0.0^{+2.0}_{-2.0}$
8	376	425	$15.0^{+6.2}_{-5.8}$	$-4.9^{+5.3}_{-4.9}$	$3.2^{+3.9}_{-3.9}$
9	426	475	$21^{+13}_{-11}$	$2^{+11}_{-10}$	$4.5^{+8.3}_{-8.2}$

**Table 8.1:** Band-combined CMB power spectra from the QUIET Q-band measurements. Note ( $\dagger$ ) that the  $EE$  power spectrum of the patch CMB-1 at the lowest  $\ell$  bin ( $b = 1$ ;  $25 \leq \ell \leq 75$ ) is significantly contaminated by the foreground as discussed in the text.

with an assumption of  $C_\ell^{BB} = C_\ell^{EB} = 0$  is 31.6 with 24 degrees of freedom, which leads to a PTE of 14%. All the statistics provide that our results are consistent with the fiducial cosmology.

We detected the  $E$ -mode power with more than  $10\text{-}\sigma$  significance by the likelihood functions ([97], as shown in § 5.3.2). At large angular scales of  $76 \leq \ell \leq 175$ , we detected the  $E$ -mode power with more than  $6\text{-}\sigma$  significance. QUIET and BICEP are only experiments to detect the  $E$ -mode signals at those large angular scales. The important thing is that they consistently detected at different frequencies: QUIET detected at 43 GHz, on the other hand, BICEP detected at 100 GHz and 150 GHz.

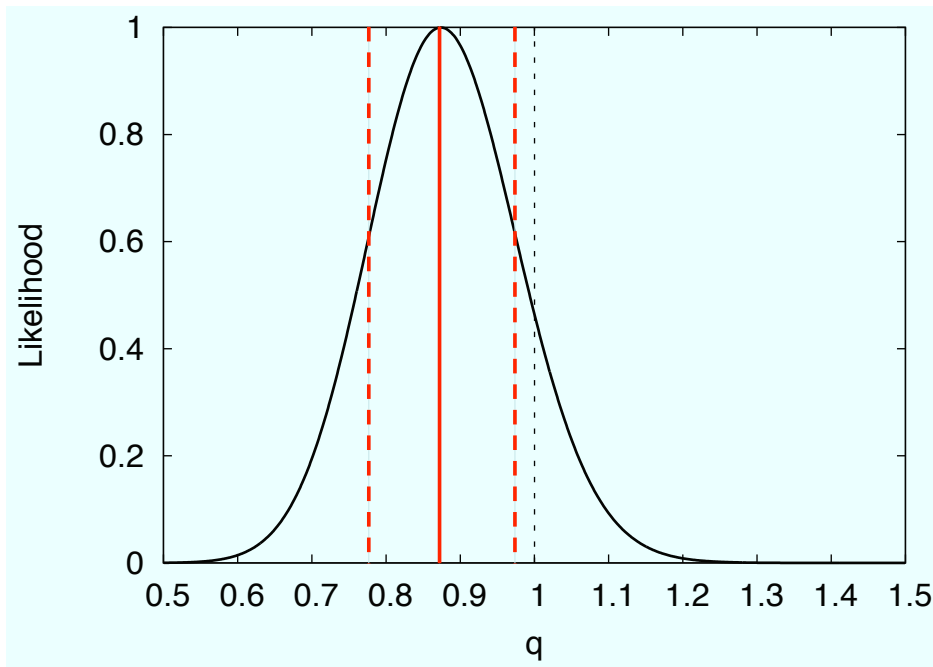


**Figure 8.3:** Likelihood curve as a function of  $q$  as defined in Equation (8.1). Red-solid line corresponds to  $q = 0.87$ , and red-dashed lines correspond to two-sided 68% confidence intervals. Black-dashed line corresponds to  $q = 1$ .

## 8.2 Foreground

Foreground emission should be removed from the B-mode. We choose the four CMB patches which have the lowest contamination of synchrotron emission, which is a dominant foreground source at lower frequencies less than 90 GHz. In our frequency, thermal

dust emission is negligible because of its frequency dependence as shown in Figure 1.13. Spinning dust emission, which is a possible foreground source, is also negligible because the polarization fraction of the spinning dust should be no more than a few percent in our frequency [101, 102, 103, 104]. Thereby our possible foreground sources are compact radio sources and the Galactic diffuse synchrotron emission.

### 8.2.1 Compact Radio Sources

When we calculated power spectra as described in § 5.3.1, we masked compact radio sources (54 sources) in the patches. In order to check the impact of that mask and possible residual, we calculated power spectra both with and without the mask based on the *WMAP* temperature compact radio source catalog [105]. We found there is no significant difference between with and without the mask. This provides that the possible contamination from the compact radio sources which were detected by the *WMAP* to CMB power spectra is much small. We concluded that our results with the mask is conservative for the contamination on the compact radio sources.

### 8.2.2 Galactic Diffuse Synchrotron

Since the Galactic diffuse synchrotron emission is highly polarized, we have to manage it exactly. We found the significant excess power of the *E*-mode at the lowest  $\ell$  bin ( $b = 1$ ;  $25 \leq \ell \leq 75$ ) for the patch CMB-1 (Figure 8.4). The value is  $0.55 \pm 0.14 \mu\text{K}^2$ , which corresponds to a  $3\text{-}\sigma$  outlier relative to the fiducial  $\Lambda\text{CDM}$  prediction of  $0.13 \mu\text{K}^2$ . Sample variance as predicted by the  $\Lambda\text{CDM}$  is included here. Table 8.2 shows that the *E*-mode power spectra at the lowest  $\ell$  bin based on the QUIET Q-band (43 GHz) data and the seven-year *WMAP* K-band (23 GHz) data. In our calculation,

- $\mathcal{C}_{b=1}^{\text{QQ}}$  is evaluated using the QUIET Q-band data ( $\tilde{a}_{\ell m}^{\text{Q}}$ ),
- $\mathcal{C}_{b=1}^{\text{KK}}$  is evaluated using the seven-year *WMAP* K-band data ( $\tilde{a}_{\ell m}^{\text{K}}$ ),
- $\mathcal{C}_{b=1}^{\text{QK}}$  is evaluated taking cross-correlations between the QUIET and *WMAP* data.

From those results, we also found significant excess power for  $\mathcal{C}_b^{\text{KK}}$  and  $\mathcal{C}_b^{\text{QK}}$  as well as  $\mathcal{C}_b^{\text{QQ}}$ . To evaluate the the *WMAP* K-band contamination in the patch CMB-1, we processed the

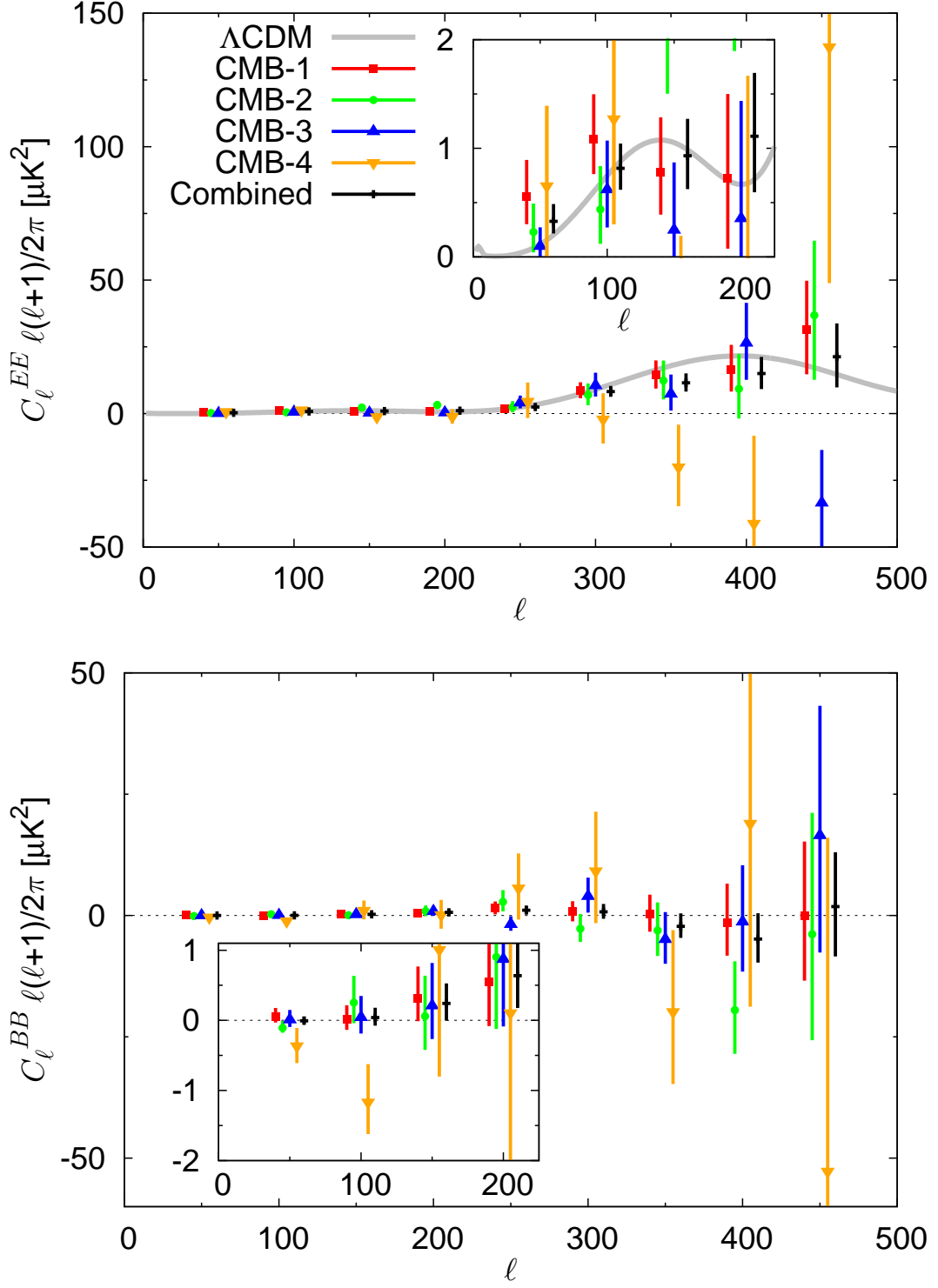


**Figure 8.4:** Power spectra (top:  $E$ -mode, bottom:  $B$ -mode) from the QUIET Q-band measurements for each patch individually. The differences of each error bar among the patches come from the amounts of the observation time for each patch. The CMB-1  $E$ -mode power for the lowest  $\ell$  bin is significantly away from the  $\Lambda$ CDM prediction.

Patch	Flavor	$\mathcal{C}_{b=1}^{\text{KK}}$	$\mathcal{C}_{b=1}^{\text{QK}}$	$\mathcal{C}_{b=1}^{\text{QQ}}$
CMB-1	$EE$	<b><math>17.4 \pm 4.7</math></b>	<b><math>3.30 \pm 0.55</math></b>	<b><math>0.55 \pm 0.14</math></b>
	$BB$	$4.8 \pm 4.5$	$0.40 \pm 0.41$	$0.06 \pm 0.08$
	$EB$	$-6.2 \pm 3.2$	$0.27 \pm 0.38$	$0.10 \pm 0.08$
CMB-2	$EE$	$5.5 \pm 3.7$	$0.01 \pm 0.56$	$0.23 \pm 0.19$
	$BB$	$4.6 \pm 3.4$	$0.18 \pm 0.48$	$-0.11 \pm 0.13$
	$EB$	$-5.5 \pm 2.8$	$-0.39 \pm 0.41$	$-0.20 \pm 0.12$
CMB-3	$EE$	$0.2 \pm 1.9$	$0.64 \pm 0.43$	$0.10 \pm 0.18$
	$BB$	$-0.3 \pm 2.6$	$0.33 \pm 0.35$	$0.01 \pm 0.13$
	$EB$	$1.4 \pm 1.7$	$-0.34 \pm 0.30$	<b><math>-0.27 \pm 0.11</math></b>
CMB-4	$EE$	$-5.2 \pm 5.1$	$0.7 \pm 1.2$	$0.65 \pm 0.58$
	$BB$	$-2.6 \pm 5.2$	$-0.1 \pm 1.1$	$-0.37 \pm 0.52$
	$EB$	$-1.0 \pm 3.9$	$0.0 \pm 0.9$	$-0.15 \pm 0.47$

**Table 8.2:** Power spectra for the first  $\ell$  bin ( $b = 1$ ;  $25 \leq \ell \leq 75$ ) for each patch using the QUIET Q-band data and the seven-year *WMAP* data in  $\mathcal{C}_\ell^{XX} = \ell(\ell+1)C_b^{XX}/(2\pi) \mu\text{K}^2$  units in thermodynamic temperature. The superscript Q and K of  $\mathcal{C}_{b=1}^{XX}$  represents the QUIET Q-band data and the seven-year *WMAP* K-band data, respectively. The errors for  $\mathcal{C}_{b=1}^{\text{KK}}$  and  $\mathcal{C}_{b=1}^{\text{QK}}$  only include the noise. For only  $\mathcal{C}_{b=1}^{\text{QQ}}$ , they additionally include CMB sample variance as predicted by the  $\Lambda\text{CDM}$  model. The values in bold are more than  $2\text{-}\sigma$  away from zero.

*WMAP* K-band map with our analysis framework. Since we included contributions of the instrumental noises, the uncertainties for  $\mathcal{C}_b^{\text{KK}}$  and  $\mathcal{C}_b^{\text{QK}}$  are given by only the instrumental noises because foreground signals do not contribute to the sample variance.

The frequency dependence of diffuse synchrotron emission also supports our results. Diffuse synchrotron intensity (and polarization) in radio frequency ( $\nu < 100$  GHz) decreases as a function of frequency with a power-law model described as

$$S(\nu) = S(\nu_0) \left( \frac{\nu}{\nu_0} \right)^{\beta_s}, \quad (8.3)$$

where  $\beta_s$  is a spectral index of synchrotron emission of  $\beta_s = -3.1$  [106]. Using this relation, we estimated power spectra at the frequency of the QUIET Q-band from the *WMAP* K-band as follows:

$$\begin{aligned} \frac{1.05}{1.01} \left( \frac{43.1}{23} \right)^{\beta_s} \mathcal{C}_{b=1}^{\text{KK}} &= 2.57 \pm 0.69 \mu\text{K}^2 \quad \leftrightarrow \quad \mathcal{C}_{b=1}^{\text{QK}} = 3.30 \pm 0.55 \mu\text{K}^2, \\ \left\{ \frac{1.05}{1.01} \left( \frac{43.1}{23} \right)^{\beta_s} \right\}^2 \mathcal{C}_{b=1}^{\text{KK}} &= 0.38 \pm 0.10 \mu\text{K}^2 \quad \leftrightarrow \quad \mathcal{C}_{b=1}^{\text{QQ}} = 0.55 \pm 0.14 \mu\text{K}^2, \end{aligned} \quad (8.4)$$

where coefficients of 1.05 and 1.01 come from the antenna-to-thermodynamic correction relative to the CMB temperature because Equation (8.3) is defined in antenna temperature units. The predictions from the *WMAP* K-band results (left side of Equation (8.4)) are well consistent with the observed values (right side). Figure 8.5 shows the consistency and also implies that synchrotron contamination would be free down to the level of  $r = 0.05$  at the W-band frequency (95 GHz). Since we only detected the foreground *E*-mode, the amplitude of the *B*-mode foreground might be smaller than that of the *E*-mode. Difference of foreground detection between the *E*-mode and *B*-mode might result from the geometry of the synchrotron emission in the patch.

For those two reasons, we concluded the excess power at the lowest  $\ell$  bin in the patch CMB-1 comes from diffuse synchrotron emission.

### 8.3 Primordial Gravitational Waves

The tensor-to-scalar ratio ( $r$ ) is obtained using our results of the *BB* power spectrum at large angular scale, which corresponds to multipole range  $25 \leq \ell \leq 175$  around the first

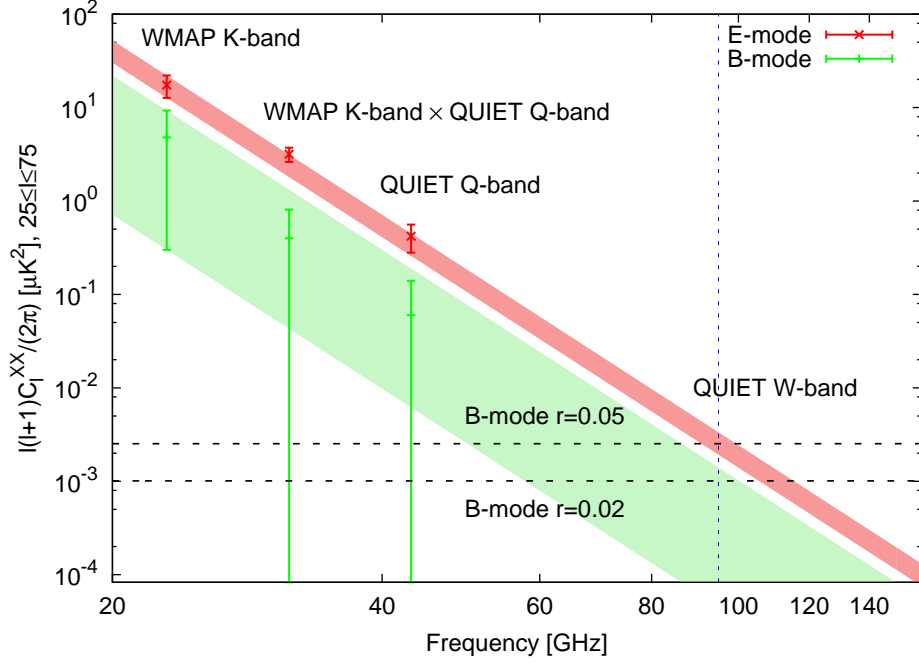


**Figure 8.5:** Variations of the  $E$  (red markers) and  $B$  (green ones)-mode power spectra at the first  $\ell$  bin from the *WMAP* K-band data and QUIET Q-band data for the patch CMB-1 as a function of frequency. Red and green bands represent the  $E$ - and  $B$ -mode prediction of diffuse synchrotron emission from the *WMAP* K-band results with an assumption of  $\beta_s = -3.1$ , which is consistent with our results. For this result, we would have synchrotron contamination at the level of  $r = 0.05$  at the W-band frequency (vertical dashed blue line, 95 GHz), which is the foreground minimum band.

peak of the  $BB$  power spectrum<sup>a</sup>. Here we defined  $r$  as the ratio of the primordial-tensor-perturbation power spectrum to the scalar-perturbation power spectrum as defined by Equation (1.18) at a scale of  $k_{\text{pivot}} = 0.002 \text{ Mpc}^{-1}$  as same as BICEP defined. We fitted our results to a  $BB$  power spectrum template given by the fiducial  $\Lambda\text{CDM}$  model with only changing  $r$  with an assumption of the tensor index  $n_t = 0$  for simplicity as discussed in § 1.3.1. We note again that the  $B$ -mode power spectrum is simply proportional to  $r$  with this assumption. As same as obtaining the free amplitude of the  $E$ -mode ( $q$ ) in § 8.1, we modeled the  $B$ -mode power described as

$$C_b^{BB}(r) = \frac{r}{r_{\text{fiducial}}} C_b^{BB, \text{fiducial}}, \quad (8.5)$$

then maximize the likelihood function for the tensor-to-scalar ratio,  $r$ . We found  $r = 0.35^{+1.06}_{-0.87}$ , which also leads to  $r < 2.2$  at 95% confidence interval (Figure 8.6).

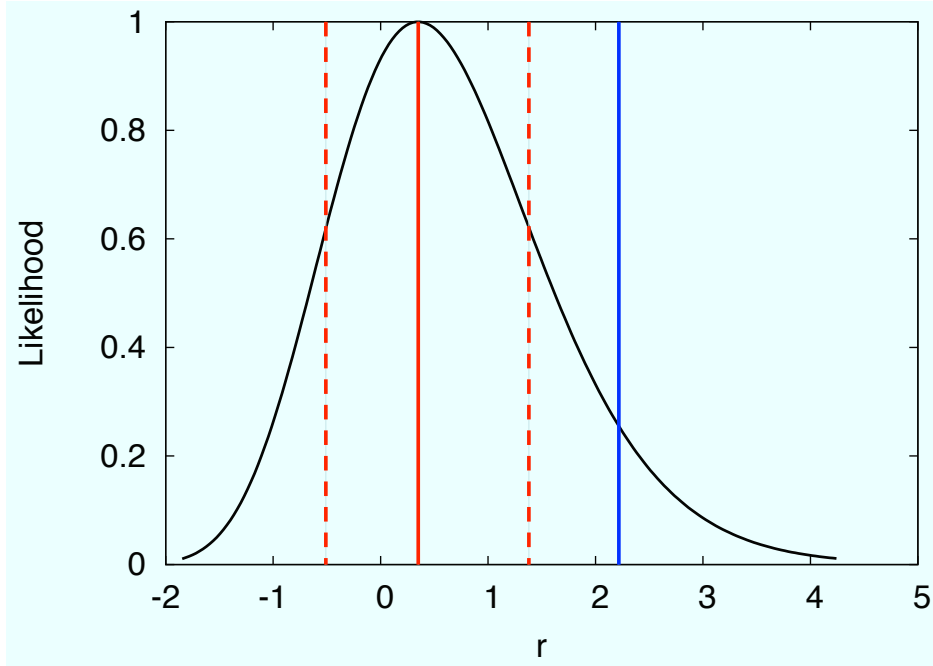


**Figure 8.6:** Likelihood curve as a function of  $r$ . Red-solid line corresponds to  $r = 0.35$ , and dashed lines correspond to two-sided 68% confidence intervals. Blue line corresponds to one-sided 95% confidence interval (upper bound).

---

<sup>a</sup> At small angular scales ( $\ell > 200$ ), power spectrum due to the gravitational lensing is bigger than that of primordial gravitational waves. We can consider that effect, which dose not matter to the results in our case.



Figure 8.7 shows our limits on the  $B$ -mode power spectrum in comparison with the  $B$ -mode power spectra from BICEP, QUaD, and *WMAP*. Our  $B$ -mode limits are between BICEP ones and *WMAP* ones for our sensitive multipole ranges.

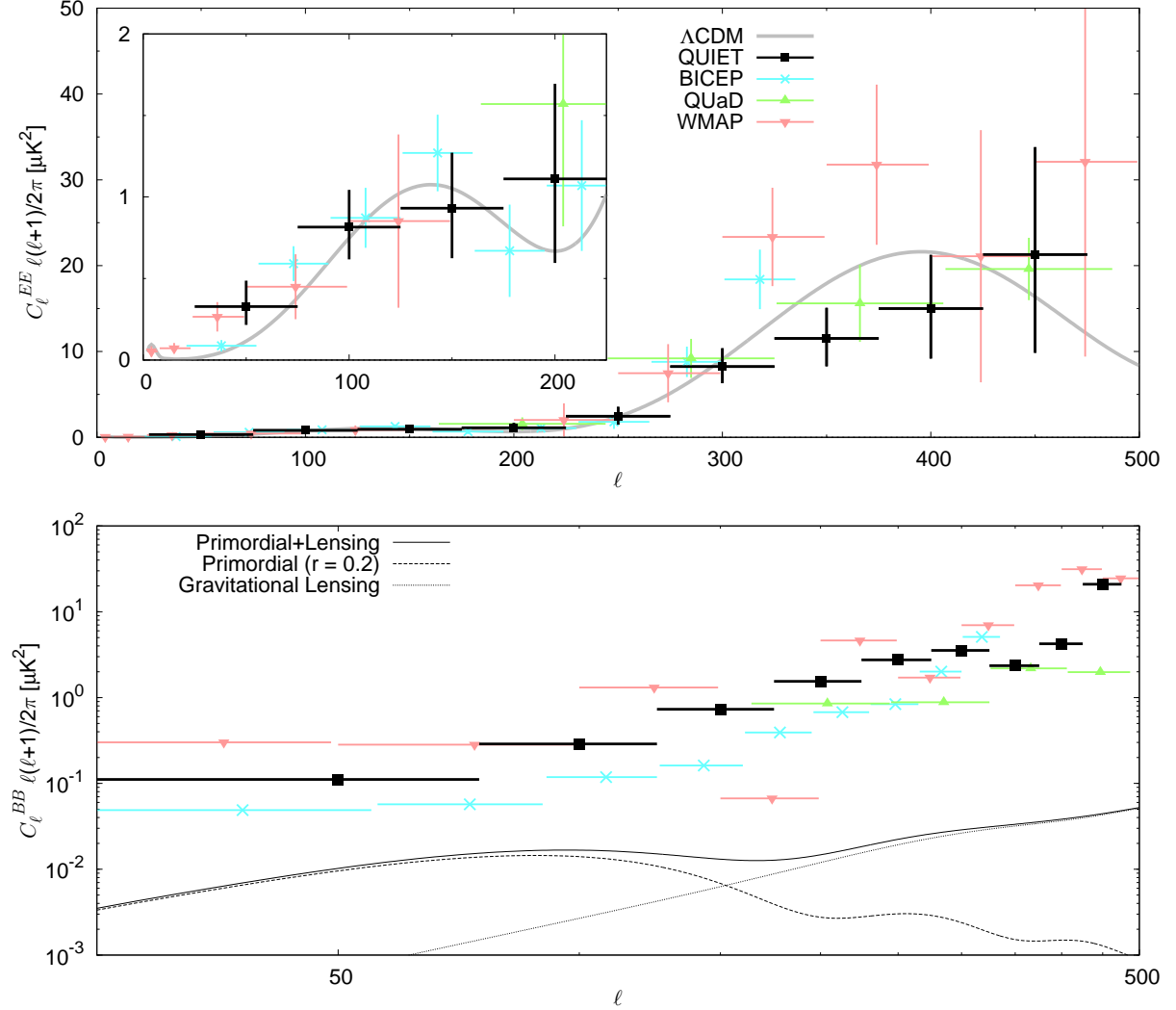


**Figure 8.7:** Power spectra comparison with QUIET, BICEP, QUaD, and *WMAP*. Top panel shows  $EE$  power spectrum with 68% confidence interval error bars. Bottom panel shows 95%  $BB$  upper limits. Note that the *WMAP* data points do not represent 95% upper limits, they just represent one-side 1.645- $\sigma$  intervals.



# Chapter 9

## Systematic Errors

### 9.1 Overview and Summary

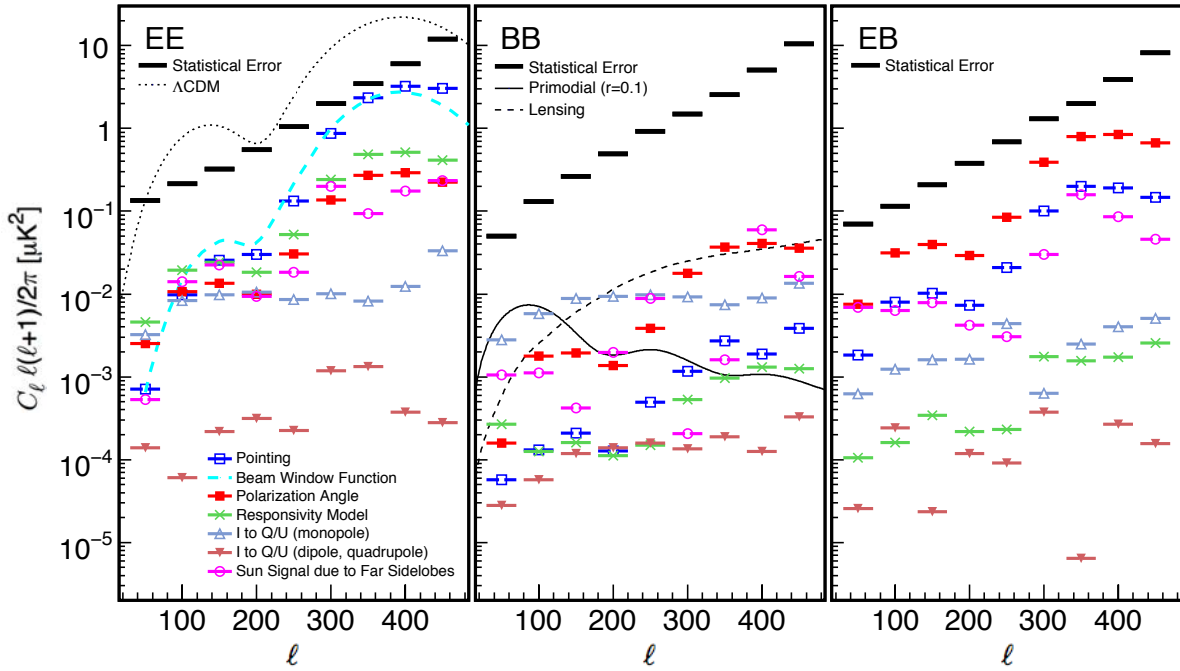


**Figure 9.1:** Seven types of the systematic errors for the  $EE$ ,  $BB$ , and  $EB$  power spectra are shown. Details on each systematic error are discussed in the text. Note that all the systematic errors are well below the statistical errors and these in the  $B$ -mode power are below the primordial  $B$ -mode power of  $r = 0.1$  at large angular scales. These results lead that the systematic errors in the QUIET Q-band are well controlled. Tables 9.1 and 9.2 list all the systematic errors for each type.

<b><math>EE</math> power spectrum</b>	$25 \leq \ell \leq 75$	$76 \leq \ell \leq 125$	$126 \leq \ell \leq 175$	$176 \leq \ell \leq 225$	$226 \leq \ell \leq 275$	$276 \leq \ell \leq 325$	$326 \leq \ell \leq 375$	$376 \leq \ell \leq 425$	$426 \leq \ell \leq 475$
Multiplicative Responsivity	$+1.60 \times 10^{-2}$	$+9.50 \times 10^{-2}$	$+1.30 \times 10^{-1}$	$+7.72 \times 10^{-2}$	$+2.79 \times 10^{-1}$	$+1.04 \times 10^0$	$+2.05 \times 10^0$	$+2.41 \times 10^0$	$+1.77 \times 10^0$
Pointing	$+7.09 \times 10^{-4}$	$+9.80 \times 10^{-3}$	$+2.58 \times 10^{-2}$	$+3.02 \times 10^{-2}$	$+1.32 \times 10^{-1}$	$+8.72 \times 10^{-1}$	$+2.33 \times 10^0$	$+3.21 \times 10^0$	$+3.03 \times 10^0$
Beam window function	$+6.52 \times 10^{-4}$	$+1.48 \times 10^{-2}$	$+4.31 \times 10^{-2}$	$+4.22 \times 10^{-2}$	$+2.14 \times 10^{-1}$	$+9.96 \times 10^{-1}$	$+2.23 \times 10^0$	$+2.73 \times 10^0$	$+1.89 \times 10^0$
Polarization angle	$+2.54 \times 10^{-3}$	$+1.06 \times 10^{-2}$	$+1.36 \times 10^{-2}$	$+9.90 \times 10^{-3}$	$+3.06 \times 10^{-2}$	$+1.38 \times 10^{-1}$	$+2.70 \times 10^{-1}$	$+2.93 \times 10^{-1}$	$+2.23 \times 10^{-1}$
Responsivity model	$+4.58 \times 10^{-3}$	$+1.95 \times 10^{-2}$	$+2.41 \times 10^{-2}$	$+1.82 \times 10^{-2}$	$+5.22 \times 10^{-2}$	$+2.40 \times 10^{-1}$	$+4.82 \times 10^{-1}$	$+5.18 \times 10^{-1}$	$+4.15 \times 10^{-1}$
Leakage (monopole)	$+3.25 \times 10^{-3}$	$+8.39 \times 10^{-3}$	$+9.85 \times 10^{-3}$	$+1.05 \times 10^{-2}$	$+8.62 \times 10^{-3}$	$+1.01 \times 10^{-2}$	$+8.18 \times 10^{-3}$	$+1.24 \times 10^{-2}$	$+3.33 \times 10^{-2}$
Leakage (dipole, quadrupole)	$+1.39 \times 10^{-4}$	$+6.03 \times 10^{-5}$	$+2.20 \times 10^{-4}$	$+3.16 \times 10^{-4}$	$+2.25 \times 10^{-4}$	$+1.18 \times 10^{-3}$	$+1.34 \times 10^{-3}$	$+3.76 \times 10^{-4}$	$+2.81 \times 10^{-4}$
Far-sidelobes	$-5.29 \times 10^{-4}$	$+1.41 \times 10^{-2}$	$-2.24 \times 10^{-2}$	$+9.43 \times 10^{-3}$	$+1.84 \times 10^{-2}$	$+1.98 \times 10^{-1}$	$+9.36 \times 10^{-2}$	$+1.74 \times 10^{-1}$	$+2.35 \times 10^{-1}$
<b>Total</b>	$+1.72 \times 10^{-2}$	$+1.00 \times 10^{-1}$	$+1.44 \times 10^{-1}$	$+9.63 \times 10^{-2}$	$+3.82 \times 10^{-1}$	$+1.72 \times 10^0$	$+3.86 \times 10^0$	$+4.90 \times 10^0$	$+4.02 \times 10^0$

**Table 9.1:** Systematic errors for the  $EE$  power spectrum. The bold entry in each column is the largest systematic error for each  $\ell$  band.

<i>BB</i> power spectrum		$25 \leq \ell \leq 75$	$76 \leq \ell \leq 125$	$126 \leq \ell \leq 175$	$176 \leq \ell \leq 225$	$226 \leq \ell \leq 275$	$276 \leq \ell \leq 325$	$326 \leq \ell \leq 375$	$376 \leq \ell \leq 425$	$426 \leq \ell \leq 475$
Pointing		$+5.68 \times 10^{-5}$	$+1.32 \times 10^{-4}$	$+2.08 \times 10^{-4}$	$+1.27 \times 10^{-4}$	$+4.95 \times 10^{-4}$	$+1.16 \times 10^{-3}$	$+2.72 \times 10^{-3}$	$+1.89 \times 10^{-3}$	$+3.83 \times 10^{-3}$
Polarization angle		$+1.59 \times 10^{-4}$	$+1.78 \times 10^{-3}$	$+1.93 \times 10^{-3}$	$+1.37 \times 10^{-3}$	$+3.83 \times 10^{-3}$	<b><math>+1.78 \times 10^{-2}</math></b>	<b><math>+3.66 \times 10^{-2}</math></b>	$+4.09 \times 10^{-2}$	<b><math>+3.59 \times 10^{-2}</math></b>
Responsivity model		$+2.69 \times 10^{-4}$	$+1.25 \times 10^{-4}$	$+1.61 \times 10^{-4}$	$+1.11 \times 10^{-4}$	$+1.50 \times 10^{-4}$	$+5.28 \times 10^{-4}$	$+9.69 \times 10^{-4}$	$+1.31 \times 10^{-3}$	$+1.26 \times 10^{-3}$
Leakage (monopole)		<b><math>+2.81 \times 10^{-3}</math></b>	<b><math>+5.79 \times 10^{-3}</math></b>	<b><math>+8.84 \times 10^{-3}</math></b>	<b><math>+9.42 \times 10^{-3}</math></b>	<b><math>+9.80 \times 10^{-3}</math></b>	$+9.26 \times 10^{-3}$	$+7.39 \times 10^{-3}$	$+8.95 \times 10^{-3}$	$+1.35 \times 10^{-2}$
Leakage (dipole, quadrupole)		$+2.82 \times 10^{-5}$	$+5.71 \times 10^{-5}$	$+1.19 \times 10^{-4}$	$+1.40 \times 10^{-4}$	$+1.59 \times 10^{-4}$	$+1.34 \times 10^{-4}$	$+1.89 \times 10^{-4}$	$+1.25 \times 10^{-4}$	$+3.29 \times 10^{-4}$
Far-sidelobes		$+1.05 \times 10^{-3}$	$+1.11 \times 10^{-3}$	$+4.18 \times 10^{-4}$	$-1.96 \times 10^{-3}$	$+8.89 \times 10^{-3}$	$+2.06 \times 10^{-4}$	$+1.62 \times 10^{-3}$	<b><math>-5.97 \times 10^{-2}</math></b>	$-1.62 \times 10^{-2}$
<b>Total</b>		<b><math>+3.02 \times 10^{-3}</math></b>	<b><math>+6.16 \times 10^{-3}</math></b>	<b><math>+9.06 \times 10^{-3}</math></b>	<b><math>+9.72 \times 10^{-3}</math></b>	<b><math>+1.38 \times 10^{-2}</math></b>	<b><math>+2.01 \times 10^{-2}</math></b>	<b><math>+3.75 \times 10^{-2}</math></b>	<b><math>+7.30 \times 10^{-2}</math></b>	<b><math>+4.18 \times 10^{-2}</math></b>

141

<i>EB</i> power spectrum		$25 \leq \ell \leq 75$	$76 \leq \ell \leq 125$	$126 \leq \ell \leq 175$	$176 \leq \ell \leq 225$	$226 \leq \ell \leq 275$	$276 \leq \ell \leq 325$	$326 \leq \ell \leq 375$	$376 \leq \ell \leq 425$	$426 \leq \ell \leq 475$
Pointing		$1.82 \times 10^{-3}$	$7.96 \times 10^{-3}$	$1.03 \times 10^{-2}$	$7.26 \times 10^{-3}$	$2.10 \times 10^{-2}$	$1.01 \times 10^{-1}$	$1.98 \times 10^{-1}$	$1.92 \times 10^{-1}$	$1.48 \times 10^{-1}$
Polarization angle		<b><math>7.47 \times 10^{-3}</math></b>	<b><math>3.15 \times 10^{-2}</math></b>	<b><math>3.97 \times 10^{-2}</math></b>	<b><math>2.91 \times 10^{-2}</math></b>	<b><math>8.47 \times 10^{-2}</math></b>	<b><math>3.91 \times 10^{-1}</math></b>	<b><math>7.91 \times 10^{-1}</math></b>	<b><math>8.42 \times 10^{-1}</math></b>	<b><math>6.68 \times 10^{-1}</math></b>
Responsivity model		$1.05 \times 10^{-4}$	$1.61 \times 10^{-4}$	$3.44 \times 10^{-4}$	$2.19 \times 10^{-4}$	$2.33 \times 10^{-4}$	$1.76 \times 10^{-3}$	$1.57 \times 10^{-3}$	$1.72 \times 10^{-3}$	$2.58 \times 10^{-3}$
Leakage (monopole)		$6.21 \times 10^{-4}$	$1.24 \times 10^{-3}$	$1.62 \times 10^{-3}$	$1.64 \times 10^{-3}$	$4.38 \times 10^{-3}$	$6.29 \times 10^{-4}$	$2.47 \times 10^{-3}$	$4.05 \times 10^{-3}$	$5.10 \times 10^{-3}$
Leakage (dipole, quadrupole)		$2.59 \times 10^{-5}$	$2.42 \times 10^{-4}$	$2.34 \times 10^{-5}$	$1.19 \times 10^{-4}$	$9.10 \times 10^{-5}$	$3.77 \times 10^{-4}$	$6.47 \times 10^{-6}$	$2.68 \times 10^{-4}$	$1.57 \times 10^{-4}$
Far-sidelobes		$6.92 \times 10^{-3}$	$6.36 \times 10^{-3}$	$7.83 \times 10^{-3}$	$4.22 \times 10^{-3}$	$3.07 \times 10^{-3}$	$3.02 \times 10^{-2}$	$1.58 \times 10^{-1}$	$8.63 \times 10^{-2}$	$4.57 \times 10^{-2}$
<b>Total</b>		<b><math>1.04 \times 10^{-2}</math></b>	<b><math>3.32 \times 10^{-2}</math></b>	<b><math>4.18 \times 10^{-2}</math></b>	<b><math>3.03 \times 10^{-2}</math></b>	<b><math>8.74 \times 10^{-2}</math></b>	<b><math>4.05 \times 10^{-1}</math></b>	<b><math>8.30 \times 10^{-1}</math></b>	<b><math>8.68 \times 10^{-1}</math></b>	<b><math>6.86 \times 10^{-1}</math></b>

**Table 9.2:** Systematic errors for the *BB* and *EB* power spectra. The bold entry in each column is the largest one for each  $\ell$  band.

The succeeded null-suites described in Chapter 7 imply that our results are statistically reliable; however, we have not shown how systematic errors limit the results yet. Estimation of systematic errors is important because systematic errors will dominate the sensitivity of the  $B$ -mode measurement rather than statistical errors in the near future. Since we target to measure the  $B$ -mode power with the tensor-to-scalar ratio at the level of  $r = \mathcal{O}(0.1)$ , we have to control systematic errors below that level in our analysis.

To evaluate all the possible systematic errors is challenging because propagation of systematic errors in the CMB analysis is quite complicated. Our analysis methodology based on the MASTER and pseudo- $C_\ell$  techniques described in Chapter 5 makes it possible to evaluate them by using Monte Carlo simulations, so that we can estimate the possible systematic errors by the full-season pipeline simulations.

Figure 9.1 shows summary of our systematic errors for the  $EE$ ,  $BB$ , and  $EB$  power spectra, and Tables 9.1 and 9.2 list their quantities. All the possible systematic errors are well below the statistical errors. For the  $B$ -mode, even the largest error is not only well below the statistical errors but also less than the power of the tensor-to-scalar ratio of  $r = 0.1$  at large angular scales.

QUIET reported the least systematic errors and no other experiments measuring the CMB polarization have reported this level of  $B$ -mode systematic errors. This result is a strong proof of our technology and methodology for the future experiment, which targets the tensor-to-scalar ratio of  $r = \mathcal{O}(0.01)$  level.

We describe details of each systematic error in the following sections.

## 9.2 Multiplicative Responsivity Error

In Figure 9.1, we do not show possible uncertainties due to the responsivity model described in (§ 4.2.1.6, 4.3 and 4.7), which leads to a 6.3% of the  $E$ -mode signal (13% in power spectrum units)<sup>a</sup>. The systematic error due to these uncertainties are given by multiplying the  $E$ -mode signal by 13% for each  $\ell$  bin. We call this type of uncertainty

---

<sup>a</sup>3.2% from the uncertainty of the Tau A polarization intensity; 3.8% from the uncertainty of the solid angle; 3.3% from the possible difference between the demod and total power responsivity; and 1.9% from the possible time-dependence of the responsivities.

“multiplicative uncertainty”. The multiplicative responsivity error provides the largest systematic uncertainty in the  $E$ -mode power spectrum at larger angular scales.

### 9.3 Responsivity

Responsivity shifts within CESes due to the bad cryostat or electronics regulation lead to distortions in the maps. We performed full-season simulations about these shifts. Responsivity variation among the Tau A, the Moon, and wire grid rather than sky dips is also used for the simulations. We also incorporated the uncertainty in the atmospheric-temperature model used in the analysis of the sky-dip data. The responsivity shift is the largest systematic uncertainty in the  $E$ -mode power spectrum at large angular scales except the multiplicative responsivity error.

### 9.4 Polarization Angle

Uncertainty of the polarization axis of the modules can create the  $E$ – $B$  mixing ( $E \rightarrow B$  leakage for the  $B$ -mode). To evaluate possible systematic bias due to the mixing, we repeated power spectra calculation using the results from the different angle calibration sources—Tau A, the Moon, and wire grid (§ 4.4). The largest difference among three power spectra are taken as the systematic uncertainty. The uncertainty of the polarization angle is the largest systematic error in the  $EB$  power spectrum at all the  $\ell$  ranges and in the  $B$ -mode power spectrum at small angular scales.

The  $E$ – $B$  mixing is also given semi-analytically as follows by [107, 108]:

$$\Delta C_\ell^{BB} = C_\ell^{EE} \sin^2(2\Delta\gamma) + C_\ell^{BB} \cos^2(2\Delta\gamma), \quad (9.1)$$

$$\Delta C_\ell^{EB} = \frac{1}{2} (C_\ell^{EE} - C_\ell^{BB}) \sin(4\Delta\gamma), \quad (9.2)$$

where  $\Delta\gamma$  is a constant shift of the rotation angle on the polarization plane. Since we already know that the primordial  $B$ -mode is smaller than the  $E$ -mode and the angle difference is small in our case, we may ignore  $C_\ell^{BB}$  and expand on the right hand side to

obtain

$$\Delta C_\ell^{BB} = 4C_\ell^{EE} \Delta\gamma^2, \quad (9.3)$$

$$\Delta C_\ell^{EB} = 2C_\ell^{EE} \Delta\gamma. \quad (9.4)$$

We found that the semi-analytic forms are order-of-magnitude agreement with the simulated results because the mean angle difference among three measurements is a few degrees.

## 9.5 Pointing

The uncertainty in pointing provides distortion in polarization maps, so that the  $E$ -mode is diluted and fake  $B$ -mode is created by a non-linear effect like the gravitational lensing [109]. To evaluate the systematic uncertainty due to the pointing, we repeated power spectra calculation with two independent pointing models: one is the fiducial model for the analysis and the other is based on a different calibration measurement. We also included the mechanical problem effect with the deck angle during the first two months of our observation season. Differences in the power spectra between the fiducial result and the other are taken as the systematic uncertainties. The pointing uncertainty dominates the systematic error in the  $E$ -mode power spectrum at smaller angular scales except the multiplicative responsivity error.

## 9.6 Beam Window Function

The uncertainty in the beam window function is also multiplicative uncertainty. This is evaluated by the comparison of the window function between the center feedhorn and the feedhorn at the edge of the array. The difference is statistically significant due to the different location on the focal plane and expected from the pre-season antenna range measurement.



## 9.7 Far-Sidelobe Contamination due to the Sun

We have already found the contamination due to the two far-sidelobes seeing the Sun is negligibly small for the full season data and removed the contamination in data selection as described in § 6.2; however, we have not estimated the possible residual. Since we already have Sun-centered coordinates maps based on full-season observation, we can add the signal from the Sun in the full-pipeline simulations. Taking difference of power spectra between with and without the Sun signal simulations, we obtained the small excesses due to the Sun. These excesses are taken as systematic uncertainties.

## 9.8 Instrumental Polarization

The  $I \rightarrow Q/U$  leakage can create fake polarization signal from the temperature anisotropy. The  $I \rightarrow Q/U$  leakage of our modules is small as described in § 4.5. The coefficient is 1% (0.2%) for the  $Q$  ( $U$ ) diodes. With a combination of these small values, diurnal sky rotation and weekly boresight rotation, the leakage effect is well suppressed in QUIET. We estimated spurious  $Q$  and  $U$  signals in the maps for each CES-diode using the *WMAP* temperature anisotropy map with our leakage values, so that we evaluated the leakage power spectra from the full-simulated maps.

Differential beam ellipticities can also induce polarization signal at higher-order multipoles. We measured these leakages from Tau A and Jupiter observations and found that the higher-order multipoles are at most 0.1% of the mainbeam peak amplitude. We evaluated the corresponding effect on the power spectra.

## 9.9 Ground-pickup Signals

Since QUIET has two known far-sidelobes, they might see the ground at particular elevations and deck angles. The constant ground pickup in each CES is subtracted by our filtering as described in § 5.1.3.2 and the residual of this filtering is  $\approx 1 \mu\text{K}$  in the full-season maps. The cross-correlation technique could also eliminate the effect from the ground structure (§ 5.3.2). Our concern is the residual of time-dependent ground signals during very short time period of a single CES which can not be removed by the filtering.

We estimated an upper limit on the residual  $B$ -mode power from the possible pickup of the time-dependent ground signals. The limit is less than  $10^{-4} \mu\text{K}^2$  at large angular scales of  $\ell < 100$ .

## 9.10 Type-B Glitch

The Type-B correction is necessary for QUIET as described in § 5.1.1.1. The possible residuals after the Type-B correction result in similar effects to the  $I \rightarrow Q/U$  leakage and the variation of the responsivity during a single CES. We estimated these effects based on the Type-B correction parameters. We found a 3% additional effect for the leakage bias and small effect for the responsivity, which is less than half of the systematic errors due to the original responsivity uncertainty discussed in § 9.3.

## 9.11 Data Selection Bias

Data selection itself could bias the result if they are too stringent. We confirmed the smallness of such a bias with 144 CMB plus noise simulations with our selection criteria. The possible systematic uncertainty on the  $B$ -mode is less than  $10^{-3} \mu\text{K}^2$  at large angular scales of  $\ell < 100$ .

# Chapter 10

## Conclusions

No experiment can measure power spectrum by coherent polarimeters with excellent sensitivity except QUIET today. We detected the polarization  $E$ -mode and measured its power spectrum at 43 GHz. The significance of the detection around the first acoustic peak ( $76 \leq \ell \leq 175$ ) is more than  $6\text{-}\sigma$ , which is one of the best measurements in the world. We also searched for the  $B$ -mode signal at angular scales of  $25 \leq \ell \leq 475$  and obtained upper limits on the power spectrum. From our measurements, we obtained the tensor-to-scalar ratio of  $r = 0.35^{+1.06}_{-0.87}$ . The  $B$ -mode upper limit at 95% confidence intervals is  $r < 2.2$ .

These results come from our polarimeter array, which is the most sensitive and largest one based on the HEMT technology. Our polarimeters have a sensitivity ( $Q$  and  $U$  combined) of  $280 \mu\text{K}\sqrt{\text{s}}$ , which leads to an array sensitivity of  $69 \mu\text{K}\sqrt{\text{s}}$ . We demonstrated that our coherent technology can reduce not only the  $1/f$  noise from the HEMT amplifiers and detector diodes but also low-frequency atmospheric fluctuations. As a result, we achieved a very low knee frequency of the  $1/f$  noise: the median is just 5.5 mHz. A summary table of the QUIET Q-band experiment is found in Chapter G.

Our calibration method based on the Tau A measurements—from which we can obtain polarization responsivity, detector angle, and  $I \rightarrow Q/U$  leakage—made it possible to construct the stable, reliable, and simple calibration model. We confirmed that uncertainties of the model are well understood, and possible systematic errors are well below the statistical errors.

Our results were confirmed by the null-suites based on more than 42 null tests and blind analysis. We finalized our 33 data selection criteria through the null tests. We verified that systematic errors are well controlled and less than the statistical errors. Moreover, they are smaller than the  $B$ -mode amplitude for the tensor-to-scalar ratio of  $r = 0.1$  at large angular scales. These low level systematic errors result from the combination of unique design of our experiment such as double-demodulation technique, Mizuguchi-Dragone optics, natural sky rotation, and frequent deck rotation. In addition, we evaluated the power spectra by taking cross-correlations at the different divisions of azimuth direction and boresight rotation. The cross-correlation technique can cancel possible residuals of the ground-emission pickup and bad weather. All the analysis procedure had been performed before we saw the power spectra themselves. This “blind analysis” concept is extremely important to avoid the experimenter’s bias.

We observed four CMB patches on the sky. Comparing the power spectra for each patch and checking consistency among them, we could detect the Galactic synchrotron emission with a  $3\text{-}\sigma$  significance level in one of our CMB patches. Extrapolating from the Q-band frequency to the W-band frequency, which is the most foreground minimum band, we would have synchrotron contamination at the level of  $r = 0.05$ . QUIET is the only two CMB polarization experiments to observe at frequencies suitable for addressing synchrotron contamination. This is also very useful because observations at different frequencies have not only different systematics but also different foreground contaminations. In the near future, the contamination from the Galactic foreground emission is one of the limiting factors for the  $B$ -mode measurements. Combining our results with other experiments that observe at frequencies larger than 100 GHz, at which dust emission is dominant, we can understand the contamination from the foregrounds.

We can directly access the inflationary era by measuring the CMB  $B$ -mode. We showed that QUIET is one of the most sensitive polarization measurements today. The leading  $B$ -mode measurements in the future must be the CMB polarization measurement although the best upper limit on the tensor-to-scalar ratio today ( $r < 0.19$  at 95% C.L.) is still given by temperature anisotropy measurements combined with BAO and SN because these measurements will not be much improved because uncertainties in temperature anisotropy measurements are already limited by cosmic variance.

Our coherent technology, our observation and analysis methodology which were proved in this dissertation can easily be scaled up to a future experiment which has hundreds or a thousand of sensitive polarimeter modules. By such an experiment, we will achieve detection of primordial gravitational waves, or place a stringent upper limit on the tensor-to-scalar ratio at the level of  $r = \mathcal{O}(0.01)$ . For such an experiment, the limiting factor will not be polarimeter sensitivity itself but systematic errors in the near future. Our total systematic errors on the  $B$ -mode are remarkably smaller than those which are reported by any other experiments today. The fact shows that our technology and methodology are suitable for future  $B$ -mode search, and promise that we can improve results in the future.



# Appendix A

## Basic Formula of CMB Angular Power Spectrum

The basic formula of the CMB polarization field and the well-known “Knox formula” are reviewed in this appendix.

### A.1 Basic Formula

The linear polarization is related to the two Stokes  $Q$  and  $U$  parameters [110, 111], whose magnitude and orientation are given as

$$P = \sqrt{Q^2 + U^2}, \quad \gamma = \frac{1}{2} \arctan \left( \frac{U}{Q} \right). \quad (\text{A.1})$$

As spin  $\pm 2$  fields, the Stokes  $Q$  and  $U$  parameters change under a rotation by an angle of  $\psi$  as

$$(Q \pm iU)(\vec{n}) \rightarrow e^{\mp 2i\psi} (Q \pm iU)(\vec{n}). \quad (\text{A.2})$$

Because of that,  $(Q \pm iU)(\vec{n})$  can be expanded with spin  $\pm 2$  spherical harmonics [32]

$$(Q \pm iU)(\vec{n}) = \sum_{\ell, m} a_{\ell m}^{(\pm 2)} Y_{\ell m}(\vec{n}), \quad (\text{A.3})$$

where the multipole coefficients  $(a_{\ell m}^{(\pm 2)})$  can be evaluated by

$$a_{\ell m}^{(\pm 2)} = \int d\Omega(\vec{n}) (Q \pm iU)(\vec{n}) Y_{\ell m}(\vec{n}). \quad (\text{A.4})$$

In terms of the coefficients ( $a_{\ell m}^{(\pm 2)}$ ), the  $E$ -mode and  $B$ -mode are defined as

$$a_{\ell m}^E = -\frac{1}{2} \left( a_{\ell m}^{(+2)} + a_{\ell m}^{(-2)} \right), \quad a_{\ell m}^B = -\frac{1}{2i} \left( a_{\ell m}^{(+2)} - a_{\ell m}^{(-2)} \right); \quad (\text{A.5})$$

therefore, angular power spectra of the  $E$ -mode and  $B$ -mode are constructed as follows:

$$C_\ell^{EE} = \frac{1}{2\ell+1} \sum_{m=-\ell}^{+\ell} \langle a_{\ell m}^E a_{\ell m}^{E*} \rangle, \quad C_\ell^{BB} = \frac{1}{2\ell+1} \sum_{m=-\ell}^{+\ell} \langle a_{\ell m}^B a_{\ell m}^{B*} \rangle. \quad (\text{A.6})$$

If the fluctuations are Gaussian distributed, all of the cosmological information are imprinted in the angular power spectra. Moreover, although there six power spectra taking auto- and cross- correlations among the temperature anisotropy ( $T$ ),  $E$ -mode and  $B$ -mode of harmonic coefficients. Only  $C_\ell^{TT}$ ,  $C_\ell^{TE}$ ,  $C_\ell^{EE}$ ,  $C_\ell^{BB}$  are non-zero because the  $E$ -mode has positive parity and the  $B$ -mode has negative parity.

## A.2 Knox Formula

The error of the CMB angular power spectrum for the temperature anisotropy is described as

$$\Delta C_\ell^{TT} = \sqrt{\frac{2}{(2\ell+1)f_{\text{sky}}}} [C_\ell^{TT} + w^{-1}W_\ell^{-1}], \quad (\text{A.7})$$

where  $f_{\text{sky}}$  is sky coverage of observation,  $C_\ell$  represents a CMB power spectrum itself,  $w^{-1/2}$  is noise for each pixel, and  $W_\ell$  is a window function. Equation (A.7) is called ‘‘Knox formula’’ because Knox [58] defined it analytically. The unit of  $w^{-1/2}$  is usually given by  $\mu\text{K-arcmin}$ . For the Gaussian beam, the  $W_\ell$  is described as

$$W_\ell = \exp[-\ell(\ell+1)\sigma_\theta^2], \quad (\text{A.8})$$

where  $\sigma_\theta$  is the width of the Gaussian beam, which gives a cut-off multipole scale of  $\ell_{\text{cut}} \approx 1/\sigma_\theta$ .

When we compare noise sensitivity of an experiment with a theoretical expectation of the  $E$ - or  $B$ -mode power spectrum, we usually use  $\mathcal{C}_\ell \equiv \ell(\ell+1)C_\ell/(2\pi)$  for the expectation and  $\mathcal{N}_\ell \equiv \ell(\ell+1)w^{-1}W_\ell^{-1}/(2\pi)$  for the noise. The  $\mathcal{C}_\ell$ -to- $\mathcal{N}_\ell$  ratio corresponds to ‘‘signal-to-noise’’ ratio of an experiment. The  $\mathcal{C}_\ell$  is useful for two reasons: it is the logarithmic average of  $C_\ell$  that gives the variance of the data; for scale-invariant theories of structure



formation, the  $\mathcal{C}_\ell$  is roughly constant at large scales [112]. The  $2/\{(2\ell+1)f_{\text{sky}}\}$  factor in Equation (A.7) corresponds to uncertainty due to finite sampling of events from a random process. This sampling variance is known as cosmic variance [113] in cosmology. When we are interested in the error of power spectrum, we should consider the whole part of Equation (A.7) with  $\ell(\ell+1)$  factor such as  $\ell(\ell+1)/(2\pi)\Delta\mathcal{C}_\ell \equiv \Delta\mathcal{C}_\ell$ .

We also obtain almost the same formulas for the polarization as follows ([114, 96]):

$$\Delta C_\ell^{EE} = \sqrt{\frac{2}{(2\ell+1)f_{\text{sky}}}} [C_\ell^{EE} + w_P^{-1}W_\ell^{-1}], \quad (\text{A.9})$$

$$\Delta C_\ell^{BB} = \sqrt{\frac{2}{(2\ell+1)f_{\text{sky}}}} [C_\ell^{BB} + w_P^{-1}W_\ell^{-1}], \quad (\text{A.10})$$

$$\Delta C_\ell^{TE} = \sqrt{\frac{2}{(2\ell+1)f_{\text{sky}}}} \left[ (C_\ell^{TE})^2 + (C_\ell^{TT} + w_T^{-1}W_\ell^{-1}) (C_\ell^{EE} + w_P^{-1}W_\ell^{-1}) \right]^{1/2}, \quad (\text{A.11})$$

$$\Delta C_\ell^{EB} = \sqrt{\frac{2}{(2\ell+1)f_{\text{sky}}}} [(C_\ell^{BB} + w_P^{-1}W_\ell^{-1}) (C_\ell^{EE} + w_P^{-1}W_\ell^{-1})]^{1/2}, \quad (\text{A.12})$$

$$(\text{A.13})$$

where  $w_T$  and  $w_P$  represent noises for each pixel for temperature and polarization, respectively because they could be different.



# Appendix B

## Formula How QUIET Polarimeters Measure Polarization Signal with Suppressing the $1/f$ Noise

In this appendix, our demodulation and double-demodulation techniques which can suppress the  $1/f$  noise due to the HEMT amplifiers, detector diodes, electronics, and low-frequency bad weather fluctuations are described. The whole schematic picture of our module has already been shown in Figure B.1.

### B.1 Basic Definition

The circularly polarized radiations ( $E_R$  and  $E_L$ ) separated by a septum polarizer are amplified by factors of  $g_A$  and  $g_B$  on the leg A and leg B respectively. The phase switch alternately multiplies the signals by  $\pm 1$  synchronized with 50 Hz for the leg A and 4 kHz for the leg B. At first, we focus on the 4 kHz phase switching on the leg B. Thereby we can write the electronic field amplitudes on each leg down

$$E_{\text{legA}}(t, +) = +g_A E_L + n_A, \quad E_{\text{legB}}(t, \pm : 4 \text{ kHz}) = \pm g_B E_R + n_B, \quad (\text{B.1})$$

here we ignore order of amplifying and phase switching on each leg, and  $n_A$  and  $n_B$  are noises, which come from the amplifiers, the detector diodes, and low frequency atmospheric fluctuation on each leg. Power spectrum of the noise for our polarimeters is given

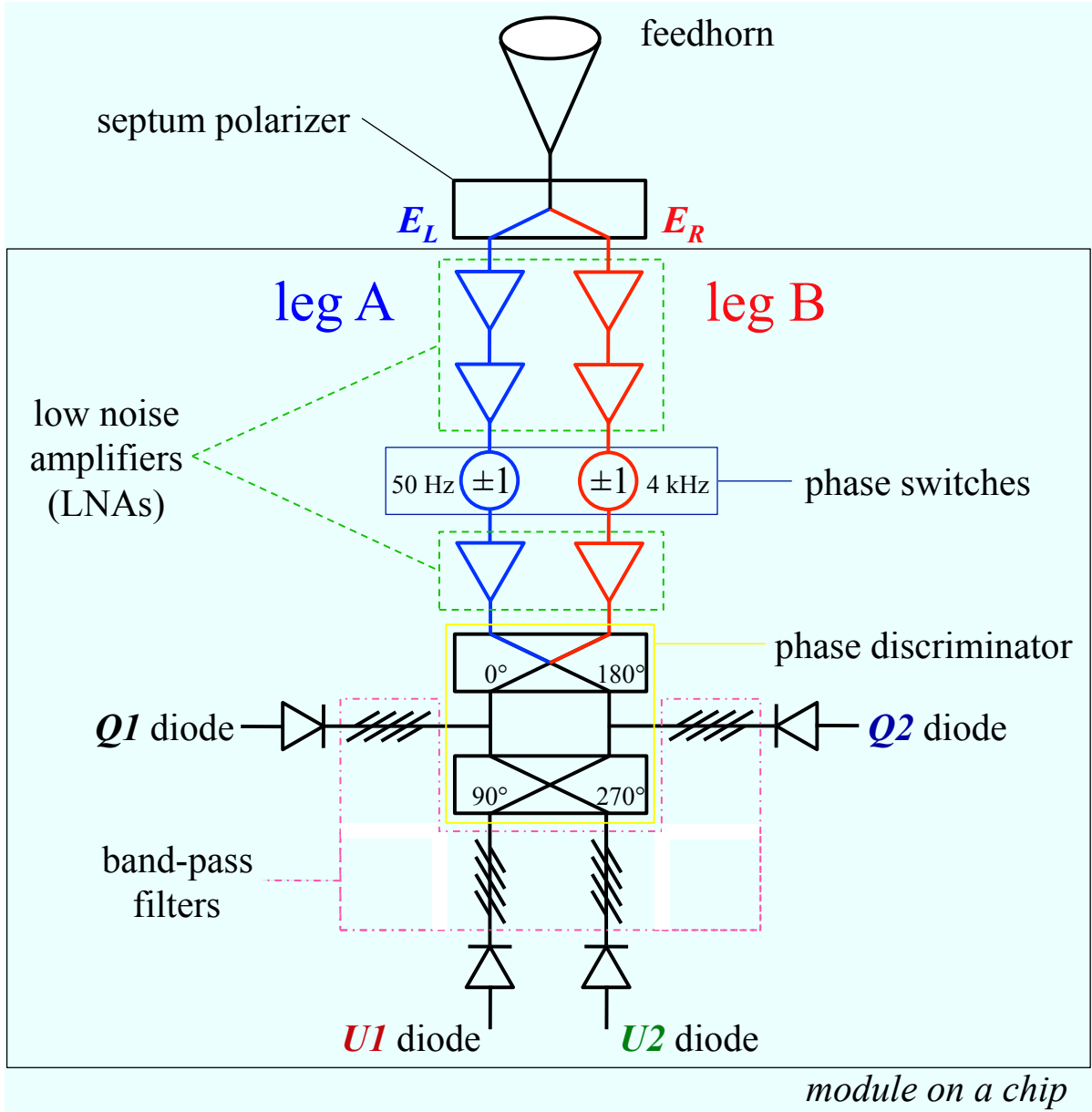


**Figure B.1:** Schematic diagram of a QUIET Q-band polarimeter module with a feedhorn and septum polarizer. All the components except a feedhorn and septum polarizer are integrated in a module package on a chip. The incident signal runs from the top to bottom. This is the same figure as Figure 2.4.

by

$$\Sigma(f) = \sigma_0^2 \left[ 1 + \left( \frac{f_{\text{knee}}}{f} \right)^\alpha \right]. \quad (\text{B.2})$$

Here we have two noise components: the white noise and  $1/f$  noise;  $\sigma_0$  represents the white noise level,  $f_{\text{knee}}$  is the knee frequency, at which the power spectrum equals to twice the white noise level, and  $\alpha$  corresponds to the slop of the  $1/f$  noise. The phase discriminator couples each signal from the legs with extra phase shifts by  $0^\circ$ ,  $-90^\circ$  ( $270^\circ$ ),  $+90^\circ$ , and  $180^\circ$ . Then the resulting signals are rectified by the  $Q1$ ,  $U1$ ,  $U2$ , and  $Q2$  detector diodes respectively. The ADC converts those timestreams to digital ones with a 800 kHz sampling, and averages them synchronized with a 4 kHz phase switching.

Focusing on the  $Q1$  diode for simplicity, the rectified signal synchronized with the 4 kHz is given by

$$\begin{aligned} \langle |E_{Q1}|_{800\text{ kHz}}^2 \rangle(t, +, \pm : 4\text{ kHz}) &= \langle |E_{\text{legA}}(t, +) + E_{\text{legB}}(t, \pm : 4\text{ kHz})|^2 \rangle \\ &= g_A^2 |E_L|^2 + g_B^2 |E_R|^2 + n_A^2 + n_B^2 \pm g_A g_B |E_L^* E_R + E_L E_R^*| \\ &= (g_A^2 + g_B^2) (|E_X|^2 + |E_Y|^2) + (n_A^2 + n_B^2) \\ &\quad \pm 2g_A g_B (|E_X|^2 - |E_Y|^2) \\ &= 2G_{A+B}I + N_{A+B} \pm 2G_{AB}Q, \end{aligned} \quad (\text{B.3})$$

where  $E_L$  and  $E_R$  are defined with the Cartesian coordinate system on each polarimeter; therefore, they are given as  $E_L = E_X + iE_Y$  and  $E_R = E_X - iE_Y$ . In the Cartesian coordinate system on each polarimeter, we define the Stokes parameters<sup>a</sup> as follows:

$$I = \frac{|E_X|^2 + |E_Y|^2}{2}, \quad Q = \frac{|E_X|^2 - |E_Y|^2}{2}, \quad U = \frac{E_X^* E_Y + E_X E_Y^*}{2}. \quad (\text{B.4})$$

Where we also define averaged gain factors  $G_{A+B} = g_A^2 + g_B^2$  and  $G_{AB} = 2g_A g_B$ , and averaged and squared noise level  $N_{A+B} = n_A^2 + n_B^2$ , whose definition is not completely correct because  $n_A$  and  $n_B$  include the  $1/f$  noise. But this description is convenient to understand the formula.

---

<sup>a</sup>We ignore the Stokes  $V$  parameter, which is defined as  $V = i(E_X^* E_Y - E_X E_Y^*)/2$  because it never appear in our measurement at all as well as in CMB polarization measurement themselves.

## B.2 Demodulation and Total Power

Equation (B.3) consists of three terms: the first term is proportional to total intensity, the second is proportional to averaged noise, and the last is proportional to the Stokes  $Q$  parameter, whose sign is synchronized with 4 kHz phase switching. In order to obtain only the Stokes  $Q$  parameter, we take difference between neighboring two samples of Equation (B.3),

$$d_{Q1}(t = t_{4\text{kHz}}) = \frac{\langle |E_{Q1}|^2 \rangle(t_i, +, +) - \langle |E_{Q1}|^2 \rangle(t_{i+1}, +, -)}{2} \\ = G_{A+B}(t_i)I(t_i) - G_{A+B}(t_{i+1})I(t_{i+1}) \quad (\text{B.5})$$

$$+ \frac{N_{A+B}(t_i) - N_{A+B}(t_{i+1})}{2} \quad (\text{B.6})$$

$$+ G_{AB}(t_i)Q(t_i) + G_{AB}(t_{i+1})Q(t_{i+1}). \quad (\text{B.7})$$

With an assumption that gain factors, total intensity, and the Stokes  $Q$  parameter do not change in neighboring two sample ( $= 0.25\text{ msec.}$ ), Equation (B.5) becomes zero and Equation (B.7) represents  $2G_{AB}Q$ . Since on one hand,  $N_{A+B}$  consists of the  $1/f$  noise at lower frequency, which is highly correlated among samples, the  $1/f$  noise component in Equation (B.6) is totally suppressed; on the other hand, since  $N_{A+B}$  also consists of the white noise at higher frequency, which is not correlated among samples, the white noise component in Equation (B.6) is not suppressed but added. For this reason, we can get the Stokes  $Q$  parameter without the  $1/f$  noise

$$d_{Q1}(t = t_{4\text{kHz}}) = 2G_{AB}Q(t) + N_{A+B}^w(t) \quad (\text{B.8})$$

where  $N^w$  corresponds to only the white noise on both legs of the 4 kHz timestreams. These operations of phase switching—modulation and demodulation—make it possible to not only measure polarization but also suppress the  $1/f$  noise. Moreover, we do not have to match gain factors though experiments which use bolometer technology have to match them at the  $10^{-4}$  level [109] in order to avoid instrumental polarization. This demodulation technique is very unique and advantageous among CMB polarization experiments today.

Meanwhile, not taking difference between neighboring samples of Equation (B.3) but

adding them, we can get 4 kHz total power timestreams as follows:

$$tp_{Q1}(t = t_{4\text{kHz}}) = 2G_{A+B}I(t) + N_{A+B}(t). \quad (\text{B.9})$$

The total power timestreams are useful to track the weather condition (§ 6.3) and the stability of the detector responsivities (Appendix D.1), but suffered from too much contamination of the  $1/f$  noise to measure the CMB temperature anisotropy itself.

Since the phase discriminator adds the signals with phase shifts by  $-90^\circ$ ,  $+90^\circ$ , and  $180^\circ$  for the  $U1$ ,  $U2$ , and  $Q2$  diodes respectively, applied with the same way of the  $Q1$  diode, the rectified signals for the  $U1$ ,  $U2$ , and  $Q2$  are also described as

$$\begin{aligned} \langle |E_{U1}|_{800\text{kHz}}^2 \rangle(t, +, \pm : 4\text{kHz}) &= \left\langle \left| E_{\text{legA}}(t, +) + e^{-i\pi/2} E_{\text{legB}}(t, \pm : 4\text{kHz}) \right|^2 \right\rangle \\ &= 2G_{A+B}I + N_{A+B} \mp 2G_{AB}U, \end{aligned} \quad (\text{B.10})$$

$$\begin{aligned} \langle |E_{U2}|_{800\text{kHz}}^2 \rangle(t, +, \pm : 4\text{kHz}) &= \left\langle \left| E_{\text{legA}}(t, +) + e^{+i\pi/2} E_{\text{legB}}(t, \pm : 4\text{kHz}) \right|^2 \right\rangle \\ &= 2G_{A+B}I + N_{A+B} \pm 2G_{AB}U, \end{aligned} \quad (\text{B.11})$$

$$\begin{aligned} \langle |E_{Q2}|_{800\text{kHz}}^2 \rangle(t, +, \pm : 4\text{kHz}) &= \left\langle \left| E_{\text{legA}}(t, +) + e^{i\pi} E_{\text{legB}}(t, \pm : 4\text{kHz}) \right|^2 \right\rangle \\ &= 2G_{A+B}I + N_{A+B} \mp 2G_{AB}Q. \end{aligned} \quad (\text{B.12})$$

Thereby, 4 kHz timestreams of demodulation for each diode are obtained as

$$d_{Q1}(t = t_{4\text{kHz}}) = 2G_{AB}Q(t) + N_{A+B}^w(t), \quad (\text{B.13})$$

$$d_{U1}(t = t_{4\text{kHz}}) = -2G_{AB}U(t) + N_{A+B}^w(t), \quad (\text{B.14})$$

$$d_{U2}(t = t_{4\text{kHz}}) = 2G_{AB}U(t) + N_{A+B}^w(t), \quad (\text{B.15})$$

$$d_{Q2}(t = t_{4\text{kHz}}) = -2G_{AB}Q(t) + N_{A+B}^w(t), \quad (\text{B.16})$$

and those of total power are given as

$$tp_{Q1}(t = t_{4\text{kHz}}) = 2G_{A+B}I(t) + N_{A+B}(t), \quad (\text{B.17})$$

$$tp_{U1}(t = t_{4\text{kHz}}) = -2G_{A+B}I(t) + N_{A+B}(t), \quad (\text{B.18})$$

$$tp_{U1}(t = t_{4\text{kHz}}) = 2G_{A+B}I(t) + N_{A+B}(t), \quad (\text{B.19})$$

$$tp_{U1}(t = t_{4\text{kHz}}) = -2G_{A+B}I(t) + N_{A+B}(t). \quad (\text{B.20})$$

Since Equations (B.13), (B.14), (B.15), and (B.16) are not suffered from the  $1/f$  noise, a single QUIET polarimeter module can provide the Stokes  $+Q$ ,  $-U$ ,  $+U$ , and  $-Q$

parameters for the  $Q1$ ,  $U1$ ,  $U2$ , and  $Q2$  diode respectively. From Equations (B.17), (B.18), (B.19), and (B.20), our module also provide the Stokes  $I$  parameter, but which is suffered from the  $1/f$  noise. Figure B.2 shows comparison of the noise power spectrum between demodulation and total power.

### B.3 Double-Demodulation

Unequal transmission coefficients in the phase switch do not suppress the  $1/f$  noise completely. In the previous section, we considered impeccable transmission coefficients; however, the coefficients are not perfect actually. We consider that the phase switch on the leg B is not perfect. Thereby the electric field amplitude on the leg B is written down

$$E_{\text{legB}}(t, f_B(t) : 4 \text{ kHz}) = f_B(t)g_B E_R + n_B, \quad (\text{B.21})$$

here  $f_B(t)$  represents the phase state on the leg B switching between  $+1$  and  $-\beta_B$  synchronized with 4 kHz, which corresponds to imperfection of the phase switch (when  $\beta_B = 1$ , the phase switch is perfect). The rectified signal for the  $Q1$  diode is given by

$$\begin{aligned} \langle |E_{Q1}|_{800\text{kHz}}^2 \rangle (t, +, f_B(t) : 4 \text{ kHz}) &= \langle |E_{\text{legA}}(t, +) + E_{\text{legB}}(t, f_B(t) : 4 \text{ kHz})|^2 \rangle \\ &= 2 (g_A^2 + f_B^2 g_B^2) I + (n_A^2 + f_B^2 n_B^2) + 4 f_B g_A g_B Q. \end{aligned} \quad (\text{B.22})$$

Then 4 kHz timestreams of demodulation for the  $Q1$  diode is described as

$$\begin{aligned} d_{Q1}(t = t_{4\text{kHz}}) &= \frac{\langle |E_{Q1}|^2 \rangle (t_i, +, 1) - \langle |E_{Q1}|^2 \rangle (t_{i+1}, +, -\beta_B)}{2} \\ &= (1 - \beta_B^2) G_B I(t) + (1 + \beta_B) G_{AB} Q(t) \\ &\quad + [n_A^2(t_i) - n_A^2(t_{i+1})] / 2 + [n_B^2(t_i) - \beta_B^2 n_B^2(t_{i+1})] / 2. \end{aligned} \quad (\text{B.23})$$

Equation (B.23) shows that the  $1/f$  noise on the leg B is not suppressed completely, though that on the leg A is suppressed completely. In addition, total power also still remains.

In order to reduce the residuals, we introduce additional phase switching on the leg A synchronized with 50 Hz

$$E_{\text{legB}}(t, f_A(t) : 50 \text{ Hz}) = f_A(t)g_A E_L + n_A \quad (\text{B.24})$$



where  $f_A(t)$  represents the phase state on the leg A switching between 1 and  $-\beta_A$  synchronized with 50 Hz. Taking difference between neighboring two samples of the rectified signals, we get 4 kHz timestreams of demodulation for the  $Q1$  diode again

$$\begin{aligned} d_{Q1}(t = t_{4\text{kHz}}, f_A(t) : 50\text{ Hz}) &= \frac{\langle |E_{Q1}|^2 \rangle(t_i, f_A, 1) - \langle |E_{Q1}|^2 \rangle(t_{i+1}, f_A, -\beta_B)}{2} \\ &= (1 - \beta_B^2) G_B I(t) + f_A (1 + \beta_B) G_{AB} Q(t) \\ &\quad + f_A^2 [n_A^2(t_i) - n_A^2(t_{i+1})] / 2 + [n_B^2(t_i) - \beta_B^2 n_B^2(t_{i+1})] / 2. \end{aligned} \quad (\text{B.25})$$

Since Equation (B.25) has two phase state synchronized with 50 Hz of the leg A, we can demodulate those demodulated timestreams again. After averaging Equation (B.25) synchronized with 100 Hz, we take difference between two neighboring samples synchronized with the phase state of the the leg A, so that we get 50 Hz timestreams of “double-demodulation” for the  $Q1$  diode

$$\begin{aligned} DD_{Q1}(t = t_{50\text{ Hz}}) &= \frac{\langle d_{Q1} \rangle_{100\text{ Hz}}(t_i, 1) - \langle d_{Q1} \rangle_{100\text{ Hz}}(t_{i+1}, -\beta_A)}{2} \\ &= \frac{(1 + \beta_A)(1 + \beta_B)}{2} G_{AB} Q(t) + \frac{(1 + \beta_A^2) N_A^w(t) + (1 + \beta_B^2) N_B^w(t)}{2} \Big|_{50\text{ Hz}}. \end{aligned} \quad (\text{B.26})$$

Here we assumed gains factors, total power, and Stokes  $Q1$  parameters do not change within 0.02 sec, and the white noise on each leg is evaluated by 50 Hz timestreams. The residuals of total power and  $1/f$  noise in Equation (B.25) are successfully canceled by double-demodulation.

In Equation (B.26), replacing gain factors including the imperfection of the phase switch with  $G_{AB}(\beta_A, \beta_B)$ , and the noise with  $N_{A+B}^w(t, \beta_A, \beta_B)$ , we get 50 Hz double-demodulated timestreams for each diode as follows:

$$DD_{Q1}(t = t_{50\text{ Hz}}) = 2G_{AB}(\beta_A, \beta_B)Q(t) + N_{A+B}^w(t, \beta_A, \beta_B), \quad (\text{B.27})$$

$$DD_{U1}(t = t_{50\text{ Hz}}) = -2G_{AB}(\beta_A, \beta_B)U(t) + N_{A+B}^w(t, \beta_A, \beta_B), \quad (\text{B.28})$$

$$DD_{U2}(t = t_{50\text{ Hz}}) = 2G_{AB}(\beta_A, \beta_B)U(t) + N_{A+B}^w(t, \beta_A, \beta_B), \quad (\text{B.29})$$

$$DD_{Q2}(t = t_{50\text{ Hz}}) = -2G_{AB}(\beta_A, \beta_B)Q(t) + N_{A+B}^w(t, \beta_A, \beta_B). \quad (\text{B.30})$$

Equations (B.27), (B.28), (B.29), and (B.30) show that double-demodulation can cancel out the imperfection of the phase switches and suppress the remaining  $1/f$  noise. Fig-

Figure B.2 shows comparison of the noise power spectrum between double-demodulation and demodulation.

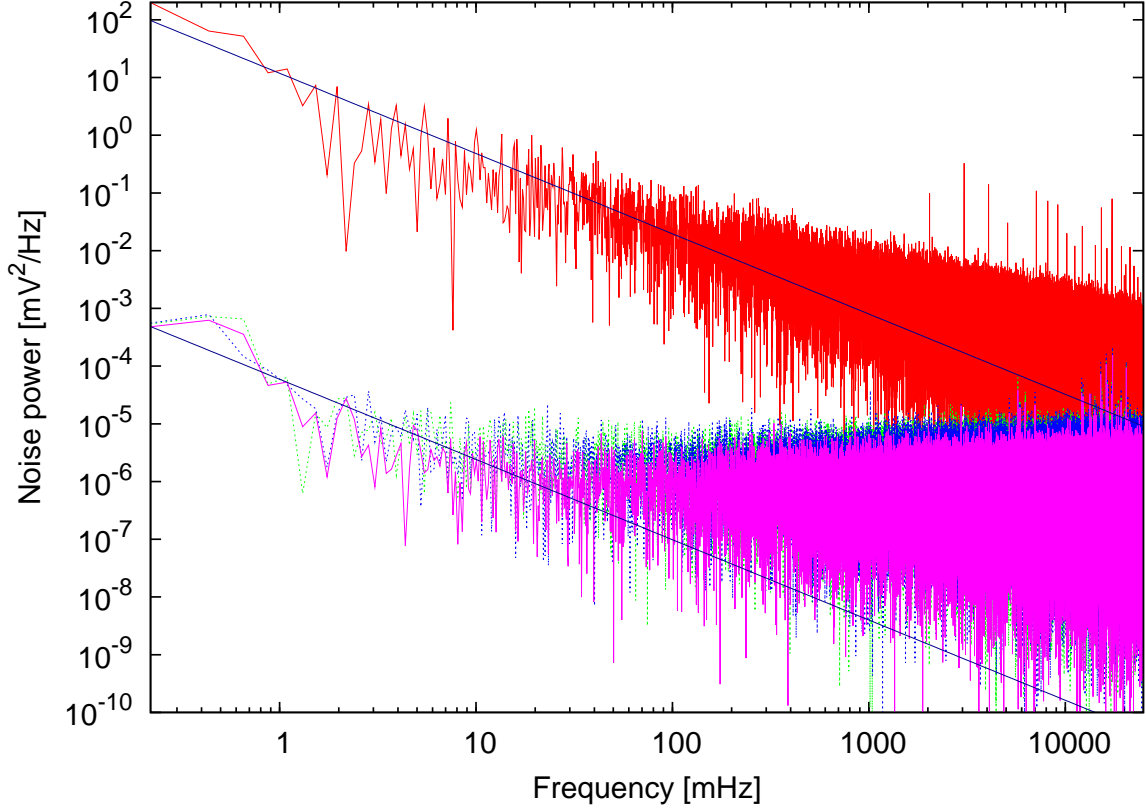


**Figure B.2:** Comparison of noise power spectra for the total power (red line), demodulation (the green line corresponds to “+” state of the 50 Hz phase switch, and blue one corresponds to the “−” state multiplied by  $-1$  in order to obtain the same sign) and double-demodulation (magenta line) from the  $Q1$  diode during the CMB observation. Dark blue lines corresponds to the  $1/f$  component for the total power and demodulated signals, which show that phase switching suppresses the  $1/f$  noise by a factor of  $\approx 10^5$ . This is the same figure as Figure 2.6.

Using a QUIET polarimeter module with both demodulation and double-demodulation techniques, we can simultaneously measure the Stokes  $+Q$ ,  $-U$ ,  $+U$ , and  $-Q$  parameters without the  $1/f$  noise contamination for the  $Q1$ ,  $U1$ ,  $U2$ , and  $Q2$  diode respectively. Here we do not have to take care of not only gain matching of both legs, but also perfection of the phase switching of each leg.

# Appendix C

## Impact of Possible Responsivity Fluctuation

### C.1 Overview

The error increase due to the absolute responsivity fluctuation is estimated in this appendix. This type of the error increase is so-called “multiplicative uncertainty” as also discussed in Chapter 9. because the error is proportional to the signal, e.g 10% of the  $E$ -mode or  $B$ -mode signal, and it has no  $E$ – $B$  mixing in general.

Mis-calibration of absolute responsivities increases errors directly; 10% of the mis-calibration results in 10% deviation on the maps and 20% deviation in the power spectra. In the following, we only discuss the error increase due to the absolute responsivity fluctuation.

Since we assume the coverage of the polarization angle is uniform and each responsivity of the Stokes  $Q$  and  $U$  parameters has no systematic bias, there is no difference between  $Q$  and  $U$ . For this reason, we only focus on  $Q$  in this appendix.

### C.2 Derivation of Formula

The RMS noise of each pixel in a map is given by  $\sigma_\alpha(i)$ , where the subscripts  $\alpha$  and  $i$  corresponds to indexes over maps and pixels, respectively. We can assume each map denoted with  $\alpha$  comes from observation of a single day. Performing naïve map-making

without any responsivity fluctuation over the season, we obtain an averaged map  $\bar{Q}(i)$  as follows:

$$\bar{Q}(i) = \frac{1}{\sum_{\alpha} 1/\sigma_{\alpha}^2(i)} \sum_{\alpha} \frac{Q_{\alpha}(i)}{\sigma_{\alpha}^2(i)} = \frac{1}{\sum_{\alpha} N_{\alpha}(i)} \sum_{\alpha} \mathcal{N}_{\alpha}(i) Q_{\alpha}(i) = \frac{1}{\mathcal{N}(i)} \sum_{\alpha} \mathcal{N}_{\alpha}(i) Q_{\alpha}(i), \quad (\text{C.1})$$

where  $Q_{\alpha}(i)$  is a reconstructed map from data for each map (day).

We introduce the factor of the mis-estimation for each map,  $R_{\alpha}$ , which is defined as

$$R_{\alpha} \equiv \frac{G_{\alpha}^{\text{m}}}{G_{\alpha}^{\text{t}}} \equiv R_0 (1 + \delta g_{\alpha}), \quad (\text{C.2})$$

where  $G_{\alpha}^{\text{m}}$  and  $G_{\alpha}^{\text{t}}$  correspond to the measured responsivity and true responsivity, respectively. Since we ignored shift of the responsivity, an averaged or expectation of  $\delta g_{\alpha}$  is zero, but deviation of the responsivity (or responsivity fluctuation) is given by

$$\sigma_g^2 \equiv \frac{1}{n_{\alpha}} \sum_{\alpha}^{n_{\alpha}} \delta g_{\alpha}^2. \quad (\text{C.3})$$

In contrast with Equation (C.1), we introduce a map with the mis-calibration:  $Q_{\alpha}^{\text{m}}(i) = Q_{\alpha}(i)/R_{\alpha}$ , and a noise with the mis-calibration:  $\sigma_{\alpha}^{\text{m}}(i) = \sigma_{\alpha}(i)/R_{\alpha}$ . Then an averaged map based on the measurement with the mis-calibration is

$$\bar{Q}^{\text{m}}(i) = \frac{1}{\mathcal{N}^{\text{m}}(i)} \sum_{\alpha} \mathcal{N}_{\alpha}^{\text{m}}(i) Q_{\alpha}^{\text{m}}(i) = \frac{1}{\mathcal{N}^{\text{m}}(i)} \sum_{\alpha} \frac{R_{\alpha} Q_{\alpha}(i)}{\sigma_{\alpha}^2(i)}, \quad (\text{C.4})$$

where

$$\mathcal{N}_{\alpha}^{\text{m}}(i) \equiv \sum_{\alpha} \frac{1}{(\sigma_{\alpha}^{\text{m}}(i))^2} = \sum_{\alpha} \frac{R_{\alpha}^2}{\sigma_{\alpha}^2(i)}. \quad (\text{C.5})$$

Here we have two assumptions which are very realistic:

- the (true) noise level  $\sigma_{\alpha}(i)$  is uncorrelated with the responsivity fluctuation.
- we can measure the correct RMS noise  $\sigma_{\alpha}^{\text{m}}(i)$  independently of the mis-calibration.

We define the expectation value of  $Q_{\alpha}(i)$  as follows:

$$\langle Q_{\alpha}(i) \rangle = Q^{\text{t}}(i). \quad (\text{C.6})$$

where  $Q^t(i)$  is the true values of the  $i$ -th pixel. Assuming that the overall responsivity calibration is correct, we obtain

$$\begin{aligned} Q^t(i) &= \langle Q_\alpha(i) \rangle = \langle \bar{Q}_\alpha^m(i) \rangle \\ &= \left\langle \frac{1}{\mathcal{N}^m(i)} \sum_\alpha \frac{R_\alpha Q_\alpha(i)}{\sigma_\alpha^2(i)} \right\rangle = \frac{1}{\mathcal{N}^m(i)} \sum_\alpha \frac{R_\alpha \langle Q_\alpha(i) \rangle}{\sigma_\alpha^2(i)} \\ &= Q^t(i) \times \frac{1}{\mathcal{N}^m(i)} \sum_\alpha \frac{R_\alpha}{\sigma_\alpha^2(i)}. \end{aligned} \quad (\text{C.7})$$

Combining Equation (C.7) with Equation (C.5), we obtain the following relation:

$$\sum_\alpha \frac{R_\alpha^2}{\sigma_\alpha^2(i)} = \sum_\alpha \frac{R_\alpha}{\sigma_\alpha^2(i)} \quad (\text{C.8})$$

If  $R_\alpha(i)$  is more stable than  $\sigma_\alpha(i)$ , which is a realistic assumption, and  $R_\alpha(i)$  and  $\sigma_\alpha(i)$  are independent each other, we can ignore contribution of  $\sigma_\alpha^2(i)$  terms in summation of Equation (C.8). Therefore, we obtain

$$\sum_\alpha R_\alpha^2 = R_0^2 \sum_\alpha (1 + \delta g_\alpha)^2 = n_\alpha R_0^2 \times \frac{1}{n_\alpha} \sum_\alpha (1 + \delta g_\alpha)^2 = n_\alpha R_0^2 (1 + \sigma_g^2), \quad (\text{C.9})$$

and

$$\sum_\alpha R_\alpha = n_\alpha R_0. \quad (\text{C.10})$$

Therefore we obtain the following relation

$$R_0 = \frac{1}{1 + \sigma_g^2}. \quad (\text{C.11})$$

Now we can evaluate the mis-estimation of the maps due to the mis-calibration. The expected fluctuation of a reconstructed map with and without the responsivity variation are given by

$$\delta \bar{Q}^m(i) \equiv \bar{\sigma}^m(i) = \frac{1}{\sqrt{\mathcal{N}^m(i)}} \quad \text{and} \quad \delta \bar{Q}(i) \equiv \bar{\sigma}(i) = \frac{1}{\sqrt{\mathcal{N}(i)}}, \quad \text{respectively.} \quad (\text{C.12})$$

Their ratio is

$$\begin{aligned} \frac{(\bar{\sigma}^m(i))^2}{\bar{\sigma}^2(i)} &= \frac{\sum_\alpha (\mathcal{N}_\alpha(i))^{-1}}{\sum_\alpha (\mathcal{N}_\alpha^m(i))^{-1}} = \frac{\sum_\alpha 1/\sigma_\alpha^2(i)}{\sum_\alpha R_\alpha^2/\sigma_\alpha^2(i)} = \left\{ \left( \sum_\alpha \frac{1}{\sigma_\alpha^2(i)} \right)^{-1} \left( \sum_\alpha \frac{R_\alpha^2}{\sigma_\alpha^2(i)} \right) \right\}^{-1} \\ &= \{R_0^2 (1 + \sigma_g^2)\}^{-1} = \left\{ (1 + \sigma_g^2)^{-2} (1 + \sigma_g^2) \right\}^{-1} = 1 + \sigma_g^2. \end{aligned} \quad (\text{C.13})$$

Consequently, we obtain the expected error increase on the map

$$\frac{\bar{\sigma}^{\text{m}}(i)}{\bar{\sigma}(i)} = \sqrt{1 + \sigma_g^2} \simeq 1 + \frac{\sigma_g^2}{2}. \quad (\text{C.14})$$

Even if we ignore 20% of the absolute responsivity fluctuation, Equation (C.14) leads that the error increases by only 2% on the maps, or only 4% in the power spectra.

### C.3 Requirement for QUIET Q-band

We can ignore error increase if it is much smaller than the statistical error. Even if we obtain an additional error by 10% of the statistical error, the error increase in total is negligible ( $\sqrt{1.00^2 + 0.10^2} \approx 1.00$ ). For that reason and Equation (C.14), less than 14% of the absolute responsivity fluctuation can be permitted as show in Figure C.1.

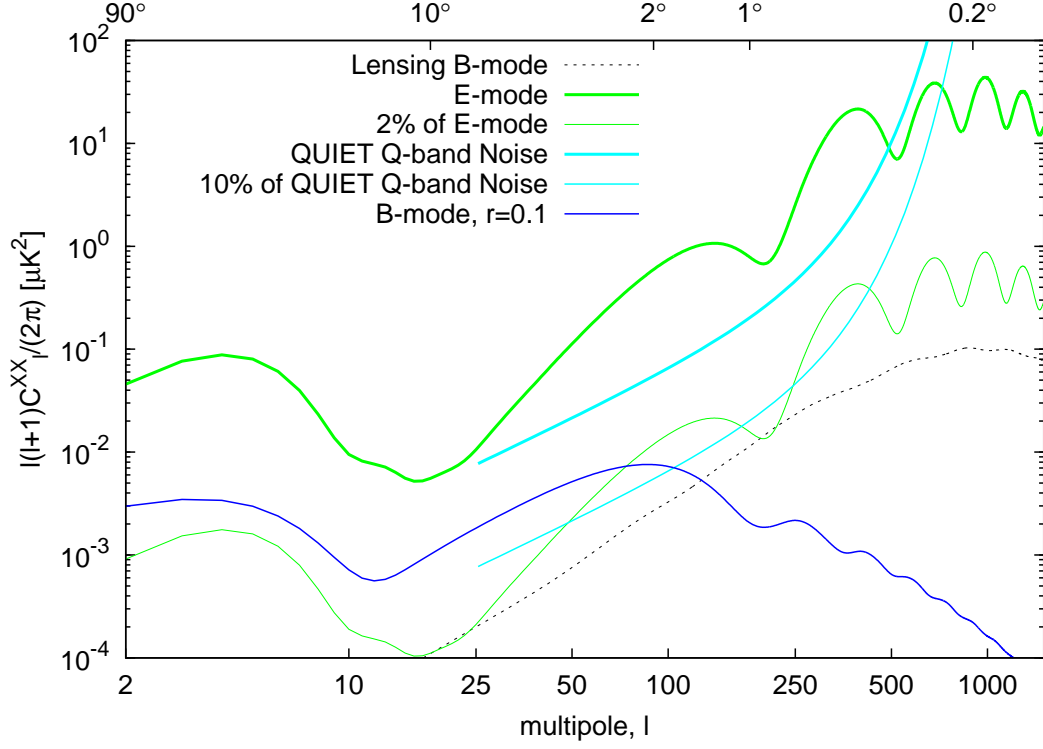


**Figure C.1:** Comparison between the  $E$ -mode signal level (green curves) and permitted error increase (cyan curves). An additional error by 10% of the statistical error (thin cyan curve) is allowed to ignore because the error increase in total is negligibly small. Roughly speaking, 10% of the statistical error is equivalent to about 2% of the  $E$ -mode signal (thin green curve). Therefore, less than 14% of the absolute responsivity fluctuation can be permitted from Equation (C.14).





# Appendix D

## Calibration Sources

Three sources (the sky dips, Moon, and sparse wire grid) also used for the calibration. In Chapter 4, we mainly discussed comparison between the calibration using Tau A and them. We summarize further details for each calibration in this appendix.

### D.1 Sky dips

#### D.1.1 Overview

By changing the elevation of the telescope boresight, we can measure relative temperature shifts. We can use them for the relative responsivity calibration. This is called a sky dip measurement (also known as an elevation nod). Our sky dip typically consists of three elevation nods of a  $3^\circ$  amplitude. However, calibration of the absolute detector responsivity is difficult because absolute temperature of the atmosphere in microwave frequency highly depends on the model.

The sky dip measurements were performed at the beginning of each CES. Therefore, it is the most frequent measurements in our calibrations. As a result, we can track the time-trend of the relative detector responsivities, which may vary due to different environmental conditions in the electronics enclosure, for each module and for each diode throughout the day. In the combination with the sky dips and the Tau A results, we can construct a detector responsivity model for each module-diode in our whole observation season. More details on the responsivity model is discussed in § 4.3.

### D.1.2 TOD Analysis

A two-dimensional (elevation:  $\theta$ , and time:  $t$ ) maximum likelihood analysis is performed to analyze the sky dips data. We parameterized three quantities for each module and each diode, the relative responsivity:  $g_0$  (mV/K), the time-drift:  $\gamma$  (mV/sec.), and the receiver temperature:  $\kappa$  (K).  $\kappa$  is equal to receiver temperature if we know the temperature model of the atmosphere perfectly. If not, it is just a parameter of the time constant. The likelihood and its PDF is given by

$$\mathcal{L} = \prod_i f_i(v_i, \sigma_i, \theta_i, t_i; g_{\text{skydip}}, \gamma, \kappa), \quad (\text{D.1})$$

$$f_i = \exp \left[ -\frac{\{v_i - V_i(\theta_i, t_i; g_{\text{skydip}}, \gamma, \kappa)\}^2}{2\sigma_i^2} \right], \quad (\text{D.2})$$

where  $v_i$  is the total power voltage,  $\theta_i$  is the elevation angle,  $t_i$  is time for each sample  $i$ , and  $V_i$  is a model of the total power voltage given by

$$V_i = g_{\text{skydip}} \{T_{\text{sky}}^0(\theta_i; T_z^0) + \kappa + T_{\text{CMB}}\} + \gamma t_i, \quad \text{where } T_{\text{sky}}^0 = \frac{T_z^0}{\sin \theta_i} = T_z^0 \csc \theta_i. \quad (\text{D.3})$$

$\sigma_i$  is the RMS from  $v_i$  samples every one second, where an effect of the elevation change to  $\sigma_i$  is negligibly small. We assume that the constant temperature of the atmosphere is  $T_z^0 = 8.5$  K, and the CMB temperature is  $T_{\text{CMB}} = 2.73$  K.

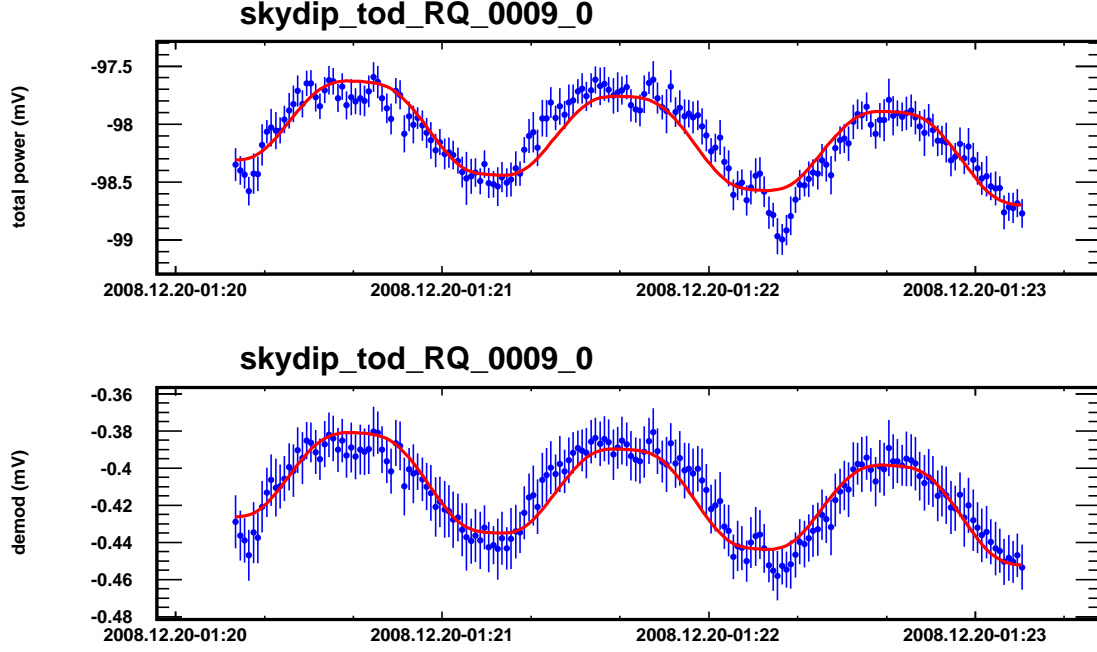
On the sky dips measurement, the polarization output voltage is given by just the leakage from the total power voltage with an offset. The comparison between the demod and the total power provides the  $I \rightarrow Q/U$  leakage.

Figure D.1 shows an example of the sky dips data and the fitted results. Since the time-drift is followed very well, the temperature change due to the elevation change is well fitted.

### D.1.3 Sky Temperature Correction

The zenith temperature, which depends on both frequency and the PWV, is based on the ATM model mentioned in Chapter 3. In our frequency region, the PWV dependence on the temperature is smaller than the frequency dependence. We assume a linear relation between the PWV and the temperature,

$$T_z(x) = T_z^0(1 + \alpha x), \quad (\text{D.4})$$



**Figure D.1:** The skydip data (blue dots) and fitted results (red line) as a function of time. Each data point is averaged by one second and its error is evaluated by the RMS for one second.

where  $x$  is the PVW (mm),  $\alpha$  is the slope of the first order correction ( $\text{mm}^{-1}$ ), and  $T_z^0 = T_z(x = 0)$ . From the data, we found  $\alpha \sim 4\% \text{ mm}^{-1}$  during our observation season, then we corrected it in the analysis. This result is consistent with the expectation from the ATM model.

#### D.1.4 Results

We confirmed that the total power detector responsivities were stable and almost time independent. Figure D.2 shows the time-trend of the total power detector responsivity on the center module and their histograms.

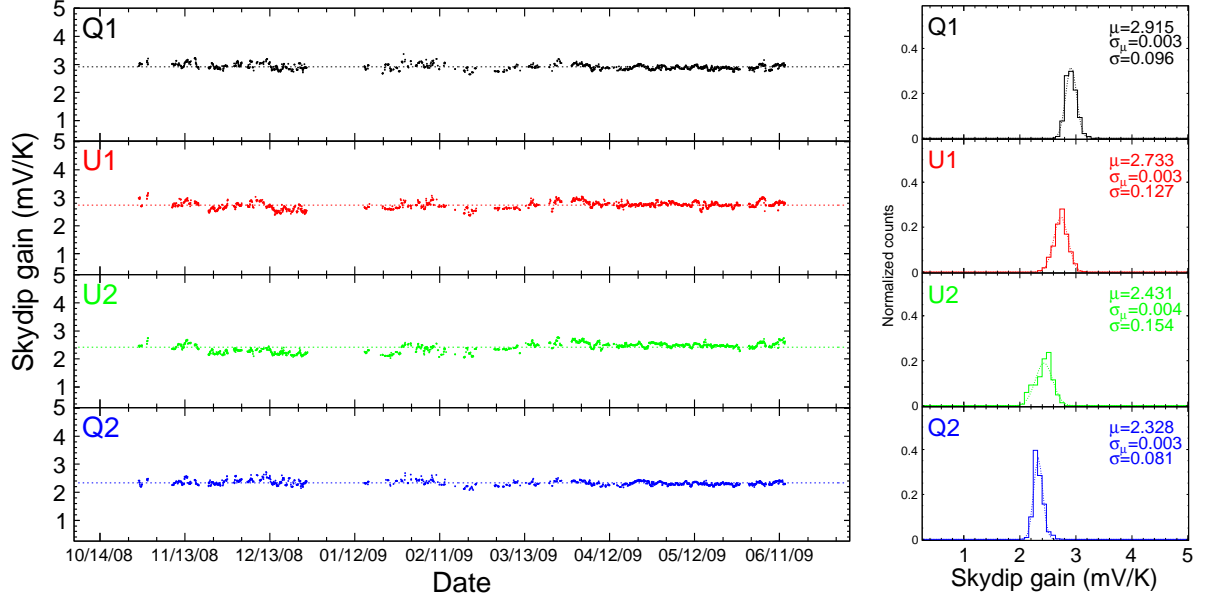


**Figure D.2:** Left: Time-trend of the detector responsivities from the sky dips measurements on the center module. Right: Histograms of the left plots.

## D.2 The Moon

### D.2.1 Overview

The Moon is a useful calibration source because it is much brighter than the other calibration sources. However, it is difficult to extract the calibration quantities from the Moon observations without systematic errors because of the complicated nature of the Moon source modeling. The Moon angular diameter is slightly bigger than the QUIET beamwidth. It means that internal details such as the temperature profile across the Moon's face appear in the data and cause confusion in the analysis.

The main purpose of the Moon observations for QUIET is to measure the detector angle for each module-diode during the whole observation season. We can determine the polarization and total power detector responsivities and the  $I \rightarrow Q/U$  leakage.

### D.2.2 Measurements, Analysis, and Results

Our measurements, analysis, and results of the Moon are reported in [115]. The comparison of the detector angle among the Tau A, Moon, and wire grid is found in § 4.4. The comparison of the  $I \rightarrow Q/U$  leakage is also found in § 4.5. Here we showed the results

of the possible detector angle fluctuation (Table D.1), which are used for the systematic error estimation as described in § 9.4.

Module	<i>Q1-0</i>	<i>Q1-1</i>	<i>U1-0</i>	<i>U1-1</i>	<i>U2-0</i>	<i>U2-1</i>	<i>Q2-0</i>	<i>Q2-1</i>
<i>RQ00</i>	1.03°	0.91°	0.78°	0.82°	1.11°	1.11°	0.99°	0.87°
<i>RQ01</i>	1.81°	1.40°	1.61°	1.86°	2.19°	2.19°	1.69°	1.73°
<i>RQ02</i>	3.42°	3.17°	3.71°	3.22°	2.84°	2.64°	3.34°	3.26°
<i>RQ03</i>	1.23°	1.36°	0.84°	0.76°	0.85°	0.64°	1.19°	0.85°
<i>RQ04</i>	1.02°	1.02°	1.02°	0.72°	0.85°	0.93°	1.02°	0.93°
<i>RQ05</i>	0.98°	0.98°	0.89°	0.98°	0.72°	0.93°	0.81°	1.02°
<i>RQ06</i>	1.02°	1.32°	0.89°	1.02°	1.27°	0.85°	1.10°	1.27°
<i>RQ07</i>	1.48°	1.61°	1.48°	1.48°	1.61°	1.48°	1.27°	1.44°
<i>RQ08</i>	1.23°	1.32°	0.89°	0.85°	–	–	0.93°	0.98°
<i>RQ09</i>	0.93°	1.06°	0.93°	1.02°	0.85°	0.93°	0.85°	0.85°
<i>RQ10</i>	0.81°	0.89°	0.98°	0.98°	1.06°	0.72°	0.72°	0.85°
<i>RQ11</i>	1.24°	0.89°	2.06°	0.93°	1.03°	1.06°	1.07°	1.10°
<i>RQ12</i>	0.87°	1.11°	0.87°	1.07°	0.87°	0.91°	0.78°	0.74°
<i>RQ13</i>	0.91°	0.91°	1.03°	0.87°	0.91°	1.07°	0.87°	1.11°
<i>RQ14</i>	1.06°	0.85°	1.70°	1.70°	1.61°	1.61°	1.06°	0.98°
<i>RQ15</i>	2.19°	2.43°	2.47°	2.02°	1.28°	1.03°	2.06°	1.73°

**Table D.1:** The RMS of the detector angles obtained by the Moon measurements from [115]. The suffix of each column (0 or 1) corresponds to the two states of the 50 Hz phase switching because the Moon measurements provide independent angle results for each. We average the results of the two phase states and use it the RMS of the corresponding diode.

### D.3 Sparse Wire Grid

The wire grid is also a useful calibration source to determine the detector angle. It is difficult to determine the absolute angle from the wire grid measurements in the QUIET Q-band because the setup of the measurement was not appropriate for that purpose (we

had no encoder). The wire grid measurements were taken at the end of the Q-band observation.

A thin wire scatters radiation that is polarized with its electric field parallel to the wire while allowing the orthogonal polarization to pass<sup>a</sup> [116]. As the wires rotate, the polarization signal is modulated at twice the rotation frequency. Hence we can obtain the detector angle for each module-diode. It is very difficult to calculate the absolute amplitude of the unpolarized and polarized signal induced by such a wire grid because it would be necessary to determine where all of the reflected rays are terminated. For this reason, we use the wire grid results only for the detector angle model.

Our analysis and results are described in [117]. Table D.2 shows the results of the detector angles from the wire grid measurements. The comparison of the detector angle among the Tau A, Moon, and wire grid is found in [118], which is used in § 4.4 to evaluate the systematic error of the detector angles.

---

<sup>a</sup>For parallel wires with spacing much less than the wavelength, the wire array fully reflects one linear polarization while transmitting the other. Sparse arrays are used for QUIET.

Module	$Q1$	$U\ 1$	$U2$	$Q2$
$RQ00$	$62.0^\circ \pm 2.0^\circ$	$105.9^\circ \pm 0.7^\circ$	$15.9^\circ \pm 0.6^\circ$	$144.8^\circ \pm 0.6^\circ$
$RQ01$	$78.0^\circ \pm 0.5^\circ$	$122.2^\circ \pm 0.7^\circ$	$34.6^\circ \pm 0.8^\circ$	$162.9^\circ \pm 0.4^\circ$
$RQ02$	$74.1^\circ \pm 1.0^\circ$	$115.0^\circ \pm 1.4^\circ$	$25.1^\circ \pm 0.6^\circ$	$159.8^\circ \pm 0.5^\circ$
$RQ03$	$70.0^\circ \pm 1.8^\circ$	$112.5^\circ \pm 0.6^\circ$	$22.0^\circ \pm 0.6^\circ$	$155.1^\circ \pm 0.7^\circ$
$RQ04$	$59.6^\circ \pm 0.6^\circ$	$105.2^\circ \pm 0.7^\circ$	$15.0^\circ \pm 0.7^\circ$	$142.4^\circ \pm 0.7^\circ$
$RQ05$	$67.9^\circ \pm 0.7^\circ$	$110.2^\circ \pm 0.7^\circ$	$23.3^\circ \pm 0.6^\circ$	$151.9^\circ \pm 0.4^\circ$
$RQ06$	$65.2^\circ \pm 2.4^\circ$	$108.7^\circ \pm 0.8^\circ$	$18.5^\circ \pm 0.8^\circ$	$148.7^\circ \pm 1.2^\circ$
$RQ07$	$57.6^\circ \pm 0.6^\circ$	$105.0^\circ \pm 1.2^\circ$	$15.5^\circ \pm 1.4^\circ$	$142.5^\circ \pm 0.4^\circ$
$RQ08$	$66.4^\circ \pm 0.6^\circ$	$109.9^\circ \pm 0.6^\circ$	—	$149.8^\circ \pm 0.4^\circ$
$RQ09$	$72.5^\circ \pm 0.8^\circ$	$116.7^\circ \pm 0.4^\circ$	$25.2^\circ \pm 0.5^\circ$	$154.9^\circ \pm 0.4^\circ$
$RQ10$	$64.4^\circ \pm 0.6^\circ$	$106.9^\circ \pm 0.6^\circ$	$17.2^\circ \pm 1.3^\circ$	$147.8^\circ \pm 0.4^\circ$
$RQ11$	$65.7^\circ \pm 0.9^\circ$	$113.2^\circ \pm 1.5^\circ$	$24.5^\circ \pm 1.1^\circ$	$151.1^\circ \pm 0.9^\circ$
$RQ12$	$67.0^\circ \pm 0.6^\circ$	$111.1^\circ \pm 0.7^\circ$	$21.6^\circ \pm 0.8^\circ$	$151.9^\circ \pm 0.4^\circ$
$RQ13$	$52.7^\circ \pm 0.6^\circ$	$094.9^\circ \pm 0.7^\circ$	$06.0^\circ \pm 1.0^\circ$	$136.5^\circ \pm 0.6^\circ$
$RQ14$	$60.8^\circ \pm 1.2^\circ$	$106.2^\circ \pm 0.7^\circ$	$14.0^\circ \pm 0.7^\circ$	$146.0^\circ \pm 1.6^\circ$
$RQ15$	$53.1^\circ \pm 0.9^\circ$	$108.2^\circ \pm 0.8^\circ$	$-8.0^\circ \pm 2.4^\circ$	$139.4^\circ \pm 0.4^\circ$

**Table D.2:** The detector angles obtained by the wire grid measurements from [117].





# Appendix E

## Antenna-to-Thermodynamic Correction

The relation between the blackbody spectrum ( $I_\nu$ ) given by Equation (1.4) and the antenna temperature ( $T_{\text{ant}}$ ) is generally defined as

$$T_{\text{ant}} \equiv \frac{c^2}{2\nu^2 k} I_\nu(T). \quad (\text{E.1})$$

The antenna temperature relative to the CMB temperature is given by

$$\frac{T_{\text{ant}}^{\text{CMB}}}{T} = \frac{x}{e^x - 1} + \frac{\Delta T}{T} \frac{x^2 e^x}{(e^x - 1)^2}, \quad \text{where } x = \frac{h\nu}{kT} \quad (\text{E.2})$$

The first term is the correction for the temperature itself and second one is that for the anisotropy. Because of that, it is useful to stick to antenna temperature units for purpose of calibration and foreground.

The correction of the polarization (power spectrum) for the QUIET Q-band is 1.049 (1.100); the correction of the polarization (power spectrum) for the QUIET W-band is 1.253 (1.571), respectively. Figure E.1 shows the correction factors from 10 GHz to 150 GHz.

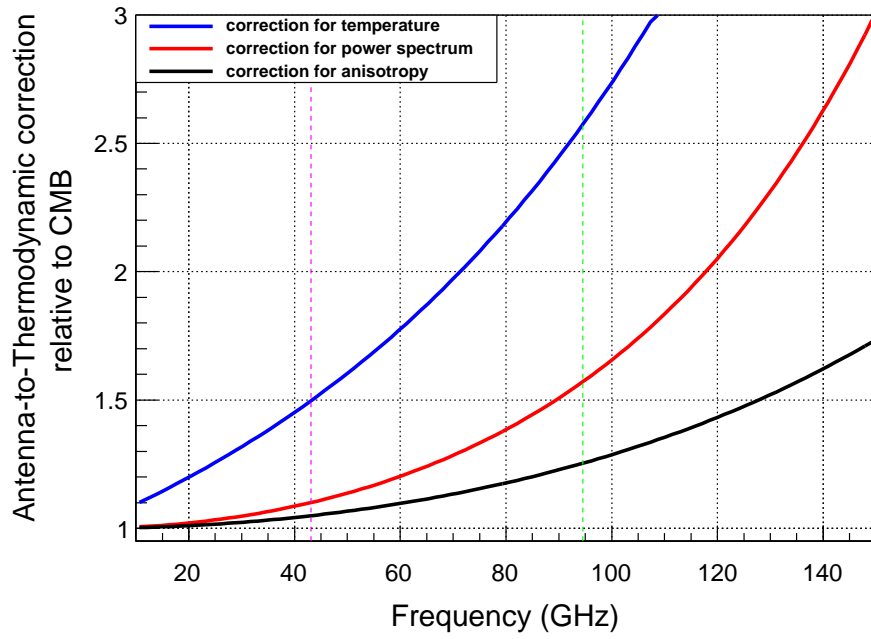


**Figure E.1:** Factors of antenna-to-thermodynamic units correction for the temperature itself (blue), both temperature and polarization anisotropy (black), and their power spectra (red) relative to the CMB temperature given by Equation (E.2) for frequency ranges from 10 GHz to 150 GHz. The vertical magenta (green) line corresponds to the QUIET Q-band (W-band) frequency, respectively.

# Appendix F

## Power Spectrum Estimation in the Null Tests

The simple difference map,  $m_{\text{diff}} = (m_0 - m_1)/2$ , does not provide perfect null power spectrum except the ideal case. The following three effects in real dataset are the reasons of such effect:

- (a) the noise maps are NOT always the same among the divided datasets.
- (b) the averaged transfer functions are NOT always the same among the datasets.
- (c) the cross-linking is NOT always the same among the datasets.

Therefore, we can not obtain a null power spectrum from the difference map,  $m_{\text{diff}}$ , in these cases. In order to obtain a true null power spectrum, we have to incorporate those effects for the null spectrum estimation as follows:

1. We fix the pseudo- $C_\ell$  common weighting function from two maps:

$$W_i = \frac{1}{\sigma_{0i}^2 + \sigma_{1i}^2}, \quad (\text{F.1})$$

then we evaluate the mode-mode coupling kernel ( $M_{\ell\ell'}$ ) for this weighting function.

2. We compute the transfer function  $F_\ell^{00}$ ,  $F_\ell^{11}$  and  $F_\ell^{01}$  using MC simulations. These

three are defined as

$$\left\langle \tilde{C}_\ell(m_0) \right\rangle = \sum_{\ell'} M_{\ell\ell'} F_{\ell'}^{00} B_{\ell'}^2 \langle C_{\ell'} \rangle + (\text{noise bias}) \quad (\text{F.2})$$

$$\left\langle \tilde{C}_\ell(m_1) \right\rangle = \sum_{\ell'} M_{\ell\ell'} F_{\ell'}^{11} B_{\ell'}^2 \langle C_{\ell'} \rangle + (\text{noise bias}) \quad (\text{F.3})$$

$$\left\langle \tilde{C}_\ell(m_0, m_1) \right\rangle = \sum_{\ell'} M_{\ell\ell'} F_{\ell'}^{01} B_{\ell'}^2 \langle C_{\ell'} \rangle + (\text{noise bias}). \quad (\text{F.4})$$

3. We can define a null power spectrum estimator as

$$\tilde{C}_\ell^{\text{null}} = \frac{\tilde{C}_\ell(m_0)}{F_\ell^{00}} - 2 \frac{\tilde{C}_\ell(m_0, m_1)}{F_\ell^{01}} + \frac{\tilde{C}_\ell(m_1)}{F_\ell^{11}}; \quad \therefore \quad \hat{C}_\ell^{\text{null}} = \sum_{\ell'} M_{\ell\ell'}^{-1} \tilde{C}_{\ell'}. \quad (\text{F.5})$$

4. We assign statistical errors using MC simulations.

# Appendix G

## Experiment Summary Table

Table G.1 summarizes the QUIET Q-band experiment. Details on the instrument are described in Chapters 2 and 5; those on the site and observation are found in Chapter 3; those on the result are evaluated in Chapter 8.

Category	Name	Value	Description
Instrument	Array sensitivity	$69 \mu\text{K}\sqrt{\text{s}}$	
	Sensitivity per module	$280 \mu\text{K}\sqrt{\text{s}}$	$Q$ and $U$ diodes combined
	Sensitivity per diode	$625 \mu\text{K}\sqrt{\text{s}}$	for each diode ( $Q1/U1/U2/Q2$ )
	White noise correlation	0.22	averaging over $Q1Q2/U1U2$ pairs
	$1/f$ noise knee frequency	5.5 mHz	median ( $\ll f_{\text{scan}} = 100 \text{ mHz}$ )
	Phase switch frequency	4 kHz / 50 Hz	primary (leg A) / secondary (leg B)
	Number of elements	62 / 68	worked / total
	Central frequency	$43.1 \pm 0.4 \text{ GHz}$	average
	Bandwidth	$7.6 \pm 0.5 \text{ GHz}$	average
	Primary mirror diameter	1.4 m	
	Field of view	$7^\circ$	diameter on the sky
	Beamwidth	$27.3'$	FWHM ( $= \sigma\sqrt{8\ln 2}$ )
Site	Altitude	5,080 m	Chajnantor plateau,
	Coordinates	$67^\circ 45' 42''\text{W}$ $23^\circ 01' 42''\text{S}$	Atacama desert, Chile
Observation	Duration	Oct. 24, 2008 – Jun. 13, 2009	
	Observing hours	3,458 hours	all (CMB/Calibration/Galactic)
	Number of CMB patches	4	
	Observed area	$\approx 1,000$ square degrees	all four CMB patches combined
	Scan half-amplitude	$7.5^\circ$	on the sky
	Scan speed	$4.5^\circ/\text{sec.}$	average, in azimuth
	Scan period	10–22 seconds	
Patch	CMB-1	$12^{\text{h}} 04^{\text{m}}, -39^\circ 00'$	(closest to the Galactic plane)
	CMB-2	$5^{\text{h}} 12^{\text{m}}, -39^\circ 00'$	RA, Dec. (center position),
	CMB-3	$0^{\text{h}} 48^{\text{m}}, -48^\circ 00'$	patch size: $15^\circ \times 15^\circ$
	CMB-4	$22^{\text{h}} 44^{\text{m}}, -36^\circ 00'$	
Result	Tensor-to-scalar ratio	$r = 0.35^{+1.06}_{-0.87}, r < 2.2$	68% C.L., 95% C.L. upper limit

**Table G.1:** Summary table of the QUIET Q-band experiment described in this dissertation.

# Bibliography

- [1] S. Burles, K. M. Nollett, and M. S. Turner. Big-Bang Nucleosynthesis: Linking Inner Space and Outer Space. *ArXiv Astrophysics e-prints*, March 1999.
- [2] D. J. Fixsen and J. C. Mather. The Spectral Results of the Far-Infrared Absolute Spectrophotometer Instrument on COBE. *ApJ*, 581:817–822, December 2002.
- [3] J. C. Mather, D. J. Fixsen, R. A. Shafer, C. Mosier, and D. T. Wilkinson. Calibrator Design for the COBE Far-Infrared Absolute Spectrophotometer (FIRAS). *ApJ*, 512:511–520, February 1999.
- [4] D. J. Fixsen, E. S. Cheng, J. M. Gales, J. C. Mather, R. A. Shafer, and E. L. Wright. The Cosmic Microwave Background Spectrum from the Full COBE FIRAS Data Set. *ApJ*, 473:576–+, December 1996.
- [5] COsmic Background Explorer / FIRAS. FIRAS PROJECT DATA SETS.
- [6] E. Corbelli and P. Salucci. The extended rotation curve and the dark matter halo of M33. *MNRAS*, 311:441–447, January 2000.
- [7] B. Carr. Dark matter: problems and solutions. *Helvetica Physica Acta*, 69:434–453, November 1996.
- [8] Scott Dodelson. *Modern Cosmology*. Academic Press, 1 edition, March 2003.
- [9] T. Padmanabhan. *Structure Formation in the Universe*. Cambridge University Press, June 1993.
- [10] Andrew R. Liddle and David H. Lyth. *Cosmological Inflation and Large-Scale Structure*. Cambridge University Press, April 2000.

- [11] W. Hu, N. Sugiyama, and J. Silk. The Physics of Microwave Background Anisotropies. *ArXiv Astrophysics e-prints*, April 1996.
- [12] WMAP Science Team. WMAP data product images.
- [13] D. Larson, J. Dunkley, G. Hinshaw, E. Komatsu, M. R. Nolta, C. L. Bennett, B. Gold, M. Halpern, R. S. Hill, N. Jarosik, A. Kogut, M. Limon, S. S. Meyer, N. Odegard, L. Page, K. M. Smith, D. N. Spergel, G. S. Tucker, J. L. Weiland, E. Wollack, and E. L. Wright. Seven-Year Wilkinson Microwave Anisotropy Probe (WMAP) Observations: Power Spectra and WMAP-Derived Parameters. *ArXiv e-prints*, January 2010.
- [14] E. R. Harrison. Fluctuations at the Threshold of Classical Cosmology. *Phys. Rev. D*, 1:2726–2730, May 1970.
- [15] Y. B. Zel’Dovich. Gravitational instability: An approximate theory for large density perturbations. *A&A*, 5:84–89, March 1970.
- [16] P. J. E. Peebles and J. T. Yu. Primeval Adiabatic Perturbation in an Expanding Universe. *ApJ*, 162:815–+, December 1970.
- [17] A. A. Starobinskiĭ. Spectrum of relict gravitational radiation and the early state of the universe. *Soviet Journal of Experimental and Theoretical Physics Letters*, 30:682–+, December 1979.
- [18] A. A. Starobinsky. A new type of isotropic cosmological models without singularity. *Physics Letters B*, 91:99–102, March 1980.
- [19] K. Sato. Cosmological baryon-number domain structure and the first order phase transition of a vacuum. *Physics Letters B*, 99:66–70, February 1981.
- [20] A. H. Guth. Inflationary universe: A possible solution to the horizon and flatness problems. *Phys. Rev. D*, 23:347–356, January 1981.
- [21] A. D. Linde. A new inflationary universe scenario: A possible solution of the horizon, flatness, homogeneity, isotropy and primordial monopole problems. *Physics Letters B*, 108:389–393, February 1982.



- [22] A. Albrecht and P. J. Steinhardt. Cosmology for grand unified theories with radiatively induced symmetry breaking. *Physical Review Letters*, 48:1220–1223, April 1982.
- [23] A. D. Linde. Chaotic inflation. *Physics Letters B*, 129:177–181, September 1983.
- [24] L. Kofman, A. Linde, and A. A. Starobinsky. Reheating after inflation. *Physical Review Letters*, 73:3195–3198, December 1994.
- [25] H. Kodama and M. Sasaki. Cosmological Perturbation Theory. *Progress of Theoretical Physics Supplement*, 78:1–+, 1984.
- [26] R. Brandenberger, H. Feldman, and V. Mukhanov. Classical and quantum theory of perturbations in inflationary universe models. In *Evolution of the Universe and its Observational Quest*, pages 19–30, 1994.
- [27] K. A. Malik and D. Wands. Cosmological perturbations. *Phys. Rep.*, 475:1–51, May 2009.
- [28] J. M. Bardeen, P. J. Steinhardt, and M. S. Turner. Spontaneous creation of almost scale-free density perturbations in an inflationary universe. *Phys. Rev. D*, 28:679–693, August 1983.
- [29] N. D. Birrell and P. C. W. Davies. *Quantum fields in curved space*. 1982.
- [30] E. Komatsu, K. M. Smith, J. Dunkley, C. L. Bennett, B. Gold, G. Hinshaw, N. Jarosik, D. Larson, M. R. Nolta, L. Page, D. N. Spergel, M. Halpern, R. S. Hill, A. Kogut, M. Limon, S. S. Meyer, N. Odegard, G. S. Tucker, J. L. Weiland, E. Wollack, and E. L. Wright. Seven-Year Wilkinson Microwave Anisotropy Probe (WMAP) Observations: Cosmological Interpretation. *ArXiv e-prints*, January 2010.
- [31] T. L. Smith, M. Kamionkowski, and A. Cooray. Direct detection of the inflationary gravitational-wave background. *Phys. Rev. D*, 73(2):023504–+, January 2006.
- [32] Matias Zaldarriaga and Uro š Seljak. All-sky analysis of polarization in the microwave background. *Phys. Rev. D*, 55(4):1830–1840, Feb 1997.

- [33] M. Zaldarriaga. *Fluctuations in the cosmic microwave background*. PhD thesis, MASSACHUSETTS INSTITUTE OF TECHNOLOGY, 1998.
- [34] W. Hu and M. White. A CMB polarization primer. *New Astron*, 2:323–344, October 1997.
- [35] Matias Zaldarriaga and Uro š Seljak. Gravitational lensing effect on cosmic microwave background polarization. *Phys. Rev. D*, 58(2):023003, Jun 1998.
- [36] A. Challinor and H. Peiris. Lecture notes on the physics of cosmic microwave background anisotropies. In M. Novello & S. Perez, editor, *American Institute of Physics Conference Series*, volume 1132 of *American Institute of Physics Conference Series*, pages 86–140, May 2009.
- [37] A. Lewis, A. Challinor, and A. Lasenby. Efficient Computation of Cosmic Microwave Background Anisotropies in Closed Friedmann-Robertson-Walker Models. *ApJ*, 538:473–476, August 2000.
- [38] S. Hild, S. Chelkowski, and A. Freise. Pushing towards the ET sensitivity using ‘conventional’ technology. *ArXiv e-prints*, October 2008.
- [39] B. P. Abbott, R. Abbott, F. Acernese, R. Adhikari, P. Ajith, B. Allen, G. Allen, M. Alshourbagy, R. S. Amin, S. B. Anderson, and et al. An upper limit on the stochastic gravitational-wave background of cosmological origin. *Nature*, 460:990–994, August 2009.
- [40] H. V. Peiris. *First year Wilkinson Microwave Anisotropy Probe results: Cosmological parameters and implications for inflation*. PhD thesis, PRINCETON UNIVERSITY, 2003.
- [41] H. C. Chiang, P. A. R. Ade, D. Barkats, J. O. Battle, E. M. Bierman, J. J. Bock, C. D. Dowell, L. Duband, E. F. Hivon, W. L. Holzapfel, V. V. Hristov, W. C. Jones, B. G. Keating, J. M. Kovac, C. L. Kuo, A. E. Lange, E. M. Leitch, P. V. Mason, T. Matsumura, H. T. Nguyen, N. Ponthieu, C. Pryke, S. Richter, G. Rocha, C. Sheehy, Y. D. Takahashi, J. E. Tolan, and K. W. Yoon. Measurement of cosmic

microwave background polarization power spectra from two years of bicep data. *The Astrophysical Journal*, 711(2):1123, 2010.

- [42] C. L. Reichardt, P. A. R. Ade, J. J. Bock, J. R. Bond, J. A. Brevik, C. R. Contaldi, M. D. Daub, J. T. Dempsey, J. H. Goldstein, W. L. Holzapfel, C. L. Kuo, A. E. Lange, M. Lueker, M. Newcomb, J. B. Peterson, J. Ruhl, M. C. Runyan, and Z. Staniszewski. High-Resolution CMB Power Spectrum from the Complete ACBAR Data Set. *ApJ*, 694:1200–1219, April 2009.
- [43] M. L. Brown, P. Ade, J. Bock, M. Bowden, G. Cahill, P. G. Castro, S. Church, T. Culverhouse, R. B. Friedman, K. Ganga, W. K. Gear, S. Gupta, J. Hinderks, J. Kovac, A. E. Lange, E. Leitch, S. J. Melhuish, Y. Memari, J. A. Murphy, A. Orlando, C. O’Sullivan, L. Piccirillo, C. Pryke, N. Rajguru, B. Rusholme, R. Schwarz, A. N. Taylor, K. L. Thompson, A. H. Turner, E. Y. S. Wu, M. Zemcov, and The QUaD collaboration. Improved Measurements of the Temperature and Polarization of the Cosmic Microwave Background from QUaD. *ApJ*, 705:978–999, November 2009.
- [44] J. Dunkley, R. Hlozek, J. Sievers, V. Acquaviva, P. A. R. Ade, P. Aguirre, M. Amiri, J. W. Appel, L. F. Barrientos, E. S. Battistelli, J. R. Bond, B. Brown, B. Burger, J. Chervenak, S. Das, M. J. Devlin, S. R. Dicker, W. Bertrand Doriese, R. Dunner, T. Essinger-Hileman, R. P. Fisher, J. W. Fowler, A. Hajian, M. Halpern, M. Hasselfield, C. Hernandez-Monteagudo, G. C. Hilton, M. Hilton, A. D. Hincks, K. M. Huffenberger, D. H. Hughes, J. P. Hughes, L. Infante, K. D. Irwin, J. B. Juin, M. Kaul, J. Klein, A. Kosowsky, J. M. Lau, M. Limon, Y. Lin, R. H. Lupton, T. A. Marriage, D. Marsden, P. Mauskopf, F. Menanteau, K. Moodley, H. Moseley, C. B. Netterfield, M. D. Niemack, M. R. Nolta, L. A. Page, L. Parker, B. Partridge, B. Reid, N. Sehgal, B. Sherwin, D. N. Spergel, S. T. Staggs, D. S. Swetz, E. R. Switzer, R. Thornton, H. Trac, C. Tucker, R. Warne, E. Wollack, and Y. Zhao. The Atacama Cosmology Telescope: Cosmological Parameters from the 2008 Power Spectra. *ArXiv e-prints*, September 2010.

- [45] W. J. Percival, S. Cole, D. J. Eisenstein, R. C. Nichol, J. A. Peacock, A. C. Pope, and A. S. Szalay. Measuring the Baryon Acoustic Oscillation scale using the Sloan Digital Sky Survey and 2dF Galaxy Redshift Survey. *MNRAS*, 381:1053–1066, November 2007.
- [46] A. G. Riess, L. Macri, S. Casertano, M. Sosey, H. Lampeitl, H. C. Ferguson, A. V. Filippenko, S. W. Jha, W. Li, R. Chornock, and D. Sarkar. A Redetermination of the Hubble Constant with the Hubble Space Telescope from a Differential Distance Ladder. *ApJ*, 699:539–563, July 2009.
- [47] M. Hicken, W. M. Wood-Vasey, S. Blondin, P. Challis, S. Jha, P. L. Kelly, A. Rest, and R. P. Kirshner. Improved Dark Energy Constraints from  $\sim 100$  New CfA Supernova Type Ia Light Curves. *ApJ*, 700:1097–1140, August 2009.
- [48] E. M. Leitch, J. M. Kovac, N. W. Halverson, J. E. Carlstrom, C. Pryke, and M. W. E. Smith. Degree Angular Scale Interferometer 3 Year Cosmic Microwave Background Polarization Results. *ApJ*, 624:10–20, May 2005.
- [49] T. E. Montroy, P. A. R. Ade, J. J. Bock, J. R. Bond, J. Borrill, A. Boscaleri, P. Cabella, C. R. Contaldi, B. P. Crill, P. de Bernardis, G. De Gasperis, A. de Oliveira-Costa, G. De Troia, G. di Stefano, E. Hivon, A. H. Jaffe, T. S. Kisner, W. C. Jones, A. E. Lange, S. Masi, P. D. Mauskopf, C. J. MacTavish, A. Melchiorri, P. Natoli, C. B. Netterfield, E. Pascale, F. Piacentini, D. Pogosyan, G. Polenta, S. Prunet, S. Ricciardi, G. Romeo, J. E. Ruhl, P. Santini, M. Tegmark, M. Veneziani, and N. Vittorio. A Measurement of the CMB  $\langle EE \rangle$  Spectrum from the 2003 Flight of BOOMERANG. *ApJ*, 647:813–822, August 2006.
- [50] F. Piacentini, P. A. R. Ade, J. J. Bock, J. R. Bond, J. Borrill, A. Boscaleri, P. Cabella, C. R. Contaldi, B. P. Crill, P. de Bernardis, G. De Gasperis, A. de Oliveira-Costa, G. De Troia, G. di Stefano, E. Hivon, A. H. Jaffe, T. S. Kisner, W. C. Jones, A. E. Lange, S. Masi, P. D. Mauskopf, C. J. MacTavish, A. Melchiorri, T. E. Montroy, P. Natoli, C. B. Netterfield, E. Pascale, D. Pogosyan, G. Polenta, S. Prunet, S. Ricciardi, G. Romeo, J. E. Ruhl, P. Santini, M. Tegmark, M. Veneziani, and N. Vittorio. A Measurement of the Polarization-Temperature

Angular Cross-Power Spectrum of the Cosmic Microwave Background from the 2003 Flight of BOOMERANG. *ApJ*, 647:833–839, August 2006.

- [51] J. L. Sievers, C. Achermann, J. R. Bond, L. Bronfman, R. Bustos, C. R. Contaldi, C. Dickinson, P. G. Ferreira, M. E. Jones, A. M. Lewis, B. S. Mason, J. May, S. T. Myers, N. Oyarce, S. Padin, T. J. Pearson, M. Pospieszalski, A. C. S. Readhead, R. Reeves, A. C. Taylor, and S. Torres. Implications of the Cosmic Background Imager Polarization Data. *ApJ*, 660:976–987, May 2007.
- [52] J. H. P. Wu, J. Zuntz, M. E. Abroe, P. A. R. Ade, J. Bock, J. Borrill, J. Collins, S. Hanany, A. H. Jaffe, B. R. Johnson, T. Jones, A. T. Lee, T. Matsumura, B. Rabii, T. Renbarger, P. L. Richards, G. F. Smoot, R. Stompor, H. T. Tran, and C. D. Winant. MAXIPOL: Data Analysis and Results. *ApJ*, 665:55–66, August 2007.
- [53] C. Bischoff, L. Hyatt, J. J. McMahon, G. W. Nixon, D. Samtleben, K. M. Smith, K. Vanderlinde, D. Barkats, P. Farese, T. Gaier, J. O. Gundersen, M. M. Hedman, S. T. Staggs, and B. Winstein. New Measurements of Fine-Scale CMB Polarization Power Spectra from CAPMAP at Both 40 and 90 GHz. *ApJ*, 684:771–789, September 2008.
- [54] M. R. Nolta, J. Dunkley, R. S. Hill, G. Hinshaw, E. Komatsu, D. Larson, L. Page, D. N. Spergel, C. L. Bennett, B. Gold, N. Jarosik, N. Odegard, J. L. Weiland, E. Wollack, M. Halpern, A. Kogut, M. Limon, S. S. Meyer, G. S. Tucker, and E. L. Wright. Five-Year Wilkinson Microwave Anisotropy Probe Observations: Angular Power Spectra. *ApJS*, 180:296–305, February 2009.
- [55] W. Hu and T. Okamoto. Mass Reconstruction with Cosmic Microwave Background Polarization. *ApJ*, 574:566–574, August 2002.
- [56] A. Lewis and A. Challinor. Weak gravitational lensing of the CMB. *Phys. Rep.*, 429:1–65, June 2006.
- [57] The Planck Collaboration. The Scientific Programme of Planck. *ArXiv Astrophysics e-prints*, April 2006.

- [58] L. Knox. Determination of inflationary observables by cosmic microwave background anisotropy experiments. *Phys. Rev. D*, 52:4307–4318, October 1995.
- [59] Y. Mizugutch, M. Akagawa, and H. Yokoi. Offset dual reflector antenna. *IEEE Antennas and Propagation Society International Symposium*, 14:2–5, 1976.
- [60] C. Dragone. Offset multireflector antennas with perfect pattern symmetry and polarization discrimination. *Bell Syst. Tech. J.*, 57:2663–2684, 1978.
- [61] William A. Imbriale, Joshua Gundersen, and Keith L. Thompson. The 1.4 meter Telescope for the Q/U Imaging Experiment. *To appear in the Special Issue on Radio Astronomy in the IEEE Transactions on Antennas and Propagation*, 2010.
- [62] J. Gundersen and E. Wollack. Millimeter Wave Corrugated Platelet Feeds. *Journal of Physics: Conf. Ser.*, 155:012005, 2009.
- [63] J. Bornemann and V. A. Labay. Ridge waveguide polarizer with finite and stepped-thickness septum. *IEEE Trans. MTT*, 43:95, 1995.
- [64] S. Padin, M. C. Shepherd, J. K. Cartwright, R. G. Keeney, B. S. Mason, T. J. Pearson, A. C. S. Readhead, W. A. Schaal, J. Sievers, P. S. Udomprasert, J. K. Yamasaki, W. L. Holzapfel, J. E. Carlstrom, M. Joy, S. T. Myers, and A. Otterola. The Cosmic Background Imager. *PASP*, 114:83–97, January 2002.
- [65] L. Newburgh et al. Measuring CMB Polarization with QUIET: The Q/U Imaging Experiment. *to appear in Proceedings of the Twelfth Marcel Grossmann Meeting on General Relativity*, 2010.
- [66] A. Kusaka et al. The QUIET experiment. *to appear in Proceedings of the 45th Rencontre de Moriond*, 2010.
- [67] Immanuel Buder. Q/U Imaging Experiment (QUIET): a ground-based probe of cosmic microwave background polarization. *Proc. SPIE*, 7741(1):77411D, 2010.
- [68] Kieran A. Cleary. Coherent polarimeter modules for the quiet experiment. volume 7741, page 77412H. SPIE, 2010.

- [69] T. Gaier, C. R. Lawrence, M. D. Seiffert, M. M. Wells, P. Kangaslahti, and D. Dawson. Amplifier arrays for CMB polarization. *New Astronomy Review*, 47:1167–1171, December 2003.
- [70] J. R. Pardo, J. Cernicharo, and E. Serabyn. Atmospheric transmission at microwaves (ATM): an improved model for millimeter/submillimeter applications. *IEEE Transactions on Antennas and Propagation*, 49:1683–1694, December 2001.
- [71] R. Güsten, L. Å. Nyman, P. Schilke, K. Menten, C. Cesarsky, and R. Booth. The Atacama Pathfinder EXperiment (APEX) - a new submillimeter facility for southern skies -. *A&A*, 454:L13–L16, August 2006.
- [72] N. Jarosik, C. L. Bennett, J. Dunkley, B. Gold, M. R. Greason, M. Halpern, R. S. Hill, G. Hinshaw, A. Kogut, E. Komatsu, D. Larson, M. Limon, S. S. Meyer, M. R. Nolta, N. Odegard, L. Page, K. M. Smith, D. N. Spergel, G. S. Tucker, J. L. Weiland, E. Wollack, and E. L. Wright. Seven-Year Wilkinson Microwave Anisotropy Probe (WMAP) Observations: Sky Maps, Systematic Errors, and Basic Results. *ArXiv e-prints*, January 2010.
- [73] S. Hanany and P. Rosenkranz. Polarization of the atmosphere as a foreground for cosmic microwave background polarization experiments. *New Astronomy Review*, 47:1159–1165, December 2003.
- [74] L. Pietranera, S. A. Buehler, P. G. Calisse, C. Emde, D. Hayton, V. Oommen John, B. Maffei, L. Piccirillo, G. Pisano, G. Savini, and T. R. Sreerekha. Observing cosmic microwave background polarization through ice. *MNRAS*, 376:645–650, April 2007.
- [75] J. J. Hester. The Crab Nebula: An Astrophysical Chimera. *ARA&A*, 46:127–155, September 2008.
- [76] J. L. Weiland, N. Odegard, R. S. Hill, E. Wollack, G. Hinshaw, M. R. Greason, N. Jarosik, L. Page, C. L. Bennett, J. Dunkley, B. Gold, M. Halpern, A. Kogut, E. Komatsu, D. Larson, M. Limon, S. S. Meyer, M. R. Nolta, K. M. Smith, D. N. Spergel, G. S. Tucker, and E. L. Wright. Seven-Year Wilkinson

Microwave Anisotropy Probe (WMAP) Observations: Planets and Celestial Calibration Sources. *ArXiv e-prints*, January 2010.

- [77] L. Page, G. Hinshaw, E. Komatsu, M. R. Nolta, D. N. Spergel, C. L. Bennett, C. Barnes, R. Bean, O. Doré, J. Dunkley, M. Halpern, R. S. Hill, N. Jarosik, A. Kogut, M. Limon, S. S. Meyer, N. Odegard, H. V. Peiris, G. S. Tucker, L. Verde, J. L. Weiland, E. Wollack, and E. L. Wright. Three-Year Wilkinson Microwave Anisotropy Probe (WMAP) Observations: Polarization Analysis. *ApJS*, 170:335–376, June 2007.
- [78] H. D. Aller and S. P. Reynolds. The decrease with time of the radio flux of the Crab Nebula. *ApJ*, 293:L73–L75, June 1985.
- [79] J. Aumont, L. Conversi, E. Falgarone, J. F. Macias-Perez, F. Piacentini, E. Pointecouteau, N. Ponthieu, J. L. Puget, C. Rosset, C. Thum, M. Tristram, and H. Wiesemeyer. Measurement of the Crab nebula polarization at 90 GHz as a calibrator for CMB experiments. *ArXiv e-prints*, December 2009.
- [80] F. James and M. Roos. Minuit: A System for Function Minimization and Analysis of the Parameter Errors and Correlations. *Comput. Phys. Commun.*, 10:343–367, 1975.
- [81] L. Page, C. Barnes, G. Hinshaw, D. N. Spergel, J. L. Weiland, E. Wollack, C. L. Bennett, M. Halpern, N. Jarosik, A. Kogut, M. Limon, S. S. Meyer, G. S. Tucker, and E. L. Wright. First-Year Wilkinson Microwave Anisotropy Probe (WMAP) Observations: Beam Profiles and Window Functions. *ApJS*, 148:39–50, September 2003.
- [82] Raul A. Monsalve. Beam characterization for the quiet q-band instrument using polarized and unpolarized astronomical sources. *Proc. SPIE*, 7741(1):77412M, 2010.
- [83] M. Abramowitz and I. A. Stegun. *Handbook of Mathematical Functions*. 1972.
- [84] K. M. Huffenberger, B. P. Crill, A. E. Lange, K. M. Górski, and C. R. Lawrence. Measuring Planck beams with planets. *A&A*, 510:A58+, February 2010.



- [85] K. M. Górski, E. Hivon, A. J. Banday, B. D. Wandelt, F. K. Hansen, M. Reinecke, and M. Bartelmann. HEALPix: A Framework for High-Resolution Discretization and Fast Analysis of Data Distributed on the Sphere. *ApJ*, 622:759–771, April 2005.
- [86] E. Hivon, K. M. Górski, C. B. Netterfield, B. P. Crill, S. Prunet, and F. Hansen. MASTER of the Cosmic Microwave Background Anisotropy Power Spectrum: A Fast Method for Statistical Analysis of Large and Complex Cosmic Microwave Background Data Sets. *ApJ*, 567:2–17, March 2002.
- [87] F. K. Hansen and K. M. Górski. Fast cosmic microwave background power spectrum estimation of temperature and polarization with Gabor transforms. *MNRAS*, 343:559–584, August 2003.
- [88] M. L. Brown, P. G. Castro, and A. N. Taylor. Cosmic microwave background temperature and polarization pseudo- $C_\ell$  estimators and covariances. *MNRAS*, 360:1262–1280, July 2005.
- [89] M. Tegmark, A. N. Taylor, and A. F. Heavens. Karhunen-Loeve Eigenvalue Problems in Cosmology: How Should We Tackle Large Data Sets? *ApJ*, 480:22–+, May 1997.
- [90] J. R. Bond, A. H. Jaffe, and L. Knox. Estimating the power spectrum of the cosmic microwave background. *Phys. Rev. D*, 57:2117–2137, February 1998.
- [91] B. D. Wandelt, E. Hivon, and K. M. Górski. Cosmic microwave background anisotropy power spectrum statistics for high precision cosmology. *Phys. Rev. D*, 64(8):083003–+, October 2001.
- [92] H. A. Feldman, N. Kaiser, and J. A. Peacock. Power-spectrum analysis of three-dimensional redshift surveys. *ApJ*, 426:23–37, May 1994.
- [93] A. Challinor and G. Chon. Error analysis of quadratic power spectrum estimates for cosmic microwave background polarization: sampling covariance. *MNRAS*, 360:509–532, June 2005.

- [94] K. M. Smith and M. Zaldarriaga. General solution to the E-B mixing problem. *Phys. Rev. D*, 76(4):043001–+, August 2007.
- [95] Kendrick M. Smith. Pseudo- $c_\ell$  estimators which do not mix e and b modes. *Phys. Rev. D*, 74(8):083002, Oct 2006.
- [96] J. Grain, M. Tristram, and R. Stompor. Polarized cmb power spectrum estimation using the pure pseudo-cross-spectrum approach. *Phys. Rev. D*, 79(12):123515, Jun 2009.
- [97] S. Hamimeche and A. Lewis. Likelihood analysis of CMB temperature and polarization power spectra. *Phys. Rev. D*, 77(10):103013–+, May 2008.
- [98] C. Barnes, R. S. Hill, G. Hinshaw, L. Page, C. L. Bennett, M. Halpern, N. Jarosik, A. Kogut, M. Limon, S. S. Meyer, G. S. Tucker, E. Wollack, and E. L. Wright. First-year wilkinson microwave anisotropy probe (wmap) observations: Galactic signal contamination from sidelobe pickup. *The Astrophysical Journal Supplement Series*, 148(1):51, 2003.
- [99] J. R. Hinderks, P. Ade, J. Bock, M. Bowden, M. L. Brown, G. Cahill, J. E. Carlstrom, P. G. Castro, S. Church, T. Culverhouse, R. Friedman, K. Ganga, W. K. Gear, S. Gupta, J. Harris, V. Haynes, B. G. Keating, J. Kovac, E. Kirby, A. E. Lange, E. Leitch, O. E. Mallie, S. Melhuish, Y. Memari, A. Murphy, A. Orlando, R. Schwarz, C. O. Sullivan, L. Piccirillo, C. Pryke, N. Rajguru, B. Rusholme, A. N. Taylor, K. L. Thompson, C. Tucker, A. H. Turner, E. Y. S. Wu, and M. Zemcov. QUaD: A High-Resolution Cosmic Microwave Background Polarimeter. *ApJ*, 692:1221–1246, February 2009.
- [100] D. L. Sackett. Bias in analytic research. *J Chronic Dis*, 32(1-2):51–63, 1979.
- [101] E. S. Battistelli, R. Rebolo, J. A. Rubiño-Martín, S. R. Hildebrandt, R. A. Watson, C. Gutiérrez, and R. J. Hoyland. Polarization Observations of the Anomalous Microwave Emission in the Perseus Molecular Complex with the COSMOSOMAS Experiment. *ApJ*, 645:L141–L144, July 2006.

- [102] B. T. Draine and A. Lazarian. Diffuse Galactic Emission from Spinning Dust Grains. *ApJ*, 494:L19+, February 1998.
- [103] B. T. Draine and A. Lazarian. Electric Dipole Radiation from Spinning Dust Grains. *ApJ*, 508:157–179, November 1998.
- [104] A. Kogut, D. J. Fixsen, S. M. Levin, M. Limon, P. M. Lubin, P. Mirel, M. Seiffert, J. Singal, T. Villela, E. Wollack, and C. A. Wuensche. ARCADE 2 Observations of Galactic Radio Emission. *ArXiv e-prints*, January 2009.
- [105] B. Gold, N. Odegard, J. L. Weiland, R. S. Hill, A. Kogut, C. L. Bennett, G. Hinshaw, X. Chen, J. Dunkley, M. Halpern, N. Jarosik, E. Komatsu, D. Larson, M. Limon, S. S. Meyer, M. R. Nolta, L. Page, K. M. Smith, D. N. Spergel, G. S. Tucker, E. Wollack, and E. L. Wright. Seven-Year Wilkinson Microwave Anisotropy Probe (WMAP) Observations: Galactic Foreground Emission. *ArXiv e-prints*, January 2010.
- [106] J. Dunkley, D. N. Spergel, E. Komatsu, G. Hinshaw, D. Larson, M. R. Nolta, N. Odegard, L. Page, C. L. Bennett, B. Gold, R. S. Hill, N. Jarosik, J. L. Weiland, M. Halpern, A. Kogut, M. Limon, S. S. Meyer, G. S. Tucker, E. Wollack, and E. L. Wright. Five-Year Wilkinson Microwave Anisotropy Probe (WMAP) Observations: Bayesian Estimation of Cosmic Microwave Background Polarization Maps. *ApJ*, 701:1804–1813, August 2009.
- [107] A. Lue, L. Wang, and M. Kamionkowski. Cosmological Signature of New Parity-Violating Interactions. *Physical Review Letters*, 83:1506–1509, August 1999.
- [108] B. Feng, M. Li, J.-Q. Xia, X. Chen, and X. Zhang. Searching for CPT Violation with Cosmic Microwave Background Data from WMAP and BOOMERANG. *Physical Review Letters*, 96(22):221302–+, June 2006.
- [109] W. Hu, M. M. Hedman, and M. Zaldarriaga. Benchmark parameters for CMB polarization experiments. *Phys. Rev. D*, 67(4):043004–+, February 2003.
- [110] G. B. Rybicki and A. P. Lightman. *Radiative processes in astrophysics*. 1979.

- [111] John D. Jackson. *Classical Electrodynamics Third Edition*. Wiley, third edition, August 1998.
- [112] R. K. Sachs and A. M. Wolfe. Perturbations of a Cosmological Model and Angular Variations of the Microwave Background. *ApJ*, 147:73–+, January 1967.
- [113] L. F. Abbott and Mark B. Wise. Large-scale anisotropy of the microwave background and the amplitude of energy density fluctuations in the early universe. *Astrophys. J.*, 282:L47–L50, 1984.
- [114] Andrew H. Jaffe, Marc Kamionkowski, and Limin Wang. Polarization pursuers’ guide. *Phys. Rev. D*, 61(8):083501, Mar 2000.
- [115] Colin Bischoff. *Observing the Cosmic Microwave Background Polarization Anisotropy at 40 GHz with QUIET*. PhD thesis, The University of Chicago, August 2010.
- [116] Martin Houde, Rachel L. Akeson, John E. Carlstrom, James W. Lamb, David A. Schleuning, and David P. Woody. Polarizing grids, their assemblies, and beams of radiation. *Publications of the Astronomical Society of the Pacific*, 113(783):622–638, 2001.
- [117] O. Tajima. Sparse wiregrid analysis in Q-band. QUIET internal memo, December 2009.
- [118] O. Tajima, C. Bischoff, and Y. Chinone. Q-band detector angle summary and systematic error. QUIET internal memo, June 2010.